# RADON DISPERSION FROM A SOUTH AFRICA GOLD MINE-TAILINGS DAM – MEASUREMENT AND MODELLING

**FRANK SOLOMON TONNY KOMATI**

Thesis submitted in fulfilment of the requirements for the Degree

**DOCTOR of PHILOSOPHY:**

**ENVIRONMENTAL HEALTH**

in the

Department of Health Sciences
Faculty of Health and Environmental Sciences

at the

Central University of Technology, Free State

Promoter: Prof OM Ntwaeaborwa (PhD)
Co-promoter: Dr R Strydom (PhD)
Co-promoter: Dr NJ Malebo (PhD))

BLOEMFONTEIN
February 2020

# Declaration of Independent Work

**Declaration With Regard To Independent Work**

I, FRANK SOLOMON TONNY KOMATI, identity number

and student number , do hereby declare that this research project submitted to the Central University of Technology, Free State for the Degree DOCTOR OF PHILOSOPHY: ENVIRONMENTAL HEALTH, is my own independent work; and complies with the Code of Academic Integrity, as well as other relevant policies, procedures, rules and regulations of the Central University of Technology, Free State; and has not been submitted before to any institution by myself of any other person in fulfilment (or partial fulfilment) of the requirements for the attainment of any qualification.

_____ February 2020

**Signature of Student** **Date**

# Acknowledgements

I would like to profoundly thank the many people who contributed generously to the work presented in this thesis.

Firstly, I would like to express my sincere gratitude to my enthusiastic supervisor and mentor Dr Rian Strydom for his continuous support of my study and related research, for his patience, motivation, and immense knowledge. His guidance helped me in all the time of research and writing of this thesis. I could not have imagined having a better advisor and mentor for my study. I will forever cherish fond memories of our meetings at our Mugg and Bean (Cresta) “offices”.

Similar profound gratitude goes to Prof Martin Ntwaeaborwa, who has been a truly dedicated co-supervisor and mentor. I am particularly indebted to Prof Martin for his faith in me, encouragement, guidance, insightful comments, hard questions and patience over the years.

To Dr Ntswaki Malebo, a special thank you for accepting to take the co-supervisory and administrative baton when I needed one.

My sincere thank you also goes to Dr Carien Weyers and Prof Karabo Shale for having trust in me during the initial stages of my study. Thank you for kick-starting this process and making sure that it succeeds.

Special mention goes to the late Dirk Venter (MHSRIP) (Radiation Protection Manager, Harmony Gold), Jaco Smith, Jaco Cronje (Fraser Alexander Tailings) and Motheo Security (Welkom) for allowing me access to the their tailings facilities and providing security during field sampling.

To Prof Victor Tshivhase and Prof Manny Matutu at the Centre for Applied Radiation Science and Technology (CARST), North West University, a sincere thank you for your support and for providing me with access to your equipment.

A special thank you to Dr Puseletso Mokoena for her unwavering support and assistance. Thank you for pushing me and ensuring that I see through the thesis through difficult moments. You were God send. To Dr Tabaro Kabanda, Dr Themba Tshabalala and Mr Lethani Ndwandwe at Sol Plaatje University, thank you very much for your support, assistance and valuable advice when I needed one. I also thank Terrence Noko, Tom Akinlaja, Bhekie Danisa, Boipelo Molongwane, Andisani Nkosi, Levona Leeuw, Masego Mosala, Ms Angie Sediti, "Mbes" and Hloni Molikoe for their great assistance during sampling and data analysis.

A special thank you to EDTP Seta (Kimberley) and Central University of Technology (Bloemfontein) for financial support.

Finally, but by no means least, I would like to thank my family for their unbelievable support.

Thanking you.

Frank

# Abstract

Radon has been recognised as the main contributor to the natural radiation dose exposure to human. In addition to natural radon, human activities like mining have the potential to enhance environmental radon levels. Gold-mine tailings dams contain traces of $^{238}U$ and $^{226}Ra$, leading to generation of $^{222}Rn$ gas in the tailings material due to radioactive decay. Current methods used to monitor radon from the tailings dams are only able to provide a close-up of emissions in space and time. These methods cannot distinguish between tailings radon and background radon as well as the extent each contributes towards the radon content in the atmosphere. The only way to determine the increment is through dispersion modelling. This study develops a technique to accurately validate radon dispersion modelling that assesses the radon contribution from Freddies 9 (sometimes referred to as Steyn 9) tailings dam situated in Odendaalsrus, Free State Province, South Africa. This study was structured into four parts. The first part dealt with determination of the radon exhalation rate from the tailings dam. The second part dealt with measuring the ambient radon concentration in the vicinity of the dam using Radon Gas Monitors (RGMs). The third part was to measure radon gas, individual radon daughters, and the F factor at different receptor points downwind by following the direction of the wind at hourly intervals. The fourth part involved using the ISCST3 dispersion modelling code to evaluate radon transport and the effects of local variations around the tailings dam. Field data were collected during winter months of June to August in 2016 and 2017.

Measurements of the radon exhalation rate, which is the source term for dispersion modelling from the tailings dam, were performed with the passive diffusion tube method. Twenty (20) tailings samples were collected for analysis. The exhalation rate (E) was found to vary from 0.045 Bq/($m^2$s) to 0.443 Bq/($m^2$s) with an average value of 0.102 Bq/$m^2$s and a mean standard deviation of 0.087 Bq/($m^2$s).

The ambient radon concentration values measured with the Radon Gas Monitors (RGMs), averaged over 116 locations around the tailings dam distributed over a radius of 2 km from the tailings dam, range from 38 Bq/m$^3$ to 94 Bq/m$^3$, with a mean concentration of 64 ± 11 Bq/m$^3$. These values are below the 100 Bq/m$^3$ action level stipulated by the National Nuclear Regulator (NNR) with a slight average increase compared to background levels of 60 Bq/m$^3$.

Airborne radon concentration at any given location is influenced by locally exhaled radon and dispersed radon from other locations. As a means of trying to discriminate between different radon contributors, radon gas, individual radon daughters, and the F factor were measured at different receptor points downwind and upwind by following the direction of the wind at hourly intervals. The AlphaGUARD was used to measure radon concentration and the Eberline SPA-1A alpha scintillation detector coupled to Eberline Smart Portable (ESP-2) counter were used to measure the radon daughters. The Busigin and Phillips three count method was used to calculate radon daughter concentrations and hence the F factor. The minimum value of F factor was 0.016 ± 0.012 measured upwind whereas the maximum value of F factor was 0.502 ± 0.044 measured downwind.

Calculations revealed strong influence by external meteorological effects on the distribution of radon and radon daughters some distance from the tailings and background. The F factor, which indicates the “age” of the gas, and radon gas, increased to their highest values when the wind was blowing from north-northern-east (NNE). The highest radon daughter concentrations at various locations were recorded in the mornings. However, fluctuating and conflicting effects due to different meteorological conditions on the resultant atmospheric radon concentration, radon daughters’ concentration and F factor as functions of distance from the tailings downwind, made the interpretation of results difficult. To further quantitatively explain these results, an air dispersion model was applied.

The USA Environmental Protection Agency's (EPA) Industrial Source Complex Short Term 3 (ISCST3) dispersion modelling code using a Gaussian plume model was used to evaluate radon transport and the effects of local variations around the tailings dam. The tailings was modelled as point, total emitting surface area (true geometry) and volume source. The true area geometry was considered as the baseline source geometry. To improve the accuracy of the model predictions as compared to traditional approaches, the area source term was corrected to account for cracks and fissures on the tailings and the geometry of tailings dam was modelled by taking into account all emitting surfaces as sources.

Compared to the baseline, the model over predicted the flat ground area source by up to 274 % and under predicted the top level area source by up to 50%. The volume emission source was over predicted by up to 300% in 60% of the modelling runs and under predicted by 55% in 40% of the volume model runs. While the top level area source term produced lower concentrations at near-field ground-level receptors, accounting for the wakes effect increased the radon concentrations from the top-level area source of the tailings dam by up to 239%.

From modeling results, the highest concentration predicted by the model from the true geometry source was found to be 0.843 Bq/m$^3$, which correspond to the dose of 0.012 mSv/y to the public of due to radon from the tailings. This value is less than the 1 mSv/y dose constraint stipulated by the NNR.

Model validation from statistical analysis showed a constant trend for all the scenarios, with minimum variability in the Index of Agreement (IOA), Normalized Mean Square Error (NMSE) and Fraction of predictions within a factor of two (FAC2) values. The analysis were based on the model results over five days of measurements covering both morning and afternoon. There is an under prediction in the Fractional Bias (FB) and Geometric Mean bias (MG) on day 1 afternoon. In addition, the model performed poorly on day 3 afternoon.

Further validation of the model was carried out by isolating radon from different contributors using the “age” of the gas approach and applying back calculations to identify origin of the radon measured at each point downwind. As predicted by the model, the origin of the radon source was traced back to the tailings.

**Keywords:**

Radon, progeny, radon flux, tailings dams, F factor, dispersion modelling, wake effect, validation, background radon, radon transport.

# Table of Contents

# List of Figures

# List of tables

# Chapter 1 Introduction

## 1.1 Radioactivity and gold mining in South Africa

South Africa's gold reef, commonly known as Witwatersrand (Wits), covers a 400 km stretch across the Free State, North West and Gauteng Provinces. The region has one of the world's largest gold ore reserves and is one of the major gold contributors in the world (South Africa.info, 2012, MBendi, 2012). Over the past century, this region has been characterised by geological exploration, industrialisation, mining activities and increased population boom and settlement (Durand, 2012).

According to UNSCEAR (2008) South Africa's deep underground gold deposits contain low grade uranium. Considering that the gold content in the ore is far much lower compared to uranium with gold to uranium ratio ranging from about 1:10 to 1:100 (Winde, Sandham, 2004), gold mining operations have resulted in substantial amounts of uranium and undesirable radioactive materials being brought to the surface and disposed as waste on tailings dams. Sulphuric acid leaching and uranium recovery processes extract up to 90% of the original uranium content from the ore, resulting in increased uranium concentrations in the tailings and slime dams (Wendel, 1998). On the Witwatersrand, about 6 tonnes of tailings are produced for every 1 kg of uranium extracted. To date, there is approximately 6000 tons of radioactive uranium that is disposed onto slimes dams per year by gold mining activities in South Africa (Liefferink, 2011).

The presence and widespread environmental distribution of uranium and its decay products from the tailings pose as a major environmental radiation contributor (ATSDR, 2012, Siaway, Mose and Metcalf, 2009). This has the potential to fractionally increase public exposure beyond recommended levels. Hence, it is reasonable to assume that some of the South African gold mines have directly or indirectly

contributed to the atmospheric contamination with uranium and elevation of radioactivity, including radon concentrations in areas around the mines (Karam, Venter, 2007, Simons et al., 2006, Botha, 1998). Furthermore, mine tailings dams are likely to have significantly high levels of radioactivity which could eventually pose a serious health risk to people living around the mining areas. This study aims to validate this statement by seeking to determine the actual environmental radon contribution by tailings dams.

## 1.2 Radon: An overview

Radon is an odourless, colourless and naturally occurring inert radioactive gas at room temperature. It is produced by the radioactive alpha decay of radium-226 ($^{226}$Ra), which is found in uranium ores, phosphate rock, shales, igneous and metamorphic rocks such as granite, gneiss, schist and, to a lesser degree, in common rocks such as limestone (Godish, 2000). The symbol for radon is Rn and it has atomic number of 86 and atomic weight of 222. It is the heaviest of all the inert gases at room temperature. Radon is soluble in water, absorbed by fats, oils and charcoal.

There are over 30 known isotopes of radon. However, only three are found in nature. The three naturally occurring radon isotopes are $^{219}$Rn (actinon) from the Actinium decay series, $^{220}$Rn (thoron), a by-product of the Thorium decay series and $^{222}$Rn (radon) formed from the $^{238}$U decay series. Of the three, radon ($^{222}$Rn) has the longest half-life of 3.8 days whilst thoron and actinon have half-lives of 55.6 seconds and 3.96 seconds respectively. The relatively long radon half-life allows radon formed in the mine tailings sufficient time to diffuse through the soil into the atmosphere, where it will be carried around by air movement. In terms of radiation exposure, $^{222}$Radon, or just radon, is the important isotope. Its contribution to the overall radiation exposure to humans can be measured in various environments and locations. Radon contributes about 55% of

the annual radiation dose to the general population from all sources and 70% from natural radiation sources (George, 2007).

## 1.3 Radioactivity and radioactive decay processes

Radioactivity or radioactive decay is a natural and spontaneous process whereby an unstable nucleus of an atom (parent nucleus) loses energy by emitting ionizing radiation in its quest to attain stability. The emission of this excess energy results in either an atom of the same form with lower energy or an atom with a completely different nucleus, called daughter nucleus or progeny. There are different types of ionising radiation accompanying radioactive decay. The three that are particularly relevant to this study are alpha decay, beta decay, and gamma decay.

### 1.3.1 Alpha decay

Alpha decay occurs mainly in heavier elements of atomic number 52 (tellurium) and greater. An alpha (α) particle consists of two protons and two neutrons. It has a positive charge of 2 units and a mass number of 4 (helium nucleus). During alpha decay, a nucleus of a radioactive atom ejects an alpha particle, thus reducing the atomic number of the parent atom by 2 and the mass number by 4. This can be illustrated as

$$ {}^{A}_{Z}P \rightarrow {}^{A-4}_{Z-2}D + {}^{2}_{2}He \qquad (1.1) $$

Alpha particles are very heavy and highly energetic, with energy ranges from 4 to 5 MeV. They are short ranged, with travelling distances in air of no more than few centimetres and are stopped by human skin or sheet of paper. Due to their high energy and large positive charge, alpha particles have great destructive power, causing intense ionisations within their very short distance when ingested into the body or inhaled into the lungs. Inhalation of alpha particles can lead to possible lung cancer.

### 1.3.2 Beta decay

Beta particles are electrons or positrons (electrons with positive electric charge, or anti-electrons) emitted from a nucleus. Beta decay occurs when the nucleus decays and ejects beta particles and a neutrino or an antineutrino, in a process that transforms a proton to a neutron or the other way round. During beta decay, the daughter nucleus has the same number of nucleons as the parent, but the atomic number is changed by one.

There are three basic beta decay processes. The first beta decay process occurs when the neutron to proton ratio in the nucleus is too great, thus causing instability. In this case, a neutron decays into a proton, an electron and an antineutrino. An electron ($\beta^-$) is then emitted. That is

$$n \rightarrow p + \beta^- + antineutrino \qquad (1.2)$$

The atomic number Z increases from Z to Z+1. The electron is fast moving, escape from the atom leaving behind a positively charged atom. This can be represented by the equation:

$$^{A}_{Z}P \rightarrow {}^{A}_{Z+1}D + {}^{0}_{-1}e \qquad (1.3)$$

The second beta decay process is the positron emission ($\beta^+$). This occurs when the neutron to proton ratio is too small. A proton decays into a neutron, a positron and a neutrino. A positron is basically a positively charged electron having the same mass as an electron but carries a charge of +e instead of –e.

$$n \rightarrow p + \beta^+ + neutrino \qquad (1.4)$$

In this case, the atomic number of the parent nucleus decreases from Z to Z-1 as shown in the equation below;

$$ {}^{A}_{Z}P \rightarrow {}_{Z-1}{}^{A}D + {}^{0}_{1}e \quad (1.5) $$

The third and final type of beta decay process is known as electron capture and it also occurs when the neutron to proton ratio in the nucleus is too small. The nucleus captures one of the innermost K shell orbital electron, causing a proton to convert into a neutron.

$$ p + e^{-} \rightarrow n + \nu_e \quad (1.6) $$

Beta particles are lighter than alpha particles, can travel up to several meters in air, few millimetres in the human body and are stopped by small thickness of metal or plastic.

### 1.3.3 Gamma decay

Gamma decay occurs when an excited nucleus of an atom at a high energy state 'falls down' to a lower energy state by emitting high energy electromagnetic radiation (photons) known as gamma rays. The number of protons (and neutrons) in the nucleus remains the same in this process i.e. no change in either A or Z due to gamma emission. Therefore, the parent and daughter atoms are the same element.

## 1.4 Radioactive decay series

Radioactive decay series is the sequential decay of one unstable nucleus after another until the sequence ends with a stable, non-radioactive atom. In the uranium-238 decay series, $^{238}$U is the first element in a long series of decay that produces radium and radon. Uranium is referred to as the parent element, and radium and radon are called daughters. The $^{238}$U decay series is shown in figure 1.1. There are 14 decay stages that yield 14 radioactive isotopes in the uranium ore. Of the fourteen decay stages, ten occur in the tailings. Six of those ten in the tailings occur by the emission of alpha particles.

Radon is the only radioactive gas formed in the $^{238}U$ series. It decays by emitting an alpha particle to form a number of daughter products called radon progeny. The radioactive half-lives of the progeny vary from microseconds to minutes to years. The progeny are either attached to airborne materials like fine aerosol particles or as free solid metal oxides in the air. As a result, radon progeny will always be present in significantly large quantities as long as radon is present.

There are two categories of radon progeny, namely "short-lived" and "long-lived" progenies. The short lived progenies, whose half-lives are below 30 minutes are $^{218}Po$ (RaA; 3.05 min), $^{214}Pb$ (RaB; 26.8 min), $^{214}Bi$ (RaC; 19.7 min) and $^{214}Po$ (RaC'; 164 µs); and the "long-lived" progenies are $^{210}Pb$ (RaD; 22.3 yr), $^{210}Bi$ (RaE; 5.01days) and $^{210}Po$ (RaF; 138.4 days) (Porstendörfer, 1994).

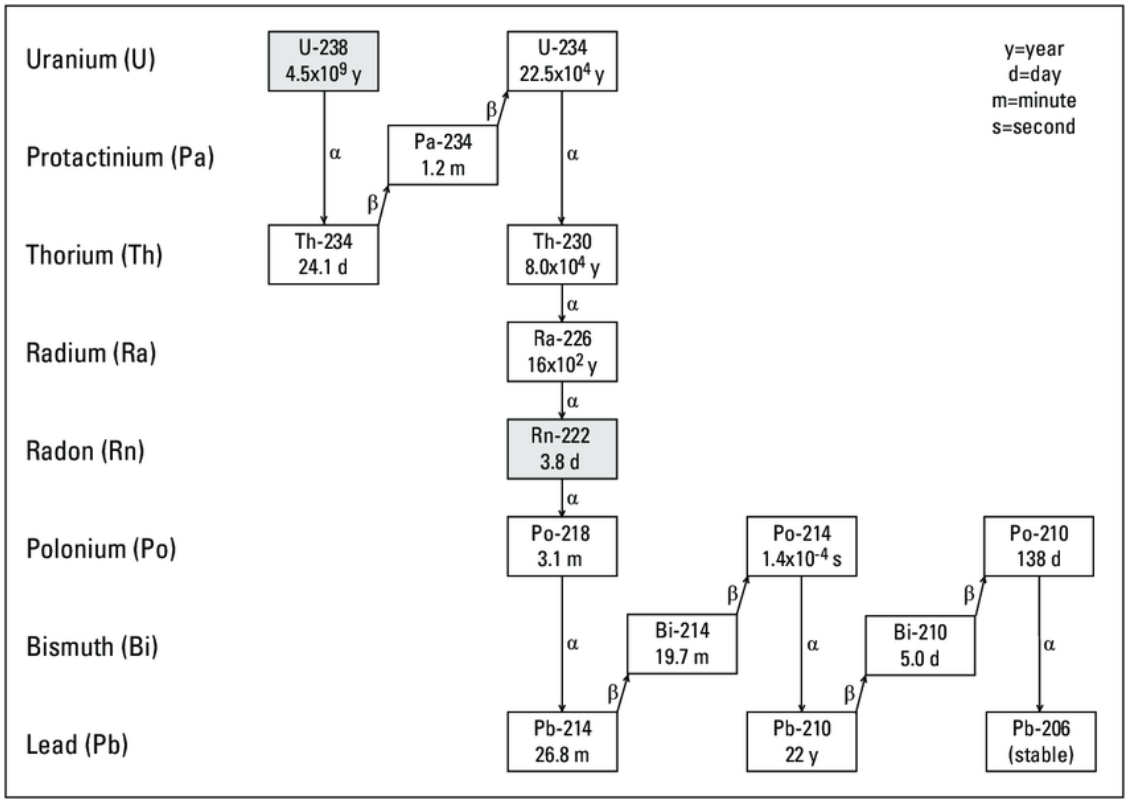


**Figure 1.1: $^{238}U$ decay chain, including $^{222}Rn$ and its decay products (Adopted from (Ayotte, Flanagan and Morrow, 2007).**

The most important radon daughters for this study are the "short-lived" daughters because of their significant contribution to the radiation doses administered to humans. Their properties and those of the parent radon are listed in table 1.1. The quantity of radon daughters in air depends on the ambient radon concentration, atmospheric dilution (dispersion) and the time for build-up during which the radon daughters have accumulated.

## 1.5 Radioactive decay law and half-life

The radioactive decay process is governed by statistical chance that is proportionally equal to the parent nucleus' degree of instability. This statistical nature of the decay process forms the basis of the fundamental law of radioactive decay. The decay probability is therefore a function of an atomic nucleus present and remains equal in time.

*Table 1.1: Radioactive properties of $^{222}Rn$ and its short-lived progeny (Keith, Doyle and Harper, 2012)*

| Isotope | Historical Symbol | Mode of radiation(s) | Q-value (MeV) | Half-life | Specific activity (Ci/g) |
|---|---|---|---|---|---|
| $^{222}Rn$ | Rn | A | 5.5903 | 3.8235 d | $1.54\times10^{5}$ |
| $^{218}Po$ | RaA | A | 6.1147 | 3.098 min | $2.78\times10^{8}$ |
| $^{214}Pb$ | RaB | β,γ | 1.023 | 26.8 min | $3.28\times10^{7}$ |
| $^{214}Bi$ | RaC | β,γ | 5.6168 | 19.9 min | $4.41\times10^{7}$ |
| $^{214}Po$ | RaC' | A | 7.8335 | 164.3 μ sec | $3.21\times10^{14}$ |

This law can be expressed mathematically as:

$$-\frac{dN}{dt} = \lambda N \qquad (1.7)$$

where $N$ is the number of radioactive nuclei at time $t$, $-dN/dt$ is the decrease (negative) of $N$ per unit of time and $\lambda$ ($s^{-1}$) is the decay constant of each specific nuclide. Equation (1.7) denotes the probability of decay per nucleus per unit time. The product λN, known as radioactivity or decay rate (A), is defined as the number of nuclear disintegrations per unit of time, i.e.

$$A = -\frac{dN}{dt} = \lambda N \tag{1.8}$$

Solving equation (1.7) by integration and applying the boundary conditions that at $t = 0$ and $N = N_0$, gives the following solution:

$$ln\left(\frac{N}{N_0}\right) = -\lambda t \tag{1.9}$$

Rearranging equation (1.9) gives the equation of exponential decay:

$$N = N_0 e^{-\lambda t} \tag{1.10}$$

or using equation (1.8):

$$A = A_0 e^{-\lambda t} \tag{1.11}$$

Equations (1.10) and (1.11) relate the rate of decrease of the original number of radioactive nuclei ($N_0$) to the original radioactivity ($A_0$).

Bateman (1910) developed a general equation for a series of decay chains, such as the heavy decay chains of $^{232}Th$, $^{235}U$, and $^{238}U$. It is a time dependent mathematical model based on the decay rates and initial abundances that describe activities and abundances in a decay chain. Assuming that the concentrations of all the daughters are initially zero,

i.e., at $t = 0$ the parent substance alone is present, thus $N_2^0 = N_3^0 = N_4^0 = \cdots = N_n^0 = 0$. Therefore for a chain of three or more radioactive products, the solution of amount of the $n^{th}$ radionuclide determined from Bateman equations is given by:

$$N_n = C_1 e^{-\lambda_1 t} + C_2 e^{-\lambda_2 t} + C_3 e^{-\lambda_3 t} + \cdots + C_n e^{-\lambda_n t} \qquad (1.12)$$

where

$$C_1 = \frac{\lambda_1 \lambda_2 \ldots \lambda_{n-1}}{(\lambda_2 - \lambda_1)(\lambda_3 - \lambda_1) \ldots (\lambda_n - \lambda_1)} N_1^0$$

$$C_1 = \frac{\lambda_1 \lambda_2 \ldots \lambda_{n-1}}{(\lambda_1 - \lambda_2)(\lambda_3 - \lambda_2) \ldots (\lambda_n - \lambda_2)} N_1^0$$

$$C_1 = \frac{\lambda_1 \lambda_2 \ldots \lambda_{n-1}}{(\lambda_1 - \lambda_n)(\lambda_2 - \lambda_n) \ldots (\lambda_{n-1} - \lambda_n)} N_1^0$$

To quantify the decay process, it is a common practice to express the decay rate of a radioactive nuclide in terms of half-life ($t_{1/2}$) instead of the decay constant ($\lambda$). The half-life is defined as the time it takes for half of any given number of radioactive nuclei to decay. It is related to the decay constant by the equation:

$$t_{1/2} = \frac{ln2}{\lambda} = \frac{0.693}{\lambda} \qquad (1.13)$$

Typical values of half-lives of radon and its progenies relevant to this study are given in table (1.1).

## 1.6 Radioactivity units

The historical unit of activity, R, is the curie, Ci (roughly the activity of 1 gram of Radium), i.e.

$$1 \text{ Ci} = 3.7 \times 10^{10} \text{ decays/second} \quad (1.14)$$

The SI unit of activity is the becquerel (Bq). One becquerel represents the activity of the quantity of radioactive material whereby a one nucleus decays in one second. That is, 1 Bq = 1 decay / second. Therefore,

$$1 \text{ Ci} = 3.7 \times 10^{10} \text{ Bq} \quad (1.15)$$

Measurements of radon in air are often expressed in terms of concentrations of activity or becquerels per cubic meter of air ($Bq/m^3$).

## 1.7 Radiological importance of radon and its decay products

Research studies on the carcinogenic effects of radon and its daughters are well documented (Edwards, 1992). According to U.S. EPA (2005) on environment, health and safety online, chronic exposure to increased levels of relatively low radiation, and hence dose received by an individual, increases the chance of developing cancer, leukaemia, eye cataracts, erythema, haematological depression and incidence of chromosome aberrations. The results of such high exposure may appear 10 to 40 years after receiving the radiation dose. Exposure to radon and its progeny accounts for half of an individual's total radiation dose from natural and anthropogenic origins, making it the single largest contributor of radiation exposure (Cooper, 2012, Watson et al., 2005).

The principal potential route for human exposure to radon is inhalation. The alpha decay of $^{222}Rn$ (half-life: 3.8 days) gives rise to the formation of $^{218}Po$, which will in turn decay within minutes and so will the other three isotopes that follows. This implies that after inhalation, these isotopes will be deposited on the surface of the lungs where further decay and alpha irradiation of the lung tissues occur. The dose from inhaled radon decaying in the lungs is very low because most radon atoms are rapidly exhaled again.

The risk of radon-induced lung cancer following exposure to a given radon concentration is much higher among current cigarette smokers than among lifelong non-smokers. This has been verified by the pooled analysis of European, North American and Chinese residential radon studies (ICRP, 2009, WHO, 2009, Tomasek et al., 2008, Krewski et al., 2006, Darby et al., 2005, Lubin et al., 2004, BEIR VI, 1999). These studies have led to increased interest in radon with a view of identifying various sources and their emission mechanisms, implementing various controlling measures and developing measuring techniques in order to minimise environmental emissions.

## 1.8 Tailings dams as sources of radon exposure

Almost all minerals, rocks, raw materials, soils and water naturally contains radioactive materials or radionuclides, albeit in low concentrations. These radioactive sources are called Naturally Occurring Radioactive Materials (NORMs). They include uranium, thorium, radium, radioisotopes of potassium, lead, polonium, radon and their decay products. These radionuclides are present in the earth's crust (terrestrial), atmosphere (cosmological) and some are even found within the tissues of all living beings.

Although the concentration of NORM in most natural substances is low, higher concentrations may arise as the result of human activities. For most of human activities that involves minerals and raw materials, the levels of exposure to these radionuclides are not significantly greater than normal background levels. Such exposures, while having been the subject of much research, are not of concern for radiation protection. However, certain human activities can significantly increase NORM concentrations in the environment, thus requiring some controlling regulation (IAEA, 2008). When naturally occurring radioactive materials in their undisturbed natural state (NORM) become purposefully or inadvertently concentrated either in waste by-products or in a product, they become

technologically enhanced naturally occurring radioactive materials (TENORMs). These TERNOMs include waste products generated from gold and uranium mine and milling facilities, zircon plants, coal and phospho-gypsum industries.

Tailings are finely ground ore bearing rock and mineral waste products of mineral extraction processing operations. They also contain large quantities of unused processing chemicals and radioactive nuclides that include $^{230}$Th, $^{226}$Ra, $^{222}$Rn (radon gas) and the daughter isotopes of radon decay, including $^{210}$Po. Up to 85% of the ore's original radioactivity can be retained in the tailings. Due to the wet extractive mining process, tailings discharges are usually deposited as water-based slurry form into tailings dams.

Tailings dams are structures built to capture and store both the tailings and the water that transports the tailings to the dam. It is a common practice in South African mining and industry that the outer structure of the tailings dam is constructed using the materials from the tailings itself (Wortmann, 2007).

## 1.9 Problem Statement

Radon has been recognised as the main contributor to the natural radiation dose exposure to humans. Natural concentrations of atmospheric radon are of the order varying between 0.1 and 10 Bq/m$^3$ (UNSCEAR, 2000). In addition to natural radon, human activities like mining have the potential to enhance environmental radon contribution.

Gold mine tailings dams contain traces of $^{238}$U and $^{226}$Ra, leading to generation of $^{222}$Rn gas in the tailings material due to radioactive decay. The gas is emitted into the pores of the material and permeates to the surface of the tailings dam by diffusion and convection. At the surface radon is exhaled into the atmosphere, from where it is transported into the environment by local weather conditions, i.e. wind and atmospheric

turbulence. Due to its relatively long half-life of 3.8 days, the gas is carried long distances from the tailings, and potentially exists at elevated levels at receptor locations where members of the public reside, resulting in a radiological dose impact due to inhalation.

Radon gas also exhales from almost all soil surfaces on earth, since all soils contain naturally occurring uranium-series radionuclides to different extent. This leads to an ambient or background radon concentration which exists at various levels at any location, irrespective of the presence of anthropogenic radon sources like tailings dams. That being so, a measurement of radon gas concentration in air at a public member location cannot differentiate between natural background radon and radon from a TERNOM facility like a tailings dam in the near vicinity, and only yields the total radon concentration.

Nuclear regulations require mine operators to assess the radiological impact of their operations on members of the public. In terms of radon gas, the impact relates to the radon concentration increase caused by the operation, which cannot be discriminated from radon gas measurements.

Currently, methods used to monitor radon from the tailings dams are only able to provide a close-up of emissions in space and time. The passive methods of measuring atmospheric radon concentrations only establish the presence of radon in the ambient air. This is the first step of determining the extent to which the presence of radon in the vicinity of the tailings dam is affecting the surrounding atmosphere. However, these methods cannot distinguish between tailings radon and background radon as well as the extent to which each contributes towards the radon content in the atmosphere. The only way to determine the increment is through air dispersion modelling.

Air dispersion modelling is used amongst other reasons, to help determine the origin of radon source and to assess the impact of the tailings as radon source on the air quality. It mathematically simulates the

physics governing the transport, dispersion and transformation of atmospheric radon. The dispersion model estimates downwind radon concentrations given information about the pollutant emissions and nature of the atmosphere. This information relates to contaminant emission rate, source characteristics, local topography, meteorology of the area and ambient or background concentrations of pollutant.

However the accuracy and reliability of this approach is severely hampered by the assumptions and simplifications that have to be made. It is often stated that radon from mining operations has a severe impact on the public, exceeding allowed exposure limits. Yet this statement has not been validated in the light of uncertainties regarding the methods currently being used to assess the radon impact from tailings dams.

## 1.10 Aims of the study

The aim of this study is to develop a technique to accurately validate radon dispersion modelling that assesses the radon contribution from typical tailings dams. In order to realise this aim, critical knowledge omissions are identified and used to formulate the research objectives.

Overall two key gaps in knowledge were identified:

- there is lack of proper quantification of the source term model input values used within the air dispersion model when simulating radon from tailings dams. Dispersion modelling can only be successfully conducted if the source-term input data are correct. It is therefore crucial to identify and quantify the radon source term as accurately as possible.
- the performance of the steady-state Gaussian plume Industrial Source Complex Short Term 3 (ISCST3) model in respect of radon

measurements from tailings dams has not been fully evaluated and validated by comparing measured data to model outputs

## 1.11 Objectives

The objectives of the study are:

- to investigate the current methods of radon flux measurements (source term) from the tailings dams and to select the best method;
- to select an existing representative tailings dam and measure its source term (flux) using the selected method;
- to measure radon gas concentrations at a number of locations around the tailings dam within a radius of about 2 km from the source using Radon Gas Monitors (RGMs). Conventionally this method is used to assess radon contributions from tailings and is included here for comparison purposes;
- to determine the contribution of the tailings dam as a radon source at a location by measuring F-factors or equilibrium factors, which represent a measure of the degree of radioactive equilibrium between radon and its short-lived radioactive decay products, and deducing the “age” of the gas compared to the “age” from background sources;
- to model the geometry of the selected tailings dam as accurately as possible, including the effects of recirculation behind the trailing edge of the tailings dam (wake effect);
- to apply the steady-state Gaussian plume Industrial Source Complex Short Term 3 (ISCST3) commercial atmospheric dispersion software package by BREEZE AERMOD GIS Pro (Version 4.0., Trinity Consultants Inc., 2002) and local weather data to calculate radon concentrations in the surroundings of the tailings dam;
- to develop a new technique based on the “age” of the gas that will allow discrimination between the different radon contributors;

- to use the data and new technique to validate (or calibrate) the air dispersion model, and
- to use the information gained from this study to recommend the best modelling practise when using dispersion models to accurately estimate radon emissions from tailings dams.

## 1.12 Legal Requirements

All mines and related mineral processing activities in South Africa are controlled by the National Nuclear Regulator (NNR); Act 47 of 1999. The act, as stipulated in the GD 1032 document, prescribe that the mine perform a Radiation Hazard Assessment for Members of the Public and the Environment. The NNR imposed a minimum action reference level for the dose to a member of the public to be less than 1 mSv/y (with a dose constraint of 250 µSv/y per single source). This corresponds to a reference radon concentration level of 6 Bq/m$^3$.

## 1.13 Study area

A representative and isolated tailings dam, Freddies 9 (sometimes referred to as Steyn 9) shown in figure 1.2 was selected for the study. The tailings dam contains gold mine tailings from an old, non-operational closed mine shaft called Freddies 9 situated on the south of tailings dam. It is located in Lejweleputswa District Municipality, Free State province, (South Africa) between Odendaalsrus and Allanridge towns. The tailings is surrounded by Nyakallong township next to Allanridge on the north, R30 main road connecting Bothaville and Welkom as well as maize farm on the west, a small water pond and a hostel accommodating about two hundred people on the south-east. The closest tailings dam to the Freddies 9 is about 5 km on the northwest. This tailings dam is still “active” with wet slurry from the adjacent operating gold mine. Other tailings dams are 8.6 km and 16 km on the south and south east side of the tailings respectively.

There are no tailings dams or other anthropogenic sources on the north, north east and east of the dam.

,

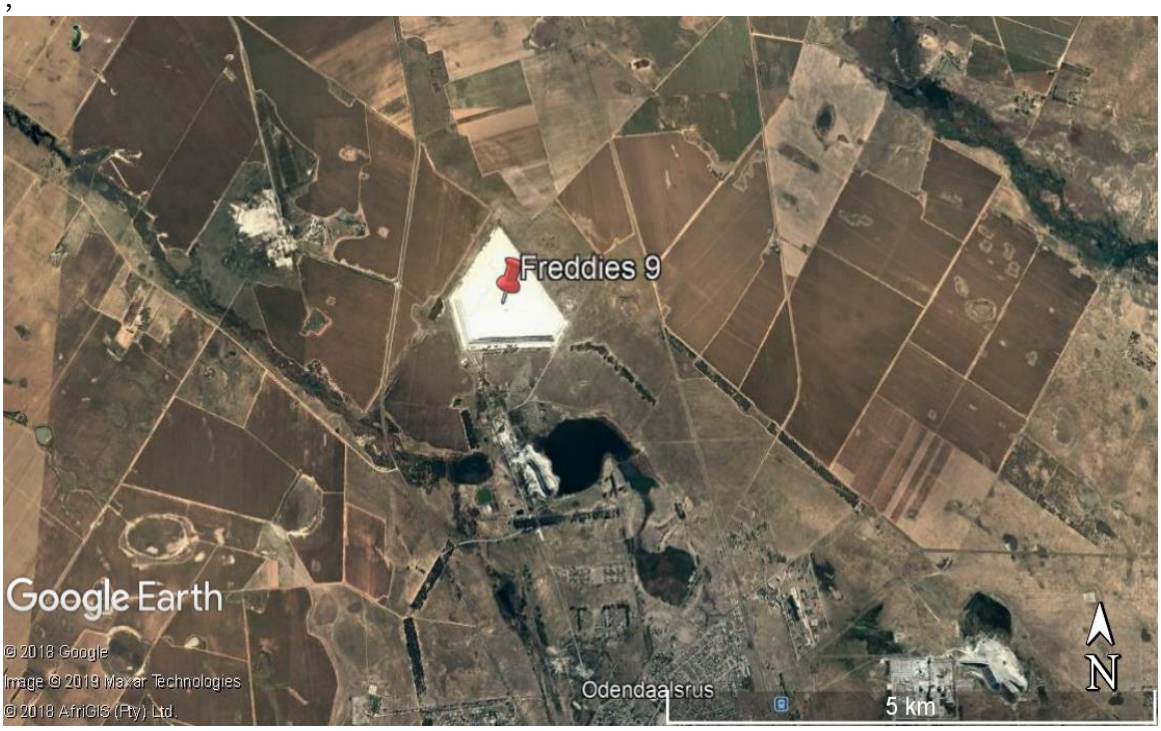


**Figure 1.2: Steyn 9 tailings dam (Google Earth®)**

The climate in Odendaalsrus is referred to as a local steppe climate and the Köppen-Geiger climate classification is BSk. Odendaalsrus receives on average, about 554 mm of rain per year, with most rainfall occurring mainly during mid-summer. August is the driest month with an average rainfall of 8 mm and January is the wettest with an average rainfall of 93 mm (Climate data.org, 2019). The average midday temperatures for Odendaalsrus range from 17°C in June to an average of 30°C in January. The region is the coldest during June/July when the mercury drops to 1 °C on average during the night (Climate data.org, 2019). The annual predominant wind directions are the north-north-east (10.8%), north-north-west (9.4%), west-north-west (9.1%), north-west (8.7%) and north (8.4%). Seasonally, the dominant wind direction during summer is the north-north-east while during cold winter months, the wind direction varies between west-north-west and north-east (Windfinder, 2019).

## 1.14 Thesis Outline

Chapter 2 provides a literature review of outdoor radon and radon progeny concentrations and radon exhalation measurements (source term). Research on radon modelling is evaluated, specifically from tailings dams in South Africa and other related outdoor sources.

Chapter 3 outlines the physics, theoretical background, methodology and materials that were used to determine radon flux from the tailings dam. The chapter concludes by determining radon flux from the dam

Chapter 4 details passive environmental radon measurements around the dam. This chapter outlines the assessment of radon concentrations levels in the vicinity of the tailings dam by employing passive detectors over long period. From the data, doses to the public around the tailings dam are calculated.

Chapter 5 evaluates different radon progeny measurement methods and a suitable method is identified and used to measure individual short term radon daughters as well as F factors as a function of distance from the dam.

Chapter 6 examines the different source geometries that have been previously applied and the proposed source geometry approach needed in accurate radon modelling from tailings dams is presented. The dispersion model is validated by applying the "age" of the gas concept to isolate tailings radon from other sources. Predicted concentrations are compared with the measured data. The findings from this analysis are discussed at the end of this chapter.

The conclusion in chapter 7 summarises the main findings of the study, providing recommendations for the improved and practical source

term parameterisation for use in modelling radon dispersion from the mine tailings dams.

# Chapter 2 Literature review

## 2.1 Introduction

The purpose of this chapter is to extensively review and analyse the prior art and literature surrounding the techniques and measurement methods applied to characterise radon from tailing dams. The most significant aspect of this chapter is to identify any knowledge gaps and limitations associated with respective techniques. Furthermore, limitations associated with each method will be addressed in subsequent chapters. The methods critically studied are radon concentration and flux, and radon progeny measurement techniques. A number of dispersion modelling theories applied to radon emitted from tailings dam will also be reviewed.

## 2.2 Overview

Radon release from the radium-bearing tailings dam to the atmosphere is a result of a series of processes, namely: emanation, transport and exhalation (Moed, Nazaroff and Sextro, 1988). These processes are illustrated in figure 2.1. Only a fraction of the radon atoms created from radium decay in the tailings will be able to escape from the mineral grains and enter the void space (IAEA, 2013).

The emanated radon atoms that have been transported by diffusion and advection to the soil surface boundary will diffuse into the atmosphere. This atmospheric radon release process is called radon exhalation. The quantity of the radon released expressed as the amount of radon emitted per unit area per unit time or activity of radon exhaled over a surface area per unit of time is known as radon exhalation rate (sometimes referred to as radon flux density). It is usually expressed as becquerel (Bq) or picocuries (pCi) per square-meter per second (Bq/($m^2$ s) or pCi/($m^2$ s)).

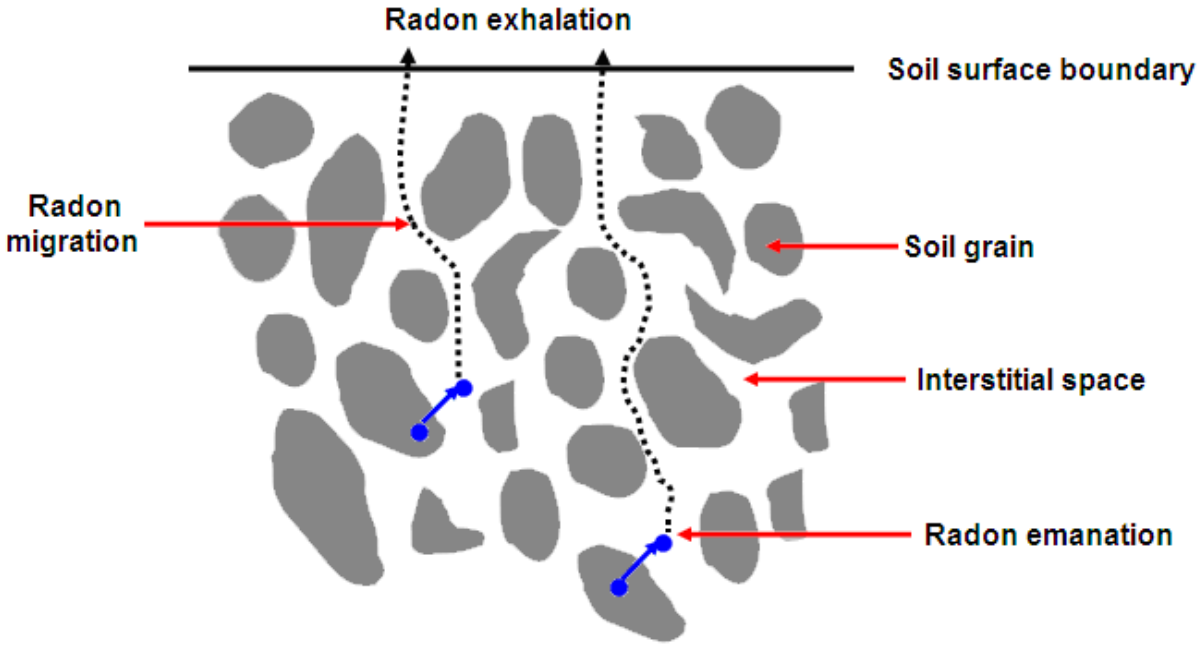


**Figure 2.1: Radon emanation, transport and exhalation processes leading to radon escape to the atmosphere from a porous medium (Ongori et al., 2015).**

Radon exhalation is measured differently from radon concentration in air and the environment, even though there are similarities in some of the approaches between the two measurement techniques. The common characteristic is that both techniques measure radon concentration. The difference is that radon flux monitors takes into account the surface area when measuring radon concentration, whereas radon concentration monitors only measure ambient radon concentration. Radon flux measurements quantify the atmospheric dispersion source term and are needed for atmospheric transport calculations and modelling (Hofmann et al., 2015, Sakashita et al., 2004).

Atmospheric measurement of radon concentrations, and of the exhalation fluxes from sources causing those concentration levels, is a primary indicator of the potential health hazard associated with the sources. A large amount of literature is dedicated to different techniques used by various researchers over time to quantify the sources and

concentrations of radon and radon progeny from outdoor NORM residues such as uranium ore (AquiSim Consulting (Pty) Ltd, 2014) and backfill tailings has been published (UNSCEAR, 2000, IAEA, 2013, Ongori et al., 2015, AquiSim Consulting (Pty) Ltd, 2014, Altic, 2014, Brenner, 1989, Dinh Chau, Chruściel and Prokólski, 2005, Ferry et al., 2001, Guan, Jianping and Guo, 2006, Ielsch et al., 2002, Ishimori, Maruo, 2005, Kakati, Kakati and Ramachandran, 2013, Lawrence et al., 2009, Lindsay et al., 2004, López-Coto et al., 2009, Mudd, 2008, Saegusa et al., 1996, Sahoo et al., 2010, Tan et al., 2012, Turner, 2015, Momeni, Yuan and Zielen, 1979, Krizman, Stegnar, 1991, Furuta, Ito and Ishimori, 2002, Akber, Pfitzner, 1994, IAEA, 1992, Hassan et al., 2009). These techniques are based on the independent or simultaneous detection and measurement of types of radioactive emissions (α, β, and γ radiation) from radioactive decay of radon and its progeny due to $^{226}$Ra decay chain.

The most common methods of radon detection are based on detection of alpha particles. Radon monitors like RAD7 (Durridge, USA), measure radon concentration by detecting alpha particles with fixed energies emitted during the decay from $^{222}$Rn to $^{218}$Po to quantify radon isotope in air. Scintillation counters are used to count the three alpha particles produced during the decay of $^{222}$Rn, $^{218}$Po and $^{214}$Po. Other techniques detect radionuclides that emit gamma rays during the radioactive decay of $^{214}$Bi and $^{214}$Pb radon progeny (Ongori et al., 2015, Lindsay et al., 2004) while few techniques detect beta particles to measure radon and its progeny (Singh et al., 2005).

## 2.3 Radon concentration measurement techniques

Short and long term measurement techniques have been used to assess radon concentration levels. These measurement techniques are classified as active and passive based on the way that air and radon are sampled. In the passive method, no electrical components are required and air movement into the measuring chamber is due to natural diffusion of

radon and/or its progeny. There are three types of passive detectors that have been extensively used for radon measurements, namely charcoal canisters (Countess 1976, Al-Azmi, Mustapha and Karunakara, 2012); electret ion detectors (Rad Elec Inc., 2018) and nuclear track detectors .

In the active method, some form of electrical source is required to operate the detector and pumps as well as to apply pressure and force air into the measuring chamber. Active techniques are based on scintillation chambers coupled to silicon surface barrier detectors or photomultiplier tubes. Many of the active techniques available measure directly the alpha particles emitted by radon and its short-lived progeny $^{218}$Po and $^{214}$Po. The detection and interaction occurs simultaneously, thus providing results almost instantaneously. The most popular active devices used for outdoor radon monitoring are the electronic integrating devices (EIDs) and the continuous radon monitors (CRMs). The three types of active detectors that are more frequently used for radon measurements are solid-state surface barrier detectors (Scott, Mackenzie, 1984, Scott, Mackenzie, 1985, Porstendörfer, 1994, Tokonami et al., 1996, Whittlestone, Zahorowski, 1998, Brunke et al., 2002, Hofmann et al., 2015, Howard, Johnson and Strange, 1990, Iida, Ikebe and Tojo, 1991, Iida et al., 1996, Iimoto et al., 1998), Lucas cell (Eappen, Nair and Mayya, 2008, Severino, 2014), and ionisation chambers (IAEA, 2013, Severino, 2014).

The main advantage of the active systems is their ability to perform prompt, short term $^{222}$Rn measurements whilst passive systems measure time-averaged radon concentrations over long periods of time ranging from few days to months. Some of these measurement techniques are outmoded, while others were reviewed, modified and improved. It is not the aim of this study to present a detailed account on the available methods for radon concentration measurements. Details of the techniques used for the radon concentration measurements in this study, both passive and active, are discussed in the sub-sections below.

### 2.3.1 Passive detectors used in this study

#### 2.3.1.1 Nuclear track detectors

Passive integrated nuclear track detectors are the most widely used radon detectors (Abu-Jarad, Fremlin and Bull, 1980, Amin, 2015, Andriamanatena et al., 1997, Jönsson, 1987, Jönsson, 1991, Jönsson et al., 1995, Jönsson, 1995, Jönsson, 1997, Kamal, Doulatdarb and Mehdizadeha, 2007, Matiullah et al., 2005, NCRP, 1988, Ng, Nikezic and Yu, 2007, Nikolaev, Ilić, 1999, Srivastava, 2004). This widespread usage can be attributed to their ease of operation and data processing, low cost materials, insensitiveness to beta and gamma particles, small size, rigidness and their ability to almost infinitely maintain their track record (Barooah, 2005).

The nuclear track detectors are made up of a small, alpha-sensitive, plastic chip or cellulose film such as cellulose nitrate, polycarbonate or poly-allyl-diglycol carbonate (PADC) placed inside a small container (decay chamber) with a membrane filter. Only radon gas (not the solid progeny) is allowed to diffuse through the filter to enter the chamber. As radon diffuses passively through the filter into the chamber, the alpha particles from both radon decay and its progeny produced inside the chamber impinge on the film, thus causing microscopic radiation damage trails called latent tracks on the film. After the exposure period, the detector is sealed, carefully packaged and sent to the laboratory for analysis.

The distinguishable microscopic latent tracks produced by the alpha particle are detected by a method called etched track detection. The tracks, shown in figure 2.2, are sufficiently enlarged to microscopically visible size by either chemically etching the film in an alkaline solution (typically NaOH or KOH) for cellulose nitrate and allyl diglycol carbonate materials or electrochemical etching for polycarbonate by applying an alternating voltage across the etching detector (Miles, 2004).

Factors influencing the track etching process include: (i) detector material composition (molecular weight, density and chemical composition); (ii) the incident alpha particle parameters (charge, mass and velocity); and (iii) etching parameters (nature of etching solution, concentration, time and temperatures etc.). After the chemical etching process, the latent tracks are viewed and counted using an optical microscope or by automated scanning and counting technology (IAEA, 2013).

**Figure 2.2: Nuclear tracks made visible by etching in concentrated hot NaOH (PARC RGM, 2018)**

The track density (number of tracks per unit area) is proportional to the radon concentration and varies linearly with the average exposure rate. The integrated radon concentration per unit time C, is calculated from the average number of tracks per unit area to which it was exposed to using the equation (Severino, 2014):

$$C = k\rho \left[\frac{kBq \cdot h}{m^3}\right] \qquad (2.1)$$

where

$\rho$ is the track density per unit exposure time ($cm^{-2}s^{-1}$)

$k$ is calibration factor in $(kBq{\cdot}h/m^3)/(tracks/cm^2)$

The measurement certainty and detection limits depend on the total number of tracks counted. Due to relatively low collection efficiency or sensitivity of alpha track detector on short integrated exposure time scales, longer exposure periods of up to a year may be required depending on the expected level of radon concentration.

Several alpha track detector materials have been developed over the years. The two most popular track detectors that are used in radon dosimetry are the LR-115 (cellulose nitrate) and CR-39 (poly-allyl-diglycol carbonate). The CR-39 based track detector, called Radon Gas Monitor (RGM) manufactured by PARC RGM shown in figure 2.3 is the one adopted for this study and is discussed further in chapter 3.


**Figure 2.3: Radon Gas Monitor (RGM), a CR-39 based track detector (PARC RGM, 2018)**

### 2.3.2 Active detector used in this study

#### 2.3.2.1 Ionisation chamber

Ionisation chambers are gas filled cylindrical condenser systems with central anode and an outer cathode for collecting electrons and positive ions respectively. Their detection principle is based on the collection of the ions produced by alpha particles from decaying radon and its progeny on the electrodes and then measure their charge with an electrometer.

An air sample is drawn inside the detector volume cell through a filter to prevent any radon progeny present in the inlet air from entering the chamber. Alpha particles from the decay of radon and its progeny ionise the air inside the chamber, creating a pair of positive ions and negative electrons. These ions are attracted and collected by the electrodes, producing a current measured by means of an electrometer. Measurements can be carried out in closed or flow-through mode any time after the filling of the chamber. Taking into account the background and the chamber volume limitations, the theoretical sensitivity of this instrument for a typical 30 minute measuring time can be in the order of $10^{-14}$ Ampere/Bq (Severino, 2014) and their detection limit can be as low as 4 Bq/m$^3$ (IAEA, 2013).

The AlphaGUARD radon monitor, produced by SAPHYMO GmbH in Germany, is one of the most widely used commercially available ionisation chambers. It is a multi-sensor, continuous active radon sampling device that incorporates a pulse-counting ionization chamber (alpha spectroscopy) to measure radon concentrations in air, soil and water while simultaneously recording pressure, humidity, and temperature values and variations. The AphaGUARD was used to determine the equilibrium factor during this study. The equilibrium factor is fully discussed in section 2.6.3.

### 2.3.3 Sampling

Radon collection and measurement methods can be classified into three different modes: instantaneous (also known as grab sampling), semi-integrating (also known as continuous real time or short-term continuous) and fully integrating (also known as time averaging or time integrating).

#### 2.3.3.1 Instantaneous or grab sampling

In this sampling technique, radon gas measurements are essentially instantaneous, with sampling time ranging from several seconds to minutes or hours. Most radon grab sample techniques use active devices like the RAD7 (DURRIDGE) solid state detector and alpha scintillation cells to measure radon concentration. The result of the measurement is the radon activity during the sampling time.

There are two ways by which collection of a representative air sample can be made. An air sample may be sucked directly into the silicon detector or alpha scintillation cell by a vacuum pump where it is immediately measured or air sample may be stored in an airtight radon-proof collapsible bag where it will be later transferred to a scintillating cell for alpha counting. This technique can measure radon concentration as low as 0.1 pCi/L or 4 Bq/$m^3$ (Brenner, 1989).

The advantages of these techniques include their sensitivity, low cost, ability to provide immediate results and minimum labour requirements. These techniques are suitable for large-scale surveys where a large number of measurements can be taken in a relatively short period of time. Some of the disadvantages include their inability to account for spatial and temporal variations of radon in the environment and their detection limit's dependence on among others, the scintillator cell size, the silicon detector size as well as background level.

#### 2.3.3.2 Semi-integrating

In the continuous, semi-integrating technique, sampling and counting occur simultaneously while estimating radon concentrations at regular time intervals over a long period of time. Sampling periods may vary from few minutes to several hours depending on the measuring systems being applied. Sample collection may be through natural diffusion or the air sample may be pumped (flow-through mode). Detection and counting of radon and its progeny can be obtained by alpha spectrometry, ionization chamber methods or by gross alpha counting techniques. The alpha spectrometry and the gross alpha counting methods are discussed in detail in chapter 5.

This method can give information on the radon concentration variations throughout the measurement interval. In addition, their superior sensitivity, reduced systematic errors and capacity to measure a time changing signal, makes them a preferred choice over instantaneous modes.

#### 2.3.3.3 Fully integrating (or time averaging or time integrating)

Time-integrated modes of radon and progeny measurements involve the build-up of radon over longer time periods of the order of weeks or months. Sampling occurs passively by diffusion, while at the same time maintaining integrated record of each and every alpha particle that impact on the medium of measurement. Radon measurement is either made by directly or indirectly detecting the radioactive decay products of radon and its progeny. After sampling, all the exposure information contained in the collection device is maintained until it is analysed.

Passive integrating methods are particularly useful due to their simplicity, low cost, and ability to average out short-term variations of low level radon concentration due to seasonal and diurnal fluctuations. Examples of these passive integrating devices include nuclear track

detectors, electret ion chambers, solid surface barrier detectors, scintillation cells, activated charcoal and ionization chambers.

## 2.4 Radon exhalation-rate measurement techniques

There are three main approaches to radon flux measurements from outdoor porous materials (IAEA, 2013). The first approach is the application of theoretical equations that describe flux from a surface by just measuring $^{226}Ra$ concentration and assuming theoretical and empirical values for other parameters. The second technique is the *in situ*, direct measurement of flux. This method involves the use of some kind of monitor placed directly on the surface of the tailings material, thus measuring the flux from radon concentration accumulation inside the monitor. The third approach involves taking a physical material sample to the laboratory, placing it inside an enclosed chamber and allowing radon to accumulate and reach secular equilibrium with its progeny. This will be followed by determining the $^{226}Ra$ content and measuring all other remaining parameters in the laboratory. The third method was adopted for this study.

Fundamentally, the detection methods of radon are the same in both second and third cases, but their difference is based on collection methods i.e. in-situ field measurements vs laboratory. The details of some of the most widely used flux measurement methods that have been mostly applicable to NORM residue like mine tailings are emphasised and described and their merits and demerits are briefly discussed.

### 2.4.1 Adsorption technique

The adsorption method for radon exhalation was first outlined by Megumi (1973). It is one of the simplest and low cost radon exhalation rate measuring techniques (IAEA, 2013). This method involves the use of an inverted canister containing an adsorption medium (mainly activated charcoal) placed on top of the surface to be investigated (Countess, 1976).

A schematic diagram of a charcoal adsorption canister is shown in figure 2.4.

Prior to use, the charcoal is oven heated for up to 24 hours to remove any previously adsorbed radon and moisture. This process is carried out when the charcoal is already in the canister. After heating, the canister is sealed to prevent adsorption of ambient radon or moisture onto the charcoal and taken to the sampling location where it is unsealed, inverted and pressed firmly into the ground to ensure a good seal between the edge of the canister and the ground.

The canister is left unperturbed for a predetermined time (2 to 7 days depending on design) to expose exhaled radon from the soil into the canister volume for adsorption onto the activated charcoal. After exposure, the canister is again sealed and sent to the laboratory to measure the activities of the radon progeny $^{214}$Pb and $^{214}$Bi using gamma spectrometry. For increased counting efficiency, liquid scintillation counting may be used as an additional measurement technique (Lawrence et al., 2009).

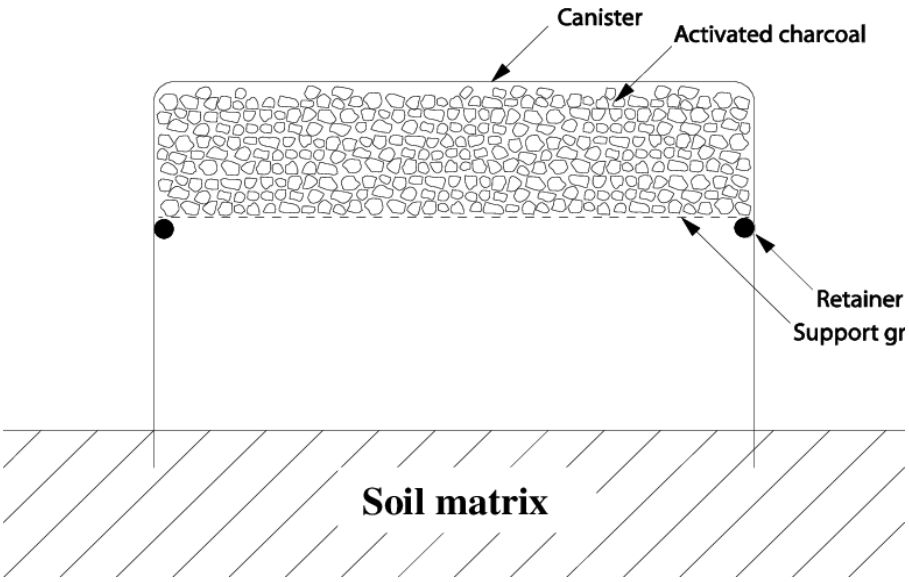


**Figure 2.4: A schematic diagram of a charcoal adsorption canister used to measure radon flux from the soil (IAEA, 2013)**

Radon exhalation rate is calculated based on the surface area of the canister, sampling period, and the activity of radon progeny from gamma spectroscopy measurements. The radon exhalation rate over a given exposure period can be estimated using the following equation (Bollhöfer et al., 2003):

$$f = \frac{N \cdot t_c \cdot \lambda^2 \cdot \exp(\lambda t_d)}{\varepsilon \cdot A \cdot [1 - \exp(-\lambda t_e)] \cdot [1 - \exp(-\lambda t_c)]} \quad (2.2)$$

where:

$f$ is the radon exhalation rate [Bq/m$^2$ s];

$N$ is the net count rate after background subtraction, obtained during the counting period [counts per sec, or s$^{-1}$];

$t_c$ is the counting period [s];

$\lambda$ is the radioactivity decay constant for $^{222}$Rn [s$^{-1}$];

$t_d$ is the delay period from the end of the exposure to the beginning of the counting interval [s];

$\varepsilon$ is the counting efficiency of the system relative to the activity of adsorbed radon [Bq/s];

$A$ is the area of the canister [m$^2$]; and

$t_e$ is the period of exposure of the charcoal in the canister [s]

The canister method has the advantage of being inexpensive and simple to operate. However, there are a number of limitations that should be acknowledged. One main drawback of this method is that its application is limited by the sampling area and time. Therefore, exhalation rate measurements should be taken at several locations and at several times at each location to obtain the average radon flux. On the other hand, due to the use of a diffusion barrier over the charcoal, various environmental conditions of temperature, atmospheric pressure and humidity may affect the measurements results, thus yielding high uncertainties. Furthermore, gamma spectroscopic measurements should take place as soon as practicable after exposure in order to minimise decay of the adsorbed

radon. Another disadvantage of this method is high cost of processing due to man-hours and equipment (Altic, 2014, Altic, 2011).

### 2.4.2 The flow-through method

There is a close resemblance between the flow method and the closed accumulator method of flux measurement. In the closed accumulator design, there is no exchange of air between the sample collection chamber and the ambient environment. The determination of radon concentration is based on radon concentration build-up in the chamber with time. The flow-through ventilation method on the other hand is a modification of the accumulator method. The method aims to minimise the effects of surface disturbance, back-diffusion and chamber leakage caused by the closed chamber method (Tan et al., 2012, Hosoda et al., 2009).

It involves an inverted sample collection chamber with one open face incorporated in the radon emitting surface. Moving air through the chamber with a pumping arrangement creates a constant air exchange between an inverted chamber defining the area of the soil to be measured and the ambient environment, thus continuously removing the air inside the chamber. Due to this constant and continuous air exchange, an equilibrium between radon concentration inside the detector and radon surface flux is established, creating a steady flow of low radon concentration in ambient air from which radon flux can be measured. Radon concentration in the container can be measured using both passive and active radon detectors like electret ion chambers (Kotrappa, Stieff, 2008), flow-through scintillators (Schery, Gaeddert and Wilkening, 1984), activated charcoal (Altic, 2011), AlphaGUARD (Zhuo, Furukawa and TokonamiI, 2007) and RAD 7 (Tan et al., 2013).

At steady state equilibrium, the exhalation flux density is proportional to the radon concentration of radon in the pumped air stream and to the flow rate, and inversely proportional to the active surface area of the chamber. This relation can be expressed as (Stieff et al., 1994):

$$J = \frac{(R\ x\ F)}{(A\ x\ 60)} \qquad (2.3)$$

where:

J is in Bq/(m$^2$·s);

R radon concentration in Bq/L;

F flow rate in L/min; and

A area of soil being measured in m$^2$

The constant 60 is a flow rate conversion factor from L/min to L/sec. Any other factor that may be incorporated in the calculation will depend on the type of system used and its calibration.

At very low flux rates, the flow method is a better option compared to the charcoal canister method (Kotrappa, Stieff, 2008) although the flow system measures the radon flux over a shorter time period than the charcoal canister (Sahu et al., 2014). Furthermore, more time is needed for the radon concentration in the chamber to reach steady state (Tan et al., 2013).

### 2.4.3 Accumulation method

The accumulation method is the earliest, easy to implement and most commonly used radon flux measurement technique (Brenner, 1989). It is based on the accumulated radon gas that escaped from the emanating surface at a given time. This method involves placing an inverted container called an accumulator or chamber of known volume on the sample or surface of interest. Both the sample and the detector are enclosed within the accumulator. To prevent any leakage of the accumulating radon, the container is sealed to a soil surface by inserting the rim of the accumulator several centimetres into the residue matrix. A simplified depiction of an accumulator set-up is shown in figure 2.5.

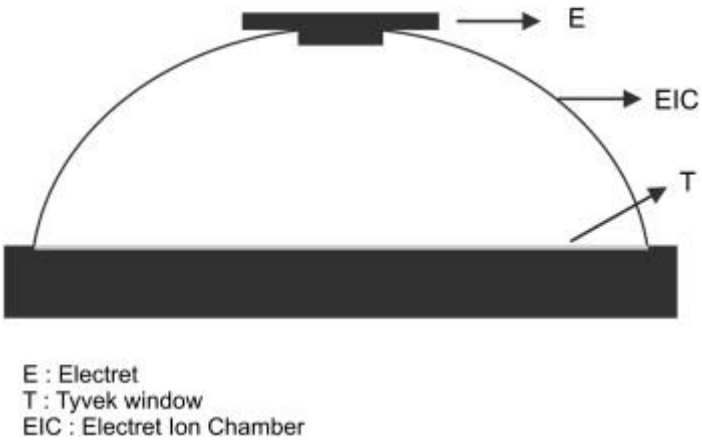


**Figure 2.5: Accumulation chamber for determining radon exhalation from soil (Grossi et al., 2011).**

The exhaled radon atoms from the residue surface beneath the chamber enter the accumulator headspace, causing a gradual build-up of the radon activity concentration. Integrating radon detectors such as electret ion chambers (Kotrappa, Stieff, 2008, Grossi et al., 2011), nuclear track detectors (Guo, Sun and Cheng, 2004, Maged, Ashral, 2005), charcoal canisters (Chalupnik, Wysocka, 2003), scintillation cells (Sahu et al., 2014, Chalupnik, Wysocka, 2003, Duenas et al., 1997) or active online monitors like AlphaGUARD (López-Coto et al., 2009, Sahoo et al., 2010, Kozłowska et al., 2016, Bavarnegin et al., 2012) and RAD7 (Kozłowska et al., 2016) are used to measure the gradual build-up of the radon concentration at several integrated regular intervals or in some instances, just once at the end of the deployment period.

The exhalation rate can be quantified by taking into account the accumulation time, surface area and volume of the accumulation chamber, using the formula (Chałupnik, Wysocka, 2003):

$$\varphi_{Rn} = \frac{A_{Rn}}{St} \qquad (2.4)$$

where:

$\phi_{Rn}$ is the exhalation rate, can be defined as the radon flux from the ground into atmosphere, [Bq/(m$^2$.s)]

$A_{Rn}$ is the activity of radon in accumulation chamber [Bq], a product of radon concentration $C_{Rn}$ and chamber volume V;

$S$ is the exhalation surface [$m^2$]; and

$t$ is the accumulation period [s]

The calculation of the exhalation rate should take into account the effect of back diffusion, chamber leakage and degree of ventilation during flow-through mode operations.

Accumulators of many sizes and shapes have been used over time, ranging from a simple glass jar having a nominal volume of 4 litres (Kotrappa, Jester, 1993, Kotrappa, Stieff, 1994) to the popularly preferred large drum barrel accumulators (Rogers, Nielson and Kalkwarf, 1984).

The disadvantages of this method are that it is expensive and the experimental arrangement is time consuming. Other limitations that may affect the results includes the occurrence of back diffusion, radon adsorption on the accumulator material and air leakages caused by longer experiment period (Mayya, 2004). For drums with large height, a small fan may be required to uniformly mix radon inside the drum whereas smaller volume (≤1L) accumulators increase back diffusion significantly (Mayya, 2004). In addition, large drums are not portable, especially for large scale measurements.

A major limitation of all these techniques is that the number of samples is limited because of cost and logistics. This means that a large area cannot be covered effectively and the average exhalation rate over such an area is not represented by the small number of samples

### 2.4.4 Radon mass exhalation rate

The mass exhalation rate is defined as the activity of radon escaping per unit mass of the soil matrix into the air per unit time. Its measurement

follows the same principle as the accumulation method. A sample of known mass, volume and water content is enclosed in an air tight exhalation chamber of known volume $V$ coupled to a continuous passive or active radon monitor. The build-up of radon concentration inside the chamber is continuously monitored at regular time intervals until a radioactive secular equilibrium between radon and radium is attained (Dinh Chau, Chruściel and Prokólski, 2005, Amasi et al., 2015).

The radon concentration build-up $C(t)$ at time $t$ after the closing of the chamber is quantified by the formula (IAEA, 2013):

$$C(t) = \frac{J_m M}{V\lambda_e}\left[1 - e^{-\lambda_e t}\right] + C_0 e^{-\lambda_e t} \qquad (2.5)$$

where

$J_m$ is the mass exhalation rate [Bq/(kg.s)];

$C_0$ is the $^{222}$Rn concentration present in the chamber volume at t = 0 [Bq/m$^3$];

$M$ is the total dry mass of the sample [kg];

$V$ is the effective volume (volume of chamber + internal volume of $^{222}$Rn monitor — volume of sample) [m$^3$];

$\lambda_e$ is the effective decay constant for $^{222}$Rn, which is the sum of the leak rate (if existing) and the radioactive decay constant of $^{222}$Rn [s$^{-1}$]; and

$t$ is the measurement time [s].

Knowing the dry mass $M$ of the sample, the mass exhalation rate, $J_m$ may be obtained from the fitted parameters of equation (2.5) above.

### 2.4.5 Sealed “can” technique

The sealed “can” technique (Abu-Jarad, Fremlin and Bull, 1980, Somogyi et al., 1986) has been widely used in combination with different passive radon monitors such as solid state nuclear track detectors (Baruah, Deka and Rahman, 2013, Yousef et al., 2015, Choudhary, 2014) and CR-39 detectors (Youssef et al., 2015) to measure radon mass exhalation rate from different soil samples. In this method, the samples of interest are dried, crushed to fine powder, enclosed in a plastic “cylindrical can” (Yousef et al., 2015, Tufail et al., 2000, Sharma et al., 2016) and sealed for about three weeks to attain secular equilibrium between radium and radon. The detector is placed inside the “can” to measure radon concentration in a similar way described in section 2.4.3 above. The exhalation rate depends on the type and amount of the material as well as on the dimension and geometry of the “can”. A diffusion tube method, which is a modified “can” technique, was used in this study to determined radon exhalation rates from the tailings dam. This method is fully discussed in chapter 3.

### 2.4.6 Gamma-ray mapping

Radon flux mapping from the South African mine tailings has been conducted using a method based on the gamma ray spectroscopy called MEDUSA (Multi-Element Detector System for Underwater Sediment Activity) technology developed in the Netherlands by the Nuclear Geophysics Division of Groningen (Ongori et al., 2015, Lindsay, Newman and Speelman, 2008, Lindsay et al., 2004, Talha et al., 2010). This field based detector is used in conjunction with a laboratory based hyper-pure germanium (HPGe) detector. The MEDUSA system uses a 15 cm in length and 7cm in diameter cylindrical gamma-ray detector (CsI (Na)) mounted on a 4x4 vehicle at 60 cm off the ground. Incorporated within the detector is the ALADIN box containing data acquisition system, MPA (MEDUSA Post

Analysis) software tool for gamma ray spectra analysis and global positioning system (GPS). Due to the attenuation of the gamma rays by the soil, the sensitivity of the detector is limited up to a depth of 30 cm (Ongori et al., 2015).

Disadvantages of this method include high operational and maintenance costs, long and complicated procedure with multiple analyses using HPGe and MEDUSA and diffusion length limited to 30 cm below the soil surface.

## 2.5 Radon exhalation from South African mine tailings

There is limited literature that reports on radon exhalation rates measurements from South African mine tailings (Ongori et al., 2015, Altic, 2014, Altic, 2011, Lindsay, Newman and Speelman, 2008, Lindsay et al., 2004, Talha et al., 2010, van As et al., 1992, van Vuuren et al., 1995, Strydom, 1996, Strydom et al, 1998, Human, Botha, 1998, Strydom, 1999, Strydom, 2000, Strydom, 2002). Of these reports, the most published reports are based on the MEDUSA gamma ray detectors system (Ongori et al., 2015, Lindsay, Newman and Speelman, 2008, Lindsay et al., 2004) discussed in section 2.4.6.

Notwithstanding this limitation, several *in situ* techniques have being used to directly measure radon exhalation from the tailings in South African mine (Van Vuuren et al., 1995, Strydom et al, 1998, Human, Botha, 1998, Strydom, 2000, Strydom, 2002).

Van Vuuren et al. (1995) measured the exhalation rates at three different mine tailings using the diffusion tube method. The standard deviation of the exhalation rates from the individual sources varied between 6 - 48%. The error on individual exhalation rates amounted to 22%. The accuracy of the measurement was deemed acceptable; however it was recommended that a larger variation and more measurements were necessary to obtain more accurate spatial average exhalation rate values.

Strydom (2000) presented the most comprehensive study of different techniques that report on exhalation rates used in South African tailings. Radon flux was measured at four different tailings dams around the Free State gold mining areas. The average $^{226}Ra$ concentration of the dams was about 1 Bq/g. Due to uncertainties in the accuracy of the flux measurements, four different techniques were explored and their results compared. The four methods were: (1) the closed box or accumulation method incorporating AlphaGUARD active radon monitor, (2) closed box E-PERM flux monitors, (3) diffusion tube method with Radon Gas Monitors (RGM) and (4) dynamic flow through method with AlphaGUARD monitor. The flux values from these methods were compared with the theoretical calculations based on the assumption of some parameters. The results of the average flux for each method are shown in table 2.1.

*Table 2.1: Comparison of four different radon flux measurements methods with theoretical approach*

| **Technique** | **Average flux measurement ($Bq.m^{-2}.s^{-1}$)** | **SD ($Bq.m^{-2}.s^{-1}$)** |
|---|---|---|
| E-PERM Flux Monitors | 0.046 | 0.034 |
| Closed Box Method (AlphaGUARD) | 0.050 | 0.007 |
| Dynamic flow-through method | 0.076 | 0.011 |
| Diffusion tube method | 0.211 | 0.040 |
| Theoretical Calculation | 0.245 | |

From the results in table 2.1, the diffusion tube method yielded approximately the same values as the theory predicts. Based on these results, the diffusion tube method incorporating the CR-39 based Radon Gas Monitor (RGM) was adopted for this study as the most convenient and reliable method. This method is further discussed in chapter 3.

## 2.6 Atmospheric Radon progeny measurements and the F factor

### 2.6.1 Introduction

Atmospheric radon continuously undergoes spontaneous sequential radioactive decay to form four solid, short-lived radioactive decay products, namely $^{218}$Po, $^{214}$Pb, $^{214}$Bi and $^{214}$Po. These decay products, commonly referred to as radon progeny or radon daughters, are sometimes designated as RaA, RaB, RaC and RaC', respectively. Of the four, the polonium isotopes are alpha emitters and the lead and bismuth isotopes are beta emitters. These radioisotopes attach themselves to fine airborne aerosol particles, thus contributing to the overall atmospheric radioactivity concentration.

The formation and activity behaviour of each of the short-lived isotopes from radon decay is illustrated in the plot of activity as a function of time for initially pure $^{222}$Rn in figure 2.6. Due to longer $^{222}$Rn half-life compared to the four short-lived products, the progeny will attain similar activity (number of decays per unit time) as the parent radon or secular equilibrium. The combined radon and progeny mixture will continue to decay with the 3.8 day half-life of the radon. Each $^{222}$Rn decay yields four progeny decay products such that the total activity is then the sum of these individual decay-product concentrations.

Ambient radon progeny activity concentrations are important for determining the "age" of the gas after some release time and evaluating effective radiation dose. Their concentrations and that of radon in ambient air vary from time to time due to changes in meteorological conditions such as temperature, relative humidity, wind speed, rainfall, etc. As a consequence, different measuring methods and devices have been developed over time to account for these differences and variations. The theory and fundamental principles of radon progeny measurements are described in Appendix A.

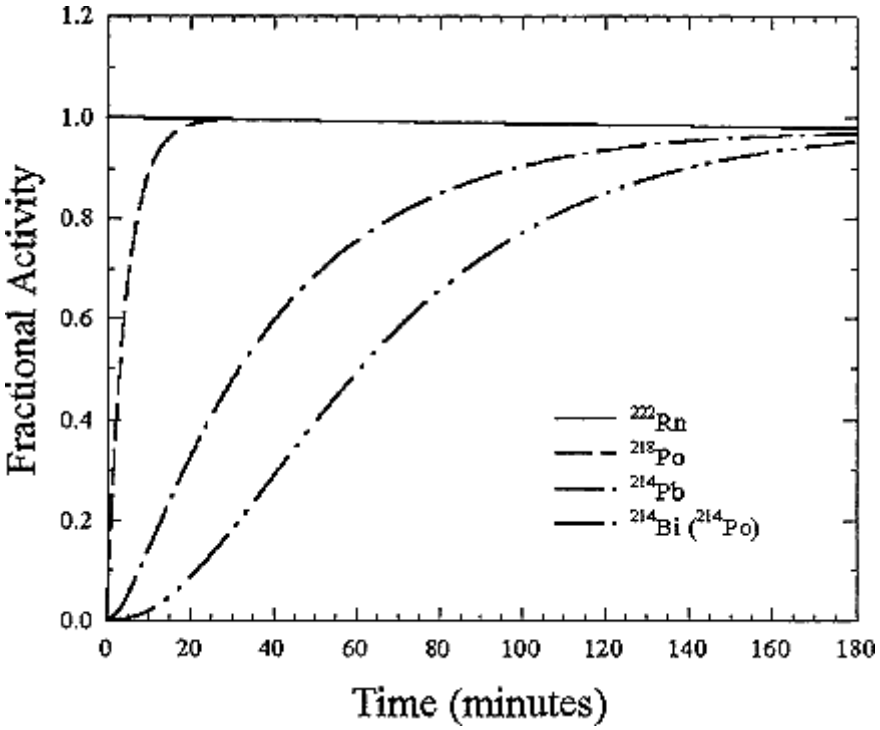


**Figure 2.6: Normalised in-growth activity behaviour of each of the short-lived radon decay isotopes initially containing only $^{222}$Rn in the atmosphere (BEIR VI, 1999).**

### 2.6.2 Outdoor radon progeny measurement methods related to this study

Radon progeny concentration measurements can be classified into three categories: (a) measurement of the individual activity concentration of one or more short lived progeny; (b) measurement of linear combination of each progeny's concentration called Potential Alpha Energy Concentration (PAEC); and (c) measurement of Equilibrium Equivalent activity Concentration (EEC). For many applications, measurements of the individual progeny concentrations provide more information than from the total PAEC or EEC. For this project, it was important to determine the "age" of the gas as well as radon daughter behaviour using measurements of individual progeny concentrations, whereas PAEC are more suitable for routine surveys (Nazaroff, 2010) and thus not used in this study.

Radon progeny measuring techniques are in principle, similar to those of measuring radon in that the measuring devices can be classified in terms of grab sampling and continuous or integrating measurements. All these methods require drawing air of known volume through a filter in a given time, on which the radon progeny activity can be measured either during or after sampling. Since radon is an inert gas, it does not attach to the filter. Therefore the choice of the filter is determined by their high collection efficiency, low flow resistance and low deposition of non-respirable particulates. According to Holmgren et al. (1977), filters having pore sizes below 1 μm have high collection efficiencies of > 99.9% for aerosol particle sizes to which the radon progeny are attached as well as for unattached or "free" progeny. The individual progeny ($^{218}$Po, $^{214}$Pb and $^{214}$Bi) concentrations can then be determined by applying the three independent gross alpha counts technique or by applying the alpha spectroscopic method using surface barrier or diffused junction detectors coupled with a multichannel analyser.

The radon progeny measurement methods applied in the field under uncontrolled conditions of ambient temperature, moisture and dust levels and from which the most suitable technique for this study was selected are described below. Under these conditions, instrumentation should be rugged and the method used should be insensitive to these conditions. Each method is characterised by the overall time of the measurement cycle.

#### 2.6.2.1 The Kusnetz Method - PAEC Measurements

The Kusnetz method (Kusnetz, 1956) is the simplest method designed to measure radon progeny by applying a single alpha count to obtain the working level (WL). The working level (WL) is a historical unit for expressing rates of radon progeny exposure originally applied to the uranium mining environment. One working level refers to any combination of short-lived radon daughters in one litre of air that will emit 1.3 x $10^5$

MeV of potential alpha energy. The potential alpha energy concentration is the concentration of radon progeny corresponding the total alpha energy released during the decay of radon through the decay chain up to but not including stable $^{210}Pb$.

The method was first developed by Kusnetz and later modified by Rolle (1972). According to this method, at about 60 minutes after sampling at a given flow rate, the rate of the alpha decay of the radon daughters per WL on a filter is virtually insensitive to the degree of radioactive equilibrium. Air is sampled on a filter for 2 to 10 minutes followed by gross alpha activity counting for 10 minutes after allowing the radon to decay for a period of 40 to 90 minutes. The working level can then be calculated from the equation:

$$PAEC = \frac{R}{KVE} \tag{2.6}$$

where

PAEC is the potential alpha energy concentration in working levels;

R is the net count rate in cpm;

V is the volume of air sampled in liters; and

K is a correction factor.

Using this method, the working level could be estimated to within 13% accuracy.

Borak (1986) described a technique that optimises single gross alpha count from radon progeny collected on a filter in order to determine the PAEC in air. By taking into account the independence of the decay rate to the radioactive equilibrium, Borak (1986) optimised timing intervals by considering accuracy (intrinsic uncertainty) and precision (counting statistics) to immediately estimate the PAEC. From his method, the combined uncertainties of accuracy and precision at 0.1 WL and timing

sequences below 10 min of the total duration yielded PAEC with 20% less uncertainties.

The advantages of the Kusnetz technique is its simplicity and no calibration in the radon/radon progeny chamber is required. The only requirement is the counting efficiency of the alpha detector. However, this technique cannot distinguish individual progeny.

#### 2.6.2.2 Tsivoglou and Modified Tsivoglou Methods

The earliest method for the determining individual radon daughter concentrations was created by Tsivoglou, Ayer and Holaday (1953). In this classical Tsivoglou method, a ratemeter was used to record gross alpha count rates at 5, 15, and 30 minutes after a 5, 10 or 30 minute sampling period at sampling flow rates of 5 to 10 litres per minute. The decay rates of the sample, measured as a function of time, are obtained from a graph of count rate vs time at 5, 15 and 30 minutes after sampling. The method required that the alpha counter's response be independent of the 6.00 to 7.69 alpha energy range (NCRP, 1988). The three-radon progeny concentrations of $^{218}$Po, $^{214}$Pb and $^{214}$Bi are then calculated by solving three simultaneous equations obtained from Bateman equations (Bateman, 1910).

The derivation of these simultaneous equations inherently assumed that for the duration of the sampling process, the concentration of each airborne progeny remain constant for the duration of the sampling process and the pump velocity, collection and counting efficiencies remain unchanged during measurement. In addition Tsivoglou incorrectly assumed that the rate meter accurately recorded the total average values for the count rate at each interval, which contributed to large measurements uncertainties.

Breslin, George and Weinsteinm (1969) established that the count rate for this method was to some degree, inaccurate, specifically for

determining $^{218}$Po. Replication errors for $^{214}$Pb:$^{218}$Po and $^{214}$Bi:$^{218}$Po ratios were found to be 15-25% and 25-35% respectively (NCRP, 1988).

Raabe (1969) recorded the alpha count rates at every 3 minutes over the whole decay interval from the end of the sampling period to 30 minutes after sampling. This method applied the least-square fit method to calculate the individual progeny concentrations using a computer program with improved precision.

Thomas (1970, 1972) modified the Tsivoglou method to allow for counting over finite intervals by replacing the ratemeter with a scaler to optimise the count interval timing and record total counts instead of count rates. In his modification, Thomas neglected the effects of all random errors, except for the counting errors, which should be accounted for by Poisson statistics. Considering that the total measurement time was limited to 35 minutes in the Tsivoglou method, Thomas recommended alpha counting from 2 to 5, 6 to 20, and 21 to 30 minutes after the end of a 5 minute sampling period, with a sensitivity of the order of 40 Bq/m$^3$ for each nuclide (NCRP, 1988, Nazaroff, 2010, Nazaroff, Nero, 1988).

The individual concentrations of $^{218}$Po, $^{214}$Pb and $^{214}$Bi in pCi/L are calculated from the following equations (Thomas, 1972):

$$C_{218_{Po}} = \frac{1}{FE}[0.1689C_1 - 0.0820C_2 + 0.0775C_3 - 0.0562R_b] \quad (2.7)$$

$$C_{214_{Pb}} = \frac{1}{FE}[0.0012C_1 - 0.0206C_2 + 0.0491C_3 - 0.1571R_b] \quad (2.8)$$

$$C_{214_{Bi}} = \frac{1}{FE}[-0.0225C_1 + 0.0332C_2 - 0.0377C_3 - 0.058R_b] \quad (2.9)$$

where

F is the flow rate in L/min;

E is the alpha counting efficiency in cpm/dpm;

$R_b$ is the background count rate in cpm;

$C_1$ is the gross count in interval 2-5 minutes after sampling (a three minute count);

$C_2$ is the gross count in interval 6-20 minutes after sampling (a 14 minute count); and

$C_3$ is the gross count in interval 21-30 minutes after sampling (a 9 minute count).

The Thomas-Tsivoglou three-count method is still one of the most widely used to measure individual radon progeny (Kadir et al., 2013). In spite of that, this technique in this form is not sufficiently sensitive for environmental applications where low concentrations of the order of 37 Bq/m$^3$ are needed to obtain reasonable standard deviations (Nazaroff, 2010, Nazaroff, Nero, 1988, Nazaroff, 1984). The main problem is getting a satisfactory number for $^{218}$Po due to its half-life of three minutes. Consequently, more than half of the $^{218}$Po deposited on the filter will decay prior to counting using the times suggested by Thomas (1972). In addition, under the equilibrium conditions, the concentration of $^{218}$Po will be less than that of the other two isotopes.

Several modifications of the Thomas method aimed at optimising the counting intervals to improve sensitivity and precision have been proposed (Nazaroff, 1984, Busigin, van der Vooren and Phillips, 1978, Busigin, Phillips, 1980, Khan, Busigin and Phillips, 1982, Pogorski, Phillips, 1985, Cliff, 1978). These methods offer different sampling times and counting intervals.

After a series of radon progeny measurements using the Thomas method, Busigin, van der Vooren and Phillips (1978) observed that poor precision and the uncertainties in measurements cannot be explained in terms of counting errors alone. Busigin and Phillips (1980) proposed that there may be other factors other than counting errors that contribute to radon progeny measurements uncertainties. They optimised the Thomas-

Tsivoglou method by taking into account the uncertainties related to fluctuations in concentration (about 3%) and flow rate (about 6%) (Leung, 1987). They suggested counting intervals that showed improved precision when more than one minute delays between intervals is applied. Their proposed counting intervals of 2 to 5, 7 to 15, and 25 to 30 minutes yielded improved insensitivity to fluctuations due to flow rate and concentration. The optimised modified Thomas equations for calculating $^{218}$Po, $^{214}$Pb and $^{214}$Bi concentrations in pCi/L that correspond to the counting interval of 2-5, 7-15, and 25–30 minutes as proposed by Busigin and Phillips (1980) are:

$$C_{218_{Po}} = \frac{1}{FE}[0.16821C_1\,(2,5) - 0.11435C_2\,(7,15) + 0.09297C_3\,(25,30)] \quad (2.10)$$

$$C_{214_{Pb}} = \frac{1}{FE}[-0.00082C_1\,(2,5) - 0.02466C_2\,(7,15) + 0.07179C_3\,(25,30)] \quad (2.11)$$

$$C_{214_{Bi}} = \frac{1}{FE}[-0.02184C_1\,(2,5) + 0.04541C_2\,(7,15) - 0.04799C_3\,(25,30)] \quad (2.12)$$

The precision of the $^{218}$Po measurement was enhanced from 1.3 % to 3.5 % for the Thomas-Tsivolglou method to the Busigin and Phillips (1980) method respectively. Overall, the optimized modified Thomas-Tsivoglou method by Busigin and Phillips (1980) demonstrated experimentally to have a 37% better precision than the original modified Tsivoglou method. The optimised Busigin and Phillips (1980) method of measuring individual radon progeny was adopted for this study. The method and experimental procedure are further described in chapter 5.

Khan, Busigin and Phillips (1982) and Quindos et al. (1988) extended the Busigin and Phillips method to measure $^{222}$Rn and $^{220}$Rn decay products simultaneously by proposing five counting intervals after a ten minute sampling period. The proposed optimised counting intervals were taken from 12 - 14, 15 - 30, 40 - 70, 150 - 210 and 280 - 330 minutes after the start of ten minutes sampling.

Nazaroff (1984) reduced the counting error by extending the overall measurement time from 30 minutes as proposed by Thomas to 60 minutes. According to Nazaroff (1984), a one minute post sampling delay time, as compared to the 2 minutes proposed by Thomas, minimises the statistical uncertainty related to $^{218}Po$, thereby improving measurement sensitivity by factors of 3, 7, and 4 for $^{218}Po$, $^{214}Pb$, and $^{214}Bi$ respectively. The proposed timing sequence for one minute delay was 1 to 4, 7 to 24, and 35 to 55 minutes after the end of the ten minute sampling period.

Pogorski and Phillips (1985) carried out mathematical optimisation using the Monte Carlo simulation techniques to quantify the net precision of the three-count gross alpha sampling and counting method. Their simulation results showed that for flow rate variations with relative standard deviations of less than two percent from measurement to measurement, precision estimates emanating from counting statistics alone can be considered valid. Furthermore, for concentration variations with relative standard deviations of less than five percent from litre to litre, predictions by previous models on uncertainty measurements based on counting statistics only can also be deemed reliable.

James and Strong (1973) designed an instrument that allowed for simultaneous gross alpha counting and sampling to measure RaA, RaC and WL with minimum calculations and within the shortest possible time. A silicon diffused junction detector was used to measure the alpha activity of the filter. The first alpha count gave the RaA concentration during sampling and a second alpha count was noted for the same period post sampling. The WL was obtained from the second count from which the PAEC can be calculated.

Cliff (1978) improved the James and Strong concept to include the third gross alpha count by showing that for a 5 minutes sampling period and a total measurement time of 35 minutes, the sensitivity of the $^{218}Po$ assessment can be improved by a factor of up to 5, as compared to the Thomas method. The main problems associated with this method are poor

statistics, clogging of filters and correction of previously collected data for each subsequent counting (Hill, 1986).

Other alternative methods to gross alpha counting for measuring individual radon daughter concentrations are the alpha spectrometry (Martz et al., 1969, Jonassen and Hayes, 1974, Hill, 1975, Tremblay et al., 1979, Nazaroff, Nero and Revzan, 1981, Kerr, 1975, Kritidis, Uzunov and Miniv, 1977, Brenner, 1989) and continuous radon progeny measurements techniques (Momeni, 1979, Haider and Jacobi, 1974, Holmgren, 1974, Leung, 1987, Droullard, Holub, 1977, Droullard, 1982, Kawaji, Pai and Phillips, 1981, Nazaroff, 1983, Hill, 1986, Brenner, 1989). A major disadvantage of the alpha spectroscopic method is that it is a sensitive and sophisticated detection system not suitable for field measurements where conditions are unpredictable and sometimes harsh. The system needs to be placed at or near the sampling point.

Commercially available continuous monitors equipped with a solid state detector and microcomputer having lower limits of detection of 0.0001 WL have been reported (Brenner, 1989). These units are light weight, battery powered and easy to operate. The downside of these units is that they are very expensive and are not suitable for long term measurements at the same location.

### 2.6.3 Equilibrium Factor (F Factor)

In undisturbed atmospheric conditions with little air circulation, where loss of short lived radon progeny is due to radioactive decay only, e.g. in a sealed container, secular equilibrium between the progeny and the parent radon will be established in about 3 hours. i.e. $^{222}$Rn (3.82 d) $\xrightarrow{\alpha}$ $^{218}$Po (3.05 min) $\xrightarrow{\alpha}$ $^{214}$Pb (26.8 min) $\xrightarrow{\beta}$ $^{214}$Bi (19.9 min) $\xrightarrow{\beta}$ $^{214}$Pb (164 ms) $\xrightarrow{\alpha}$ $^{210}$Pb (22.3 y). Under these conditions, the specific activity of the parent radon will be equal to that of its daughters. However such a state of equilibrium is not often realised in nature. During the decay of radon and

its progeny, individual ions or neutral atoms are produced. These ions or atoms may become attached to aerosol particles. The rate of attachment will depend on the complexities related to the distribution of aerosol in the atmosphere. Some progeny atoms will never attach to aerosol resulting in an unattached mode. These unattached radon progeny may plate out or settle out before decaying. It therefore follows that the state of secular equilibrium will be primarily dependent on the "age" of the gas and secondarily on the factors contributing towards the removal of the some of the daughters.

In addition to the effects of diurnal temperature oscillations, outdoor radon and progeny concentration values are significantly affected by experimental and meteorological conditions like wind speed and direction, changes in barometric pressure, soil moisture content and the physical state of the ground. This complex interaction of these soil and meteorological conditions affect radon and progeny outdoor activity levels, making it difficult to isolate cause and effect relationships, particularly when more than one of these conditions changes at the same time. This will lead to the disequilibrium between the radon parent and its progeny.

The disequilibrium between activity concentrations of radon and its progeny can be quantified by a useful quantity called the F factor (or equilibrium factor or radioactivity equilibrium ratio). The F factor is a percentage measure of radon decay progeny in air relative to total produced from radon gas. It measures the magnitude of disequilibrium between radon and its progeny and is therefore a good indication of the "age" of radon/progeny mixture.

The F factor is defined as the ratio of the equilibrium equivalent activity concentration (EEC) to the radon activity concentration ($C_{Rn}$) (Chen, Marro, 2011). It is sometimes defined in terms of the potential alpha energy concentration (PAEC) as the ratio of the potential alpha energy concentration in the mixture to that which would exist if secular equilibrium existed whereby all short-lived progeny were in equilibrium

with the radon present (Chambers et al., 2015). The equilibrium equivalent activity concentration (EEC) is defined as the equivalent concentration of the decay products that is in equilibrium with the parent radon having the same total potential alpha energy concentration per unit volume as the existing non equilibrium mixture. (UNSCEAR, 2000) provided the following expression for computing EEC:

$$EEC = 0.105(f_1) + 0.515(f_2) + 0.38\,(f_3) \tag{2.13}$$

where $(f_1)$, $(f_2)$ and $(f_3)$ are concentrations of $^{218}$Po, $^{214}$Pb and $^{214}$Bi in becquerel per cubic meter respectively. The F factor can then be calculated from the UNSCEAR equation (UNSCEAR, 2000):

$$F = \frac{EEC\ (Bq/m^3)}{C_R\ (Bq/m^3)} \tag{2.14}$$

F factor values have no units and can only range between 0 (for freshly produced radon) and 1 (for radioactive equilibrium between parent radon and its short lived progeny). The radon progeny concentrations will always be lower than that of the parent radon. The F factor is directly dependent on the aerosol concentration which in turn affects the progeny plate out on large surfaces like ground trees, buildings, large structures like tailings etc. as well as “age” of the gas. It is therefore expected that the F factor will vary with height as well. For regulatory purposes and dose determination, UNSCEAR (2000) has recommended the F factor values for outdoor radon to be 0.8, while the NCRP (1988) recommended the F values to be 0.7 for outdoor atmosphere radon.

### 2.6.4 Implications of F factor

The F factor provides helpful information about the actual measured activity levels of radon and progeny. The F factor values in the open air are necessary to identify and compare different areas with potential radon exhalation problems. In reality, the outdoor radon and progeny

concentrations vary significantly with time, distance from the source, meteorology, etc. Therefore, the recommended and assumed outdoor F factor values cannot give a clear reflection of the actual conditions as reported in other studies (Eappen et al., 2006, Križman, Rojc and Peter, 2010, Yu et al., 1997, Kojima, 1996, Raviart et al., 1996, Rozas et al., 2016). It is therefore necessary to estimate the equilibrium factor F under different types of conditions (Rozas et al., 2016).

One of the aims of this study is to validate radon dispersion modelling by applying the concept of the "age" of the gas at various distances from the tailings dam. To achieve this, measurements of equilibrium factor at various distances from the dam under different conditions is desirable. This will give an indication of how "fresh" or "old" the gas is at each receptor point. High radon concentration values compared to progenies, and hence low equilibrium factor, indicate that the radon gas at that receptor point is still "fresh". This low F factor occur when there is high disequilibrium between radon and its progeny in the atmosphere. Under these conditions, radon is of "local" origin, instead of radon transported from other distant sources. With time and distance from the source, the gas gets "old" by decaying into respective daughters, increasing the F factor. This is illustrated in figure 2.7.

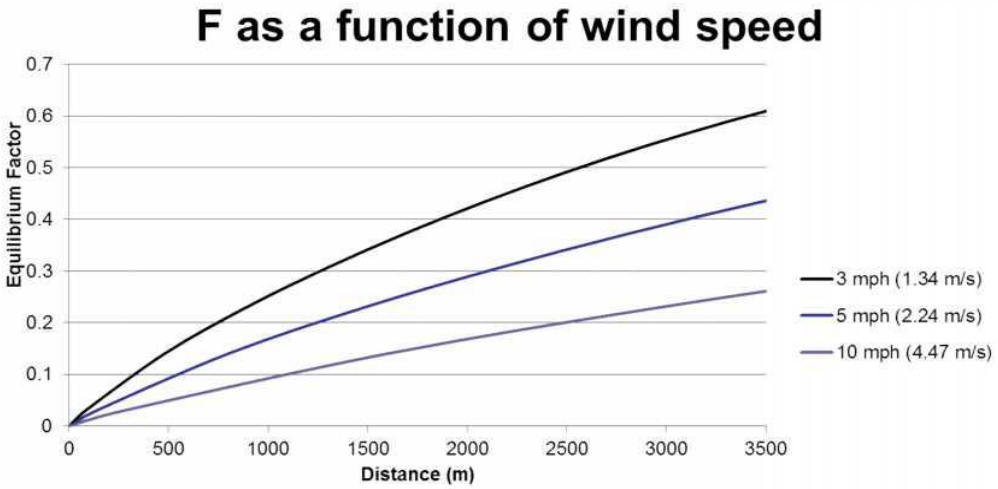


**Figure 2.7: F as a function of distance for different wind speeds (Evans, 1969).**

Porstendörfer (1994) and, Akber and Pfitzner (1994) assessed the diurnal nature of the equilibrium factor by measuring the F factor at different hours of the day. Low equilibrium factor values shown in figure 2.8 were measured during the early morning. The early morning time is characterised by low temperatures and pressure and relatively high radon activity levels (Akber, Pfitzner, 1994). Higher values were measured during daytime under sunny and high pressure conditions (Porstendörfer, 1994).

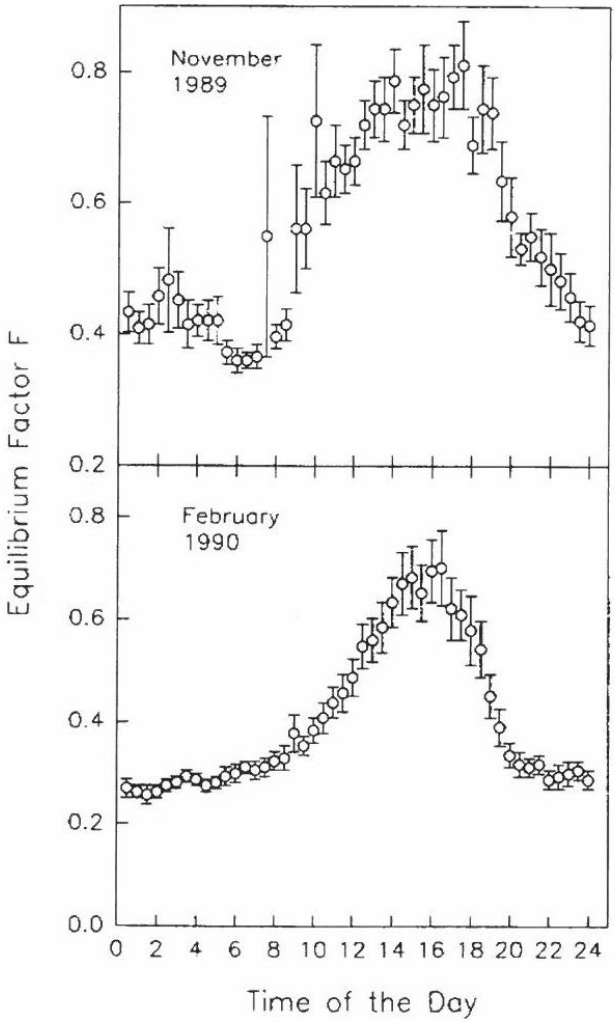


**Figure 2.8: Diurnal variation of equilibrium factor (Akber, Pfitzner, 1994)**

Measurements of the individual radon daughters, notably the ingrowing RaA, RaB and to some extent RaC, will give a much clearer indication on how “fresh” the gas is at a particular point from the source.

To calculate the equilibrium factor, it is required that concentrations of radon and its daughters be measured simultaneously at the same location. Another way of determining the "age" of the gas is to consider the ratios of the individual radon daughter to radon ratios at receptors.

## 2.7 Atmospheric radon dispersion modelling

### 2.7.1 Introduction

When radon and its daughters are introduced into the atmosphere, they will be subjected to dispersion from the source by both convective diffusion and bulk air movements and transport. This movement is controlled by a complex combination of meteorological conditions, emission source strength and the site topography. In view of this dispersion process, the dispersed radon and daughter concentration will vary with the distance from the source. This concentration distribution and dispersion in air depends on a number of factors, including air turbulence, release concentration and height, wind strength and direction, vertical temperature gradient etc.

Atmospheric dispersion can be classified into transport and diffusion processes. The transport of the pollutants is mainly affected by wind speed and direction as well as vertical temperature gradient. The extent of the pollutant's bulk movement or transport associated with increasing dispersion is a function of wind speed. Furthermore, the capping effect due to temperature gradient can lead to the pollutant being trapped close to the surface of the ground, causing the ground level concentrations to increase.

Turbulent or convective diffusion is the random mixing of pollutants by the convective turbulent eddies in air which totally overshadows molecular diffusion as transport mechanism. Molecular diffusion is the spreading of the pollutant due to random motion called Brownian motion emanating from random collisions between molecules. It is a function of

the energy of the particles, the temperature and nature of the diffused medium.

Other factors that could affect the dispersion of pollutants in the atmosphere are source characteristics and meteorological conditions. Source characteristics include rate of emission or release of the pollutant, stack height and exit pollutant temperature whereas meteorological conditions include atmospheric stability and ambient air temperature and pressure. In cases where the exit temperature of the pollutant is higher than the ambient temperature, the pollutant will be elevated to higher levels due to buoyancy effect. Conversely, lower air pressure on the downside of point of release will cause the released pollutant to be drawn towards the downwash. The rate at which the concentration of the pollutant is distributed and deposited in the atmosphere can be estimated by the use of atmospheric dispersion models.

Atmospheric dispersion models uses mathematical codes designed to simulate and predict the movement and distribution of pollutants in the atmosphere by taking into account dominant meteorological and process conditions in the atmospheric boundary layer. The model should also be able to predict convective diffusion rates of the pollutant based on meteorological factors like wind speed, atmospheric turbulence, and thermodynamic effects.

The most common dispersion model data input parameters are background concentration information, source information, meteorological data and topographical information. The model will process these input parameters to predict and describe the movement and diffusion of the pollutant from the source. The output is a 3-dimensional field of pollutant concentration in the atmosphere. In the case of radioactive pollutants like radon and its daughters, the output is expressed in terms of activity concentration in air [Bq/m$^3$]. The model flow chart is illustrated in figure 2.9.

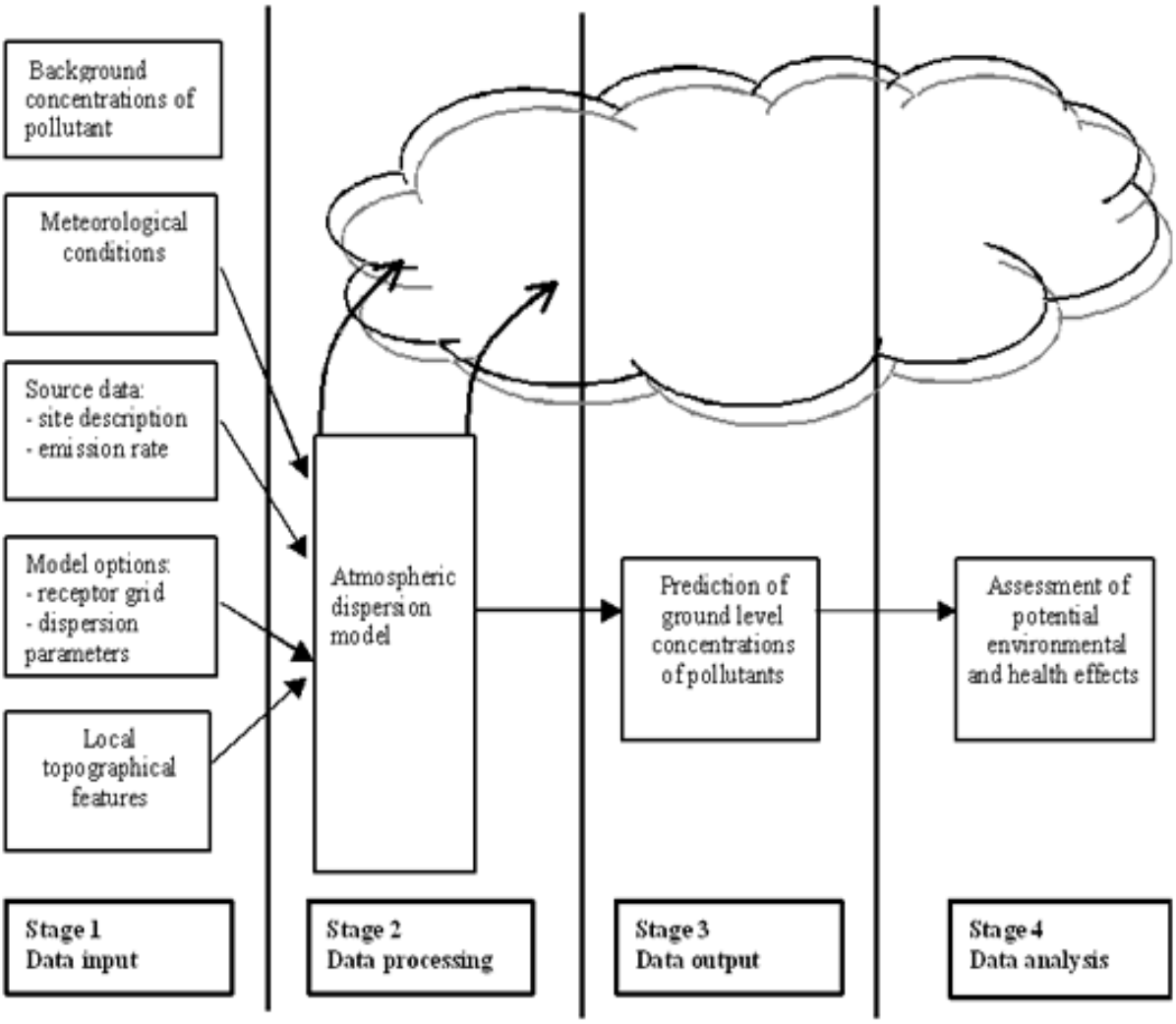


**Figure 2.9: Air pollution modelling procedure (Bluett et al., 2004)**

It follows that a dispersion model is essentially a computational procedure for predicting concentrations downwind of a pollutant source, based on knowledge of the emissions characteristics (tailings radon exit velocity, plume temperature, stack diameter, etc.), terrain (surface roughness, local topography, nearby buildings) and state of the atmosphere (wind speed, stability, mixing height, etc.).

The most common problem in dispersion modelling is to predict the rate of spread of the pollutant cloud, and the consequent decrease in mean concentration. The model has to be able to predict rates of diffusion based on measurable meteorological variables such as wind speed, atmospheric turbulence, and thermodynamic effects. The algorithms at the core of air

pollution models are based upon mathematical equations describing these various phenomena which, when combined with field data, can be used to predict concentration distributions downwind of a source. However, in spite of advancement in modelling software, no model can accurately predict the conditions observed, but can only simulate what happens naturally (Holmes, Morawska, 2006). Furthermore, factors such as errors in the input data, model physics and numerical representation can also lead to uncertainties in the model results (Chang, Hanna, 2004).

### 2.7.2 Classifications of Air Pollution Models

Currently, there exists a number of dispersion modelling approaches that are being used to model air pollutants. These approaches differ substantially in terms of their complexities and their account for different physical and chemical processes that affect the flow and transport. Owing to these differences, different mathematical expressions are required to model and represent these atmospheric processes. Consequently, various atmospheric dispersion models have been developed that are being used by scientists and applied in the industry (Holmes, Morawska, 2006, Hofman, 2011). The most commonly used dispersion models are, Box, Lagrangian, Computational Fluid Dynamics (CFD) and Gaussian Plume and Puff Models.

The next sections outline the general basic features of the four types of dispersion models, with particular attention on the Gaussian plume model as the dispersion model used in this study. A more detailed theoretical background to the Gaussian model will be given, including the general dispersion equation, parameters as well as assumptions underpinning the validity of this model.

#### 2.7.2.1 Box Model

The Box model is the simplest of all the available types of dispersion models. The model uses conservation of mass and energy to evaluate the

mass balance of a given system or airshed. The region of interest, or airshed, is treated as a box into which pollutants are transferred from one environmental domain to another. The air mass inside the box is assumed to be well mixed and concentrations homogeneously distributed. These assumptions are used to determine the concentration of the pollutants anywhere inside the box. The pollutant in the box can be described by the mass balance equation (Hofman, 2011):

*Input rate = Output rate + Transformation rate + Accumulation rate* *(2.15)*

From the mass balance equation (2.21), some pollutants may pass through the box unaltered, some may accumulate within the box, while some may transform due to chemical reactions or radioactive decay. The box model can be described by the equation (U.S. EPA, 1993):

$$C = \frac{Q}{(LS)V(MH)} \qquad (2.16)$$

where

$C$ is the amount of concentration of pollutant (mass or activity/$m^3$);

$Q$ is the total rate of emission (g/s);

$LS$ is the length of the site perpendicular to the wind direction (m);

$V$ is the average wind speed (m/s); and

$MH$ is the mixing height (m).

The observation that radon and daughters' concentrations are relatively homogeneous with altitude in the troposphere's lowest layers (Lopez et al., 1974) prompted Guedalia et al. (1980) to use the box model to determine the equivalent mixing height at the top of the box. However, their structure and application of this model was too simple for two reasons: firstly, the decay of radon was not considered and secondly, at the top of the box, the entrapment of air with different concentration was not allowed (Pasini, Salzano and Attanasio, 2014).

The box model has been used to characterise diurnal and seasonal variability of the radon tracer and to indirectly assess the amount of activity of the monthly averaged radon soil flux (De Luca et al., 2014) and to predict and measure atmospheric radon and radon daughters concentrations when combined with the measured data from tethersonde profiles (Leach, Chandler, 1992, Dinis, Fiúza, 2014).

Overall, the box model's inability to accurately predict the air dispersion is due to the fact that well mixed and homogeneous air conditions are unrealistic, thus limiting its application to calculating concentrations within small areas. Also, the model is unsuitable for application to particulate matter due to its inability to reflect on the local environmental changes of wind field and emissions (Holmes, Morawska, 2006).

#### 2.7.2.2 Lagrangian Models

Lagrangian models, like the box model, confine the region of interest to a box containing air mass with initial concentrations of the pollutants. Concentration is modelled as partial volumes (boxes) in a 3-dimensional atmospheric grid. The Lagrangian dispersion model then mathematically traces and describes the downwind path of pollution plume parcels or particles through the atmosphere using a random walk process. The model accounts for any changes in the concentration due to molecular diffusion, fluid velocity and wind profile by continuously tracing the trajectory of the particles in time and space. The model also accounts for deposition and radioactivity as a time-dependent decay term within each particle (Stohl et al., 2005).

Lagrangian models can be applied to both flat and complex terrains (Basit et al., 2008) for homogeneous and stationary conditions and for inhomogeneous and unstable media conditions respectively (Holmes, Morawska, 2006, Hofman, 2011). This model has been used to parameterise and evaluate the convective particle transport of radon

(Forster, Stohl and Seibert, 2007), analyse the influence of different transport conditions (Sakashita et al., 2004) on radon concentration by applying a receptor-oriented approach (Arnold et al., 2010), and to measure pollutant concentration over longer period of up to years even up to years (El-Harbawi, 2013).

The advantages of this model is its ease of operation and it is relatively inexpensive. Furthermore it can trace the pollutant back to the source by relating concentrations at the receptor site to that at the source of emissions (El-Harbawi, 2013).

The disadvantages of this model includes failure to account for chemical interactions between different air parcels, over-estimating concentrations of the pollutant, incorrectly predicting location of the pollutants under complex wind fields and difficulty in handling dispersion and interactions of multiple puffs (Holmes, Morawska, 2006, El-Harbawi, 2013).

#### 2.7.2.3 Computational Fluid Dynamics Models (CFD)

Computational fluid dynamics models are governed by the application and solution of the Navier-Stokes equation and the continuity equation to analyse fluid flow. These equations are used to define many single-phase (gas or liquid, but not both) fluid flows. The model is based on the conservation of mass and matter and use finite volume and finite difference methods in three dimensions to resolve the Navier-Stokes equation by assuming a laminar flow (Ojha et al., 2010). These two equations can then be solved simultaneously on a grid of points with the aid of a computer. In cases where there is turbulent flow, the Navier-Stokes equation with the continuity and k-ε turbulence closure methods is used to calculate the isotropic eddy viscosity parameter present in both the momentum and pollution transport equation (Holmes, Morawska, 2006).

The basic form of the Navier–Stokes-equation for turbulent incompressible fluids is given by the following equation (Hosch, 2009):

$$\frac{\partial \vec{v}}{\partial t} + (\vec{v}\nabla)\vec{v} = -\frac{1}{\rho}\nabla p - \vec{g} + \upsilon_\tau \nabla^2 \vec{v} \qquad (2.17)$$

where $\vec{v}$ is the wind field, $\rho$ is density, $p$ is pressure, $\upsilon_\tau$ is the eddy viscosity and $\vec{g}$ is the gravitational acceleration vector.

Key parameters of a computational fluid dynamics model are the mesh generator separating the computational domain to the cells, the partial differential equations solver that will be able to solve the Navier–Stokes and other attached (e.g. dispersion) equations and the turbulence model. Segments and 3-D plots of the calculated fields can be created using an appropriate visualisation device. For atmospheric dispersions, simulations are often executed on hexahedral mesh and/or using finite volume solvers.

Xie, Wang and Kearfott (2012) used the CFD method to numerically model dispersion mechanism of radon above the ground in the surroundings of the uranium mine shafts. The applied CFD method incorporated a commercially available Fluent (ANSYS Fluent 13.0.0, ANSYS Inc., Southpointe, 275 Technology Drive, Canonsburg, PA 15317 USA) simulating model for complex modelling of the actual physical uranium mine shafts terrain.

Xie et al., (2014) further applied the three-dimensional CFD simulation to analyse the dispersion of radon under neutral atmospheric stability conditions. The model was used for an occupied home and a farmed location around surrounding area of uranium mine ventilation shaft.

The primary disadvantages of this model are its high cost, time consuming and computationally rigorous. It is therefore unsuitable for real

time applications (Argyropoulos et al., 2010) like direct outdoor radon field measurements.

#### 2.7.2.4 Gaussian model

Gaussian models are the most basic and popular dispersion models used in atmospheric dispersion modelling, particularly for modelling odour emissions (Sarkar, Longhurst and Hobbs, 2003, Sheridan et al., 2004, Schulte et al., 2007, Al Jubori, 2016), bio aerosol emissions (Taha et al., 2007, Drew et al., 2007, Douglas, 2013) and dispersion of non-reactive radioactive gases like radon (van Vuuren et al., 1995, Strydom, 1999, Botha, Ellis and Forbes, 2009, Petzer, 2018). Their simplicity, user-friendly nature, consistency with regards to the random nature of the atmospheric turbulence and fast response time make these models an appealing choice in the scientific community (Sharma, Chandra, 2008). The Gaussian models are sometimes encapsulated within the Lagrangian and Eulerian models (Holmes, Morawska, 2006, Hofman, 2011) to realistically describe the dispersion of non-reactive pollutants at a local level for a static atmosphere (Lazaridis, 2011).

These models assume an independent Gaussian distribution of the plume concentration at each downwind distance in both horizontal and vertical directions under steady state conditions (Holmes, Morawska, 2006, Zannetti, 1990), The downwind distribution produces a cone-shaped plume of polluted air, with the apex of the cone towards the emission source (Sheridan et al., 2004). This is depicted in figure 2.10 and described mathematically in equation (2.18).

The model assumes that after some time, there exists time independent steady state conditions regarding the emissions of air pollutant and the changes in meteorological conditions. The concentration of the pollutant is maximum at the point of release and decreases in both horizontal and vertical directions following the normal distribution. Most

of the Gaussian models compute average concentration over the duration ranging from 10 min to 1h (Hoinaski, Franco and de, 2017).

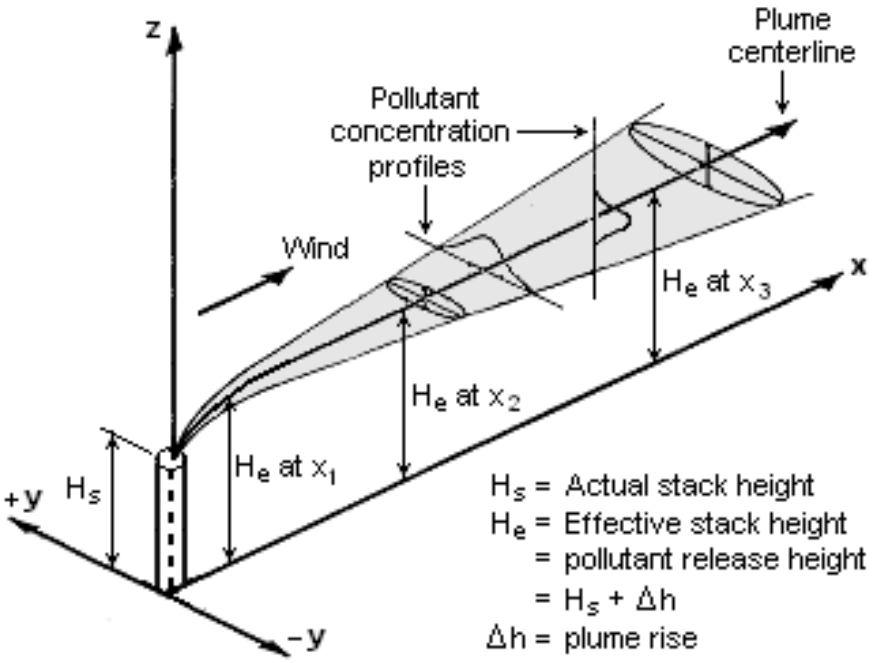


**Figure 2.10: Cone-shaped plume from elevated emission source (Bluett et al., 2004)**

There are different mathematical representations of Gaussian models, each modified to best befit the type of analysis at hand. The three dimensional concentration field of the pollutant C at some location (x,y,z) emitted from a continuous steady point source having an effective height of H is given by the Gaussian differential equation (Hoinaski, Franco and de, 2017, Aggarwal, Haritash and Kansal, 2014):

$$C(x,y,z) = \frac{Q}{2\pi U\sigma_y\sigma_z}\, exp\left(-\frac{y^2}{2\sigma_y^2}\right)\left[exp\left(\frac{-(z-H)^2}{2\sigma_z^2}\right)\right.$$

$$\left. + exp\left(\frac{-(z+H)^2}{2\sigma_z^2}\right)\right] \qquad (2.18)$$

where:

C($x,y,z$) is the steady-state concentration of the pollutant at $x$ meters downwind (source), $y$ meters horizontally from plume centerline, and $z$ meters above the ground level;

Q uniform emission rate of pollutant (mass/unit time);

U wind speed at height of release (m/s);

$\sigma_y, \sigma_z$ standard deviation coefficients of the horizontal and vertical dispersion parameters respectively (m); and

H effective height of the source (H = h + Δh), where h is the physical stack height and Δh is the plume rise (m).

From equation (2.18), the first exponential term is the crosswind factor representing the horizontal dispersion and the second exponential term is the vertical factor representing the vertical dispersion. The standard deviation coefficients are defined in terms of stability classes formulated by Pasquill (1961) and Gifford Jr. (1976) and are considered to increase with increasing downwind distance (Holmes, Morawska, 2006). These coefficients tend to also vary with atmospheric turbulence (Neshuku, 2012). That is, unstable and turbulent atmosphere will yield high standard deviation values whereas less turbulent atmospheric conditions will result in low values (Neshuku, 2012).

For continuous and infinite emissions from a ground level point source, equation (2.18) reduces to (Aggarwal, Haritash and Kansal, 2014):

$$C(x,z) = \frac{Q}{\sqrt{2\pi}U\sigma_z}\left[exp\left(\frac{-(z-\Delta h)^2}{2\sigma_z^2}\right) + exp\left(\frac{-(z+\Delta h)^2}{2\sigma_z^2}\right)\right] \quad (2.19)$$

where Δh = plume rise for ground level sources.

The Gaussian plume model is based on the following assumptions (Holmes, Morawska, 2006):

- the rate of pollutant emission is constant and uniform (steady-state);
- atmospheric stability class and wind velocity are constant;
- net downwind diffusion is negligible compared to vertical and crosswind diffusion;
- relatively flat terrain along the path of the plume;
- mass is conserved, that is there is no deposition or absorption, no chemical change and no radioactive decay of the pollutant; and
- crosswind and vertical concentration distributions follow a Gaussian distribution (Neshuku, 2012).

Although the Gaussian plume model is the most widely used dispersion model, it is not always the ideal model to utilise (Bluett et al., 2004). The primary assumption during the derivation equation (2.18) is steady state conditions. However, meteorological and emission conditions continuously change with time. Consequently, the model neglects the time of travel of the pollutant to the receptor and the vertical particle movement due to gravity during this time, making it unsuitable for far-field modelling and particle dispersion, where meteorological conditions change with distance (Holmes, Morawska, 2006). Another limitation of this model is that it's performance under low wind velocity conditions or at locations close to the point of release is not good. Further limitation is that Gaussian plume equation assumes that plumes do not interact and fail to estimate recirculation effects due to multiple buildings or at intersections (Abdel-Rahman, 2008).

To correct some of these historical model limitations, advanced Gaussian models have been developed to accommodate the chemistry and

physical processes such as dry and wet deposition and also radioactive decay within the plume and around big structures like buildings (Hofman, 2011). The dispersion coefficients can be modified to account for the effects of wakes from buildings (Holmes, Morawska, 2006). Recent hybrid models, which integrate the Gaussian plume and puff models, contains algorithms that improve the accuracy of estimating the concentration of the pollutant under low wind speed surroundings (Thomson, Manning, 2001).

## 2.8 Industrial Source Complex Model (ISC3)

ISC3 (Industrial Source Complex Model) is a steady-state Gaussian plume model specifically developed to assess concentration of pollutants due to different sources related to industrial complexes. ISC3 can accommodate the following: combination of point, line, area, volume sources; dry deposition of the pollutant downwind the stacks, different types of pollutants; adjustment of terrains; downwash; and plume rise as a function of downwind distance. It can also account for non-reactive pollutant, particulate matter as well as first order radioactive decay (U.S. EPA, 1995b).

There are two versions of the ISC3 model. The long term model (ISCLT), which evaluates average concentration values over an area of several hundred square kilometres for a period of a year or more. The short term version, the Industrial Source Complex-Short Term Version 3 (ISCST3), utilises hourly meteorological data to define conditions for plume rise, transport, diffusion and to calculate mean concentrations for a period ranging from one to few hours. The ISCST3 algorithms have been modified to improve performance with regard to: receptors in complex terrain; wake effects due to surrounding structures; and building downwash (Al Jubori, 2016).

The ISCST3 has been extensively used in air-quality modelling studies in the past (e.g., (Kumar, Bellam and Sud, 1999, Lorber, Eschenroeder and Robinson, 2000, Faulkner, Shaw and Grosch, 2008,

Behera et al., 2011, Hasan, 2001) and has a relatively good history of monitoring compliance with air quality standards. Its weaknesses and strengths are well documented (Lorber, Eschenroeder and Robinson, 2000, Silverman et al., 2007, Mahapatra, Ramjeawon, 2011, Reeves, 2001).

Radon is a dense gas that is approximately 8 times heavier than air. It is however easily influenced by air movements and pressure. Given the dense nature of radon, the use of other dense gas models like the Dense Gas Dispersion Model (DEGADIS) have been proposed. DEGADIS is used to primarily model the transport of toxic chemical releases into the atmosphere. However, the model does not characterise the density of aerosol-type releases; which must be independently assessed by the user prior to the simulation. It is especially useful in situations where density effects are suspected to be important and where screening estimates of ambient concentrations are above levels of concern. This made this model not suitable in this study, given the ISCST3 performance record in similar conditions.

The primary advantages of ISCST3 over other Gaussian models (AERMOD, ADMS, etc.) are its relative simplicity of operation and its vigorous, robust and reproducible predictions (Doğruparmak, Karademir and Ayberk, 2009, Hanna et al., 2001). For this study, the commercial software package, BREEZE AERMOD GIS Pro (Version 4.0., Trinity Consultants Inc., 2002), was used for all modelling runs. A brief overview and description of the ISCST3 model is given below.

### 2.8.1 Description of the ISCST3 model

The Industrial Source Complex Short Term 3 (ISCST3) model is a versatile, straight line, steady state Gaussian plume model that presents different options to model emissions from a wide range of sources. It can be used to model simple point source emissions from stacks, emissions from stacks that experience the effects of aerodynamic downwash due to

nearby buildings, tailings dams, storage piles, conveyor belts, etc. within 50 km of the source (U.S. EPA, 1995b).

Emission sources are classified into four basic types, i.e., point sources, volume sources, area sources, and open pit sources. Because of this multiple source handling ability, the ISCST3 uses different algorithms to enumerate atmospheric dispersion for point, area and volume sources. The algorithms used to model each of the three source types considered in this study as well as parameter characterization of each source type are briefly described in the following sections.

#### 2.8.1.1 Point source emissions

Point sources involve the release of emissions from well-defined stacks or isolated vents, at known physical stack parameters and conditions of operations. The ISCST3 model for point sources uses the steady-state Gaussian plume equation for a continuous elevated source. The ground surface at the base of the stack is taken as the origin of the source's coordinate system of the stack. The x-axis is positive in the downwind direction, the y-axis is crosswind (normal) to the x-axis and the z-axis extends vertically. This is illustrated in figure 2.10.

The fixed receptor locations are represented by each source's coordinate system for each hourly concentration calculation. Total concentration produced at each receptor by the combined source emissions is obtained by summing the hourly concentrations calculated for each source at each receptor.

For a steady-state Gaussian plume, the hourly concentration at downwind distance $x$ (meters) and crosswind distance $y$ (meters) from point emission sources is given by (U.S. EPA, 1995b):

$$C(x) = \frac{QKVD}{2\pi u_s \sigma_y \sigma_z} exp\left[-0.5\left(\frac{y}{\sigma_y}\right)^2\right] \qquad (2.20)$$

where:

$Q$ pollutant emission rate (mass per unit time);

$K$ a scaling coefficient to convert calculated concentrations to desired units (default value of 1 x $10^6$ for Q in g/s and concentration in $\mu g/m^3$);

$V$ vertical term;

$D$ decay term;

$\sigma_y$, $\sigma_z$ standard deviation of lateral and vertical concentration distribution (m) (dispersion parameters); and

$u_s$ mean wind speed (m/s) at release height.

The vertical term ($V$) includes the effects of source elevation, receptor elevation, plume rise, limited mixing in the vertical, gravitational settling and dry deposition of particulates (with diameters greater than about 0.1 microns).

Point sources can be characterised by considering basic model inputs required by the ISCST3. For any point source, the basic ISCST3 model inputs requirements are:

- Source ID: A source identification name of up to 8 characters in length;
- Stack location coordinates: The $x$ (east-west) and $y$ (north-south) coordinates of the center of the point. Units are in meters;
- Source base elevation: Applicable only if elevated terrain is being used. The default unit is meters;
- Release height above ground [m] (center of the volume);
- The emission rate of the pollutant in grams per second;
- Stack gas exit temperature in degrees Kelvin;
- Stack gas exit velocity in meters per second or the stack gas flow rate (V/s); and
- Stack inside diameter (m).

In cases where a main source has multiple stacks and buildings, the individual locations of each source should be used in the model.

#### 2.8.1.2 The Short-Term Area Source Model

Area sources are used to model low level or ground level releases that occur over an area (e.g., landfills, storage piles, slag dumps, and lagoons) (U.S. EPA, 1995a). The ISC Short Term area source model integrates numerically over the area in the upwind and crosswind directions of the Gaussian point source plume formula given in equation (2.20).

ISC-PRIME models accept rectangular areas with aspect ratios (length/width) of up to 10 to 1 that may also have a rotation angle specified relative to a north-south orientation, as well as other different irregular shapes (Bluett et al., 2004). An irregularly shaped area can be simulated by dividing the area source into multiple rectangular areas.

The ground-level concentration at a receptor located downwind of all or a portion of the source area is given by a double integral in the upwind (x) and crosswind (y) directions as (U.S. EPA, 1995b):

$$C(x) = \frac{Q_A K}{2\pi u_s} \int \frac{VD}{\sigma_y \sigma_z} \left\{ \int_y exp\left[ -0.5 \left( \frac{y}{\sigma_y} \right)^2 \right] dy \right\} dx \qquad (2.21)$$

where:

$Q_A$ area source emission rate (mass per unit area per unit time);

K units scaling coefficient (Equation (2.20);

V vertical term (see Section 2.8.1.1); and

D decay term as a function of x.

There are no limitations on the location of receptors relative to area sources. Receptors may be placed within the area itself, downwind of the

area or at the edge of an area. The U.S. EPA models (ISCST3, ISC-PRIME, and AERMOD) will estimate the integral over the portion of the area that is upwind of the receptor. The ISCST algorithm does not execute numerical integration for portions of the area that are closer than 1.0 meter upwind of the receptor. Therefore, receptors should be placed within or adjacent to areas that are at least 1 m or less wide (Bluett et al., 2004, U.S. EPA, 1995b).

ISCST3 input parameters required to characterize area sources are:

- Source ID: A source identification name of up to 8 characters in length;
- Location: The x (east-west) and y (north-south) coordinates for the vertex (corner) of the area source that occurs in the southwest quadrant of the source. Units are in meters;
- Geometry: This includes South West (SW) corner, initial vertical dimension, and angle of rotation;
- Source base elevation: Applicable only if elevated terrain is being used. The default unit is meters;
- Release height above ground [m]; and
- Emission rate [g/(m$^2$.s)]: The emission rate for area sources is input as an emission rate per unit area. For this study, the emission rate is the radon exhalation flux determined in chapter 3.

#### 2.8.1.3 The Short-Term Volume Source Model

Volume sources are used to model releases from various industrial sources, such as building structure. The ISCST3 models use a virtual point source algorithm to model the volume source by locating an imaginary or virtual point source at some distance upwind of the volume source (called the virtual distance) to account for the initial size of the volume source plume (U.S. EPA, 1995b). Therefore, equation (2.20) for point source emissions is also applicable to calculate concentrations produced by

volume source emissions. Plume dispersion of a virtual point source from a volume source is depicted in figure 2.11.

The width and height dimensions of the volume source are modified and represented as initial lateral and vertical dimensions respectively. The general procedures for estimating initial lateral ($\sigma_{yo}$) and vertical ($\sigma_{zo}$) dimensions for single volume sources and for multiple volume sources are summarized in table 2.2.

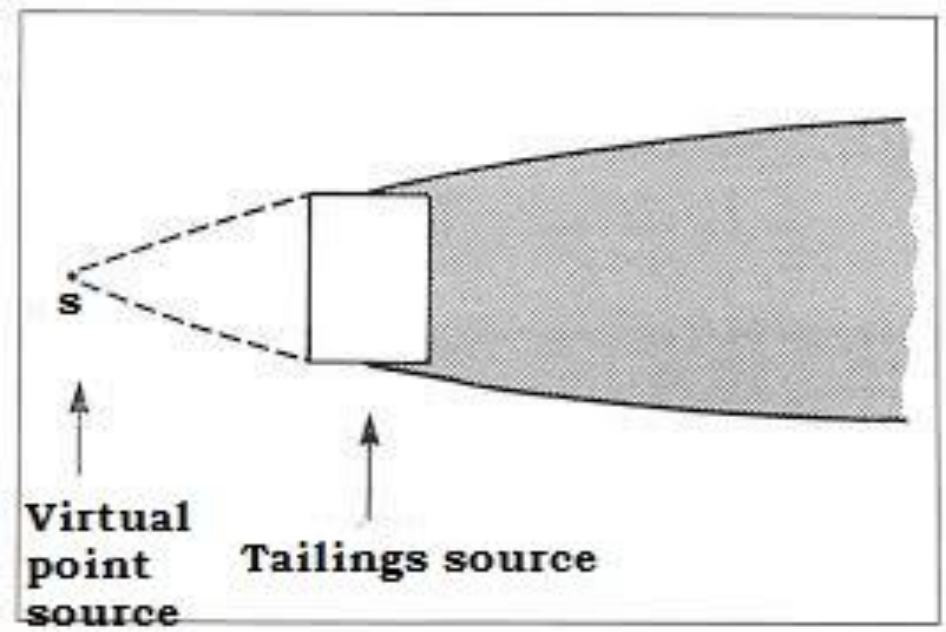


**Figure 2.11: Plume dispersion from a virtual point source (Zannetti P., 1990).**

*Table 2.2: Initial dimensions for a volume (virtual point) source (U.S. EPA, 1995b)*

| Type of Source | Procedure for Obtaining Initial Dimension |
|---|---|
| **(a) Initial Lateral Dimensions ($\sigma_{yo}$)** | |
| Single Volume Source | $\sigma_{yo}$ = length of side divided by 4.3 |
| Line Source Represented by Adjacent Volume Sources | $\sigma_{yo}$ = length of side divided by 2.15 |
| Line Source Represented by Separated Volume Sources | $\sigma_{yo}$ = center to center distance divided by 2.15 |

| (b) Initial Vertical Dimensions ($\sigma_{zo}$) | |
|---|---|
| Surface-Based Source ($h_e$ - 0) | $\sigma_{zo}$ = vertical dimension of source divided by 2.15 |
| Elevated Source ($h_e$ > 0) on or Adjacent to a Building | $\sigma_{zo}$ = building height divided by 2.15 |
| Elevated Source ($h_e$ > 0) not on or adjacent to a Building | $\sigma_{zo}$ = vertical dimension of source divided by 4.3 |

ISCST3 input parameters required to characterise volume sources for dispersion modelling are:

- Source ID: A source identification name of up to 8 characters in length;
- Location: The x (east-west) and y (north-south) coordinates of the center of the volume source. Units are in meters;
- Source base elevation: Applicable only if elevated terrain is being used. The default unit is meters;
- Release height above ground [m] (center of the volume);
- Emission Rate [g/s;]
- Side length (meters): The volume source cannot be rotated and has the X side equal to the Y side (square); and
- Initial lateral and vertical dimensions (meters).

### 2.8.2 Building wakes

Buildings and similar structures like tailings dams in the path of air flow create a turbulent wake region on the leeward (i.e., downwind) side of the building. This downwash effect leads to higher ground-level pollutant concentrations near the building than if the building was not present.

When radon air-flow meets a tailings dam (or building), it is forced up, over and around the dam, creating a turbulent wake region on the downwind side of the building. This is illustrated in figure 2.12. This effect is not only confined to the modification of the streamlines of the airflow, but also to the speed and turbulence of the air. A plume caught in the path

of this airflow is drawn into the wake, temporarily trapping it in a recirculating cavity, leading to enhanced ground level concentrations of the pollutant closer to the tailings as compared to if the tailings was not considered. This region is called the Near Wake recirculation zone (or Cavity zone). On the upwind side of the tailings, an Upwind Recirculation zone (or upwind cavity) exists.

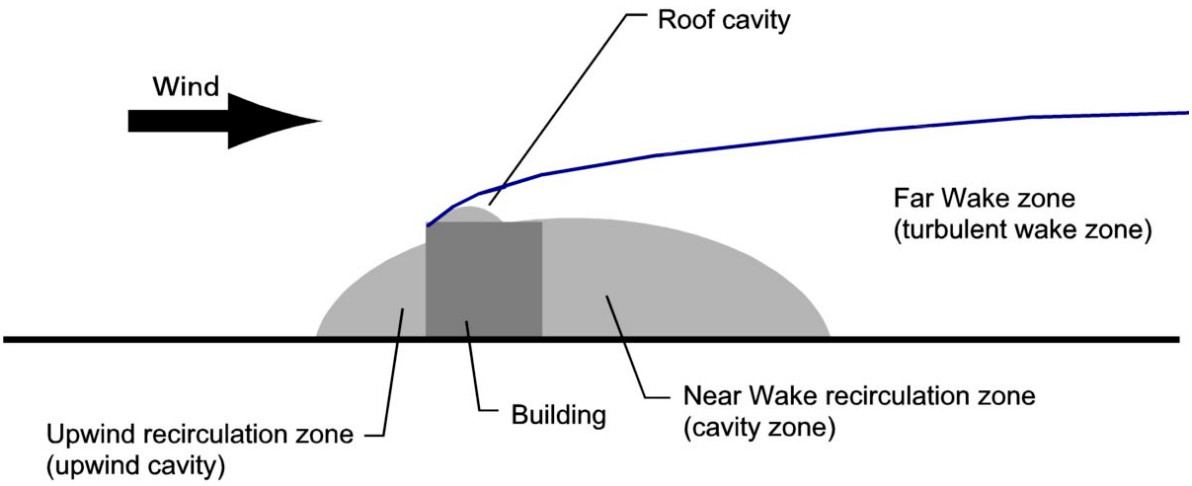


**Figure 2.12: Building wake effects on air (Olesen et al., 2005)**

At some distance downwind, the air flows will have a downward gradient, thus bringing the plume closer to the ground. This will lead to more shear and hence, increased turbulence. This region is called Far Wake zone (or the Turbulent Wake zone). Because of the increased turbulence in the wake zone, the dispersion and dilution of the plume material will be enhanced. The final effect on the ground level concentrations will depend on the combined effect of the increased dispersion and reduced plume height (Olesen et al., 2005).

The Plume Rise Model Enhancements (PRIME) algorithm was created and incorporated into the Industrial Source Complex Short Term model (ISCST3) to account for two fundamental features: enhanced plume dispersion coefficients due to the wake turbulence, and reduced plume rise caused by descending streamlines and increased entrainment in the wake of a structure.

The foundation of the PRIME model is its ability to model the downwind cavity (near wake) and far wake areas on a three-dimensional scale. The dimensions of the downwashing structure are used to form an ellipsoidal shape that may consist of a rooftop and downwind cavity, or a single recirculation cavity.

One of the major uncertainties of previous modelling results from tailings dams was due to unaccounted wake effects. All studies cited in literature review ignored their effects on the overall incremental radon contribution, primarily because of modelling complexities relating to wakes. In this study, radon contribution downwind due to wake effect of emissions from nearby or adjacent virtual point sources is investigated using the ISC PRIME algorithm.

The building wake effect algorithm is only applicable to point sources and do not apply to volume, area or open pit sources. Furthermore, additional input information is required by the algorithms to model the building wakes. These necessary inputs are generated by running the EPA Building Profile Input Program (BPIP) for all point sources (stacks). The BPIP is used to establish the probability of a point source to be subjected to wake effects due to the surrounding structures (Silverman et al., 2007). This information is added as an input to ISC.

### 2.8.3 ISCST3 Inputs

The main input requirements for ISCST3 are meteorological conditions, receptor locations and source/emission parameters.

#### 2.8.3.1 Meteorological Inputs

The model utilises meteorological data to simulate plume transport and dispersion. Input meteorological data required on hourly basis are:

- ambient temperature (K);
- wind direction;
- wind speed (m/s);
- atmospheric stability classes (A through F, entered as 1 through 6); and
- mixing height (m).

Atmospheric stability classes represents extremely turbulent conditions (A class) to very calm and inversion conditions (class F) where warm air at higher altitudes and cooler near ground air have very low to zero wind speeds that prevents the dispersion of the pollutants.

#### 2.8.3.2 Source/emission parameters inputs

The number one critical parameter in any modelling analysis is the emission rate (Bluett et al., 2004). Any errors in the rate of emission data will directly render model results erroneous. The emission rate, denoted by the symbol 'Q' in the Gaussian equation (2.18), is the modeling source term, the exhalation flux, and it represents the amount and rate of pollutant emitted from the source of the release (Barratt, 2001). For inert pollutants like radon gas, the rate of emission is directly proportional to the modelled concentration.

The dispersion equation used by ISC dispersion software can be written in generalised form as:

$$C = \mathrm{DF} \times \mathrm{S} \qquad (2.22)$$

where:

C is the concentration of pollutant [mass.m$^{-3}$];

DF is a dispersion factor accounting for all dispersion parameters e.g. stability and wind speed; and

S is the source strength of pollutant [mass.s$^{-1}$].

It therefore follows that the mass quantity used in equation 2.22 is immaterial and can be g, mg, kg or any other mass quantity since the same unit appears on both sides of the equation. The becquerel (Bq) unit of radioactivity is also a mass unit through the radioactive decay equation:

$$A = \lambda N = \frac{\lambda m A_v}{M} \tag{2.23}$$

from which:

$$m = \frac{MA}{\lambda A_v} \tag{2.24}$$

where:

$A$ activity [Bq];

$\lambda$ decay constant [s$^{-1}$];

$N$ number of atoms;

$m$ mass [g];

$M$ Molar mass [g.mole$^{-1}$]; and

$A_v$ Avogadro's number.

Equation 2.22 can be written in activity units as concentration of activity $C_A$:

$$C_A[\text{Bq}.m^{-3}] = \text{DF x } S_A\ [\text{Bq}.s^{-1}] \tag{2.25}$$

Or in mass units as:

$$C_m[\text{g}.m^{-3}] = \text{DF x } S_m\ [\text{g}.s^{-1}] \tag{2.26}$$

It follows from equation 2.24 that the conversion factor $M/\lambda Av$ is the same on both sides of equation 2.25 and therefore cancels. Radioactive decay is accounted for in ISC and is factored into the dispersion factor DF. Therefore there is no need to convert source term values or concentration values between activity and mass. It should further be noted that the ISC software allows a scaling factor in the mass units, e.g. the output concentration can be in units of $\mu g.m^{-3}$.

Source/emission data gives an indication on how the emitted pollutants are released into the atmosphere. Source/emission data required by model include:

- source dimensions;
- discharge rate of emissions; and
- release height of the emission source.

#### 2.8.3.3 Receptor locations

In addition to meteorological and source/emission parameters, the ISCST3 model also requires the receptor coordinates across the modelling area. These coordinates correspond to points of interest where occurrences of exposures are being investigated. The ISCST3 dispersion model allows the user to define the receptor location by selecting either a Cartesian (X, Y) or a polar (r, θ) receptor grid system.

## 2.9 Radon dispersion modelling from gold mine tailings dams facilities

Regulated radon sources like tailings dams near or at ground level are mostly characterised by complex geometries that are challenging to model and quantify properly. Most of these tailings dams are located close to industrial and residential properties, thus requiring regulation in terms of impact of emissions. When radon emissions exceed screening levels,

exhaustive dispersion modelling that takes into account variations in the source term, meteorology and near-field dispersion is necessary.

From a dispersion modelling perspective, tailings dams can be classified as non-point sources due to their large geometrical structures. However, the use of non-point sources like area and volume sources to model dispersed pollutant from tailings dams and other big structures like buildings have been characterised by poor source characterisation. This is both due to inadequately defined physical features and highly unreliable emissions rates (Stocker et al., 2016).

Outdoor atmospheric radon have been modelled in various environmental conditions, locations and surroundings (De Luca et al., 2014, Leach, Chandler, 1992, Dinis, Fiúza, 2014, Arnold et al., 2010, Xie, Wang and Kearfott, 2012, Xie et al., 2014, Hasan, 2001, Liland, 2015, Arnold, Vargas and Ortega, 2009, Hirao et al., 2008, Dinis, Fiúza, 2015, Belot, , Vinuesa, Galmarini, 2007, Marcazzan, Persico, 1996, Smetana, Novak, 1996, Kovalets et al., 2017, Yu, Mallants and Olyslaegers, 2011). These studies applied Gaussian (Dinis, Fiúza, 2014, Hasan, 2001, Dinis, Fiúza, 2015, Belot, , Kovalets et al., 2017), Lagrangian (Arnold et al., 2010a), Eulerian (Hirao et al., 2008), Box (De Luca et al., 2014, Leach, Chandler, 1992, Marcazzan, Persico, 1996) and Computational Fluid Dynamics (CFD) (Xie, Wang and Kearfott, 2012, Xie et al., 2014) models to predict radon from silos (Hasan, 2001), transport station (Arnold et al., 2010), solitary islands in the Pacific (Hirao et al., 2008), radioactive waste disposal facilities (Dinis, Fiúza, 2015, Yu, Mallants and Olyslaegers, 2011), uranium tailings (Dinis, Fiúza, 2014, Botha, Ellis and Forbes, 2009, Kovalets et al., 2017), in situ soil measurements (De Luca et al., 2014) and uranium mine shaft ventilation (Xie, Wang and Kearfott, 2012, Xie et al., 2014).

As part the radon monitoring programme, the environmental radon contribution from tailings dam has been the focus of several studies and regulatory programmes in South Africa due to gold mining activities.

However, literature on applicability of dispersion models to predict and quantify radon contributions from tailings dam facilities is very limited. The majority are unpublished radiological safety assessment technical reports from environmental radioactivity assessment impact studies due to uranium, gold and other related mining industries (Petzer, 2018, von Oertzen et al., 2016, de Villiers, 2018) and basic modelling data from an unpublished radon monitoring thesis (Botha, Ellis and Forbes, 2009). In all these studies, short term Gaussian models were applied to monitor and predict radon concentrations on and off site in the gold mining sector. A review of these radon dispersion studies from tailings dams is discussed below.

Van As et al. (1992) used the Gaussian AIRDOS_EPA to model radon from the tailings by assuming the tailings to be a circular ground-level flat area source and the emission rate of 0.0004 $Bq/m^2.s$. Natural background concentration assumed to be 30 $Bq/m^3$. The AIRDOS_EPA was found to be limited to ground level sources or tall stacks only and could not handle complex topography. The model gave results that significantly over-predicted radon concentrations at areas closer to the dam and under-predicted radon at areas far from the dam. In addition variability of the source term with erosion ravines was not accounted for.

As an alternative to use the commercially available modelling software, Goosen, Strydom and Leuschner (1993) classified different tailings into four clusters and solved the Gaussian dispersion equation to predict radon concentration from the four tailings dam clusters. The source term in clusters I and II were extrapolated, while for clusters III and IV the source terms were measured. The emission rates from each cluster were: Cluster I: 0.091–0.821 ($Bq.m^{-2}.s^{-1}$); Cluster II: 0.20-2.527 ($Bq.m^{-2}.s^{-1}$); Cluster III: 0.372-0.386 ($Bq.m^{-2}.s^{-1}$) and Cluster IV: 0.14 ($Bq.m^{-2}.s^{-1}$). The emission source geometry assumed was area source at heights of 28.8 m (cluster I), 29.0 m and 51.5 m (cluster II), 26.0-30.0 m (cluster III) and 20.0 m (cluster IV) respectively. The height of cluster I dams were unknown

and therefore assumed (28.8 m) from the average of the other known dams. Natural background concentration was assumed to be 10 Bq/m$^3$. However, their calculations were very conservative and unreliable due to assumptions of several critical modelling parameters, thus over-predicting radon concentration results.

Van Vuuren et al. (1995) used the ISCST2 to model tailings dam as volume source by subdividing the tailings into 16 square sub-sources each having maximum side length of 400 m at height of 5 m. Building wake effects were excluded from calculations. In addition, not all the sources were quantified. The same source strength was used for all the tailings sources on the mine site. As such, their results were inconclusive with regard to the extent of the dispersion.

Strydom (1999) predicted high radon doses after applying ISCST32 to model the tailings dams as a volume virtual point sources. Due to their large sizes, the sources were subdivided into a number of adjacent volume sub-sources. The high doses were mainly due to the large variations in the emission rates from different tailings dams and rock piles as manifested by large standard deviations values. The total emission rate was calculated from the total radon contributed from all exhalation sources. It was therefore recommended that more sampling locations be established in order to improve the statistical accuracy of the source and hence the model results.

A flat ground-level area has been the emission source geometry method of choice by several modellers using ISCST3 (Botha, Ellis and Forbes, 2009) and AERMOD (Petzer, 2018, von Oertzen et al., 2016, de Villiers, 2018) to model radon from the tailings dam. The reliability of their results were overshadowed by assuming: (i) 1 Bq/(m$^2$.s) emission rate (de Villiers, 2018), (ii) radon was released from the entire surface area of a source and (iii) a unit release rate of radon gas (Petzer, 2018). In all these instances, any physical parameters or mitigation measures which could affect the release of radon were not taken into consideration. This led to

unreliable radon concentrations predictions compared to measurement at the receptors.

Notable features from studies outlined above reveal the following:

- many of these studies have either overestimated or underestimated the source input values by assuming uniform pollutant emissions from the dam. Emission variations due to slope areas, gulleys and cracks in the tailings surface have not been accounted for;
- all area sources were modelled as ground-level flat sources, neglecting the effects of the height of the dam on the near ground receptors. This led to expecting an even bigger estimation of predicted radon concentrations at near ground level receptors;
- wake effects, which have the potential to significantly increase radon concentrations at near ground receptors, were not accounted for in all the studies; and
- a single volume source in ISCST3 is not always appropriate for 3-dimensional sources. In case of tailings dams, their massive size and design may require dividing one volume source into multiple volumes, which may have unintended consequences of misrepresenting the true size of the emitting source.

The literature review above highlights prevalent inaccurate representation of the source term, and hence the emission rate of the pollutant. The emission rates were based on measurements that misrepresented the true emissions at the source. Depending on the model input source type, this tends to over- or under-estimate radon concentration at the receptor locations, thus providing biased radon doses.

Given that the dimensions of tailings dams are quite significant, it is expected that the sizeable side areas of the dams will contribute significantly to the radon emissions and their geometrical orientation must be accounted for in the model. Hence it is necessary to assess the extent of the misrepresentation of the source term by investigating the

performance and sensitivity of ISCST3 model for radon modelling from the tailings dam in respect of the source geometry, emission rate and building wake effects or building downwash. This will be achieved by evaluating and comparing modelled downwind radon concentrations from an identified tailings dam for different source types and different input parameters (emission rates) under similar meteorological conditions.

## 2.10 Model sensitivity

Model sensitivity refers to the scale of variation of model predictions with a change of the value of a particular input parameter (Bluett et al., 2004). Sensitivity analyses is one way of prioritizing which parameters need to be quantified. Given the lack of consistency and accuracy in different model inputs, particularly with regard to source term and source geometry, sensitivity analyses are necessary to establish the models' sensitivity to these input uncertainties. This information will be used to determine source impact, evaluate control strategies and improve forecast (Sportisse, 2007).

Several sensitivity analyses have been performed on various models for different input parameters and pollutants (Faulkner, Shaw and Grosch, 2008, Stocker et al., 2016, Kovalets et al., 2017, U.S. EPA, 1998, Gulia, Shiva Nagendra and Khare, 2014, Yegnan, Williamson and Graettinger, 2002, Yegnan, Williamson and Graettinger, 2003). From these studies, sensitivity tests reported that the ISCST3 model is sensitive to changes in meteorological conditions of wind speed, wind direction, temperature and stability class (Faulkner, Shaw and Grosch, 2008, Stocker et al., 2016, Gulia, Shiva Nagendra and Khare, 2014, Yegnan, Williamson and Graettinger, 2002, Yegnan, Williamson and Graettinger, 2003), solar radiation (as it affects stability class), mixing heights below 160 m, surface roughness (Faulkner, Shaw and Grosch, 2008), source geometry (area vs volume sources) (Stocker et al., 2016, Schewe, Smith, 2009) and emission rates (Aggarwal, Haritash and Kansal, 2014, Stocker et al., 2016, Sullivan,

Holdsworth and Hlinka, 2004, Oudwater, 2017). Based on these sensitive tests, the emission rate was found to be a significant input parameter that has the highest impact for the sensitivity analyses (Aggarwal, Haritash and Kansal, 2014, Stocker et al., 2016, Sullivan, Holdsworth and Hlinka, 2004, Oudwater, 2017). Due to lack of available literature on sensitivity tests for radon dispersion from tailing dams, it was deemed imperative to perform source term sensitivity analysis on radon dispersion from tailings dams.

## 2.11 Model validation

Uncertainty in the predictions of a dispersion model occurs due to a number of sources, including atmospheric turbulence, the idealisations inherent in any mathematical model, the appropriateness of the model chosen for a specific application and the values ascribed to the various model parameters.

Model validation is an important part of modeling studies used to show if a model produces accurate and reliable output (Bluett et al., 2004). It is a way to determine the level of accuracy of the model for predicted results.

Model input data are based on assumptions and calculations using empirical formulas. The accuracy of the model results are affected by the accuracy of these calculations and assumptions. The best way for validating the model performance is to compare the estimated results from the model with the measured values.

The EPA and American Meteorological Society conducted a workshop to develop an extensive model performance validation program (Nappo et al., 1982). This lead to the development of a comprehensive library of statistics that summarises the performance of various models.

ISC dispersion model has been extensively evaluated and validated for point and area sources on atmospheric dispersion of odours, NOx, $SO_2$,

$CO_2$, bio aerosol emissions, agricultural sources, ammonia ($NH_3$) and particulate matter ($PM_{10}$) (Chang, Hanna, 2004, Hanna et al., 2001, Stocker et al., 2016, Yegnan, Williamson and Graettinger, 2002, Yegnan, Williamson and Graettinger, 2003, Bowers, Anderson and Hargraves, 1982, EPA, 1992, EPA, 1994, Schulman, Hanna, 1986, Riswadkar, Kumar, 1994, Paine, Lew, 1997, Georakis et al., 1995, Hall et al., 2002, Andretta et al., 2006, Prabha, Singh, 2006, Schroeder, 2006, Demirarslan, Çetin Doğruparmak and Karademir, 2017, Dore et al., 2015). No data is available for ISC dispersion model evaluation and validation for radon from tailings dams.

Kumar, Bellam and Sud (1999), Stocker et al. (2016), and Bandyopadhyay (2009) discussed and reported various ISCST3 performance evaluation and validating studies and their results from point, area and volume source field data. The results from most of these studies showed a good agreement at 95% confidence level between predicted concentrations and measured (observed) concentrations, particularly for point sources.

### 2.11.1 Model validation - Statistical analysis

To validate and quantify the agreement between predicted and measured data, the modelling system must be evaluated by applying various statistical descriptors associated with model validation (Prabha, Singh, 2006, Arya, 1999, Rama Krishna et al., 2005).

The statistical methods that were previously used to validate models, namely, the mean, standard deviation, regression analysis and measures of difference and correlation, were found to be suspect (Prabha, Singh, 2006). The analysis and interpretation of models' performance based on these methods tend to be very difficult and unreliable. Observations by Willmott, Wicks (1980) and Willmott (1982) showed that it is possible to obtain negative correlation for any small change in the measured and predicted concentrations. For example, measures of correlations method

is a reflection of linear relationship between two variables which is insensitive to multiplication or additive factor. It is therefore an inadequate method for model evaluation. As a consequence, Willmott and Wicks (1980) and Willmott, (1982) recommended the use of index of agreement (IOA) $d$, a dimensionless measurement which indicates the model prediction accuracy. In addition to index of agreement, other statistical descriptors that have been recommended by EPA and used in this study are Normalized Mean Square Error (NMSE), Geometric mean bias (MG), Fraction of predictions within a factor of two (FA2) and Fractional Bias (FB) (Kumar, Bellam and Sud, 1999, Arya, 1999, Rama Krishna et al., 2005). From the statistical model performance measures explained below:

$C_O$: Observed (measured) concentration

$C_P$: Modeled concentration

Overbar: average over the whole dataset

**(a) Index of agreement (IOA)**

The index of Agreement was developed by Willmott and Wicks (1980) and Willmott (1982) to predict accuracy of the model. Index of agreement is a non-dimensional and bounded standardised measure of the extent of model prediction error with values that varies between 0 and 1. A value closer to 1 indicates a good agreement and 0 signal no match at all (Willmott, 1982). The expression for the Index of agreement is given by:

$$d = 1 - \frac{\sum_{i=1}^{n}(C_P - C_O)^2}{\sum_{i=1}^{n}(|C_P - \overline{C_O}| + |C_O - \overline{C_O})|^2} \qquad (2.27)$$

**(b) Fractional Bias (FB)**

The Fractional Bias (FB) is symmetrical, bounded and normalised to make it a dimensionless number. FB is a linear measure and shows the degree of matching between the means of the predicted and observed concentration distribution. It is a convenient performance measure for comparing results from different concentration levels. The values for the fractional bias varies between +2.0 (extreme over prediction) and -2 (extreme under prediction). For a perfect and ideal model, free from bias, the FB will have an ideal value of 0 (zero). Mathematically it is represented as:

$$FB = 2x\left(\frac{\overline{C_O} - \overline{C_P}}{\overline{C_O} + \overline{C_P}}\right) \quad (2.228)$$

**(c) Geometric Mean Bias (MG)**

Geometric mean bias (MG) is a logarithmic measure that gives a more balanced predicted and observed treatment of very high and low values (Chang, Hanna, 2004). MG is an indication of the degree of bias of the geometric mean rather than the arithmetic mean. Extremely low values strongly influence MG and at zero values, MG is undefined. The expression for the Geometric Mean Bias is given by:

$$MG = exp\left(\overline{lnC_O} - \overline{lnC_P}\right) \quad (2.239)$$

**(d) Normalised Mean Square Error (NMSE)**

Normalised Mean Square Error (NMSE) estimates the overall deviations between the observed and predicted values by showing striking differences among models. It is a measure of scatter and a reflection of both random and systematic errors. NMSE is a linear measure that is also

strongly influenced by high predicted and observed concentrations. The equation representing the NMSE is given by:

$$NMSE = \frac{\overline{(C_O - C_P)^2}}{\overline{C_O} \text{ x } \overline{C_P}} \quad (2.30)$$

Low NMSE values is an indication that the model is performing well in space and time.

**(e) Fraction of predictions within a factor of two (FAC2)**

Fraction of predictions within a factor of two (FAC2) is defined as the fractional percentage of the predictions within a factor of two of the observed values. FAC2 is the most robust measure, mainly due to its immunity to influences by high and low outliers. FAC2 can be expressed as

$$FAC2 = fraction\ of\ data\ that\ satisfy\ 0.5 \leq \frac{C_P}{C_O} \leq 2.0 \quad (2.31)$$

The ideal value for the factor of two should be 1 (100%).

There is not a single measure that can be universally applied to all modelling conditions. Multiple performance measures are recommended because each measure has advantages and disadvantages as partly determined by the variable distribution. The distribution of atmospheric radon concentration as determined in chapter 3, resembles a log-normal distribution. In this instance, linear measures FB and NMSE are strongly affected by irregularly occurring high observed and predicted concentrations, whereas logarithmic measure MG present a more balanced treatment of extremely high and low concentrations. Therefore, MG would be more appropriate for a dataset where both predicted and observed concentrations vary by many orders of magnitude. FAC2, on the

other hand, is the most robust measure, mainly due to its immunity to influences by high and low outliers.

A perfect and ideal model would have the value of index of agreement (*d*), geometric mean bias (MG), fraction of predictions within a factor of two (FAC2) equal to 1.0; and fractional bias (FB) and normalised mean square error (NMSE) equal to 0. However, in real life there is no perfect model in air quality modelling. The reliability and performance of the model can be determined by following criteria suggested by Chang and Hanna (2004). The performance of a model can be deemed as "good" and acceptable if 50% of the predictions are within a factor of two of the observations, a relative mean bias (((model – observation)/model) x 100%) is about ±30%, and a relative scatter (or the extent to which a distribution is spread out) is within a factor of two or three (Chang, Hanna, 2004). In cases where the points are paired in space and time, these criteria have to be relaxed.

The criteria used in this study to determine whether the reliability and performance of the ISCST3 model can be considered acceptable was based on the guidelines suggested by Kumar et al. (2006):

$$0.4 \leq d \leq 1.0$$

$$NMSE < 0.5$$

$$-0.5 < FB < +0.5$$

$$FAC2 > 0.8$$

$$0.75 < MG < +1.25$$

The predictions of the ISCST3 model with regards to each source term are classified as "under-prediction", "exact prediction" and "over-prediction" for assessing their performance.

# Chapter 3 Radon exhalation measurements using sealed "diffusion tube" method

## 3.1 Introduction

The previous chapter identified various methods of measuring radon exhalation rates from porous materials like tailings. This chapter describes the method used in this study to measure the radon exhalation flux from the tailings dam. The theoretical background, procedure and results are presented.

Radon release from the radium bearing tailings dam to the atmosphere is a result of a series of processes, namely: emanation, transport and exhalation (Moed, Nazaroff and Sextro, 1988). Only a fraction of the radon atoms (the emanation fraction) created in porous material due to the radium decay will be able to escape from the mineral grains and enter the void space. The source term for radon expressed as the rate of production per unit volume in the residue material such as tailings, $P$ (Bq/m$^3$·s) is given by (IAEA, 1992, Ishimori et al., 2013):

$$P = \lambda \varepsilon R \rho \qquad (3.1)$$

where

$\lambda$ is the radon decay constant (2.06 x 10$^{-6}$ s$^{-1}$);

$\varepsilon$ is the emanation fraction (dimensionless);

$R$ is the radium activity concentration in the residue material (Bq/kg);

$\varepsilon R$ is the effective radium content; and

$\rho$ is the bulk density (kg/m$^3$).

From equation (3.1), it follows that the source term for radon is a function of the decay constant, emanation fraction, radium activity concentration and the bulk density of the material (IAEA, 2013).

Upon entering the pore space, emanated radon atoms' movement from the mineral grains in the tailings to the surface becomes a function of diffusion and advection transport mechanisms. However, advective flow on transport is temporal, rapid and complex to model (Guo, Sun and Cheng, 2004) and it fluctuates, resulting in high and low peaks. Thus the dominant average transport mechanism becomes the diffusion mechanism, which was considered in this study. The pore space in the soil has a higher concentration of radon than that on the atmosphere. As a result, radon atoms will migrate from the pore space with high concentration into the air at low concentration through the diffusion process. The difference in the concentration between the two media is the main cause of the diffusion process.

Following emanation and diffusion to the surface, radon near the soil surface boundary will diffuse into the atmosphere. This atmospheric radon release is called radon exhalation, sometimes it is also called exhalation flux density (IAEA, 2013). Thus radon exhalation rate depends on the $^{226}$Ra concentration in the material, emanation factor of radon from the material, porosity, convective effects due to pressure differences, permeability, density of the material, diffusion coefficient of the radon in the material, and moisture content and temperature (UNSCEAR, 2000, IAEA, 2013, Altic, 2014, Guan, Jianping and Guo, 2006, Lawrence et al., 2009, Altic, 2011). Depending on the physical structure of the tailings, the rate of escape of radon from the tailings is usually higher than from normal soils (Nuclear Energy Agency, 1984).

Radon exhalation at the ground surface between soil and atmosphere is a continuous process, and can be expressed as (IAEA, 1992):

$$E = \rho \varepsilon R \sqrt{\lambda D_e} \qquad (3.2)$$

where $D_e$ is the effective diffusion coefficient, characteristic of the material under study.

Equation (3.2) is the radon source term from the tailings to the atmosphere. There are two basic methods of measuring radon diffusion coefficient from samples (Hassan et al., 2009). The first method is based on the dependence on time of the increasing of radon concentration called transient method (Jiránek, Fronka, 2008, Sasaki, Gunji and Okuda, 2006) and the second one is based on the use of stable radon concentration (equilibrium radon concentration) called the steady-state method (Somogyi et al., 1986). Some of the methods that have been used by researchers that fall into the above two categories are: Electrostatic (Folkerts, Keller and Muth, 1984, Aldenkamp et al., 1992), Ionization Chamber (Jiránek, Fronka, 2008) and Lucas Cell (Quindos Poncela et al., 2005) methods.

The effective radium content is a function of emanation coefficient and radium activity concentration in the residue material. Many methods and techniques have been used to determine radon emanation coefficient of materials. These techniques measure maximum radon concentration emanating from samples in sealed space after radon and radium have attained radioactive secular equilibrium. The radon equilibrium concentration is then measured using gamma spectroscopy.

Somogyi et al. (1986) outlined a steady-state measurement technique which employs the track-etch method to determine all the required exhalation parameters from porous materials such as a tailings surface given in equation (3.2) except for the radium concentration. This relatively inexpensive method with reliable measurement outcomes is the method used in this study.

## 3.2 Theoretical Approach

The passive “diffusion tube technique” or sealed-can technique that uses an etched track detector is a simple and efficient method to assess

radon exhalation rates from porous materials such as mine tailings (Abu-Jarad, Fremlin and Bull, 1980, Amin, 2015, Somogyi et al., 1986, Prasad et al., 2008, Ramola, Choubey, 2004, Chen, Weng and Chu, 1993, Samuelsson, Pettersson, 1984). The geometry of the diffusion tubes is such that the exhalation of radon from a sealed sample surface inside the tube can be modelled by one-dimensional diffusion theory. This theory is used to determine both the diffusion coefficient and emanation fraction of the materials. The two parameters are determined from the radium content, bulk density and track density recorded by the etched track detectors sealed in the open space above the sample in the tube. The diffusion coefficient and emanation fraction determined in this way represent the effective quantities for the given physico-chemical state of the materials and accounts for the effects of absorption, adsorption and molecular diffusion.

In this study, samples of thickness $d$ were placed at the bottom of closed and sealed cylindrical tubes of cross-sectional area $A$ and air height above the specimen $h$. A track-etched detector called radon gas monitor (RGM) was mounted onto the center of the inner top wall of the container as shown in figure 3.1.

To avoid gross underestimation and to yield more comparable results of the true exhalation rate from the sealed tubes material, proper attention must be given to dimensions of the samples and the containers (Hassan et al., 2009), more specifically with regard to the diffusion length of the material (Samuelsson, Pettersson, 1984, Samuelsson, 1990). Therefore, the sample and container geometry must be precisely defined to determine the required exhalation parameters for the tailings samples (Solecki, Tchorz-Trzeciakiewicz, 2011).

From figure 3.1, the sample volume is given by $V_s = A \cdot d$, while the air volume is $V_a = A \cdot h$. Radon concentration accumulates in the air volume $V_a$ from where measurements may be taken using the RGM track-etched detector, thus obtaining the exhalation parameters from the shape of the

radon growth curve. In the track-etch method, the integral under the radon growth curve is obtained by the RGM measurements within the air volume $V_a$.

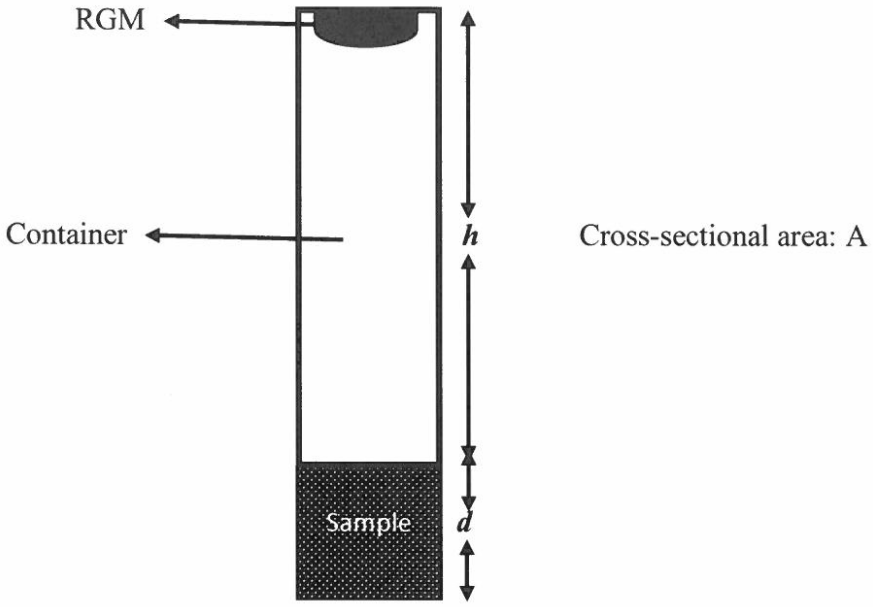


**Figure 3.1: Schematic representation of the sealed can and tube geometry**

Assuming that under steady state conditions, a radon concentration gradient exits only in the direction of depth, one dimensional radon diffusion (no convection) will take place in the sample. This steady state radon diffusion is governed by a one dimensional differential equation describing diffusion to the surface of the sample given by (Ishimori et al., 2013):

$$D_e \frac{d^2C}{dz^2} - \lambda C + \frac{\lambda \varepsilon R \rho}{P} = 0 \qquad (3.3)$$

where

*C*: interstitial radon concentration [Bq/m$^3$];

$D_e$: effective diffusion coefficient [m$^2$/s];

*Z:* sample depth measured perpendicular from surface into the material [m]; and

*P:* porosity of the soil.

There are two ways to define the diffusion coefficient of radon in porous media that have been adopted in the literature, namely the effective radon diffusion coefficient ($D_e$) and the bulk radon diffusion coefficient ($D$). However, Nazaroff and Nero (1988) identified some inconsistencies regarding how these two coefficients are defined and used in modeling the diffusion of radon through porous media. The bulk and the effective radon diffusion coefficients in soil, as stated by Nazaroff and Nero (1988), are related by the total soil porosity, $P$, according to the expression:

$$D = PD_e \tag{3.4}$$

These definitions of $D_e$ and $D$ as suggested by (Nazaroff, Nero, 1988) are the ones adopted in this study. Radon flux density at the material surface inside the tube can then be calculated from the equation (Ishimori et al., 2013):

$$\phi = -D_e\left(\frac{dC}{dz}\right) \tag{3.5}$$

The solution of equation (3.5) according to Somogyi et al. (1986) for interstitial radon concentration is

$$C(z) = C_\infty\left(1 - \frac{cosh\left(\frac{z}{L}\right)}{kcosh\left(\frac{L}{z}\right)}\right) \tag{3.6}$$

where $L = \sqrt{\frac{D_e}{\lambda}}$ is the diffusion length of radon in the material.

In the case of an open container ($V_a \rightarrow \infty$), "free exhalation" will take place from the sample and the geometrical correction factor k would be equal to 1. For a sealed container, $k$ is given by:

$$k = 1 + \frac{PL}{h}tanh\left(\frac{d}{L}\right) \tag{3.7}$$

derived from the boundary condition given by (Somogyi et al., 1986):

$$\phi_A = \lambda A h C(z)|_{z=d} \tag{3.8}$$

where:
$\phi_A$ = areal exhalation from the sample surface [Bq/(m$^2$.s)]; and
$A$ = open surface area of the material [m$^2$].

The areal exhalation rate of radon $\phi_A$ can be obtained from the solution of the one dimensional diffusion differential equation (equation 3.6) and from Fick's first law (equation (3.5)) as

$$\phi_A = \frac{C_\infty D}{kL} tanh\left(\frac{d}{L}\right) = \frac{C_\infty \lambda p L}{k} tanh\left(\frac{d}{L}\right) = \phi_A^\infty tanh\left(\frac{d}{L}\right) \tag{3.9}$$

where $\phi_A^\infty$ is the maximum value $\phi_A$ can attain.

Two important relationships can now be deduced; $\phi_A^b$ and $\phi_A^f$, for the bound (sealed container) and the free (open container) areal exhalation rates respectively. The bound areal exhalation rate is related to the free areal exhalation rate by the equation:

$$\phi_A^b = \frac{C_\infty p L \, tanh(\frac{d}{L})}{1 + \left(\frac{pL}{h}\right) tanh(\frac{d}{L})} = \frac{\phi_A^f}{k} \tag{3.10}$$

From the above relation, the bound exhalation rate is determined by the geometry of the container, i.e. by $k$.

The maximum bound exhalation rate will occur when d $\rightarrow\infty$, such that tanh (d/L) $\approx$ 1 and for given h value is:

$$\phi_A^{b\infty} = \frac{C_\infty \lambda p L}{1 + \left(\frac{pL}{h}\right)} \tag{3.11}$$

The bound mass exhalation rate in terms of (Bq/kg.s) is defined as

$$\phi_M^b = \phi_A^b \frac{A}{M} = \frac{\phi_A^b}{d\gamma} \tag{3.12}$$

where $M$ and γ are sample mass and density respectively.

From equations (3.10) and (3.12), it can be shown that:

$$\phi_M^b = \frac{C_\infty \lambda p L}{d\gamma} = \frac{tanh(\frac{d}{L})}{1 + \left(\frac{pL}{h}\right) tanh(\frac{d}{L})} = \frac{\phi_M^f}{k} \tag{3.13}$$

Thus the maximum exhalation rate ($d \rightarrow 0$, such that $d/L \approx 0$) is given by

$$\phi_M^{b\infty} = \frac{C_\infty \lambda p L}{\gamma} \tag{3.14}$$

From exhalation rate relationships, the two important parameters required for exhalation rate from mine tailings, namely, effective diffusion length ($D_e$) and emanation fraction ($\varepsilon$) can then be determined.

Consider the two cases in which one enclosed sample is much shorter than the other, i.e. in one sample, $d \rightarrow 0$ and in the other sample $d \rightarrow \infty$ (figure 3.2 (a) and (b) respectively). The two containers have the same open air height $h$. If the open air height is much larger that the diffusion length $L$ in the material, i.e. $h \gg L$, then from equations (3.11) and (3.14), it can be deduced that

$$\frac{\Phi_A^{b\infty}}{\Phi_M^{b\infty}} \cong \gamma L \tag{3.15}$$

According to equation (3.15), measurements of $\phi_A^{b\infty}$, $\phi_M^{b\infty}$ and the density γ from the two enclosed samples will yield the bulk diffusion length $L$ of the material. When radon concentration in the open volume of the

sealed can has reached steady state, this concentration is in secular equilibrium with the effective radium content. Knowing $\phi_A^b$, $\phi_M^b$ and γ, the effective radium content can be calculated from the following equation:

$$\lambda C_{eff}^{Ra} = \phi_M^b = \frac{\phi_A^b}{dL} \tag{3.16}$$

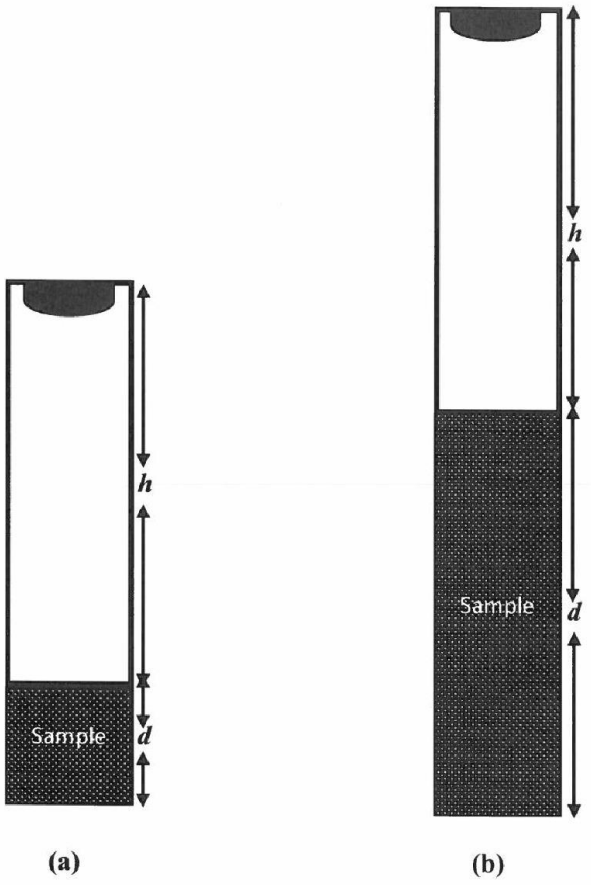


**Figure 3.2: Two containers with different sample lengths and same air space**

It therefore follows from equation (3.2) that

$$\varepsilon R = C_{eff}^{Ra} \tag{3.17}$$

Both mass and aerial exhalation rates are obtained from the measured integrated concentrations from the RGM in the sample containers.

## 3.3 Measurement methods and materials

### 3.3.1 Radon Gas Monitors (RGM)

Passive time-integrated carbon infused Radon Gas Monitors (RGMs) (see figure 3.3) manufactured by Parc RGM (South Africa) were used to measure the radon concentrations inside the diffusion tubes. The RGMs are rugged, CR-39 alpha particle etched-track passive detectors having lower detection level of up to 22 Bq/m$^3$ for one month exposure (PARC RGM, 2018).


**Figure 3.3: Radon Gas Monitor**

They are insensitive to gamma radiation, high temperature and moisture and very effective for determining average radon concentrations over long periods ranging from one to three months depending on deployment conditions. The carbon loaded outer shell reduces uncertainties and background interferences associated with the build-up of electrostatics and electric charges. Each RGM has a reference number

on both the outside and the inside of the carbon-infused casing for reference purposes.

The random statistical errors on RGM readings arising from the track density determination depend on the measured radon concentration. The random errors $\sigma_1$ (repeatability of scans), $\sigma_2$ (random counting error), $\sigma_3$ (inter-dosimeter reproducibility) and with the background error $\sigma_b$ are combined in quadrature using the equation:

$$\sigma^2 = \sum_{i=1}^{n} \sigma_i^2 \tag{3.18}$$

The resulting error is shown in figure 3.4 as a percentage of the radon exposure.

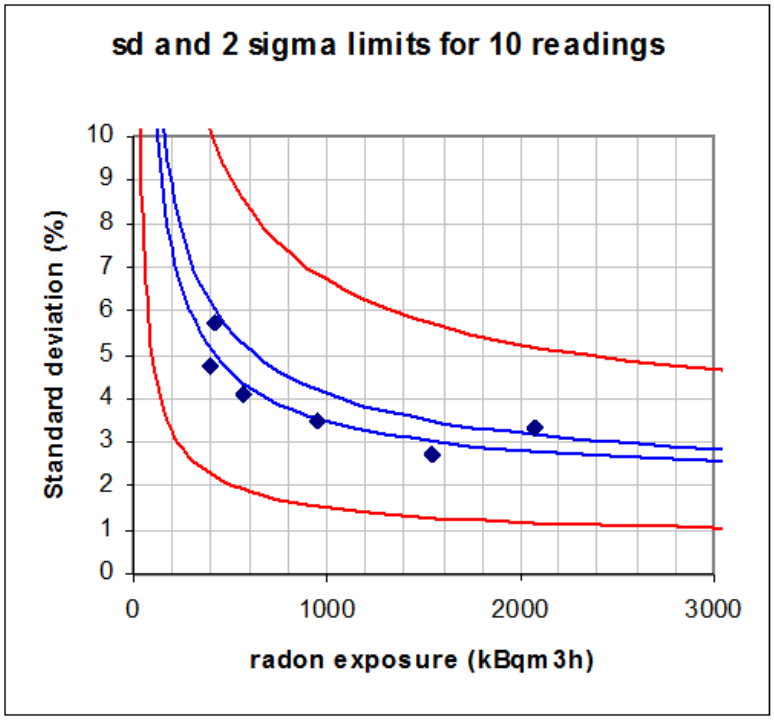


**Figure 3.4: RGM random error as a percentage of the radon exposure (PARC RGM, 2019)**

Similarly, the error can also be shown as an absolute value, as given in figure 3.5 over the range 1 to 10000 kBq h $m^{-3}$.

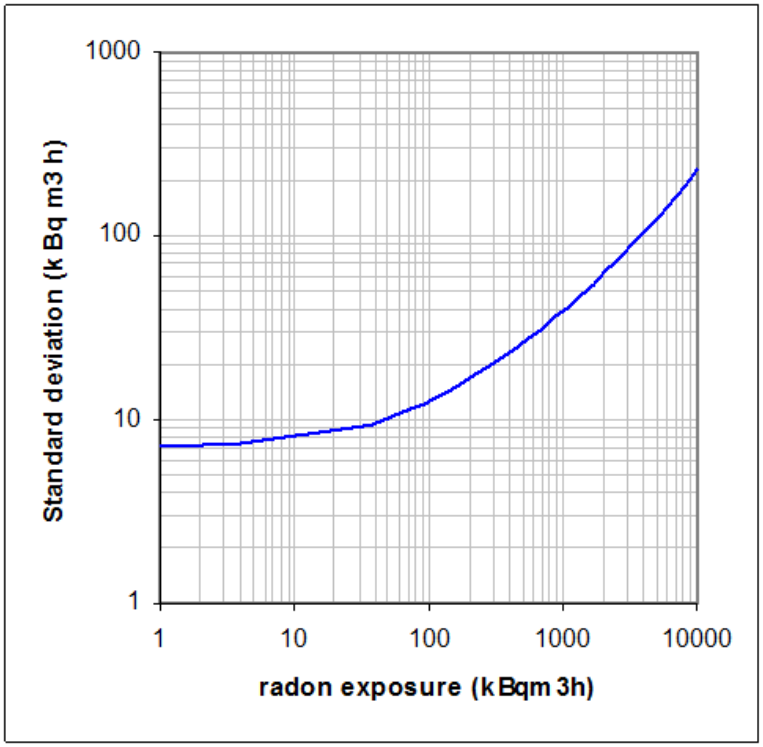


**Figure 3.5: RGM random error as an absolute value of radon exposure (PARC RGM, 2019)**

### 3.3.2 Sampling and measurement procedure

The procedure outlined below is based on the method and theory presented in a technical document of Parc Scientific (Parc Scientific, 1995). This document describes the practical procedures for sampling and collection of source materials for subsequent analysis of Rn/Tn (Radon / Thoron) generation and transport parameters.

Twenty (20) sampling locations shown in figure 3.6 were assigned on a grid-like format to the surface area of the tailings dam. Sampling points were determined by accessibility, safety and minimal saturation with water.

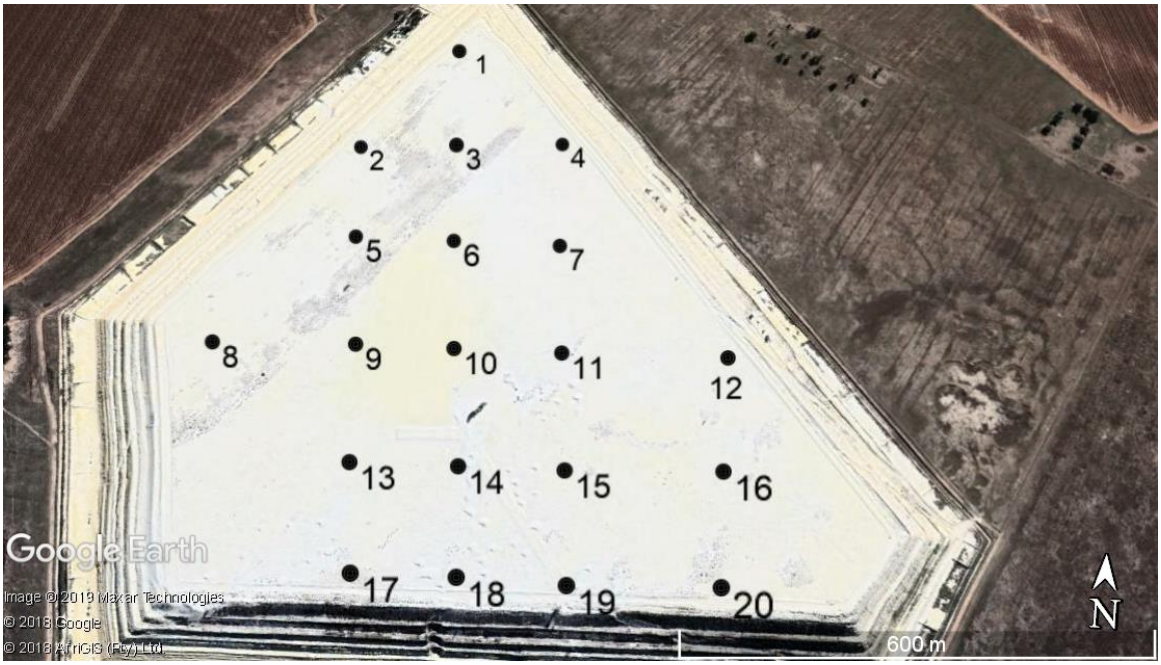


**Figure 3.6: Twenty sampling points on the tailings dam.**

Taking into account that 98 % of radon gas emitted from a thick porous body such as tailings originates in the top 1 m of material (Parc Scientific, 1995), samples were taken from this layer. Twenty (20) plastic 5L buckets with sealable lids were used to collect about 5 kg each of the material from the tailings dam. A Tractor-Loader-Backhoe (TLB) machinery was used to extract sample materials from a depth of 1 m. Sample materials were collected from different depths over one meter, and each sampling point is described below.

Approximately 1.5 ± 0.5 kg of material was removed from the first 30 ± 5.0 cm and deposited next to the sampling hole. Another 1.5 ± 0.5 kg was removed from the next 30 ± 5 cm and the material deposited on top of the previous deposit. Lastly, a further 1.5 ± 0.5 kg was removed from the last 35 ± 5 cm depth. The three samples were thoroughly mixed, collected in the containers and sealed to preserve the moisture content.

About 230 g to 320 g of material samples were compacted into 20 polyvinyl chloride (PVC) short tubes of 11 cm in length and 4.2 cm diameter. The sample containing short tubes were attached to a longer tube of 1.05 m in length to provide a well-defined air space above the

sample material. Additional ± 2.3 kg sub-samples were compacted into 20 longer tubes of 1.01 m in length and same diameter as the short tubes, referred to as “diffusion tubes”. The long tubes, also made of polyvinyl chloride (PVC) material, were also connected to an air space tube of the same length as the short tubes (1.05 m). This implies that both the long and short tubes in figure (3.2) (a) and (b) have the same air space geometry above the compacted material.

According to Southern African Institute of Mining and Metallurgy (SAIMM), gold tailings in South Africa have an average bulk density of tailings material of between 1 250 kg/m$^3$ and 1 650 kg/m$^3$. Based on this, samples in both short and long tubes were compacted using hand tools to a density around these values. The densities of the compacted materials in the short tubes ranged from 1 400 kg/m$^3$ to 1 600 kg/m$^3$ whereas the densities of the compacted materials in the long tubes ranged from around 1 500 kg/m$^3$ to 1 600 kg/m$^3$. After compaction, the diffusion tubes were sealed for twenty one days to attain secular equilibrium. The tubes were then rapidly opened and a CR-39 radon gas etched track monitor (RGM) was inserted at the headspace of each tube and then sealed for a period of 6 days. The integrated radon concentration in the head space was then recorded by the etched track detector in the RGM.

After 6 days exposure, the etched track detectors were chemically etched in a hot NaOH solution to reveal α- particle tracks on the plastic foil. The tracks were viewed and counted using an optical microscope. The number of tracks counted per unit area, $S$, is directly proportional to radon exposure through a calibration factor ŋ. The areal exhalation rate from an enclosed sample is then given by:

$$\phi_A = \frac{Sh\lambda}{\eta T_e} = \frac{Ch\lambda}{T_e} \qquad (3.19)$$

where $T_e = T_2 - T_1$ is the integration time interval, $T_1$ is the starting time of measurement, $T_2$ the end time and $C = S/\eta$ represents the integrated radon

exposure (Bq/m.h) from the RGMs. The calibration factor ŋ (expressed in terms of alpha-tracks.cm$^{-2}$)/(Bq.m$^{-3}$.h) depends on the method, the specific instrument utilised and the sensitivity of the batch of CR39 polycarbonate elements. It typically has a value between 0.002 and 0.003 and is inherently included in the concentration results from the PARC RGM laboratory. The calibration of the RGM is traceable to the 2018 Public Health England Intercomparison of Passive Radon Detectors where the PARC RGM laboratory performed very consistently under four different reference exposure values (PARC RGM, 2019).

Therefore the maximum bound aerial exhalation rate ($\phi_A^{b\infty}$) for samples shown in figure 3.2 (b) for long tubes was obtained directly from equation (3.19) whereas the maximum mass bound exhalation rate ($\phi_M^{b\infty}$) was calculated from samples depicted in figure 3.2 (a) for short tubes using equation (3.12).

The errors on the exhalation parameters are a combination of random errors emanating from the statistics of track density and the systematic errors which relates to the sampling geometry, in particular, the length of the tubes. The systematic errors on these lengths were optimised by Strydom (1996) to be less than 17% for the long tubes having column length of 2 m and air height of 1 m. For the short tubes having the same air height of 1 m but compacted to about 10 cm, the systematic errors will be less than 6%.

The moisture content of the sample was determined by weighing a subsample of the material before and after oven-drying of the sample. All samples were dried in an oven for 10 hours to ensure complete evaporation and removal of the moisture. The moisture content of the sample was recorded as the mass fraction per dry weight:

$$M_w = \frac{m_w - m_D}{m_D} \tag{3.20}$$

where $M_w$, $m_w$, and $m_D$ are dry weight mass fraction, wet mass of the sample (kg) and dry mass of the sample (kg) respectively. The moisture content $S$, expressed as the moisture saturation of the material (Rogers, Nielson, 1981) is given by:

$$S = \frac{\rho M_w}{1000P} \tag{3.21}$$

The porosity of the material was determined from the following equation:

$$P = 1 - \frac{G}{\rho} \tag{3.22}$$

where $G$ is the specific gravity of the tailings material (kg/m$^3$) whose value is 2 740 kg/m$^3$ (Rogers, Nielson, 1981) and $\rho$ is the dry bulk density of the tailings material (kg/m$^3$).

To roughly estimate radium-226 content from the tailings dam, a broad energy germanium (BEGe) detector manufactured by Canberra Industries, was used to analyse the specific activity of radium from one of the tailings' samples. The BEGe has a relative efficiency of 60 % and a resolution of 2.0 keV at 1332 keV gamma ray emission of $^{60}$Co. Measurements of the samples were done at the Centre for Applied Radiation Science and Technology (CARST), North West University. Energy and efficiency calibration of the gamma spectrometer were performed before sample measurements. The radium-226 activity was measured through one of its daughters (Pb-214). Direct measurement was no feasible since it was bound to produce more errors as its gamma energy line at 186.21 keV was likely to interfere with uranium-235 energy line at 185.79 keV.

## 3.4 Results and Discussion

From the broad energy germanium (BEGe) detector, the specific activity of one of the samples (sample number 7) for radium-226 was measured to be around 186 ± 14 Bq/kg. It should be emphasised that this is a rough estimate.

Table 3.1 list the values of aerial and mass exhalation rates, porosity and effective radium concentrations in different samples collected from the tailings dam when d → 0 (short tubes). Calculations and results of the moisture content, areas, volumes, densities, porosity and fluxes for both short and long tubes are given in appendix B.

From table 3.1, the values of the aerial exhalation rates from the surface of the short tube samples vary from 13.6 ± 1.9 to 96.9 ± 10.2 Bq/($m^2$.h). These aerial exhalation rates corresponds to mass surface exhalation rate values of 0.076 ± 0.010 to 0.579 ± 0.061 Bq/(kg.s) respectively. The values of effective radium content in the samples varied from 9.9 ± 1.4 to 76.6 ± 8.1 Bq/kg in samples 15 and 19 respectively. The effective radium activity concentration averaged at 32.9 ± 3.7 Bq/kg. The percentage error over the whole sample was 12 ± 1.0 %. Taking emanation fraction value of 0.235, the true radium activity concentration is equivalent to (33/0.235) Bq/kg = 140 Bq/kg.

The calculated values of effective diffusion coefficient and the exhalation rates from the mine tailings in the long tubes are shown in table 3.2. The effective diffusion length values ranged from 1.9E-07 ± 4.0E-08 $m^2$/s in sample 14 to 4.1E-05 ± 8.6E-06 $m^2$/s in sample 10.

Exhalation rate (E) was found to vary from 0.0410 ± 0.0042 Bq/$m^2$·s to 0.440 ± 0.045 Bq/$m^2$·s with a mean value of 0.102 ± 0.021 Bq/$m^2$·s and a standard deviation (St Dev) of 0.087 Bq/$m^2$·s.

It should however be noted that the values of integrated radon concentration were very high for sample 10 and as such should be treated with care. Extremely high values of the aerial exhalation rates, diffusion length, diffusion coefficient and exhalation rates (E) in the sample were obtained from sample 10.

*Table 3.1: Values of effective radium content, porosity and the aerial and mass radon exhalation rates for 20 soil samples obtained when $d \rightarrow 0$*

| Sample | C(Bq/m³.h) | $\Phi_A = ChA/T_e$ (Bq/(m².h)) | $\Phi_m$ (Bq/(kg.s)) | Ra eff (= εR) (Bq/kg) | Porosity |
|---|---|---|---|---|---|
| 1 | 8.7E5 | 48 | 0.27 | 35 | 0.46 |
| 2 | 4.2 E5 | 23 | 0.15 | 20 | 0.44 |
| 3 | 9.6 E5 | 53 | 0.34 | 44 | 0.43 |
| 4 | 5.1 E5 | 28 | 0.17 | 22 | 0.42 |
| 5 | 4.4 E5 | 24 | 0.15 | 19 | 0.42 |
| 6 | 9.9 E5 | 55 | 0.32 | 42 | 0.47 |
| 7 | 1.1 E6 | 63 | 0.33 | 44 | 0.44 |
| 8 | 5.6 E5 | 31 | 0.18 | 23 | 0.42 |
| 9 | 1.2 E6 | 67 | 0.33 | 44 | 0.43 |
| 10 | 7.6 E5 | 42 | 0.24 | 31 | 0.42 |
| 11 | 7.2 E5 | 40 | 0.24 | 32 | 0.44 |
| 12 | 1.2 E6 | 66 | 0.36 | 48 | 0.44 |
| 13 | 6.7 E5 | 37 | 0.22 | 29 | 0.46 |
| 14 | 1.4 E6 | 77 | 0.36 | 48 | 0.44 |
| 15 | 2.5 E5 | 14 | 0.08 | 10 | 0.42 |
| 16 | 3.0 E5 | 17 | 0.10 | 13 | 0.42 |
| 17 | 4.2 E5 | 23 | 0.13 | 17 | 0.42 |
| 18 | 4.9 E5 | 27 | 0.16 | 22 | 0.44 |
| 19 | 1.8 E6 | 97 | 0.58 | 77 | 0.44 |
| 20 | 9.1 E5 | 50 | 0.29 | 38 | 0.44 |

This unaccounted for spike in sample 10 is depicted in figure 3.7 and 3.8 for diffusion length and exhalation rate (E) respectively.

*Table 3.2: Values of diffusion coefficient and the exhalation rates (E) from the mine tailings when $d \rightarrow \infty$.*

| Sample | (C: Bq/m³.h) | $\Phi_A = Ch\lambda/T_e$ (Bq/(m².h)) | Diffusion length, L (m) | $D_e$ (m²/s) | $\sqrt{\lambda D_e}$ | Exhalation rate, E (= $\rho\varepsilon R\sqrt{\lambda D_e}$ (Bq/(m²s))) |
|---|---|---|---|---|---|---|
| 1 | 4.21 E6 | 2.21 E2 | 0.56 | 6.58E-07 | 1.18E-06 | 6.7E-2 ± 6.8E-3 |
| 2 | 4.44 E6 | 2.33 E2 | 1.01 | 2.15E-06 | 2.13E-06 | 5.9E-2 ± 6.0E-3 |
| 3 | 6.57 E6 | 3.45 E2 | 0.66 | 9.17E-07 | 1.39E-06 | 8.6E-2 ± 8.8E-3 |
| 4 | 9.07 E6 | 4.76 E2 | 1.78 | 6.62E-06 | 3.73E-06 | 1.2E-1 ± 1.2E-2 |
| 5 | 2.98 E6 | 1.56 E2 | 0.68 | 9.69E-07 | 1.43E-06 | 4.1E-2 ± 4.2E-3 |
| 6 | 4.86 E6 | 2.55 E2 | 0.55 | 6.41E-07 | 1.16E-06 | 7.4E-2 ± 7.6E-3 |
| 7 | 5.73 E6 | 3.01 E2 | 0.58 | 7.13E-07 | 1.22E-06 | 9.1E-2 ± 9.1E-3 |
| 8 | 7.94 E6 | 4.18 E2 | 1.51 | 4.82E-06 | 3.18E-06 | 1.1E-1 ± 1.1E-2 |
| 9 | 5.96 E6 | 3.13 E2 | 0.60 | 7.66E-07 | 1.27E-06 | 8.4E-2 ± 8.6E-3 |
| 10 | 3.14 E7 | 1.65 E3 | 4.39 | 4.05E-05 | 9.22E-06 | 4.4E-1 ± 4.5E-2 |
| 11 | 4.17 E6 | 2.19 E2 | 0.59 | 7.52E-07 | 1.26E-06 | 5.8E-2 ± 6.0E-3 |
| 12 | 9.15 E6 | 4.81 E2 | 0.87 | 1.58E-06 | 1.82E-06 | 1.4E-1 ±1.4E-2 |
| 13 | 3.25 E6 | 1.71 E2 | 0.52 | 5.79E-07 | 1.10E-06 | 4.8E-2 ± 4.9E-3 |
| 14 | 3.15 E6 | 1.65 E2 | 0.30 | 1.89E-07 | 6.30E-07 | 4.5E-2 ± 4.6E-3 |
| 15 | 4.55 E6 | 2.39 E2 | 1.99 | 8.27E-06 | 4.17E-06 | 6.6E-2 ± 6.8E-3 |
| 16 | 3.22 E6 | 1.69 E2 | 1.07 | 2.40E-06 | 2.24E-06 | 4.6E-2 ± 4.7E-3 |
| 17 | 7.88 E6 | 4.14 E2 | 2.04 | 8.75E-06 | 4.29E-06 | 1.1E-1 ± 1.1E-2 |
| 18 | 9.93 E6 | 5.21 E2 | 2.11 | 9.31E-06 | 4.42E-06 | 1.5E-1 ± 1.5E-2 |
| 19 | 9.22 E6 | 4.84 E2 | 0.55 | 6.31E-07 | 1.15E-06 | 1.3E-1 ± 1.4E-2 |
| 20 | 4.45 E6 | 2.33 E2 | 0.54 | 6.05E-07 | 1.13E-06 | 6.7 E-2 ± 6.8E-3 |
| Mean | | | | | | **1.02E-1** |
| Max | | | | | | **1.45E-1** |
| Min | | | | | | **4.10E-2** |
| St Dev | | | | | | **8.70E-2** |

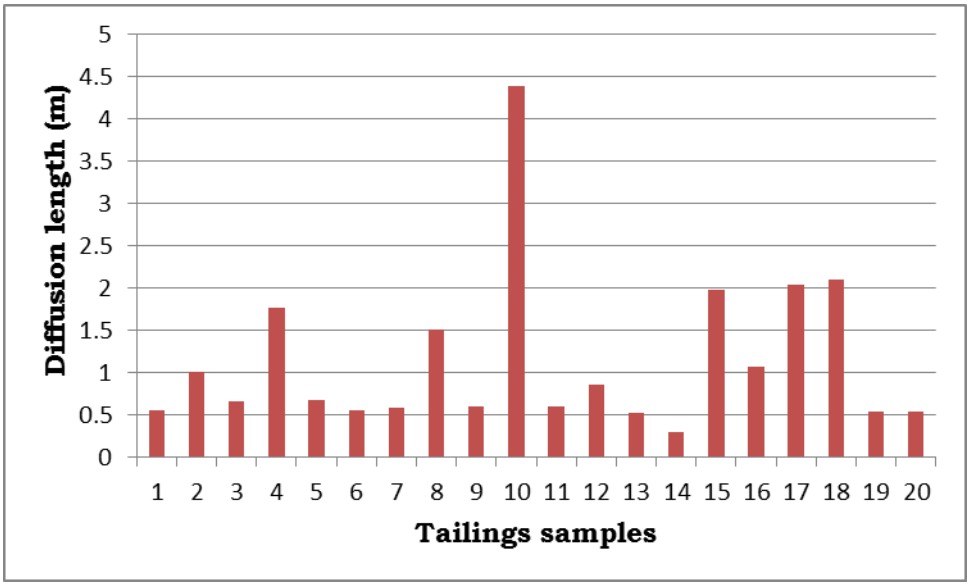


**Figure 3.7: Diffusion length for different soil samples.**

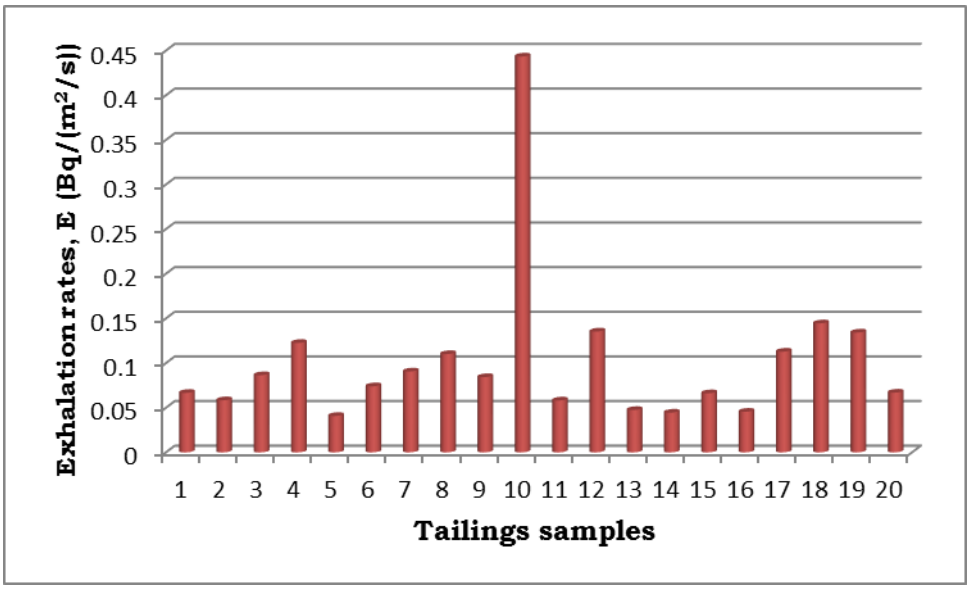


**Figure 3.8: Radon exhalation rates for different soil samples**

Nonetheless, the mean value of the exhalation rates (E) were found to be comparable to values obtained by other researchers (Ongori et al., 2015, Lindsay et al., 2004, Lindsay, Newman and Speelman, 2008,) using other methods.

## 3.5 Conclusion

The measurement of average radon flux from large mine tailings dumps presents a major challenge. The size of the dumps leads to very time consuming and labour intensive procedures if the usual methods are used (IAEA, 2013, IAEA, 1992). This is especially true if a sufficient number of samples is needed for an accurate average. Radium content, emanation fraction, diffusion length and hence and radon surface exhalation rates have been successfully measured using RGM plastic track detectors by the sealed tube technique. This passive method is a convenient and inexpensive way of determining the exhalation and diffusion parameters of radon in porous materials like tailings.

Radon exhalation studies are important for understanding the relative contribution of the material to the total radon concentration in the environment. The mean exhalation rate of 0.102 ± 0.087 Bq/($m^2$·s) obtained in table 3.2 is the source term for dispersion modelling in chapter 6.

# Chapter 4 Passive radon measurements around the tailings dam

## 4.1 Introduction

The outdoor radon levels are usually low when compared to indoor concentrations (WHO, 2009). The estimated average worldwide outdoor radon concentrations is about 10 Bq/m$^3$ (UNSCEAR, 2000).

In South Africa, tailings dams are often situated very close to the residential areas. In such cases, radon and radon daughter inhalation may be a significant and dominating radiological exposure pathway for the inhabitants. There is limited literature on environmental radon surveys around South African tailings dams. The measured average outdoor radon concentrations at areas within about 3 km from South African tailings are 62 Bq/m$^3$ (Wymer, 1997). Beyond the 3 km range, the radon concentration levels tend to rapidly move closer to the background levels (Wymer, 1997). However, large variations in outdoor concentrations exist which are a function of meteorological factors, location, season and time of the day.

Under South African law, tailings are classified as sources of radioactive material that are regulated under nuclear licence. In the vicinity of the tailings dam, $^{226}$Ra in the tailings is expected to decay to produce radon, which will migrate to the surface and elevate the outdoor ambient radon concentration around the area. Therefore long term radon monitoring around the tailings dam is often required to primarily identify and quantify significant anthropogenic contributions from the tailings. However, as this study will show, these measurements do not represent radon from the tailings only, and present estimates of the tailings contributions. This finding is one of the main motivators for using dispersion modelling to assess the tailings contribution.

As part of the broader ambient radon monitoring, passive time-integrated carbon infused Radon Gas Monitors (RGMs) were used to

measure the integrated average outdoor concentrations of environmental radon around the tailings dam. This chapter outlines the method, analysis and the environmental impact of radon on the area around the tailings dam.

## 4.2 Measuring points and method

Radon Gas Monitors (RGMs) were used in this study to determine the atmospheric radon activity concentration around the mine tailings. This widely used, relatively simple and low cost method is most suitable for environmental radon assessment where radon concentration integration over time is sufficient (Bollhöfer, 2007).

A total of 172 Radon Gas Monitors (RGMs) were placed at a number of locations shown in figure 4.1 around the area of the tailings dam. The monitors were placed both upwind and downwind of the annual average wind direction of north, northwest and north east (Petzer, 2018).

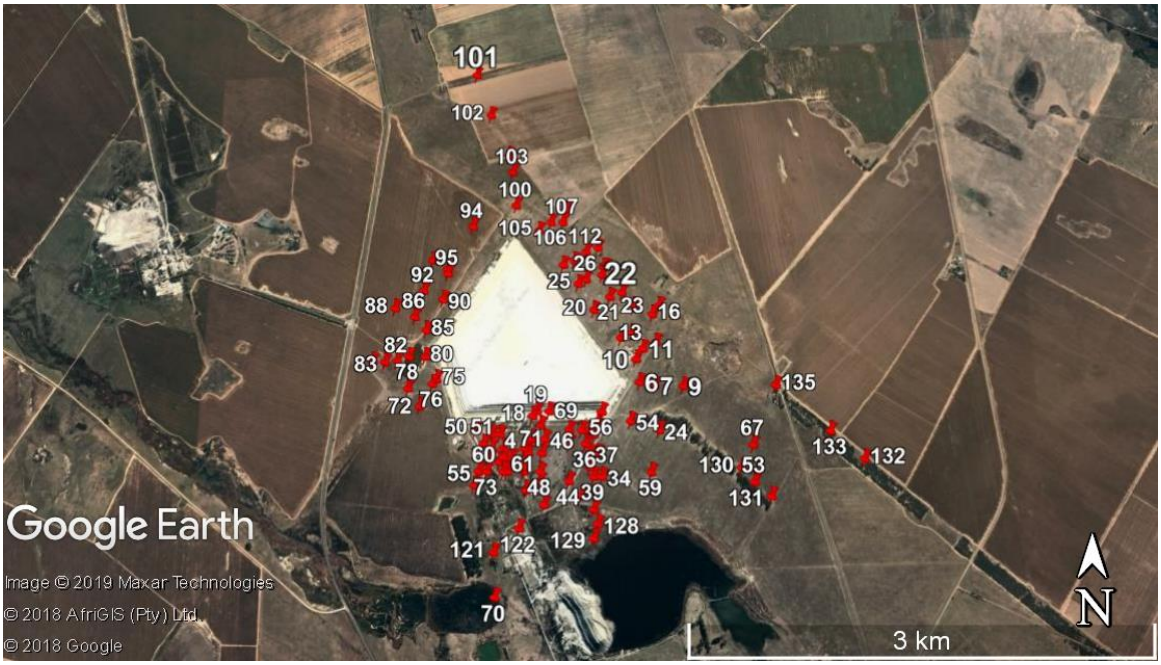


**Figure 4.1: RGM distribution around tailings dam**

Due to high activity from the public and animals, specifically grazing cattle in the vicinity of the tailings dam, efforts were made to secure the

monitors from being tampered with. The selected monitor positions were considered to be the most practical under the circumstances.

To represent breathing air, detectors were mounted on light poles at a height of between 1 – 1.5 m above the ground as depicted in figure 4.2. Some of the detectors were fixed on nearby trees at the height of up to 2m from the ground level.

**Figure 4.2: Outdoor radon measurements method.**

According to Doi, Kobayashi, (1996), the height above the ground level may affect radon concentration at the receptor point. However, Wu and co-workers (Wu et al., 2016) conducted a test to determine the extent of variation of radon concentration with height. Their results revealed no significant change in radon concentrations at heights in the range of 1 - 3 m on the same sampling spot. Accurate height was therefore deemed not

important for correlation measurements for this study at heights between 1 and 2 m from the ground level.

The detectors were covered with protective plastic to shield them from rain, strong winds and mechanical influences (Wu et al., 2016, Kümmel et al., 2014). A hole was pierced through the plastic cover to allow free entry of air containing radon. The detectors were left exposed for up to 53 days during the dry winter months of June, July and August 2016 when the wind patterns are relatively stable and level of radon flux from the surface of tailings is at its peak.

The meteorological wind rose covering the period of exposure from 28 June 2016 to 20 August 2016 was constructed. This graphical representation of the wind conditions of speed prevailing for Odendaalsrus area during the exposure period is shown in figure 4.3.

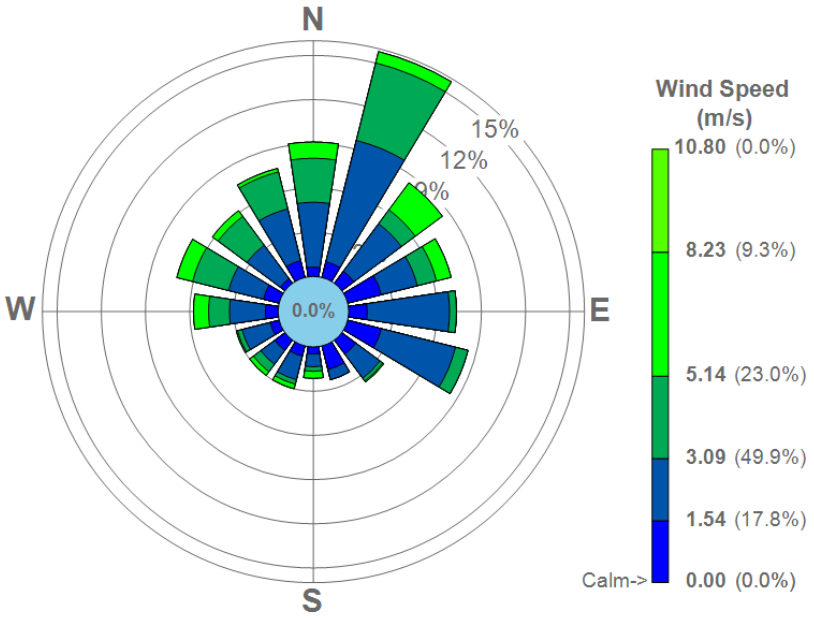


**Figure 4.3: Wind rose for the RGM exposure period around the tailings dam.**

The area was characterised by the dominating average winds from the north-east with moderate winds from the north and south-east during

the winter months from June to August. Wind speeds for the area varied between 1.5 m/s (17.8%) and 8.2 m/s (9.3%). The most dominating wind speed was 3.1 m/s (50%). There was no rainfall during this period. It is worth pointing out that there are no other tailings dams or other anthropogenic radon sources that may contribute toward the background concentration from the north east directions. It was therefore deemed important to determine and analyse the average upwind and downwind concentrations. This will give an idea on the "background" concentration and what may be the radon contribution from the tailings dam on the surroundings.

Out a total of 172 RGMs that were placed around the tailings dam, only 116 RGMs were found in place and retrieved, while the other 56 were considered lost or were found to have been tampered with. Most RGMs were lost on the southwest side on the dam, which is a privately owned maize farm with lots of movement by both people and tractors. The collected RGMs were sent to the laboratory for analysis as outlined in exhalation flux measurements procedure in chapter 3. The results for the tampered RGMs were omitted.

The annual outdoor radiological dose was calculated by applying the dose conversion factor provided by ICRP (ICRP, 2010). The dose conversion factor assumes that a person resides for 1760 hours outdoors and the outdoor equilibrium factor is 0.6. The dose conversion coefficient for calculating annual dose applied in this study is based on the ICRP (ICRP, 2010) recommendations as:

Dose conversion coefficient (inhalation) = 0.0145 mSv/y for 1 Bq/m$^3$ (4.1)

## 4.3 Results and discussion

Table 4.1 presents the result of radon concentration distributions measured at 116 points around the tailings dam and their corresponding annual doses. The annual doses were calculated using equation (4.1).

The radon concentrations varied across the sides of the dam, ranging from 38 ± 8 to 94 ± 18 Bq/m$^3$. The lowest radon concentrations recorded on the upwind direction were in the north (40 ±13 Bq/m$^3$) and north-east (38 ± 8 Bq/m$^3$) of the tailings. The highest concentration values were populated on the downwind side of southwest (94 ± 18 Bq/m$^3$). These highest radon concentrations are in line with the direction of the dominant northeast wind depicted in the wind rose diagram in figure 4.3. The radon distribution around the tailings dam is shown in figure 4.4.

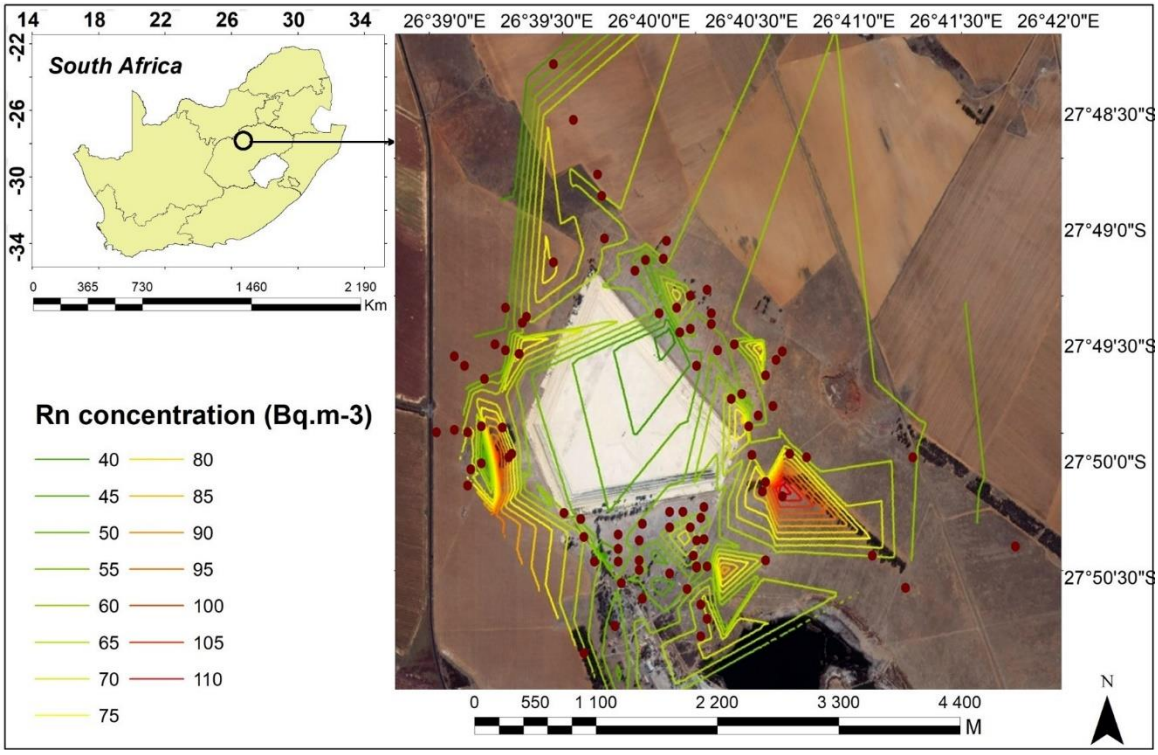


**Figure 4.4: Distribution of radon concentration around the tailings dam**

*Table 4.1: Radon concentrations at locations shown in figure 4.1 in the vicinity of the tailings*

| Monitor number | Monitor ID | LAT | LONG | Bq h $m^{-3}$ | Exposure period (h) | Rn concentration ($Bq/m^3$) per exposure period | St Dev ($Bq/m^3$) | Annual dose (mSv/y) |
|---|---|---|---|---|---|---|---|---|
| 1 | 68219 | 27˚50’8”S | 26˚40’26”E | 8.3E4 | 1272 | 65 | 13 | 0.95 |
| 2 | 68186 | 27˚50’8”S | 26˚40’32”E | 1.1E5 | 1272 | 85 | 17 | 1.23 |
| 3 | 68238 | 27˚50’11”S | 26˚40’36”E | 9.5E4 | 1272 | 75 | 16 | 1.08 |
| 4 | 84986 | 27°50'20"S | 26°39'59"E | 1.1E5 | 1272 | 82 | 16 | 1.20 |
| 5 | 84987 | 27°50'19"S | 26°40'3"E | 9.4E4 | 1272 | 74 | 15 | 1.07 |
| 6 | 68161 | 27˚50’3”S | 26˚40’30”E | 1.0E5 | 1272 | 82 | 9 | 1.19 |
| 7 | 68152 | 27˚50’4”S | 26˚40’34”E | 8.5E4 | 1272 | 67 | 9 | 0.97 |
| 8 | 84988 | 27°50'22"S | 26°40'2"E | 7.5E4 | 1272 | 59 | 15 | 0.85 |
| 9 | 68241 | 27˚50’4”S | 26˚40’41”E | 8.5E4 | 1272 | 67 | 9 | 0.97 |
| 10 | 68248 | 27˚49’58”S | 26˚40’29”E | 6.9E4 | 1272 | 54 | 8 | 0.79 |
| 11 | 68211 | 27˚49’56”S | 26˚40’31”E | 7.7E4 | 1272 | 61 | 14 | 0.88 |
| 12 | 68283 | 27˚49’53”S | 26˚40’25”E | 6.8E4 | 1272 | 53 | 8 | 0.78 |
| 13 | 68145 | 27˚49’52”S | 26˚40’28”E | 7.7E4 | 1272 | 61 | 8 | 0.88 |
| 14 | 68157 | 27˚49’54”S | 26˚40’34”E | 8.3E4 | 1272 | 65 | 15 | 0.94 |
| 15 | 84989 | 27°50'15"S | 26°39'56"E | 7.9E4 | 1272 | 62 | 14 | 0.90 |

| | | | | | | | | |
|---|---|---|---|---|---|---|---|---|
| 16 | 68170 | 27˚49’48”S | 26˚40’33”E | 6.7E4 | 1272 | 53 | 12 | 0.77 |
| 17 | 68150 | 27˚49’46”S | 26˚40’35”E | 7.9E4 | 1272 | 62 | 9 | 0.90 |
| 18 | 84990 | 27°50'11S | 26°40'4"E | 9.1E4 | 1272 | 72 | 15 | 1.04 |
| 19 | 84991 | 27°50'10"S | 26°40'5"E | 9.8E4 | 1272 | 77 | 16 | 1.12 |
| 20 | 68243 | 27˚49’47”S | 26˚40’19”E | 6.7E4 | 1272 | 53 | 8 | 0.76 |
| 21 | 68206 | 27˚49’44”S | 26˚40’23”E | 6.9E4 | 1272 | 54 | 9 | 0.79 |
| 22 | 68281 | 27˚49’43”S | 26˚40’26”E | 4.8E4 | 1272 | 38 | 8 | 0.55 |
| 23 | 68246 | 27˚49’46”S | 26˚40’29”E | 5.8E4 | 1272 | 45 | 13 | 0.66 |
| 24 | 84993 | 27°50'14"S | 26°40'35"E | 8.9E4 | 1272 | 70 | 15 | 1.02 |
| 25 | 68216 | 27˚49’41”S | 26˚40’15”E | 7.4E4 | 1272 | 58 | 9 | 0.84 |
| 26 | 68177 | 27˚49’40”S | 26˚40’17”E | 6.7E4 | 1272 | 53 | 8 | 0.76 |
| 27 | 68183 | 27˚49’39”S | 26˚40’21”E | 7.3E4 | 1272 | 57 | 8 | 0.83 |
| 28 | 68204 | 27˚49’37”S | 26˚40’21”E | 7.7E4 | 1272 | 61 | 14 | 0.88 |
| 29 | 68264 | 27˚49’37”S | 26˚40’22”E | 6.3E4 | 1272 | 50 | 8 | 0.72 |
| 30 | 68228 | 27˚50’13”S | 26˚40’20”E | 6.9E4 | 1248 | 55 | 9 | 0.80 |
| 31 | 68208 | 27˚50’15”S | 26˚40’19”E | 7.6E4 | 1248 | 61 | 8 | 0.88 |
| 32 | 84994 | 27°50'26"S | 26°39'50"E | 8.4E4 | 1248 | 67 | 15 | 0.98 |
| 33 | 68267 | 27˚50’19”S | 26˚40’20”E | 6.9E4 | 1248 | 55 | 9 | 0.80 |
| 34 | 68239 | 27˚50’24”S | 26˚40’21”E | 7.2E4 | 1248 | 58 | 9 | 0.84 |

| | | | | | | | | |
|---|---|---|---|---|---|---|---|---|
| 35 | 68253 | 27˚50’14”S | 26˚40’16”E | 7.6E4 | 1248 | 61 | 8 | 0.88 |
| 36 | 68147 | 27˚50’17”S | 26˚40’17”E | 6.8E4 | 1248 | 54 | 8 | 0.79 |
| 37 | 68144 | 27˚50’19”S | 26˚40’18”E | 7.3E4 | 1248 | 58 | 14 | 0.84 |
| 38 | 68226 | 27˚50’22”S | 26˚40’18”E | 1.1E5 | 1248 | 89 | 18 | 1.29 |
| 39 | 68242 | 27˚50’24”S | 26˚40’19”E | 7.2E4 | 1248 | 58 | 9 | 0.84 |
| 40 | 68187 | 27˚50’14”S | 26˚40’13”E | 7.4E4 | 1248 | 59 | 14 | 0.86 |
| 41 | 68257 | 27˚50’17”S | 26˚40’13”E | 7.8E4 | 1248 | 63 | 9 | 0.91 |
| 42 | 84996 | 27°50'12"S | 26°40'20"E | 7.8E4 | 1248 | 62 | 15 | 0.90 |
| 43 | 85003 | 27°50'21"S | 26°39'56"E | 9.4E4 | 1248 | 75 | 16 | 1.09 |
| 44 | 68285 | 27˚50’25”S | 26˚40’13”E | 7.3E4 | 1248 | 58 | 14 | 0.84 |
| 45 | 85004 | 27°50'23"S | 26°39'58"E | 7.9E4 | 1248 | 63 | 15 | 0.91 |
| 46 | 68237 | 27˚50’16”S | 26˚40’7”E | 6.6E4 | 1248 | 53 | 14 | 0.77 |
| 47 | 68174 | 27˚50’19”S | 26˚40’6”E | 5.8E4 | 1248 | 46 | 8 | 0.67 |
| 48 | 68182 | 27˚50’23”S | 26˚40’6”E | 6.9E4 | 1248 | 55 | 8 | 0.80 |
| 49 | 68196 | 27˚50’25”S | 26˚40’6”E | 9.1E4 | 1248 | 73 | 16 | 1.06 |
| 50 | 68265 | 27˚50’14”S | 26˚39’50”E | 6.5E4 | 1248 | 52 | 12 | 0.75 |
| 51 | 68259 | 27˚50’17”S | 26˚39’52”E | 5.4E4 | 1248 | 43 | 9 | 0.63 |
| 52 | 85007 | 27°50'20"S | 26°39'54"E | 9.0E4 | 1248 | 72 | 15 | 1.04 |
| 53 | 85008 | 27°50'25"S | 26°40'58"E | 9.5E4 | 1248 | 76 | 16 | 1.10 |

| | | | | | | | | |
|---|---|---|---|---|---|---|---|---|
| 54 | 85009 | 27°50'12"S | 26°40'28"E | 8.5E4 | 1248 | 68 | 15 | 0.98 |
| 55 | 85010 | 27°50'23"S | 26°39'51"E | 8.7E4 | 1248 | 70 | 15 | 1.01 |
| 56 | 85011 | 27°50'10"S | 26°40'21"E | 8.3E4 | 1248 | 66 | 15 | 0.96 |
| 57 | 85012 | 27°50'13"S | 26°40'6"E | 8.2E4 | 1248 | 66 | 15 | 0.95 |
| 58 | 85013 | 27°50'14"S | 26°40'18"E | 8.2E4 | 1248 | 66 | 15 | 0.95 |
| 59 | 68166 | 27°50’23”S | 26°40’33”E | 7.6E4 | 1224 | 62 | 9 | 0.90 |
| 60 | 85017 | 27°50'20"S | 26°39'57"E | 8.9E4 | 1224 | 73 | 16 | 1.06 |
| 61 | 68168 | 27°50’18”S | 26°40’2”E | 5.7E4 | 1224 | 48 | 13 | 0.69 |
| 62 | 68199 | 27°50’21”S | 26°40’2”E | 7.2E4 | 1224 | 59 | 8 | 0.85 |
| 63 | 68190 | 27°50’23”S | 26°40’2”E | 6.9E4 | 1224 | 56 | 8 | 0.82 |
| 64 | 68179 | 27°50’27”S | 26°40’2”E | 7.0E4 | 1224 | 57 | 8 | 0.83 |
| 65 | 68218 | 27°50’15”S | 26°39’54”E | 6.8E4 | 1224 | 56 | 14 | 0.80 |
| 66 | 68184 | 27°50’18”S | 26°39’54”E | 6.0E4 | 1224 | 49 | 8 | 0.71 |
| 67 | 85018 | 27°50'17"S | 26°40'58"E | 8.3E4 | 1224 | 68 | 15 | 0.99 |
| 68 | 68222 | 27°50’23”S | 26°39’57”E | 6.9E4 | 1224 | 56 | 8 | 0.82 |
| 69 | 85019 | 27°50'10"S | 26°40'8"E | 9.8E4 | 1224 | 80 | 16 | 1.16 |
| *70* | 68195 | 27°50’49”S | 26°39’55”E | 7.1E4 | 1224 | 58 | 9 | 0.84 |
| 71 | 85022 | 27°50'18"S | 26°39'57"E | 9.5E4 | 1224 | 78 | 16 | 1.13 |
| 72 | 68158 | 27°50’9”S | 26°39’36”E | 8.0E4 | 1224 | 65 | 9 | 0.95 |

| | | | | | | | | |
|---|---|---|---|---|---|---|---|---|
| 73 | 85023 | 27°50'16"S | 26°40'4"E | 7.9E4 | 1224 | 65 | 15 | 0.94 |
| 74 | 85025 | 27°50'23"S | 26°39'53"E | 8.8E4 | 1224 | 72 | 16 | 1.04 |
| 75 | 68214 | 27°50’3”S | 26°39’40”E | 1.1E5 | 1200 | 94 | 18 | 1.37 |
| 76 | 68234 | 27°50’4”S | 26°39’39”E | 8.1E4 | 1200 | 68 | 10 | 0.98 |
| 78 | 68230 | 27°50’5”S | 26°39’33”E | 1.1E5 | 1200 | 94 | 18 | 1.36 |
| 80 | 68251 | 27°49’58”S | 26°39’37”E | 5.4E4 | 1200 | 45 | 8 | 0.65 |
| 81 | 68189 | 27°49’58”S | 26°39’33”E | 8.5E4 | 1200 | 71 | 16 | 1.03 |
| 82 | 68227 | 27°49’59”S | 26°39’30”E | 8.6E4 | 1200 | 71 | 16 | 1.03 |
| 83 | 68207 | 27°49’59”S | 26°39’27”E | 7.2E4 | 1200 | 60 | 9 | 0.87 |
| 84 | 68279 | 27°49’59”S | 26°39’24”E | 6.6E4 | 1200 | 55 | 9 | 0.80 |
| 85 | 68163 | 27°49’52”S | 26°39’37”E | 8.3E4 | 1200 | 69 | 15 | 1.00 |
| 86 | 68223 | 27°49’49”S | 26°39’34”E | 6.2E4 | 1200 | 52 | 14 | 0.75 |
| 88 | 68266 | 27°49’47”S | 26°39’29”E | 8.0E4 | 1200 | 67 | 9 | 0.97 |
| 90 | 68217 | 27°49’45”S | 26°39’41”E | 6.3E4 | 1200 | 53 | 8 | 0.76 |
| 92 | 68249 | 27°49’43”S | 26°39’36”E | 8.3E4 | 1200 | 69 | 9 | 1.00 |
| 94 | 68149 | 27°49’28”S | 26°39’48”E | 7.4E4 | 1200 | 62 | 8 | 0.89 |
| 95 | 68191 | 27°49’39”S | 26°39’42”E | 6.0E4 | 1200 | 50 | 8 | 0.73 |
| 96 | 68164 | 27°49’38”S | 26°39’42”E | 6.7E4 | 1200 | 56 | 8 | 0.81 |
| 98 | 68212 | 27°49’36”S | 26°39’38”E | 8.9E4 | 1200 | 75 | 16 | 1.08 |

| | | | | | | | | |
|---|---|---|---|---|---|---|---|---|
| 100 | 68263 | 27˚49’23”S | 26˚39’59”E | 7.6E4 | 1200 | 64 | 15 | 0.92 |
| 101 | 68244 | 27˚48’51”S | 26˚39’48”E | 9.6E4 | 1200 | 80 | 9 | 1.16 |
| 102 | 68250 | 27˚49’1”S | 26˚39’52”E | 9.3E4 | 1200 | 77 | 16 | 1.12 |
| 103 | 68200 | 27˚49’15”S | 26˚39’58”E | 8.4E4 | 1200 | 70 | 9 | 1.02 |
| 104 | 68255 | 27˚49’11”S | 26˚39’57”E | 4.8E4 | 1200 | 40 | 13 | 0.58 |
| 105 | 68229 | 27˚49’29”S | 26˚40’5”E | 5.5E4 | 1176 | 47 | 9 | 0.68 |
| 106 | 68225 | 27˚49’27”S | 26˚40’8”E | 7.4E4 | 1176 | 63 | 15 | 0.92 |
| 107 | 68146 | 27˚49’27”S | 26˚40’11”E | 8.1E4 | 1176 | 69 | 16 | 1.00 |
| 108 | 68277 | 27˚49’24”S | 26˚40’12”E | 8.0E4 | 1176 | 68 | 16 | 0.99 |
| 110 | 68282 | 27˚49’37”S | 26˚40’11”E | 8.7E4 | 1176 | 74 | 9 | 1.07 |
| 111 | 68148 | 27˚49’36”S | 26˚40’14”E | 6.7E4 | 1176 | 57 | 9 | 0.83 |
| 112 | 68213 | 27˚49’34”S | 26˚40’17”E | 7.0E4 | 1176 | 60 | 9 | 0.86 |
| 113 | 68167 | 27˚49’33”S | 26˚40’20”E | 6.5E4 | 1176 | 55 | 9 | 0.80 |
| 121 | 68274 | 27˚50’40”S | 26˚39’55”E | 7.2E4 | 1152 | 63 | 9 | 0.91 |
| 122 | 68210 | 27˚50’35”S | 26˚40’1”E | 6.3E4 | 1152 | 54 | 15 | 0.79 |
| 125 | 68194 | 27˚50’30”S | 26˚40’7”E | 6.3E4 | 1152 | 55 | 9 | 0.79 |
| 126 | 68209 | 27˚50’28”S | 26˚40’16”E | 8.5E4 | 1152 | 74 | 16 | 1.07 |
| 127 | 68286 | 27˚50’31”S | 26˚40’19”E | 6.1E4 | 1152 | 53 | 14 | 0.77 |
| 128 | 68280 | 27˚50’34”S | 26˚40’20”E | 8.2E4 | 1152 | 71 | 16 | 1.03 |

| | | | | | | | | |
|---|---|---|---|---|---|---|---|---|
| 129 | 68175 | 27˚50’37”S | 26˚40’19”E | 6.5E4 | 1152 | 56 | 10 | 0.82 |
| 130 | 68270 | 27˚50’22”S | 26˚40’55”E | 6.8E4 | 1128 | 60 | 15 | 0.88 |
| 131 | 68268 | 27˚50’28”S | 26˚41’2”E | 6.0E4 | 1128 | 53 | 9 | 0.77 |
| 132 | 68203 | 27˚50’20”S | 26˚41’25”E | 6.9E4 | 1128 | 62 | 15 | 0.89 |
| 133 | 68185 | 27˚48’14”S | 26˚41’17”E | 6.6E4 | 1128 | 59 | 9 | 0.85 |
| 135 | 68240 | 27˚50’4”S | 26˚41’4”E | 6.9E4 | 1128 | 61 | 9 | 0.89 |

The average radon concentration and standard error for all the RGMs around the tailings dam were 64 Bq/m$^3$ and 11 Bq/m$^3$ respectively. This value is comparable to the average concentration of 62 Bq/m$^3$ measured by Wymer (1997). The median and 1st and 3rd quartiles are 58 Bq/m$^3$, 54 Bq/m$^3$ and 64 Bq/m$^3$ respectively.

The measured radon concentrations at any of the points shown in figure 4.4 are due to many sources, including the tailings dam and natural background. Unlike indoor radon concentrations, outdoor atmospheric radon concentrations are mostly low with land measurements ranging from 1 to 100 Bq/m$^3$ (ICRP 2010). According to UNSCEAR (UNSCEAR 2000, UNSCEAR 2008)), global outdoor radon concentrations are of the order of 10 Bq/m$^3$, with coastal regions and small islands registering lower levels.

In order to investigate the correlation between the radon concentration values upwind and downwind, two sets of data were analysed with regards to upwind and downwind minimum and maximum concentrations and their averages. The upwind and downwind points are shown in Appendix L, table A.15 and table A.16 respectively and the results are given in table 4.2.

*Table 4.2: Average upwind and downwind concentrations*

| **Place of measurements** | **Number of RGMs** | **Radon concentration (Bq/m$^3$)** | | |
|---|---|---|---|---|
| | | **Minimum** | **Maximum** | **Average** |
| Upwind | 38 | 38 ± 8 | 83 ± 16 | 62 ± 10 |
| Downwind | 78 | 43 ± 8 | 94 ± 18 | 65 ± 13 |

The results from table 4.2 indicate a 9% increase in the average radon concentration between the upwind (62 ± 10 Bq/m$^3$) and downwind (65 ± 13 Bq/m$^3$) areas from the tailings dam. In the upwind zone, the measured radon concentrations in the atmosphere went down to the lowest value of 38 ± 8 Bq/m$^3$, which may be considered as a main contributing factor in determining the average background value. This

difference might be due to the contributions from the tailings dam and the surroundings as compared to the average of 62 Bq/m$^3$ determined by Wymer (1997).

For radon exposures, the dose limit value for public is 0.25 mSv/a, which is equivalent to radon concentration of approximately 10 Bq/m$^3$ above the natural background level around that location. Minimum and maximum radon dose values around the tailing were 0.55 mSv/a and 1.4 mSv/a respectively. These dose values correspond to the minimum and maximum concentrations of 38 Bq/m$^3$ and 94 Bq/m$^3$ respectively. From figure 4.6, it is worth noting that 95% of the radon concentration measured are well below the German action level of 80 Bq/m$^3$ required for intervention with regard to mining residues (Wymer, 1997) and all of them (100%) are well below the 100 Bq/m$^3$ action level prescribed by the National Nuclear Regulator and 200 Bq/m$^3$ stipulated by Public Health of England (Hunt, 2014).

Frequency distributions and cumulative frequency distribution frequency (CFD) analysis of the radon concentrations were conducted for all the radon monitors placed around the tailings dam. The frequency distribution was approximated by a lognormal distribution and compared to the normal distribution with the same mean and standard deviation. The comparison results are depicted in figures 4.5 and 4.6.

The theory of Successive Random Dilutions (Ott, 1990) states that a concentration emanating from a series of independent random dilutions tends to be lognormally distributed. According to this theory, a source concentration *Co* will undergo a series of dilutions and complete mixing, resulting in a number of possible final concentrations *Cm* which are lognormally distributed. This theory was further validated by (Ott, 1995) to be applicable to atmospheric distribution of inert gases, of which radon is one example. Radon exhalation rates and activity levels are influenced by independent variables such as $^{226}$Ra source concentration, moisture

and mixing height (Daraktchieva, Miles and McColl, 2014). Therefore it is predicted that the distribution of radon will be skewed (Turner, 2015).

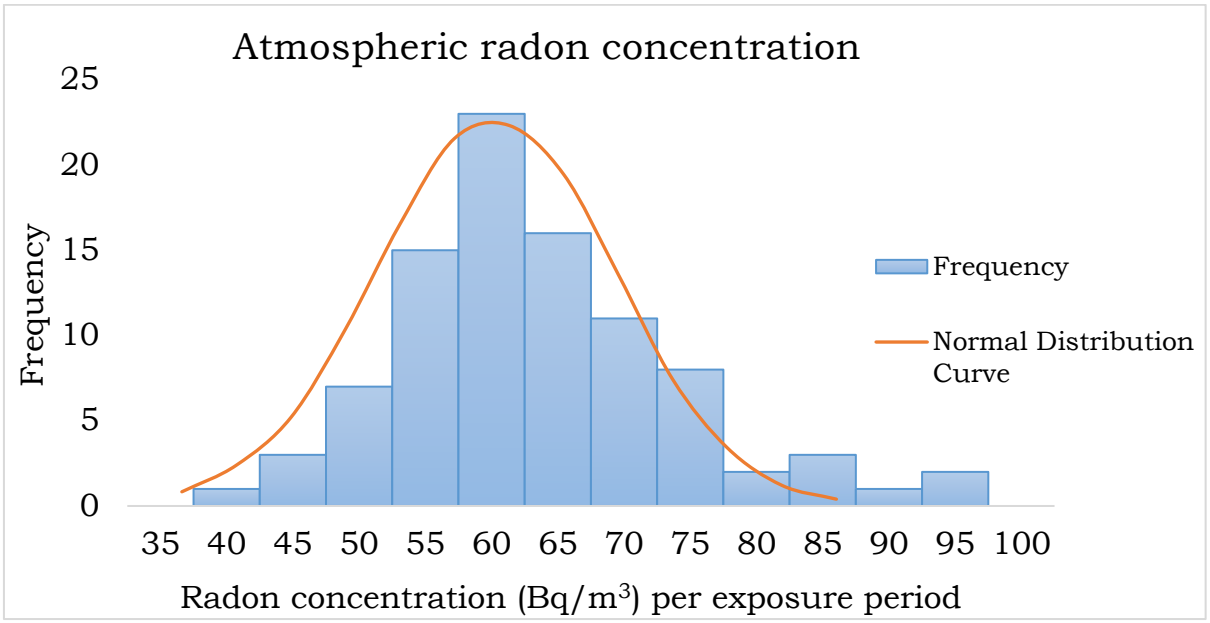


**Figure 4.5: Histogram of frequency distribution of radon concentration vs normal distribution curve with the same mean and standard deviation.**

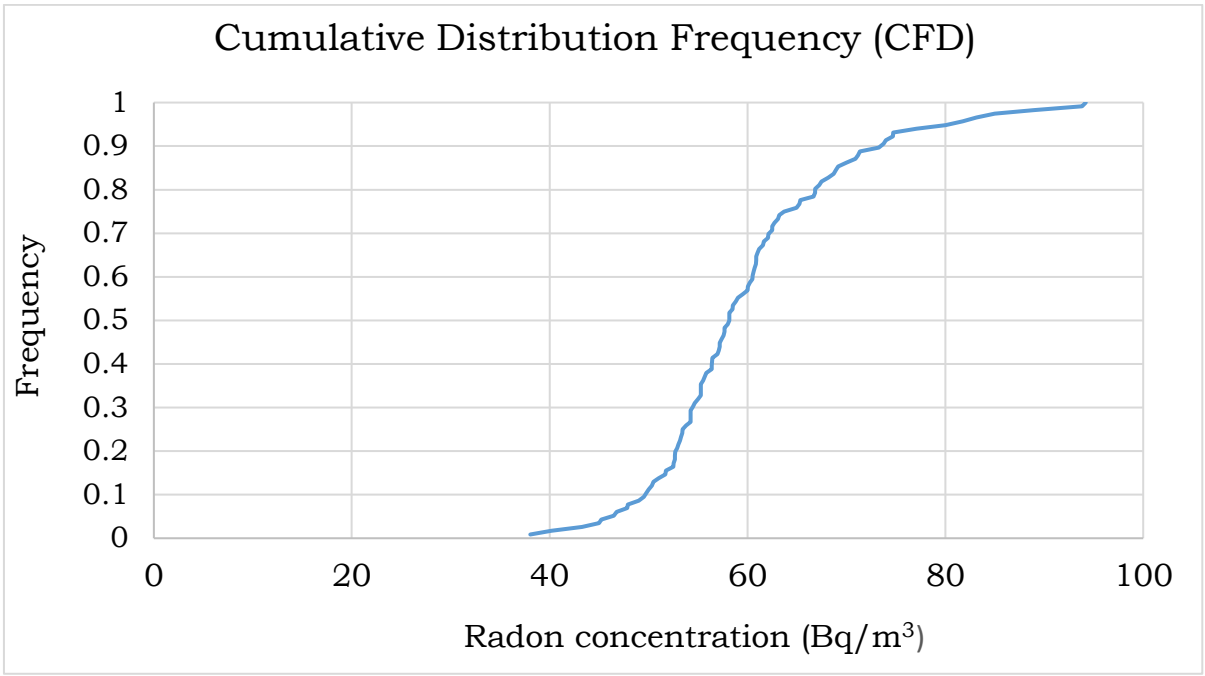


**Figure 4.6: Cumulative Frequency Distribution (CFD) plot of the outdoor atmospheric radon concentration [Bq/m³] measured around the dam**

The natural logarithms of the overall radon concentrations around the tailings appeared to be lognormally distributed (figure 4.5) as predicted by (Turner, 2015, Ott, 1990, Ott, 1995) and confirmed by (Bollhöfer, 2007, Steffens et al., 2017) in outdoor environment.

## 4.4 Conclusion

From regulatory point of view, only tailings-related, or incremental radon contributions are relevant. Therefore, this study was primarily aimed at obtaining representative data on the range of tailings-related contribution towards outdoor radon concentration. From the results of the passive measurements obtained in this chapter, it is impossible to distinguish between natural and anthropogenic contributions. However, measurements such as these, taking into account the difference between the upwind and downwind concentrations, are routinely used to assess the regulatory compliance of tailings. In this case, the dose limit for the public of 0.25 mSv/a has been exceeded and the tailings would be deemed a radiological risk. This emphasises the need for further in-depth assessment, including dispersion modelling.

# Chapter 5 Radon daughter and F factor measurements

## 5.1 Introduction

Grab sampling using a single filter method was used to measure radon daughter concentrations from the outdoor environment around the tailings dam. Sample collection and counting were conducted in the field at each sampling point. Radon daughters were collected by drawing outdoor air at a height of about 1.5 m from the ground level onto the filter, followed by gross alpha counting. Radon concentration was measured using a pulse chamber AlphaGUARD PQ2000 PRO model active radon monitor. The F factor was calculated from the ratio of equilibrium equivalent radon concentration EEC and the radon gas concentration $C_0$. This chapter gives a detailed account of the equipment, analytical techniques and the methodology used to measure radon and radon daughters in the field. Operation procedures and methods as well as sampling processes are reported here. The experimental results are presented and compared to the predicted results by applying Bateman calculations.

## 5.2 Equipment

### 5.2.1 Filter paper + cassette

The radon daughter collection filter papers used in this study were 0.8 µm Mixed Cellulose Ester (MCE) plain white filter membrane 25 mm in diameter manufactured by Zefon International®. These high purity membranes are developed from a combination of cellulose acetate and cellulose nitrate. They are 150 µm thick, with bubble point (minimum pressure required to force air through a membrane) of 0.98 bar, air flow rate of 16 (L/min/cm$^2$) and high porosity (82% open area) to allow maximum flow rates without weakening the filter durability. They

comprise low artifacts, provides minimal interference in fibre counting and are one of the mostly widely used air monitoring filters (Zefon International, 2018). The 25 mm diameter pure cellulose filter support pads were used to reinforce and support the membrane filter in filter holders and cassettes.

Sampling cassettes house and protect the filter media and allow for a convenient way of taking air samples. The 25 mm leak free polystyrene cassette housings manufactured by Sensidyne® were used in this study and are available only in three-piece style shown in figure 5.1 and figure 5.2.

**Figure 5.1: 25 mm leak-free polystyrene sampling cassette housings**

The three–piece cassettes have an advantage of being used for both "open face" and "closed face" sampling and meets sampling specifications described by EPA (Woebkenberg, Woodfin, 1983). The "closed face" sampling refers to using a cassette with the inlet in place, but only the plugs removed. On the other hand, "open face" sampling refers to using a 3-piece cassette without the inlet piece, thereby creating an "open face". The 50 mm extension centre spacing-ring ensures that microscopic fibres are properly distributed. The carbon imbedded within the cassette body reduces static charge created during sampling. For the 25 mm cassette

used in this study, “open faced” sampling was used as recommended by EPA (Woebkenberg, Woodfin, 1983).

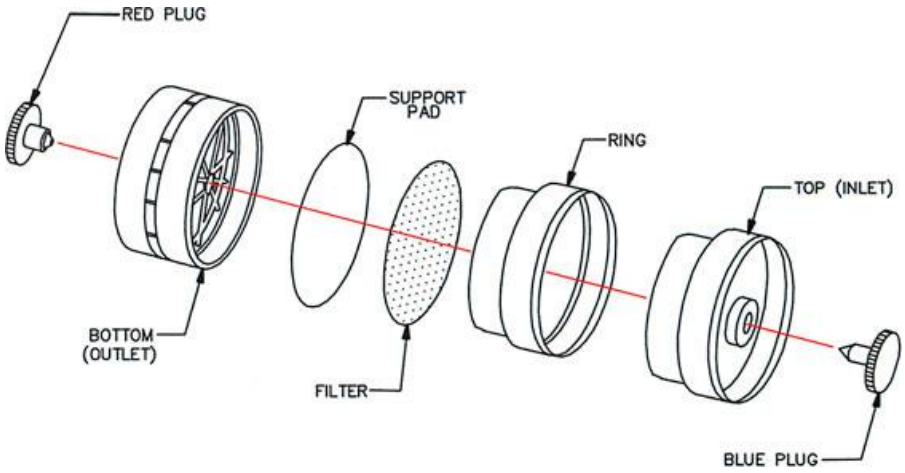


**Figure 5.2: Schematic representation of filter arrangement inside the sampling cassette**

### 5.2.2 Pump

A portable, DC 12 V battery operated Rocker 300DC oil-free vacuum pump manufactured by Rocker Scientific, Ltd shown in figure 5.3 was used to suck air at constant flow-rate onto the filter.


**Figure 5.3: A DC 12V battery operated Rocker 300DC oil free vacuum pump used for air sampling**

The maximum air flow rate attainable by this pump is 25 L/min. The pump is equipped with a vacuum regulator to adjust the vacuum, thus providing and maintaining constant and non-pulsating flow-rate throughout sampling process.

### 5.2.3 Air flow meter

To measure and regulate the volumetric air flow through the filter during sampling, Dwyer RMA-22-SSV 2 inch Scale, Stainless Steel Flow Meter, 2-25 LPM Air flow meter shown in figure 5.4 was used. The accuracy of the air flow meter is within ± 4% of full scale reading. Scales are made from brushed aluminium, coated with epoxy and the graduations are on both sides of the indicating tube.


**Figure 5.4: Dwyer air flow meter**

### 5.2.4 Radon and daughter measuring devices

A total of three devices were used to measure radon and radon daughter concentrations. Their operation modes and descriptions are given below.

#### 5.2.4.1 AlphaGUARD PQ2000 PRO

Radon concentration was measured with AlphaGUARD PQ2000 PRO model active radon monitor (figure 5.5). The portable battery operated AlphaGUARD, manufactured by Saphymo GmbH, operates like a pulse ionisation chamber.

It is designed for both short and long term monitoring of radon concentration, thus making it suitable for both indoor and outdoor monitoring. Over and above radon concentration measurement in air, AlphaGUARD simultaneously measures and records date, time, ambient temperature, relative humidity and barometric pressure with integrated sensors.


**Figure 5.5: AlphaGUARD PQ2000 PRO model active radon monitor**

The AlphaGUARD can be operated in diffusion or flow mode with linear response from 2 – 2 000 000 Bq/m$^3$. AlphaGUARD provides high detection efficiency (5 cpm at 100 Bq/m$^3$ (3 pCi/L)) and an instrument calibration error (type B) of 3% (plus uncertainty of the primary standard). The instrument is guaranteed to maintain its in-built factory calibration factors over many years (guaranteed 5 years), does not require pump when operating in diffusion mode and it is insensitive to both vibrations and high humidity. DataEXPERT software by GENITRON Instruments is used to treat and analyse the acquired data.

The AlphaGUARD instrument used in this study was purchased in 2013 and the installation and configuration of the DataEXPERT was done on the 21/08/2015. Therefore the instrument did not require any further calibration given that it was within the five years maintenance guarantee of its inbuilt calibration factor.

#### 5.2.4.2 Alpha Scintillating detector

Alpha scintillation detectors utilise scintillators to detect alpha particles instead of gas. The most commonly used scintillating detector is the zinc sulphide scintillating detector, which makes use of silver-activated zinc sulphide, ZnS(Ag), as detecting media. An Eberline Model SPA-1A scintillation detector, a rugged, alpha detector adapted for field use, was used in this study (see figure 5.6). The 1-inch diameter ZnS(Ag) scintillator and photomultiplier tube are fitted with a sliding sample tray for ease of operation. The sample holder is an O-ring sealed slider tray with a sample size of 0.06 inch deep x 1 inch diameter (0.15 cm x 2 .54 cm).

**Figure 5.6: Eberline Model SPA-1A scintillation detector**

Alpha particles move into the scintillator through the 0.4 mg/cm$^2$ aluminised Mylar window. The thin window allows alpha particles to penetrate through without significantly dissipating the energy, while at the same time preventing ambient light from activating the photomultiplier. Light pulses produced are magnified by the 1.5 inch diameter, 10-dynode and end-window with an S-11 photocathode photomultiplier. The amplified light signals are then converted to voltage signals and counted with a digital ratemeter/scaler.

#### 5.2.4.3 The Eberline Smart Portable (ESP-2)

Eberline Smart Portable (ESP-2) data logging radiation survey counter (figure 5.7) was used to count alpha particles emanating from the filter. It is a rugged, battery operated, microcomputer-based counter that allows for multiple readings and it is an ideal instrument for multi-detector field equipment. In its operation, the pulse signal from the attached detector is processed by the microcomputer and is converted to count rate. The pulse rate from the detector is proportional to the radiation field intensity at the detector. Different units can be chosen for data display with the basic unit being counts per second.

The ESP-2 can be operated either as a Ratemeter (Normal or Peak Trap) or as a Scaler (Integrating or Average Rate). In addition, there are four "utility" modes which allow configuration to data logging, to output data, to set operating parameters, and to set the time. These modes assist in data transfer, switching detectors, setting calibration parameters, reading and setting the clock, etc.

The Ratemeter Mode is ideally suited for routine surveys of surfaces, personnel or clothing for either contamination or exposure rate measurements from a radioactive source. The Scaler Mode may be used for quantitative data accumulation over a selectable time interval. This

study used the Scaler mode to measure average gross alpha counts from the filter over specified time intervals.


**Figure 5.7: Eberline Smart Portable (ESP-2) data logging radiation survey counter**

Radioactive decay is random process and all radioactive decay measured in counts can be estimated by the Poisson distribution (Cember, 1989). The best approximation based on Poisson distribution of the standard deviation for a number of counts is given by the square root of the counts:

$$s = \sqrt{c} \qquad (5.1)$$

where

$s$ is the standard deviation; and

$c$ is the number of counts

The standard deviation in a count rate over time is given by:

$$s = \frac{\sqrt{c}}{t} \qquad (5.2)$$

where $t$ is the time in minutes or seconds. From equation 5.2 it is evident that uncertainty in the measurement will decrease with longer sample counting.

In this study, equation 5.2 was used to calculate the associated statistical uncertainties of the ESP-2 alpha counter. The uncertainty in the number of counts is given at 1-sigma range or the range of one standard deviation surrounding the measurement which corresponds to 68% confidence level and correction factor $k$ = 1.

The ESP-2 is calibrated at the manufacturing factory and can store up to three sets of detector calibration parameters, rendering the instrument ready for immediate use. However, to verify if the correct calibration parameters corresponding to the Eberline Model SPA-1A scintillation detector are the same as those supplied on the Calibration Certificate, the calibration parameters were re-entered into the ESP-2 before it was ready for use. These calibration parameter levels are given in Appendix I: Table A.10.

Following calibration, the ESP-2's response to a check source was tested with an Americium-241 reference source (verified source of approximately 1410 counts per five minutes) to assure acceptable operation. The expected number of counts on the source was 1410 counts per five minutes while the measured five minute counts was 1250. This produced a variation of ±11% which was considered acceptable. Therefore the systematic error associated with this variation was calculated to be ±11%.

To further evaluate the precision of the ESP-2 alpha counter's performance, Chi-Square ($x^2$) test was performed on the instrument. This method compared the fluctuation of "successive counts" obtained with an alpha counter to the inconsistency in alpha counts predicted by a Poisson

distribution. The comparison aimed to identify any discrepancies in the respective variability that would be inconsistent with the random nature of radioactive decay.

For the purpose of testing the reproducibility of the results of an alpha counter, the $x^2$ value is acceptable if it falls between 3.33 and 16.92 for a set of 10 measurements as prescribed in the IAEA-TECDOC-602 (1991). If $x^2 < 3.33$, it is unlikely that the variation produced by the instrument would match a Poisson distribution. A value of $x^2 > 16.92$ will in all likelihood, be too good to account for randomness and is also cause for concern.

The method for determining the Chi-Square value is described in Appendix I (B) and Table A.11. The Chi-Square value was found to be 8.10, which is between acceptable range of 3.33 and 16.92 for the counter to be considered as performing well.

## 5.3 Methodology

### 5.3.1 Strategy

Radon concentration and EEC decrease notably with time and distance from the tailings and also depends on climatic and meteorological factors (Momeni, 1979). This affects both the radon flux and atmospheric dilution by mixing at sampling location. In general, a single source cannot be assigned to be the only contributor to high outdoor radon concentrations (Pressyanov, Guelev and Sharkov, 1995). The concentration of radon at any given location is influenced by two results: (a) locally exhaled radon and (b) dispersed radon from other locations. Apart from the convective radon gas transport, variations in atmospheric radon concentration can be attributed to the advective motion of air masses. The long radon half-life of 3.8 days means that radon contributions from other sources far away from the dam may be detected at this site due to atmospheric advective motion of air masses, which also

brings variations in the atmospheric radon concentration. For more remote areas some distance from the source, wind velocity will tend to influence radon exhaled locally and radon transported from other regions (Blaauboer, Smetsers, 1997). Therefore measurements of individual radon daughter, and hence the F factor, may serve as good indication of the origins of the measured radon gas. These measurements contain information of the "age" of the radon gas, from which the origin of the measured radon gas can be deduced. As such the data may also be indicative of radon transported from other regions.

After exhalation from both the background and the tailings, radon and its daughters are vertically transported, mixed in the boundary layer and become subjected to vertical and horizontal dispersion by the wind. In order to separate environmental radon contributors from other sources than the tailings, it is important to consider the fact that radon migrates and decays with distance and time. "Fresh" radon from the source (tailings) will decay with time and migrate to a receptor point, producing daughters and at the same time getting mixed with radon and radon daughters from other sources that have been either dispersed by the wind or locally produced from the soil. Furthermore, air mixing of "old" air from the tailing and "young" air from other contributors can affect the quantity of the radon daughters (Leach, Chandler, 1992).

To discriminate between the different radon contributors, this study applied a new strategy called "follow the wind" approach to measure radon and radon daughter concentrations at different receptor points. This approach measured radon and daughters downwind and upwind by following the direction of the wind, starting at the point closest to the tailings (source). Noting that outdoor F factor depends on wind velocity and travel time from source of "fresh" radon to receptor point and other distances from the source, radon concentrations and air samples were respectively measured and collected simultaneously at time intervals of about 1 hour between successive measurements from the base of the

tailing. The distances between measurements varied between 100 m and 200 m, depending on accessibility and suitability.

In order to examine the extent to which background sources may influence radon concentration at each receptor point, modified and simplified Bateman differential equations (Bateman, 1910), called recurrence equations (Maiello, Hoover, 2010) were applied to predict concentrations of radon decay and build-up of radon daughters at each successive receptor point. Full derivations and modifications of the Bateman equations as applied in this study are given in appendix C. The use of these calculations considered only the decay of radon over time and distance by assuming that the radon originated at the tailings. This served to eventually indicate the significant effects of meteorological conditions, dispersion, dilution, mixing etc. on radon transport from the tailings to the receptor. The calculated radon and radon daughter concentrations for each successive point were compared with the measured values. This study will attempt to corroborate the measured values by dispersion modelling in chapters 6.

To minimise atmospheric removal of radon daughters by deposition process, measurements were taken during the winter months of July and August 2017, when the weather was dry and wind patterns relatively stable. This coincided with the deployment period of the RGMs between June and August 2016 in terms of the weather patterns. We postulated that during winter period, radon daughters will likely lead to high equilibrium concentrations due to trapped radon under the inversion layer. This will also apply to night time and early morning conditions. The samplings and measurements for both downwind and upwind were taken in the mornings and afternoons over a period of five days. Morning samples were generally taken between 7:50 am and 12:00 am, whereas the afternoon samples were carried out between 13:00 and 16:30. For each sampling and measurement session, the initial sampling point was taken

at the point closest to the dam, followed by subsequent measurements applying the “follow the wind” method.

### 5.3.2 Sampling points

The sampling procedure followed and explained in this section was based on the “follow the wind” strategic approach described in section 5.3.1. The sampling locations were evaluated in terms of the position and meteorological characteristics of wind velocity and temperature with respect to the dam.

The annual average wind direction in the area is predominantly the north, north-west and north-east downwind. During sampling days, the wind direction varied hourly from north-east in the morning (8:00 am) to north-west in the afternoon (16:00) or the other way round from north-west to north-east. During some days, the wind direction remained relatively unchanged with small deviations. Given this wind directional properties, it was recommended that sampling points be chosen based on the hourly change in wind direction. Meteorological data for the periods of sampling were obtained from South African Weather Services (SAWS) for later use in the dispersion modelling and summarised in Appendix D.

The first sampling point was chosen as the point closest to the tailings (point A in figure 5.9), where radon activity is expected to be high in the downwind direction (Raviart et al., 1996). At this point, the radon gas from the dam is still relatively “fresh”, and although it represent radon from all sources, the predominant source is assumed to be the tailings dam. Therefore point A is expected to be characterised by very low or no activity of RaA, RaB and RaC, high radon gas activity and low F factor in the morning (Akber, Pfitzner, 1994). Higher F factor values are expected in the afternoon due to radon transport from other sources, mixing and longer daughter ingrowth duration, thus rendering the gas “old” (Raviart et al., 1996), (Porstendörfer, 1994, Porstendörfer, Gründel, 2005). In

addition, stronger mixing and dilution during the day may further lead to lower afternoon radon activity levels.

After 10 minutes of simultaneous sampling for both radon gas and radon daughters, followed by gross alpha counting, the second sampling point B was located after following the direction of the wind some distance from point A. The wind direction was determined using a light flag mounted on a car and taking into account the direction of movement of scattered soil dust. A similar approach of follow the wind was applied at point C, located some distance from point B as shown in figure 5.9.

The same procedure was followed both down wind and up wind. Seven sets of upwind data were taken, three in the mornings and four in the afternoons. Similarly, three sets of downwind data were taken, two in the mornings and one in the afternoon.

## 5.4 Experimental Procedure

### 5.4.1 Radon concentration

Radon concentration measurements were carried out with AlphaGUARD: a Saphymo GmbH system, model PQ2000PRO described in section 5.2.4.1 above. The monitor was operated in flow mode with 10 minute cycles, corresponding to 10 minute sampling period for the radon daughter measurements. The acquired data were stored and treated with DataExpert software.

Given that the sensitivity of the ionisation chamber is 5 cpm per 100 Bq/m$^3$, this information was used to calculate the number of counts per minute (cpm), and hence the gross counts for the total sampling time that correspond with each radon measurement. The calculated number of counts were then used to determine the statistical error from the counts by using Poisson distribution method described in section 5.2.4.3 Total

uncertainty was calculated from the sum of the systematic (3%) and the statistical errors. The results are given in appendix K (table A.13).

To select the most accurate representative value of the F factor, some sampling measurements were made at the same locations where some of the passive RGMs were placed. The choice of the sampling points were influenced by starting point, the relative distance between measurement points and the wind direction after each measurement. Radon concentrations from passive RGM and AlphaGUARD at those points were compared and the appropriate one chosen for the evaluation of F factor.

### 5.4.2 Airborne radon daughter sampling

Prior to filter sampling and analyses, a background count was performed on the filter to check for the instrument uncertainties and possible contamination due to radon daughter and other alpha emitting radioisotopes that may be present on the filter. This background check was done by conducting a one minute gross alpha count on a new filter paper to determine and quantify any alpha activity present before sampling. This value was then used as a background count in the calculation of radon daughter concentrations.

Air filter and supporting pads were encased in cassette in an “open face” arrangement as depicted in figure 3.2 above. An airflow meter attached to the vacuum pump was connected to the filter containing cassette through the outlet to measure the flow rate. An air control valve was attached between the pump and the airflow meter to regulate the flowrate from the pump.

Airborne daughter particles were collected on a filter paper by drawing air through the filter using the vacuum pump at a height of about 1 m above the ground. The air flow rate was kept constant at 14 L/min and the sampling duration was 10 minutes. The flow rate and the sampling

time were kept constant during the measuring period. The field setup is shown in figure 5.8.

**Figure 5.8: The setup used to deposit radon daughters on the filter paper.**

After sampling, the filter was carefully removed from the sampling head using a tweezer and inserted inside an O-ring sealed slider tray sample holder of the Eberline Model SPA-1A scintillation detector within 2 min after the end of sampling for alpha counting. A stop watch was used to measure both the sampling times and counting intervals.

### 5.4.3 Filter activity measurements

The filter containing Eberline Model SPA-1A scintillation detector was connected to the Eberline Smart Portable (ESP-2) counter with a MHV (CA-15-60) coaxial cable to measure the alpha activity of the daughter particles deposited on the filter paper during sampling. The counter was

operated in the Integrated Scaler mode to yield total gross counts in the time interval.

To calculate the individual $^{218}$Po (RaA), $^{214}$Pb (RaB) and $^{214}$Bi (RaC) radon daughter concentrations in Bq/m$^3$, the optimised modified Thomas equations that correspond to the counting interval of 2 - 5, 7 - 15, and 25 – 30 minutes as proposed by Busigin and Phillips (1980) were applied. This optimised Thomas method put more emphasis on the determination of RaA, the first radon decay daughter which is an important indicator in determining the "age" of the gas at a given receptor point. The merits and demerits of this method have been discussed in detail in 2.6.3 of literature review. The three sets of Busigin and Phillips (1980) equations modified and corrected by Deyuan (1991), which include the background term in Bq/m$^3$ are:

$$C_{218_{Po}} = \frac{1}{FE}[6.2241C_1 - 4.231C_2 + 3.441C_3 - 2.0247R_b] \quad (5.1)$$

$$C_{214_{Pb}} = \frac{1}{FE}[-0.03019C_1 - 0.91247C_2 + 2.6563C_3 - 5.8913R_b] \quad (5.2)$$

$$C_{214_{Bi}} = \frac{1}{FE}[-0.80797C_1 + 1.68C_2 - 1.7755C_3 - 2.1388R_b] \quad (5.3)$$

where

F flow rate in L/min;

E alpha counting efficiency (60%) in cpm/dpm;

$R_b$ background count rate in cpm;

$C_1$ gross count in interval 2-5 minutes after sampling (3 minute count);

$C_2$ gross count in interval 7-15 minutes after sampling (8 minute count); and

$C_3$ gross count in interval 25-30 minutes after sampling (5 minute count).

### 5.4.4 F factor calculations

The F factors at each receptor point were calculated using the following equation described in section 2.6.4:

$$F = \frac{EEC\ (Bq/m^3)}{C_R\ (Bq/m^3)} \tag{5.4}$$

Two sets of F factors were calculated using the values of radon concentration obtained from the RGMs (Chapter 4) and from the AlphaGUARD. The RGM values were those that were measured at the same location as the AlphaGUARD and the radon daughters. The EEC was calculated using the equation described earlier in literature review.

### 5.4.5 Uncertainty estimation

A fundamental property of radon and radon daughter measurement is that it is a statistically random process. Repeatedly exposing a radon detector or counter to the same radon concentration and check source, such as in a radon chamber and $^{241}$Am reference source, each of the individual results will be different because of the randomness of radiation. Irrespective of how good a radon detection system may be, it cannot improve on the natural randomness of the radiation signal which is used to quantify radon. These variations in radon instrument response at a given radon level can only add to the natural variations expected due to the randomness of radiation. This was evident particularly in the calculation of the Chi-Square test described in section 5.2.4.3 and appendix I (B).

According to the 'Guide to the Expression of Uncertainty in Measurement' (BIPM 2008), there are two kinds of methods used to evaluate uncertainty, namely Type A and Type B. Type A refers to an evaluation of uncertainty by the statistical analysis of series of observations. This method primarily includes random and counting

errors. Conversely, Type B refers to an evaluation of uncertainty by means other than the statistical analysis of series of observations. Type B evaluation of uncertainty includes systematic errors, experience of the measurement process, scientific judgement or published data. All uncertainties in this chapter have been determined by both Type A and Type B evaluation where necessary.

The individual uncertainty components were combined using the law of propagation of uncertainties, commonly called the "root-sum-of-squares" or "RSS" method. The combined standard uncertainty will then be equivalent to the standard deviation of the result, making this uncertainty value correspond with a 68% confidence interval (*k=1*). The equation for root sum of squares in given by:

$$\sigma_T^2 = \sqrt{\sigma_A^2 + \sigma_B^2} \qquad (5.5)$$

where

$\sigma_T^2$ is the total uncertainty;

$\sigma_A^2$ is the sum of all Type A uncertainty; and

$\sigma_B^2$ is the sum of all Type B uncertainty.

Therefore the uncertainties quoted in this chapter for the F factor are a combination of both systematic and statistical errors and correspond to *k=1* unless stated otherwise. The counting uncertainties (Type A) for both the AlphaGUARD and the Eberline alpha counter were calculated using Poisson distribution. Uncertainty propagation calculations are given in appendices J and K.

## 5.5 Results and analysis

When radon gas is released in the atmosphere, it is transported vertically by turbulent processes within the mixing layer and horizontally by the winds. In an attempt to describe radon and radon daughters' atmospheric transport from the tailings and other background sources to a receptor some distance from the tailings, this study adopted a simplified linear transport approach with local wind speed and direction.

This section presents the results and discussions on the measured radon concentrations and those of its short-lived daughters obtained from different locations around the tailings. The results of radon concentration, radon daughters' concentrations and the F factor predicted using the Bateman equations are also provided for comparison.

Radon and radon daughter activity concentrations measurements were carried out at locations within close proximity to where some RGM passive monitors were placed. To compare the effect of each of the two concentrations on the F factor, three representative points where both passive (RGM) and active radon (AlphaGUARD) measurements were carried out were randomly selected and listed in table 5.1. The three points correspond to receptor point A ($27^0$50'11"S $26^0$40'1"E) for AlphaGUARD and 27˚50'11"S 26˚40'36"E for RGM on day 1 morning, receptor points B ($27^0$50'15"S $26^0$40'1"E) for AlphaGUARD and 27˚49'52"S 26˚40'28"E for RGM and C ($27^0$50'18"S $26^0$39'58" E) for AlphaGUARD and 27˚50'18"S 26˚39'54"E for RGM on day 1 afternoon.

The results show significant differences between the radon concentration values recorded by the RGMs (long term) and that from AlphaGUARD (short term). RGMs recorded higher radon concentrations of the orders of magnitude 4 times to the AlphaGUARD concentrations.

*Table 5.2: Comparison of F factor values calculated from AlphaGUARD and RGM values*

| Point no | EEC (Bq/m³) | Average Rn (AlphaGUARD) (Bq/m³) (2017) | F factor (AlphaGUARD) | Average Rn (RGM) (Bq/m³) (2016) | F factor RGM |
|---|---|---|---|---|---|
| A | 5.15±0.43 | 10.25±0.23 | 0.502±0.044 | 75±16 | 0.069±0.017 |
| B | 4.44±0.44 | 15.50±0.28 | 0.287±0.029 | 61±8 | 0.073±0.014 |
| C | 0.23±0.09 | 6.190±0.18 | 0.038±0.015 | 49±8 | 0.005±0.001 |

The exact reasons for these large differences are unknown at this stage. However, it may tentatively be attributed to different measurement durations and conditions. The RGMs were left for about 65 days in the environment. They recorded the time integrated radon concentration from all sources over that period at that point, considering that there may have been adverse changes in meteorological conditions of wind velocity, temperature and moisture over time. The diurnal variation of radon and radon daughter concentrations especially in winter, where nighttime concentrations may be much higher, is quite large. The night time average can be up to 2.5 times higher than the daily average (Bollhöfer, 2007). This leads to much higher average values which are what the RGM in essence measures. These peaks would not be measured by the AlphaGUARD during the daytime measurements. Therefore the total concentration recorded over the deployed period is the sum of all the contributions from the tailings, local soil and distant background from all directions.

On the other hand, the AlphaGUARD measured the daytime radon concentrations as a function of meteorological conditions over short time intervals of 10 minutes. These measured concentrations were based on the unidirectional consideration of the wind as prescribed by the “follow the wind” method. Furthermore, higher daytime temperatures tends to lower the atmospheric outdoor radon concentration (Furuta, Ito and Ishimori, 2002).

Since both AlphaGUARD radon measurements and radon daughter sampling were carried out simultaneously, it was deemed appropriate that

the short term measurements of radon concentration by AlphaGUARD be used to calculate the F factor instead of RGM concentrations values. This will partly assist with the selective determination of incremental contribution of the tailings to the environmental radon.

The flowrates, sampling times, background counts and gross counts corresponding to the three short-lived radon daughters are given in appendix E. Results of the radon concentration measured by AlphaGUARD, radon daughter concentrations, EEC and the F factors both downwind and upwind after applying the "follow the wind" method are listed in Appendix F for reference. The measurement periods were divided into the morning and afternoon sessions, taking into account different meteorological conditions.

From the results, the highest downwind radon concentration of 23.38 ± 0.34 Bq/m$^3$ was observed during the mid-morning hours, whereas the lowest downwind radon concentration of 4.60 ± 0.16 Bq/m$^3$ was observed during the late afternoon hours. Diurnal patterns of radon activity levels have shown that maximum radon activity levels develop during the early hours of the morning, followed by a sharp decrease after around midday. This behaviour is consistent with diurnal pattern changes reported by other researchers (Porstendörfer, 1994, Pressyanov, Guelev and Sharkov, 1995, Blaauboer, Smetsers, 1997, Porstendörfer, Gründel, 2005). This phenomenon can be attributed to temperature inversions, leading to nocturnal radon accumulation due to low mixing height. With rising temperature as the day progress, these inversions are terminated, resulting in higher turbulent mixing and lower radon concentrations.

On the upwind side, where measurements were taken against the direction of the incoming wind towards the dam, the highest (16.00 ± 0.28 Bq/m$^3$) and the lowest (1.500 ± 0.091 Bq/m$^3$) radon concentrations were recorded during the mid and late morning periods respectively. It should however be pointed out that both measurements were made on different

days, under different meteorological conditions which may have had a direct influence on the ambient radon.

With regard to the radon daughter concentrations, an interesting phenomenon was observed. In the close vicinity to the dam, radon daughters, particularly RaC, presented in too low concentrations to contribute toward attaining higher EEC values, affecting the F factor calculation and resulting in different F values than those adopted by UNSCEAR for outdoor radon. This deviation has been previously reported in literature (Furuta, Ito and Ishimori, 2002). The EEC varied considerably at different receptor points from the dam, ranging from a minimum of 0.23 ± 0.28 Bq/m$^3$ in the afternoon to a maximum of 5.20 ± 0.64 Bq/m$^3$ during the morning. Most of the low values below 0.5 Bq/m$^3$ were observed in the afternoons. One possibility for very low or no RaC activity measured is that overall, the radon activity, and as a consequence, the radon daughter activity detected, was very low as explained above. RaC can only be seen after 20 minutes of counting, but due to low radon activities, its activity after 20 minutes becomes too low in some. In addition, it could also be that the measured radon is too "fresh", meaning that RaC has not had time to grow in the atmosphere. This is a possible indication that the "fresh" radon comes from the tailings.

Overall, the outdoor F factor was rather low as compared to the adopted outdoor values of 0.6–0.8 by ICRP and UNSCEAR respectively. Measurements at different receptor points from the tailings showed variations of the F factor reaching a factor of about 40 between the minimum and the maximum. The lowest values were less than 0.02 and occurred from midday to sunset whilst the highest ones reached 0.5 during the mid-morning. This has been verified by many surveys involving outdoor radon daughter measurements (Raviart et al., 1996). The low and wide range of F factor values indicate that it is not recommended to always adopt the average recommended value for dose assessment purposes. This also indicated that use of the F factor alone to evaluate radon "age" would

not be adequate and that better interpretation would be attained from the individual radon daughters.

### 5.5.1 "Follow the wind" results and discussion (downwind)

The results of the variation of radon concentration, individual radon daughter concentration (measured and calculated) and the F factor with distance and time are presented and discussed in the sections below. The measured results are compared with the Bateman calculated values.

Taking the measured values at point A as the initial concentrations of radon and its daughters, the expected concentrations of those radon atoms and daughter atoms after some time *t* can be predicted by applying the Bateman equations. Time of radon travel from point A to B was calculated from the average wind speed and the straight line distance between point A and B. The measured concentrations at point A were taken as the initial concentrations. From point B to C, point C to D and point D to E, the time taken was considered as the time difference between the two measurements.

Due to long half-life of radon (3.8 days) compared to that of its short lived daughters, the decrease in radon activity is expected to be negligible over the course of the observation period as illustrated in figure 2.9. Furthermore, Bateman calculations do not take into account other factors affecting atmospheric radon, namely; meteorological conditions; wind direction; and wind speed, which affects dispersion (dilution) of radon and radon progeny in the atmosphere through air mixing. Bateman calculations only accounted for the decay time of radon in air (the "age" of radon in air) to produce radon daughters.

#### 5.5.1.1 Set 1 (19-08-2017 downwind morning)

Figure 5.9 shows three sampling points for Set 1 measurements and their positions and distances from the tailing. Measurements were taken

from A (27$^0$50’11”S 26$^0$40’1" E) to B (27$^0$50'16"S 26$^0$39’57" E) and then to C (27$^0$50'18"S 26$^0$39’54" E) in that order while following the direction of the wind.

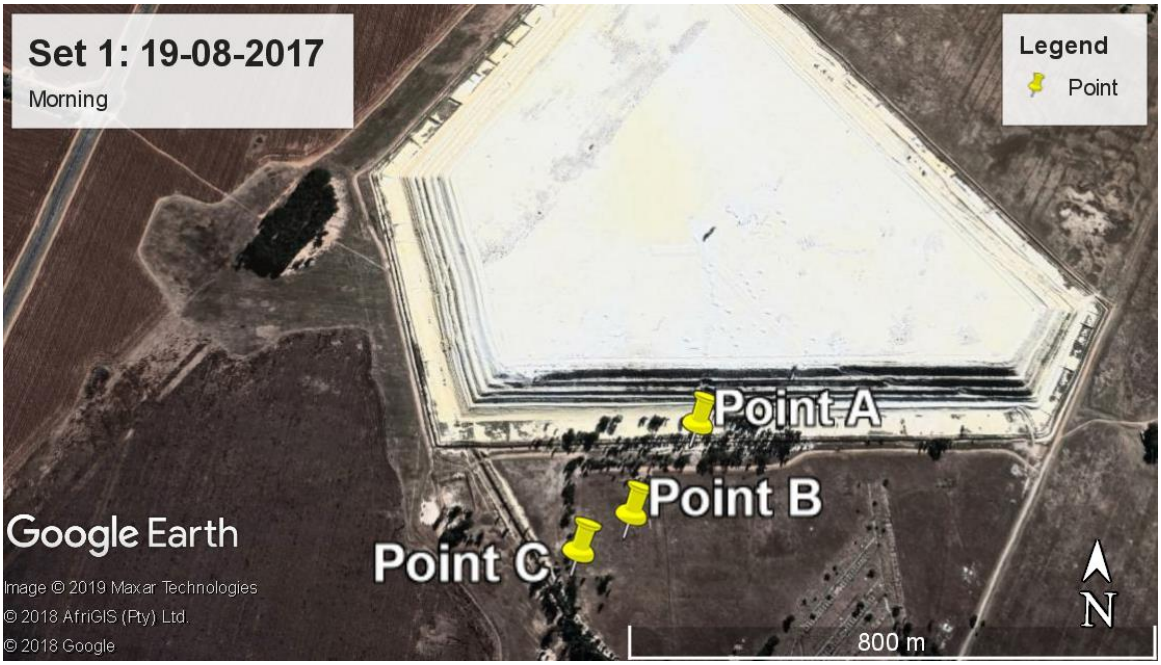


**Figure 5.9: Three sampling points for Set 1 measurements and their positions and distances from the tailing**

The results of Set 1 for predicted activities are presented in table 5.2. These results represent calculated concentrations activities of radon and radon daughters as well as the F factors by applying Bateman equations. The calculated values are a function of initial concentrations (measured at point A) and the time the radon gas has been in air.

*Table 5.3: Set 1 predicted activities of radon, radon daughters and F factor as functions of distance and time for the downwind trend.*

| Distance (m) | time (s) | RaA (Bq/m$^3$) | RaB (Bq/m$^3$) | RaC (Bq/m$^3$) | Rn (Bq/m$^3$) | F factor |
|---|---|---|---|---|---|---|
| 0 (Point A) | 0 | 17.91 | 6.35 | 0 | 10.25 | 0.50 |
| 189.2 (Point B) | 28.65 | 17.12 | 6.49 | 0.11 | 10.25 | 0.51 |
| 291.8 (Point C) | 2.88E3 | 10.19 | 9.39 | 7.22 | 10.19 | 0.85 |

Table 5.3 presents measured results of radon concentration, individual radon daughter concentrations and the F factor after applying the "follow the wind" method. The measured distances are from the first point closest to the dam (Point A at 0 m) to the last point of measurement for each set (Point C) as shown in figure 5.9.

*Table 5.4: Set 1 measured activities of radon, radon daughters and F factor as functions of distance and time for the downwind trend.*

| Distance (m) | RaA (Bq/m³) | RaB (Bq/m³) | RaC (Bq/m³) | Rn (Bq/m³) | F Factor |
|---|---|---|---|---|---|
| 0 (Point A) | 17.91±1.90 | 6.35±0.45 | 0 | 10.25±0.23 | 0.502±0.044 |
| 189.2 (Point B) | 3.00±1.3 | 0.55±0.26 | 0.41±0.34 | 8.50±0.21 | 0.089±0.047 |
| 291.8 (Point C) | 2.16±0.97 | 0.38±0.20 | 0.05±0.26 | 8.44±0.21 | 0.052±0.036 |

Figure 5.10 shows the relationship between measured radon concentration, radon daughter concentration and F factor and distance from the tailing. At point A, RaA concentration is high compared to RaB, RaC and radon. At this point, the gas has significantly decayed to yield high RaA activity, and subsequently RaB, thus rendering the gas "old". There is no RaC activity. The "old" gas could be remnant from a high value building up during night time, and not dispersing due to low wind. From figure 5.10, there is a sharp decrease from point A to point B in the concentrations of RaA (83.3%), RaB (91.4%), radon (17.1%) and F factor (82.3 %), with significant distance variations of the order 6, 3, 1.2 and 6 respectively. In addition, the concentration of RaC increased from 0 – 0.41 ± 0.35 Bq/m³.

It can be further observed from figure 5.10 that the concentration of RaA is multiple times higher than that of RaB and RaC. This is because RaA is the immediate daughter of the radon gas, and due to its positive nature, it quickly attaches itself to the aerosol particles, thus becoming a major contributor to the atmospheric concentration (Ashok, Nagaiah and Shiva Prasad, 2008).

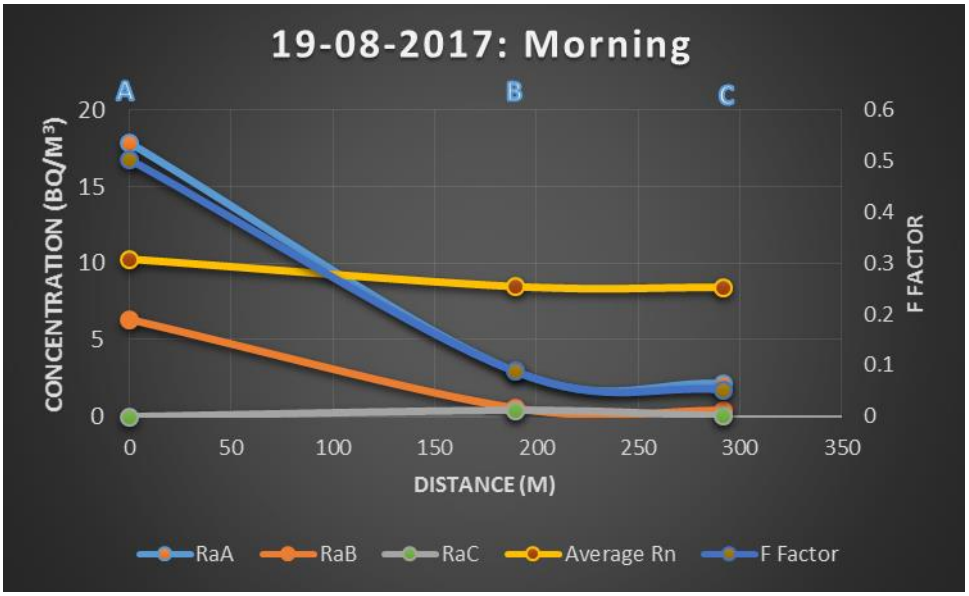


**Figure 5.10: Radon concentration (Rn), radon daughters' concentrations (RaA, RaB, RaC) and F factor as a function of distance from the tailing.**

From the five minutes weather data for the duration of the measurements provided by the South African Weather Services (SAWS), the calculated average wind speed for 10 minutes of sampling at A was found to be 6.6 m/s. This was relatively high, leading to turbulent atmospheric conditions characterised by moderate vertical mixing, surface air radon dilution, decreased EEC and low F factor (Blaauboer, Smetsers, 1997, Maeda, Hobbs, 1996).

Moving from point B to C, further away from the source, the RaA, RaB and RaC concentrations continued to remain low, with RaC showing the highest decrease of the order 10. The radon concentration did not yield any noticeable change from point B to point C as expected. This observation of decreasing radon daughter concentration as the day progresses and the temperature rises, is consistent with findings by (Ashok, Nagaiah and Shiva Prasad, 2008). Atmospheric parameters like pressure, temperature, wind velocity etc. may be responsible for such an observation.

The recorded wind speeds peaked during the morning from 9:30 am to noon at the average wind speed of 6.6 m/s during measurements at point A, continuously decreasing slightly to 6.1 m/s at point B and 5.6 m/s at point C. The direction fluctuated between $52.2^0$ (ENE) and $37.2^0$ (NNE) during the measurements at point A, between $34.7^0$ (NNE) and $19.3^0$ (NNE) at point B and between $38.4^0$ (NNE) and $30.7^0$ (NNE) at point C.

Radon concentration at point A was expected to be low due to the high wind speed at this point as compared to B and C. However this was not the case. This observation can be ascribed to the location characteristics at that point. Point A is surrounded by trees and it is the closest to the dam, both of which act as wind shields. Therefore the wind speed at that point may have been reduced, thus trapping radon gas at that point over time, and in the process decaying to produce RaA and elevated RaB.

The F factor decreased from point A to point C by a factor of 9. The main contributor to this observation was the decrease in daughter concentrations at points B and C, whilst radon concentrations remain relatively unchanged. This is an indication that no atmospheric equilibrium was attained between the parent radon and its daughter due to atmospheric mixing. As such, the radon at points B and C can be considered to be predominantly of local origin, and not the radon transported by wind from other sources, whereas the air at point A may be due to mixing of “young” air from the dam and “old” air from other sources in the north-east direction.

Radon and daughter calculations in table 5.2 predicted very high F factors compared to the measured ones, increasing from 0.50 at point A to 0.85 at point C, which is in contrast with the decreasing F factor from measured quantities. It should be noted that the calculated values did not consider other external factors like meteorological conditions etc. The only determining factor was the natural decay properties of half-life and decay constants.

The relative uncertainty in the measured radon concentration by AlphaGUARD shown in table 5.3 were between 2.3% at point A and 2.5% at both point B and point C. The systematic errors contributed 13% (point A), 14.4% (point B) and 14.5 % (point C) of the total uncertainty of activity. The major component of the systematic error was the counting error of the instrument, which contributed 11% of total error as discussed in section 5.2.4.3. The results further shows that uncertainties of RaB and RaC are higher than those of RaA, particularly at point B and C. Low radon daughter activity concentrations, made counting numbers small and caused an increase of statistical uncertainty, especially for RaB and RaC counts, which are the main contributors to total uncertainty.

The phenomenon of poor statistics always occurs at the low count rates associated with alpha particle counting, and is an integral part of radon daughter measurement at the low levels typically encountered in the open atmosphere. As indicated earlier, the concentration of radon daughters were often low, particularly RaC, which was practically undetectable for most of the time during measurements. The high uncertainty value compared to the measured concentration at point C for RaC is due to the low alpha count rate at this concentration. This increased the total uncertainty of the EEC and hence uncertainty in the F factor since both quantities are calculated from all three daughter concentration values. Based on the sources of uncertainty considered here, random errors constituted 92% of the total uncertainty of activity for RaC at point C.

#### 5.5.1.2 Set 2 (19-08-2017 downwind afternoon)

Figure 5.11 shows four sampling points for Set 2 afternoon measurements and their positions and distances from the tailings.

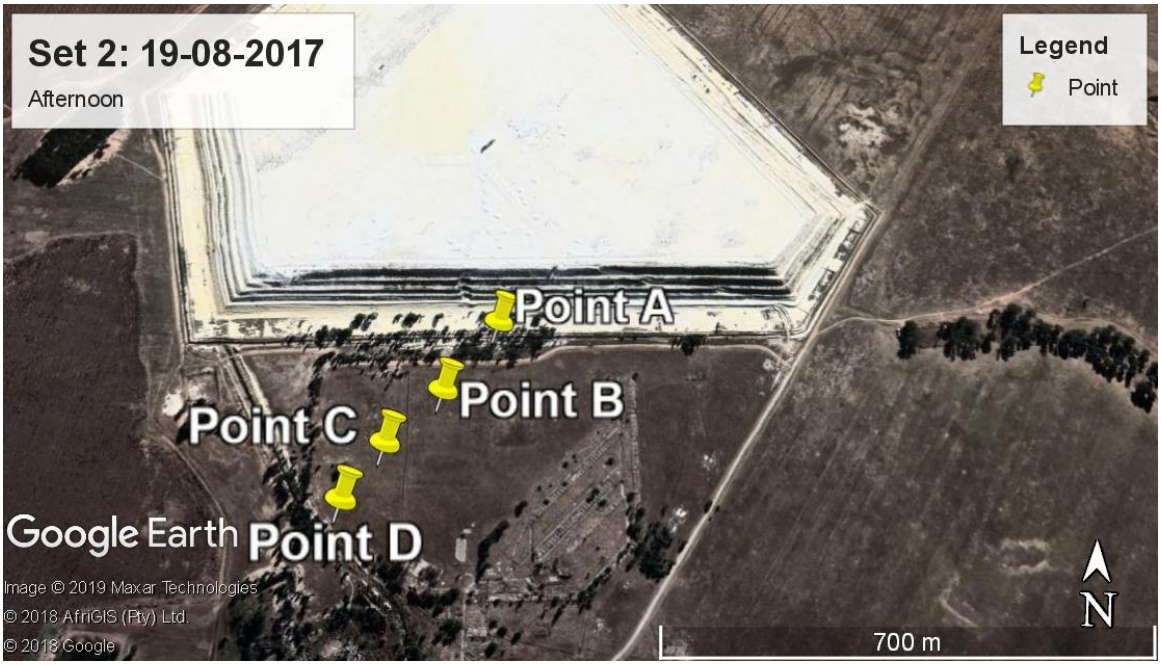


**Figure 5.11: Illustration of four sampling points for set 2 afternoon.**

Measurements were taken from point A (27$^0$50'11"S 26$^0$40’4" E) to point B (27$^0$50'15"S 26$^0$40'1" E), to point C (27$^0$50'18"S 26$^0$39’58" E) and lastly to point D (27$^0$50'21"S 26$^0$39’56" E) in that order while following the direction of the wind. The average wind speeds ranged from 3.07 m/s at point B and peaked at 3.47 m/s at point C. The recorded wind speeds at points A and D were 3.10 m/s and 3.20 m/s respectively. The wind direction fluctuated between 10.0$^0$ (NNE) and 29.8$^0$ (NNE) at point A, between 23.3$^0$ (NNE) and 65.4$^0$ (ENE) at point B, between 16.9$^0$ (NNE) and 38.5$^0$ (NNE) at point C and between 12.3$^0$ (NNE) and 30.3$^0$ (NNE) at point D.

The predicted results for set 2 are presented in table 5.4. The calculated values are a function of initial concentrations (measured at point A) and the time the radon gas has been in air.

*Table 5.5: Predicted concentrations for radon, RaA, RaB and the F factor for the afternoon downwind measurements.*

| Distance (m) | time (s) | RaA (Bq/m³) | RaB (Bq/m³) | RaC (Bq/m³) | Rn (Bq/m³) | F factor |
|---|---|---|---|---|---|---|
| 0 (Point A) | 0 | 2.25 | 0 | 0 | 6.13 | 0.04 |
| 148 (Point B) | 49 | 2.83 | 0.05 | 7.1E-4 | 6.13 | 0.05 |
| 272 (Point C) | 3.4E3 | 6.09 | 4.58 | 2.90 | 6.09 | 0.68 |
| 380 (Point D) | 2.7E3 | 6.06 | 5.61 | 4.90 | 6.05 | 0.89 |

Table 5.5 presents the measured results of radon concentration, individual radon daughter concentrations and the F factor after applying the "follow the wind" grab sampling method. Low RaC ambient concentrations made it difficult to measure, hence its absence in table 5.5.

*Table 5.6: Set 2 measured activities of radon, radon daughters and F factor as functions of distance for the downwind trend.*

| Distance (m) | RaA (Bq/m³) | RaB (Bq/m³) | Average Rn (Bq/m³) | F Factor |
|---|---|---|---|---|
| 0 (Point A) | 2.15±0.84 | 0 | 6.13±0.18 | 0.03±0.02 |
| 148 (Point B) | 7.1±1.7 | 7.17±0.51 | 15.50±0.28 | 0.29±0.03 |
| 272 (Point C) | 2.23±0.88 | 0 | 6.19±0.19 | 0.04±0.02 |
| 380 (Point D) | 1.68±0.85 | 0.50±0.20 | 4.63±0.16 | 0.09±0.04 |

Contrary to the morning pattern, afternoon measured results presented in figure 5.12 shows a different trend. At point A, only radon and RaA are present with radon concentration about a factor 3 larger on RaA. The F factor is also very low at 0.037 ± 0.014. The lower afternoon radon concentration compared to the morning could be due to negative temperature gradient, even though the wind speed is less than in the morning. Low radon activity at point A, closer to the tailings, can be

attributed to the reduced wind speed due to the close proximity of the sampling point to the tailings, thus being shielded from most of the wind transported background radon from other sources. The vegetation around that area may also contribute to the reduction of wind speed due to the presence of thick trees. Therefore the air at point A can be considered "young" because only RaA had a chance to grow from the decaying radon parent. In general, lower F factor values indicate that the radon at that point is "young", having had limited transport.

From figure 5.12, RaA, radon and F factor increased from point A to point B by 231%, 153% and 677% respectively, with significant distance variations of the order 3, 2.5 and 8 respectively. RaB increased from 0 to 7.2 Bq/m$^3$. The wind speed decreased slightly from 3.1 m/s at point A to 3.07 m/s at point B. The equivalence of the elevated RaA and RaB concentrations at this point, is responsible for spike in the F factor by a factor of 8.

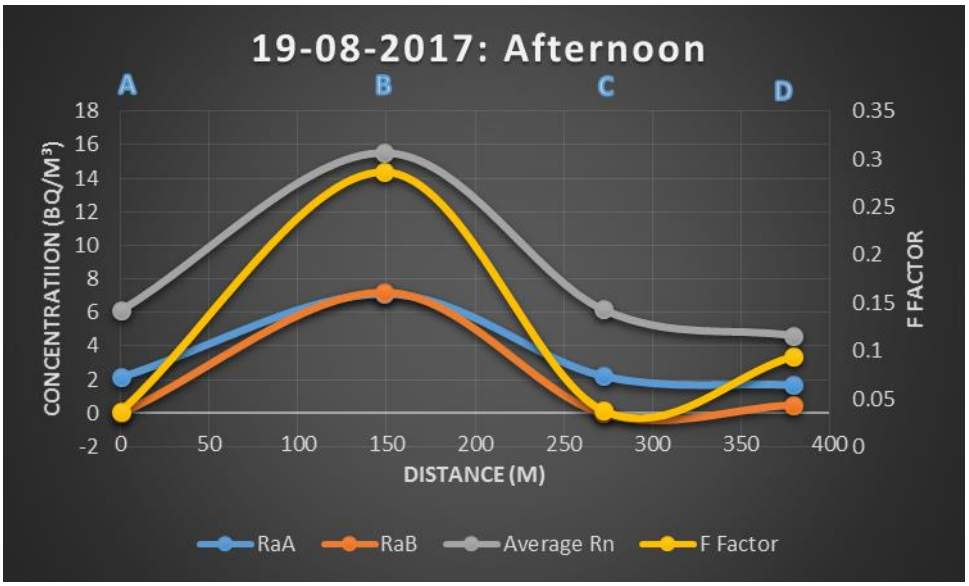


**Figure 5.12: Radon concentration (Rn), radon daughters' concentrations (RaA, RaB, RaC) and F factor as a function of distance from the tailing (Set 2)**

The decrease in wind speed lead to decreasing air mixing (Winkler et al., 2001). It is expected that radon and radon daughter concentrations will be reduced as the distance from the tailing increases as was the case with the morning trend discussed in section 6.4.1 above (Momeni, 1979).

However at any given location, wind direction can have an adverse effect on the atmospheric conditions. Radon activity can change due to a change in wind direction, an indication of a change of source (Winkler et al., 2001).

The wind direction at point A fluctuated between $10.0^0$ (NNE) and $29.8^0$ (NNE) while at point B varied between $23.3^0$ (NNE) and $65.4^0$ (ENE). From this observation, it may be suggested that the excess radon and radon daughters at point B correspond to mixing of “young” and “old” air from the tailings and other sources from eastern and north-eastern (ENE) winds. In addition, there are no other significant sources of the same order of size as the tailings in the vicinity or in that direction.

The rise of the dispersion plume (buoyant rise) due to the rising temperature during the day may cause the plume to be higher, and it may first “hit” the ground at some downwind distance, causing the “bump” in the distance graph. Together with slower wind speeds, the Rn in the plume had time to age and RaA and RaB grew in before hitting the ground.

Radon, RaA, RaB and F factor all decreased from point B to point C by 60%, 69%, 100% and 87% respectively. There is a close resemblance between point C and point A in terms of radon concentration, RaA, RaB and F factor. Even though the wind speed at point C is the highest at 3.5 m/s as compared to 3.1 m/s at point A, the dominating wind direction at both points is the NNE winds. It therefore follows that the two points are subjected to the same external radon source. At point D the gas is predominantly local and “old”, with very low mixing, confirming the observation by Momeni (1979) that radon and radon daughters decrease

with time and increasing distance from the tailings due to atmospheric dilution. The slight increase in RaB could be due to the decay of local radon and RaA with time. The predicted values could not account for the spike at point B for radon, radon daughters and the F factor. It will be seen how the predicted values will compare with the modelled values.

The absence of RaB and RaC activity at point A and point C contributed largely towards the uncertainty in the F factor values as depicted in table 5.5. This implies that If RaB and RaC values are zero, then they cannot contribute to the error in F factor. Only Ra and Rn contributed to the error of the F factor. In addition, low RaB concentration of 0.50 ± 0.20 Bq/m$^3$ measured in point D contributed towards high relative uncertainty of 44% in the F factor. The relative uncertainty in the measured concentration by AlphaGUARD ranged from 1.8% at point B to 3.4% at point D.

#### 5.5.1.3 Set 3 (20-08-2017 downwind afternoon)

Figure 5.13 shows four set 3 afternoon sampling points and their positions and distances from the tailing. Measurements were taken from point A (27$^0$50'11"S 26$^0$40'10" E) to point B (27$^0$50'13"S 26$^0$40'7" E), to point C (27$^0$50'17"S 26$^0$40'9" E) and finally to point D (27$^0$50'22"S 26$^0$40'5" E) in that order while following the wind direction.

The lowest recorded average wind speed was 2.9 m/s at point D whereas the highest wind speed was 5.8 m/s point C. Points A and B recorded wind speeds of 3.7 m/s and 3.0 m/s respectively. The wind direction fluctuated between 22.6$^0$ (NNE) and 41.2$^0$ (NNE) at A, between 358.6$^0$ (N) and 45.0$^0$ (NE) at B, between 356.6$^0$ (N) and 68.2$^0$ (ENE) at C and between 333.5$^0$ (NNW) and 36.1$^0$ (NNE) at D.

The predicted results for set 3 are presented in table 5.6 for four points given that point A measured values are the initial concentrations. The results for set 3 measured radon concentrations, radon daughter

concentrations and corresponding F factors are presented in table 5.7. Graphical representation of the trend as a function of time is shown in figure 5.14.

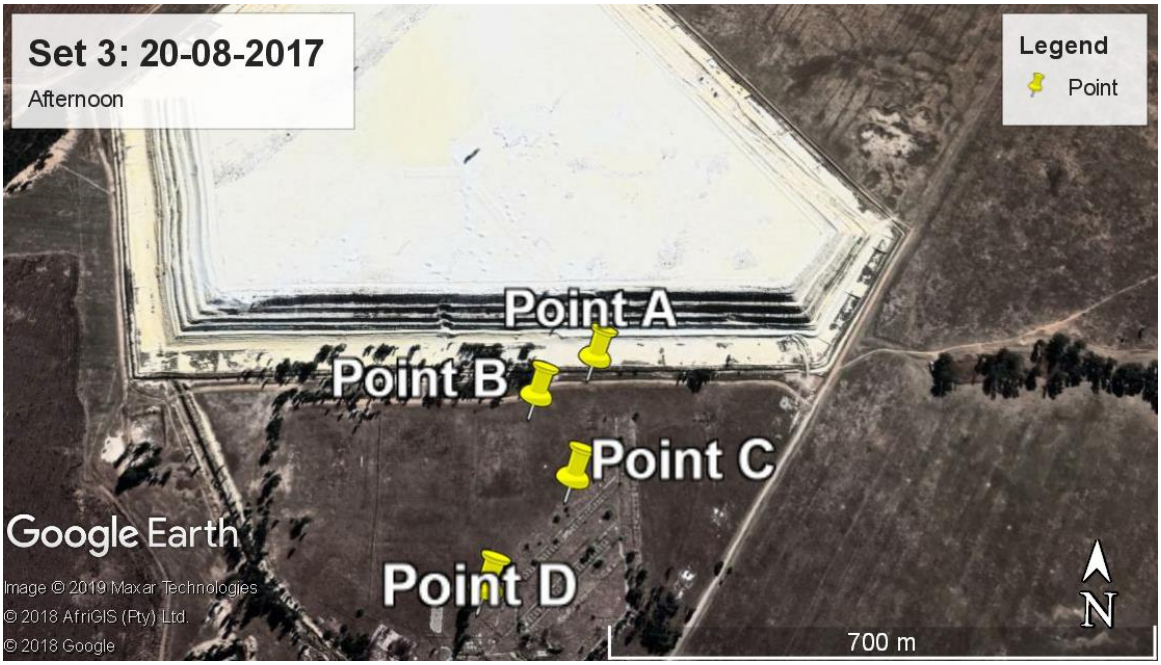


**Figure 5.13: Illustration of four sampling points for set 3 afternoon.**

*Table 5.7: Predicted concentrations for radon, RaA, RaB and the F factor for the afternoon downwind set 3 measurements.*

| Distance (m) | time (s) | RaA (Bq/m³) | RaB (Bq/m³) | RaC (Bq/m³) | Rn (Bq/m³) | F factor |
|---|---|---|---|---|---|---|
| 0 (Point A) | 0 | 1.69 | 0.84 | 0 | 10.75 | 0.04 |
| 102.6 (Point B) | 28 | 2.59 | 0.50 | 0.01 | 10.75 | 0.05 |
| 237.7 (Point C) | 3.36E3 | 10.68 | 8.06 | 5.20 | 10.67 | 0.68 |
| 521.0 (Point D) | 3.54E3 | 10.60 | 10.07 | 9.07 | 10.60 | 0.92 |

From figure 5.14, point A is characterised by high radon activity compared to RaA and RaB. The low F factor coupled with low RaA and RaB ingrowth from parent decay is a reflection of "young" air and of local origin. This trend is similar to that observed in set 2 afternoon described in section 5.5.1.2 above.

*Table 5.8: Set 3 measured activities of radon, radon daughters and F factor as functions of distance for the downwind trend*

| Distance (m) | RaA (Bq/m³) | RaB (Bq/m³) | RaC (Bq/m³) | Average Rn (Bq/m³) | F Factor |
|---|---|---|---|---|---|
| 0 (Point A) | 1.69±0.69 | 0.48±0.18 | 0 | 10.75±0.23 | 3.9E-2±1.5E-2 |
| 102.6 (Point B) | 0 | 0 | 0.68±0.24 | 20.63±0.32 | 1.3E-2±5.0E-3 |
| 237.7 (Point C) | 3.09±0.91 | 0.73±0.20 | 0 | 10.94±0.24 | 6.4E-2±1.8E-2 |
| 521.0 (Point D) | 8.04±1.30 | 0.41±0.19 | 0 | 7.66±0.19 | 1.4E-2±3.1E-2 |

The radon concentration at point A is 6.4 times that of RaA and 22 times that of RaB, indicating small build-up time for the radon daughters to be accumulated.

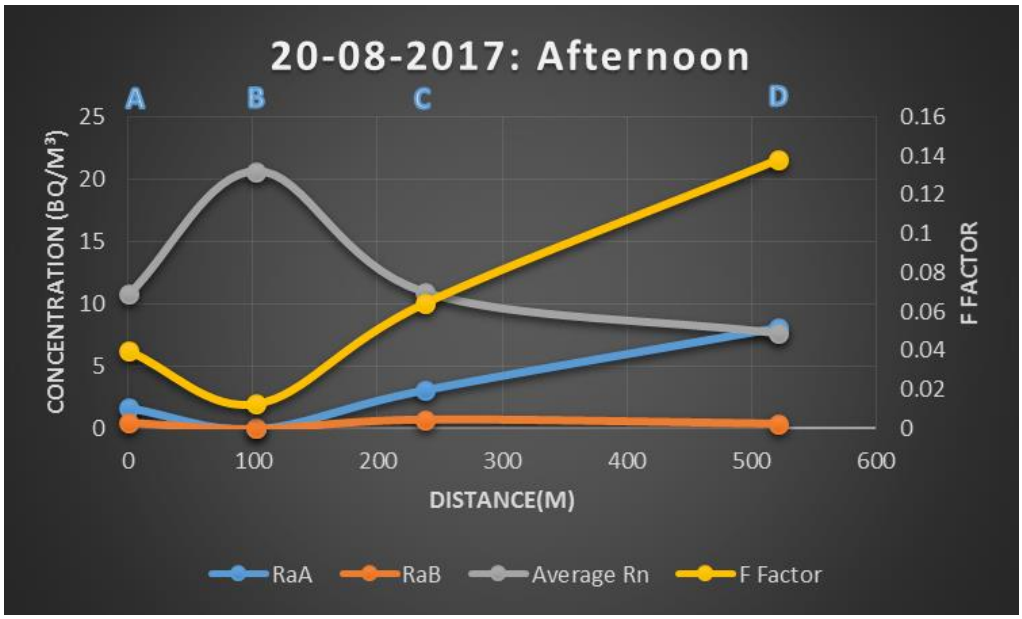


**Figure 5.14: Radon concentration (Rn), radon daughters' concentrations (RaA, RaB, RaC) and F factor as a function of distance from the tailing (Set 3).**

The sudden increase in radon at point B from 10.75 ± 0.23 Bq/m$^3$ at point A to 20.63 ± 0.32 Bq/m$^3$ (91.91%) is evidence that there is another contributing radon source from some distant background. The wind direction was fluctuating between 358.6$^0$ (N) and 45.0$^0$ (NE) at B. One possibility is that the excess radon has been transported from the northern direction, given that the wind direction at point A was mainly dominated by the north-east direction. Another possibility is that at about 100 m from the tailings dam, there is high radon exhalation from the local soil and strong vertical mixing conditions around that area. In addition, the rise of the dispersion plume (buoyant rise) due to the rising temperature during the day may cause the plume to be higher, and it may first "hit" the ground at some downwind distance, causing the "bump" in the distance graph. Together with slower wind speeds, the Rn in the plume had time to age and RaA and RaB grew in before hitting the ground. This is the same afternoon 'bump', but this time only for Rn. Higher wind speed may have caused shorter grow-in time and therefore lower "age".

Considering that the radon is progenitor of the daughters, the presence of radon at some point must force the presence of radon daughters due to radioactive decay. The presence of RaC only, albeit small concentration of the order 0.03 to the radon gas concentration, is an indication that the gas is disproportionately mixed, with high quantity of "fresh" radon exhaled from the soil and transported from other distant sources and very small amount from the "old", decayed radon. This observation has been corroborated by very low F factor of 0.013 at point B.

Point C is characterised by decreasing radon concentration (20.63 ± 0.32 Bq/m$^3$ - 10.94 ± 0.24 Bq/m$^3$), increasing RaA (0 – 3.09 ± 0.91 Bq/m$^3$), increasing RaB (0 – 0.73 ± 0.21 Bq/m$^3$) and increasing F factor (0.013 ± 0.005– 0.064 ± 0.018) from point B. Point C experienced the highest wind speed of 5.8 m/s, which may have contributed towards the removal and

transportation of radon to further distances. At the same time the emergence of the radon daughters is due radon decay at that location.

Further decrease in radon concentration from point C to point D is accompanied by an increase in both RaA and F factor and a slight decrease in RaB. Accordingly, radon decreases with distance from the source. (Momeni, Yuan and Zielen, 1979). The increased RaA concentration in figure 5.14, accompanied by increased F factor, demonstrates the presence of "old" and decayed air where RaA grows to the level of radon.

The results from table 5.7 show that at point B, only RaC was detected, albeit at low concentration of 0.68 ± 0.25 Bq/m$^3$. The absence of RaA and RaB were key in this anomaly since only RaC and Rn errors can contribute to the F factor error. The relative uncertainties for the F factors were 57.4%, 42.3% and 32.6% at points A, C and D respectively. It is worth pointing out that the relative uncertainty of RaB at point D (46%) is the highest followed by RaA at point A (38%). This is because RaB recorded the lowest concentration of 0.41 ± 0.19 Bq/m$^3$ at point D, while RaA at point A had the lowest concentration of 1.69 ± 0.69 Bq/m$^3$ thus contributing towards increasing uncertainties due to low level alpha counting.

#### 5.5.1.4 Set 4 (21-08-2017 downwind morning)

Figure 5.15 illustrates the five points for Set 4 morning measurements and their positions and distances from the tailing. Measurements were taken from point A (27$^0$50'11"S 26$^0$40'0" E) to point B (27$^0$50'15"S 26$^0$39'56" E), then point C (27$^0$50'18"S 26$^0$39'54" E), point D (27$^0$50'24"S 26$^0$39'51" E) and point E (27$^0$50'28"S 26$^0$39'51" E) in that order while following the direction of the wind.

The lowest recorded average wind speed was 3.0 m/s at point A whereas the highest wind speed was 6.1 m/s at point C. Points B, D and E recorded wind speeds of 4.8 m/s, 5.2 m/s and 4.5 m/s respectively. The

wind direction fluctuated between 16.0$^0$ (NNE) and 26.3$^0$ (NNE) at A, between 358.1$^0$ (N) and 4.6$^0$ (N) at B, between 7.4$^0$ (N) and 8.5$^0$ (NNE) at C, between 328.0$^0$ (NNW) and 0.5$^0$ (N) at D and between 318.0$^0$ (NNW) and 349.8$^0$ (NNW) at E. The predicted results for set 4 are presented in table 5.8 for the five sampling points.

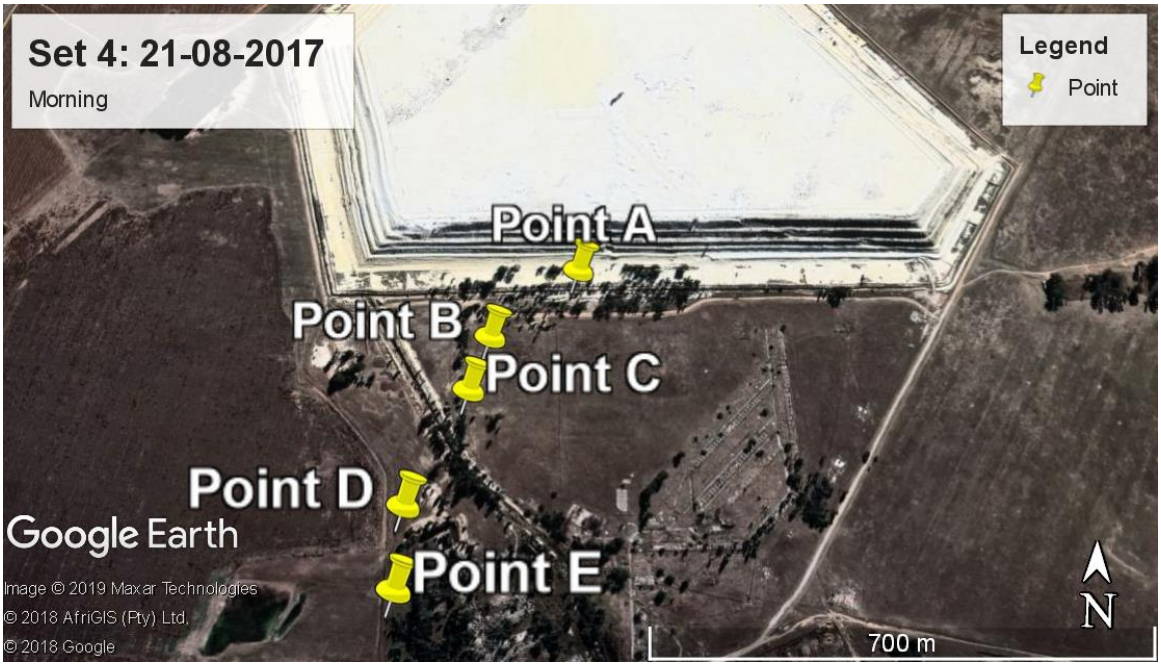


**Figure 5.15: Illustration of five sampling points for set 4 (morning)**

*Table 5.9: Predicted concentrations for radon, RaA, RaB and the F factor for the morning downwind set 4 morning measurements.*

| Distance (m) | time (s) | RaA (Bq/m$^3$) | RaB (Bq/m$^3$) | RaC (Bq/m$^3$) | Rn (Bq/m$^3$) | F factor |
|---|---|---|---|---|---|---|
| 0 (Point A) | 0 | 17.78 | 4.05 | 0 | 20.63 | 0.19 |
| 164.9 (Point B) | 55 | 18.32 | 4.38 | 0.13 | 20.63 | 0.21 |
| 272.5 (Point C) | 3000 | 20.51 | 16.02 | 10.72 | 20.49 | 0.71 |
| 475.1 (Point D) | 3780 | 20.35 | 19.54 | 17.94 | 20.34 | 0.94 |
| 598.6 (Point E) | 2760 | 20.23 | 20.05 | 19.53 | 20.22 | 0.98 |

The results for Set 4 measured radon concentration, radon daughter concentrations and F factor are presented in table 5.9. Graphical

representation of this trend as a function of distance is shown in figure 5.16.

*Table 5.10: Set 4 morning measurements of radon, radon daughters and F factor as functions of distance for the downwind trend*

| Distance (m) | RaA (Bq/m³) | RaB (Bq/m³) | Average Rn (Bq/m³) | F factor |
|---|---|---|---|---|
| 0 (Point A) | 17.8±2.4 | 4.05±0.47 | 20.63±0.32 | 0.192±0.024 |
| 164.9 (Point B) | 11.8±2.1 | 3.71±0.42 | 20.13±0.32 | 0.157±0.022 |
| 272.5 (Point C) | 12.3±1.9 | 1.96±0.35 | 23.38±0.34 | 0.099±0.016 |
| 475.1 (Point D) | 6.2±1.4 | 0.17±0.26 | 10.69±0.23 | 0.069±0.026 |
| 598.6 (Point E) | 6.9±1.3 | 1.29±0.25 | 20.25±0.32 | 0.069±0.013 |

Figure 5.16 illustrates that at point A, high activity concentrations of both radon and RaA were observed. This simultaneous elevation in both radon and RaA activity concentrations is associated with low wind speed, positive temperature gradient, weak mixing and stable atmosphere. This is common during the night and in the early morning hours (Porstendörfer, 1994, Porstendörfer and Gründel, 2005, Winkler et al., 2001, Hu, Tan, 2000). Compared to the afternoon results from set 3 within the same area, morning radon and radon daughter concentrations as well as F factor increased by a factor of 2, 10, 9 and 5 for radon, RaA, RaB and F factor respectively. The presence of high RaA and RaB activities signal the presence of "old" and predominantly local gas that may have built up close to the tailings during the night.

From point A to point B, there is no significant change in radon concentration. However, there is a drop in RaA by 33%, RaB by 8% and the F factor by 18%. This is because the short lived RaA continued to decay with time and diluted with increasing distance from the tailings, thus contributing to the decrease in the F factor.

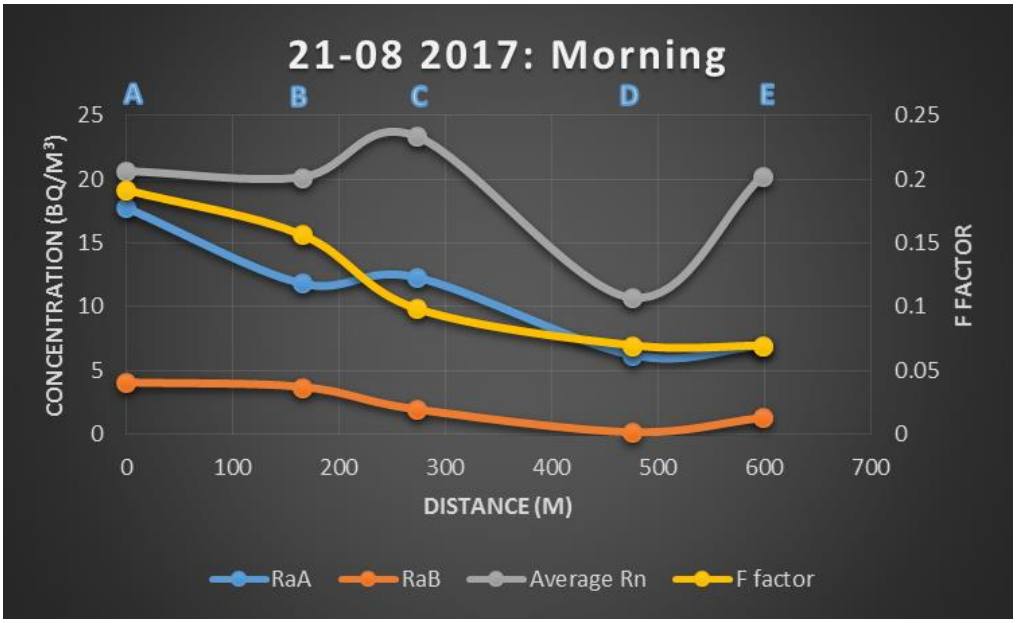


**Figure 5.16: Radon concentration (Rn), radon daughters' concentrations (RaA, RaB, RaC) and F factor as a function of distance from the tailing (Set 4, morning)**

The spike in radon concentration at point C from 20.13 ± 0.32 Bq/m$^3$ to 23.38 ± 0.34 Bq/m$^3$ is evidence that there is another contributing radon source from some distant background source or that is locally exhaled due to topographical conditions at that point. The slight RaA increase is due to the influence of "old" radon dispersed from other distant sources that continues to decay with time and distance. A similar, but smaller bump, similar to the morning pattern in Set 1, possibly again from plume rise.

During unsteady conditions of higher wind speeds and varied wind direction, vertical mixing, or wind shear cause a dilution of radon in surface air and subsequently decreasing the number of radon daughters. Hence the activities of radon, RaA and RaB as well as the F factor decreases at D.

From point D to E, there is a sharp increase of radon and moderate increase in both RaA and RaB. The F factor remained unchanged. The increased radon, RaA and RaB show that the radon at that point is a

mixture of the “old” local radon and “young” radon transported from the surroundings.

Considering the fact that wind direction is another source of additional radon, two points with highest radon concentration are points A and C, both of which are subjected to the NNE winds. Therefore it can be inferred that winds from NNE are the contributors to excess radon at those receptor points.

From the results shown in table 5.9, with exception of point D, relative uncertainties of radon from AlphaGUARD, RaA, RaB and F factor ranged from 1.4% at point C to 2.2% at point B, 13.6% at point A to 18.7% at point E, 11.4% at point B to 19.5% at point E and 18.6% at point A to 28.0% at point E respectively. This showed some consistency in terms of the performance of the measuring instruments, coupled with the observation that the ambient concentrations of radon and radon daughters were relatively higher at those points.

At point D, the magnitude of relative uncertainty was high for AlphaGUARD radon (12.9%), RaA (22.8%), RaB (151.5%) and F factor (56%). This measurement point was characterised by low counts, particularly for RaB and hence, low concentrations accompanied by large uncertainties for all the measured quantities. Overall, uncertainties of RaB were higher than those of RaA.

#### 5.5.1.5 Set 5 (21-08-2017 downwind afternoon)

Figure 5.17 illustrates the three points for set 5 afternoon measurements and their positions and distances from the tailing. Measurements were taken from point A (27$^0$50'10"S 26$^0$40'22" E) to point B (27$^0$50'15"S 26$^0$40’35" E), then point C (27$^0$50'18"S 26$^0$39’54" E) in that order while following the direction of the wind.

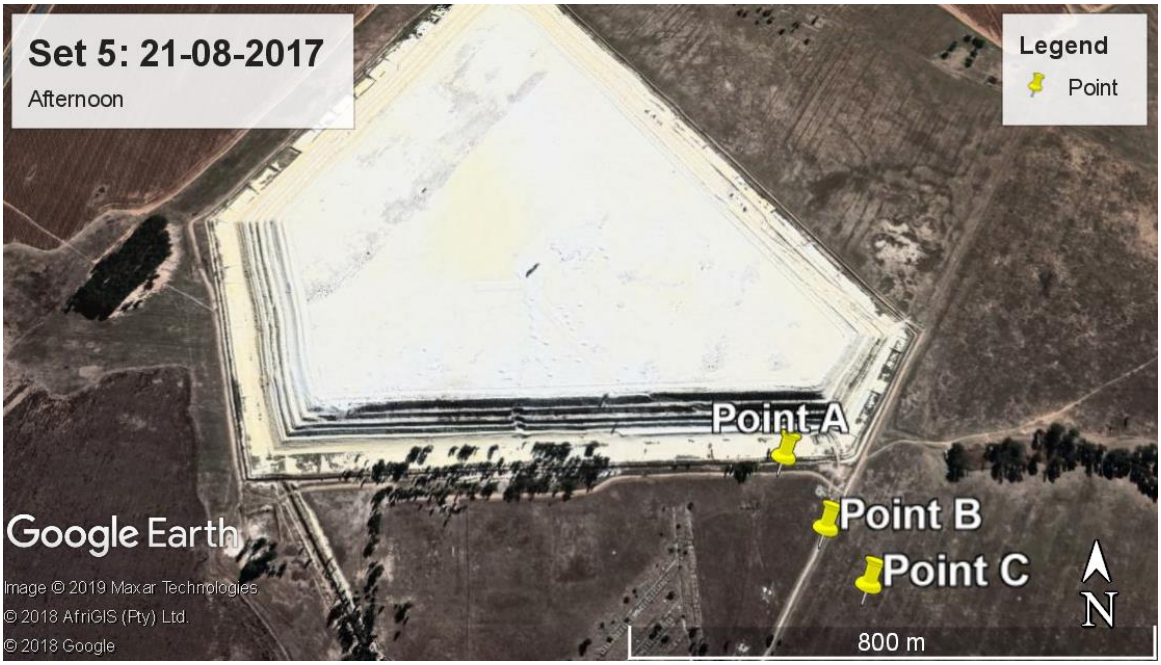


**Figure 5.17: Illustration of three sampling points for set 5 (afternoon)**

Table 5.10 shows the predicted activity concentrations and the F factor by applying Bateman equations and table 5.11 summarises the measured radon, radon daughter and F factor quantities for set 5 measurements (afternoon).

*Table 5.11: Predicted concentrations for radon, RaA, RaB and the F factor for the afternoon downwind set 5 afternoon measurements*

| Distance (m) | Time (s) | RaA (Bq/m³) | RaB (Bq/m³) | RaC (Bq/m³) | Rn (Bq/m³) | F factor |
|---|---|---|---|---|---|---|
| 0 (Point A) | 0 | 2.03 | 0.25 | 0.103 | 13.13 | 0.029 |
| 150.0 (Point B) | 36 | 3.45 | 0.29 | 0.107 | 13.13 | 0.042 |
| 392.5 (Point C) | 2700 | 12.99 | 11.73 | 9.748 | 12.98 | 0.856 |

*Table 5.12: Set 5 afternoon measurements of radon, radon daughters and F factor as functions of distance for the downwind trend*

| Distance (m) | RaA (Bq/m³) | RaB (Bq/m³) | Average Rn (Bq/m³) | F factor |
|---|---|---|---|---|
| 0 (Point A) | 2.03±1.02 | 0.25±0.21 | 13.13±0.26 | 2.9E-2±2.4E-2 |
| 150.0 (Point B) | 3.08±0.88 | 0.36±0.18 | 20.50±0.32 | 2.5E-2±9.0E-3 |
| 392.5 (Point C) | 1.52±0.71 | 0.49±0.19 | 8.38±0.21 | 4.9E-2±2.0E-2 |

Figure 5.18 shows the variation of radon and daughter activity with distance during afternoon. The average wind speeds ranged from the lowest of 3.8 m/s at point C and peaked at 4.2 m/s at point A. Point B recorded wind speeds of 3.9 m/s. The wind direction fluctuated between 294.4$^0$ (WNW) and 340.2$^0$ (NNW) at point A, 283.0$^0$ (WNW) and 313.9$^0$ (NNW) at point B and 271.4$^0$ (WNW) and 297.6$^0$ (WNW) at point C.

From figure 5.18, the presence of RaA (2.03 ± 1.02 Bq/m$^3$) and RaB (0.25 ± 0.21 Bq/m$^3$), albeit at low concentrations compared to radon gas (13.13 ± 0.26 Bq/m$^3$) at point A, is an indication of a diluted gas with strong vertical mixing. The recorded wind speed at point A was the highest for the afternoon, peaking at 4.2 m/s. The low F factor value of 0.029 ± 0.024 further characterises unstable conditions, with the wind direction fluctuating by about 46$^0$. Furthermore, the low F factor signifies the presence of "young" gas with very low daughter activity concentration. However, due to the presence of both RaA (15 % of radon concentration) and RaB (2 % of the radon concentration), the gas can be considered "old" after having decayed and simultaneously producing daughters on a shorter time scale. Taking all these factors into consideration, the situation at A may be that of a mixture of "young" gas from some distant background and "old" gas of local origin.

From point A to point B, there was 56% increase in radon concentration, 52% RaA activity increase, 43% increase in RaB activity

and a 15% decrease in F factor. The same bump is observed as with all other afternoon sets. The main contributor towards this observed radon activity concentration increase may be the transported radon from the direction 283.0$^0$ (WNW) – 294.4$^0$ (WNW) which is the range in which the wind direction has changed during measurements at point A and point B. Increased RaA and RaB at B is due to continued decay of local radon. The decreased F factor implies that there has been some mixing of the local "old" air with transported "young" air.

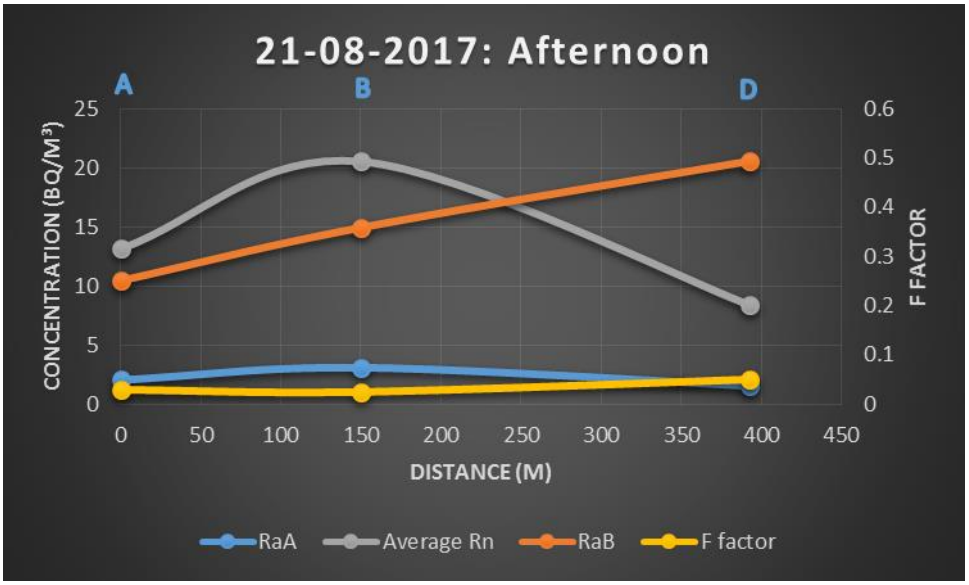


**Figure 5.18: Radon concentration (Rn), radon daughters' concentrations (RaA, RaB, RaC) and F factor as a function of distance from the tailing (Set 5, afternoon).**

At point C radon concentration decreased by 59%, RaA decreased by 103% and the F factor increased by 99%. These decreases are expected because as the distance from the tailings increases, the concentrations of radon and its daughter will decrease due to atmospheric dilution, even though the F factor increases (Momeni, 1979).

From table 5.11, point A is characterised by the smallest measured RaB concentration value of 0.25 ± 0.21 Bq/m$^3$. This observation, as has been previously the case, was accompanied by large relative uncertainty of 82% producing high relative uncertainty of 83% for the F factor.

### 5.5.1.6 Set 6 (26-08-2017 downwind afternoon)

Figure 5.19 illustrates the three points for set 6 afternoon measurements and their positions and distances from the tailing.

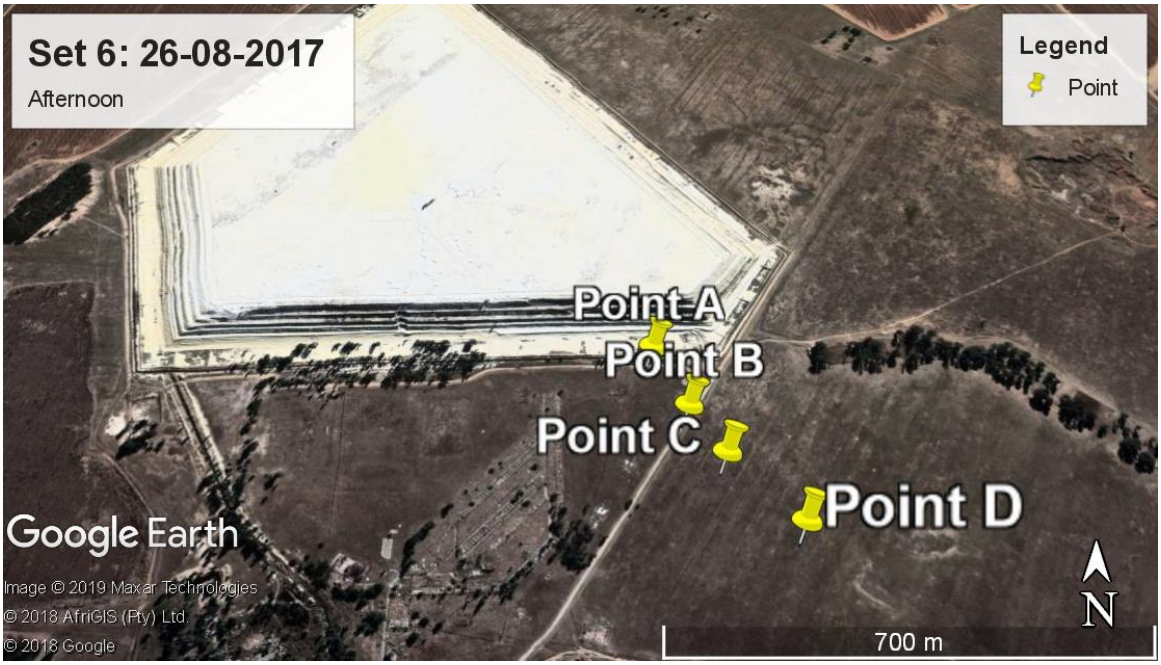


**Figure 5.19: Depiction of four sampling points for set 6 (afternoon)**

Measurements were taken from point A (27$^0$50'11"S 26$^0$40'18" E) to point B (27$^0$50'15"S 26$^0$40'20" E), point C (27$^0$50'18"S 26$^0$40'22" E) and then point D (27$^0$50'22"S 26$^0$40'26" E) in that order while following the direction of the wind.

Table 5.12 shows the predicted activity concentrations and the F factor by applying Bateman equations and table 5.13 summarises the measured radon, radon daughter and F factor quantities from set 6 measurements (afternoon).

*Table 5.13: Predicted concentrations for radon, RaA, RaB and the F factor for the afternoon downwind set 6 measurements*

| Distance (m) | time (s) | RaA (Bq/m³) | RaB (Bq/m³) | RaC (Bq/m³) | Rn (Bq/m³) | F factor |
|---|---|---|---|---|---|---|
| 0 (Point A) | 0 | 6.171 | 1.529 | 0 | 6.190 | 0.232 |
| 135.1 (Point B) | 28 | 6.173 | 1.584 | 0.025 | 6.189 | 0.238 |
| 242.7 (Point C) | 3120 | 6.153 | 4.969 | 3.459 | 6.149 | 0.735 |
| 407.6 (Point D) | 3600 | 6.106 | 5.878 | 5.413 | 6.103 | 0.938 |

*Table 5.14: Set 6 afternoon measurements of radon, radon daughters and F factor as functions of distance for the downwind trend*

| Distance (m) | RaA (Bq/m³) | RaB (Bq/m³) | Average Rn (Bq/m³) | F factor |
|---|---|---|---|---|
| 0 (Point A) | 6.17 ±1.23 | 1.53±0.26 | 6.19±0.18 | 0.232±0.042 |
| 135.1 (Point B) | 4.84±1.27 | 1.00±0.26 | 13.38±0.26 | 0.077±0.019 |
| 242.7 (Point C) | 2.66±0.92 | 0 | 10.88±0.24 | 0.026±0.009 |
| 407.6 (Point D) | 0.52±0.69 | 0.52±0.20 | 8.38±0.21 | 0.039±0.021 |

Figure 5.20 shows four measuring points for the afternoon set 6. The average wind speeds ranged from 2.2 m/s at point D and peaked at 4.9 m/s at point A. Point B and C recorded wind speeds of 4.3 m/s and 3.0 m/s respectively. The wind direction fluctuated between $343.4^0$ (NNW) and $349.6^0$ (NNW) at point A, between $331.1^0$ (NNW) and $356.9^0$ (NNW) at point B, between $316.7^0$ (NNW) and $355.6^0$ (NNW) at point C and between $338^0$ (NNW) and $7.1^0$ (NNE) at point D.

From figure 5.20 the concentrations of radon and that of RaA are equal at point A. However the concentration of RaB is about 4 times less than both radon and RaA. From this observation, the gas can be considered to be very “old”, noting that this is the lowest downwind radon

concentration to be measured in the five days of sampling, both in the morning and afternoon. The F factor was expected to be considerably higher at point A than the obtained value of 0.232 ± 0.042. This deviation from the expected trend has been observed before by (Momeni, 1979). The wind speed of 4.9 m/s at this point can be considered to be relatively high, leading to increased atmospheric dilution, thus reducing the radon activity concentration.

From point A to point B, a similar characteristic afternoon bump is observed. At these points the concentration of radon increased by 116.2%, RaA decreased by 21.6% and RaB decreased by 34.4%. The F factor dropped by 67%, thereby representing a decrease in radon daughters due to continued decay and deposition with increasing radon gas. The excess radon may be from other sources, transported by wind and air mass.

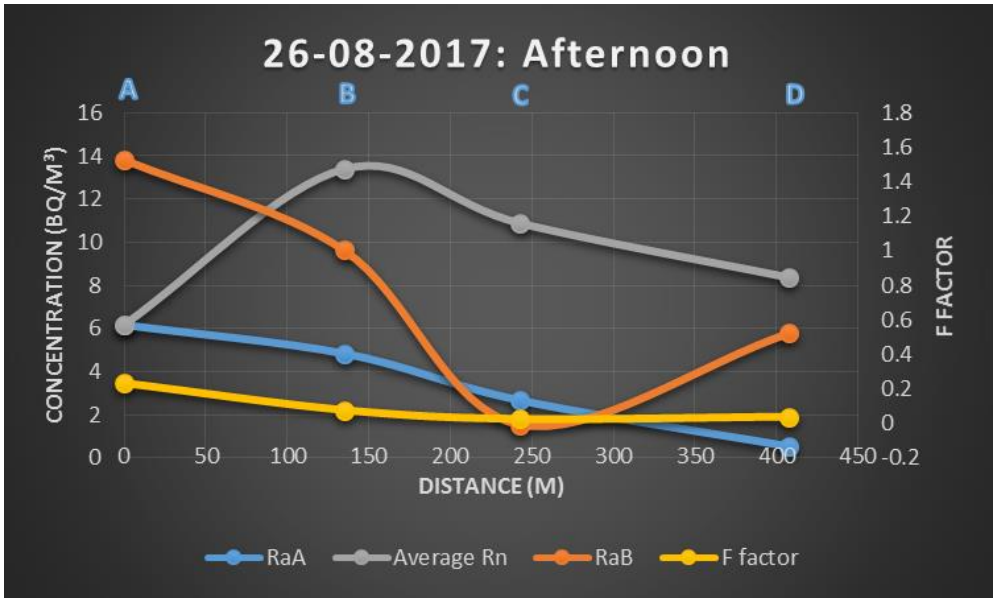


**Figure 5.20: Radon concentration (Rn), radon daughters' concentrations (RaA, RaB, RaC) and F factor as a function of distance from the tailing (Set 6, afternoon)**

From point B to point C, and from C to D, radon concentration first decreased by 18.7% followed by a further 23% decrease at point D. Activity concentration of RaA decreased by 44.9% from B to C, then decreased further by 80.6 %. The activity concentration of RaB at point C was 0

Bq/m$^3$. Therefore the air at C can be considered “young” with only RaA present. RaB increased from 0 Bq/m$^3$ at C to 0.52 ± 0.20 Bq/m$^3$ at D. The F factor decreased by 66.4% at point C due to the absence of RaB and RaC, with RaA as the only contributor. The ingrowth of RaB at point D increased the F factor by 50.1%.

The main contributor towards this observed radon increase may be the transported radon from the direction 283.0$^0$ (WNW) to 294.4$^0$ (WNW), which is the range in which the wind direction has changed during measurements at point A and point B. Increased RaA and RaB at B is due to continued decay of local radon. The decreased F factor implies that there has been some mixing of the local “old” air with transported “young” air.

Low activity concentrations for both RaA and RaB at point D contributed largely towards the high relative uncertainty in the F factor values at those points. The extremely high relative uncertainty value of RaA at point D (134%) was due to very low activity concentration of RaA at that point. The relative uncertainty in the measured concentration by AlphaGUARD ranged from 1.9% at point B to 2.8% at point A.

#### 5.5.1.7 Set 7 (27-08-2017 downwind morning)

Air sampling points for set 7 morning measurements are depicted in figure 5.21. Measurements were taken from point A (27$^0$50'11"S 26$^0$40’4" E) to point B (27$^0$50'14"S 26$^0$40’2" E) and point C (27$^0$50'18"S 26$^0$40’0" E) in that order while following the direction of the wind.

Table 5.14 shows the predicted activity concentrations and the F factor by applying Bateman equations and table 5.15 summarises the measured radon, radon daughter and F factor quantities from set 7 measurements (afternoon).

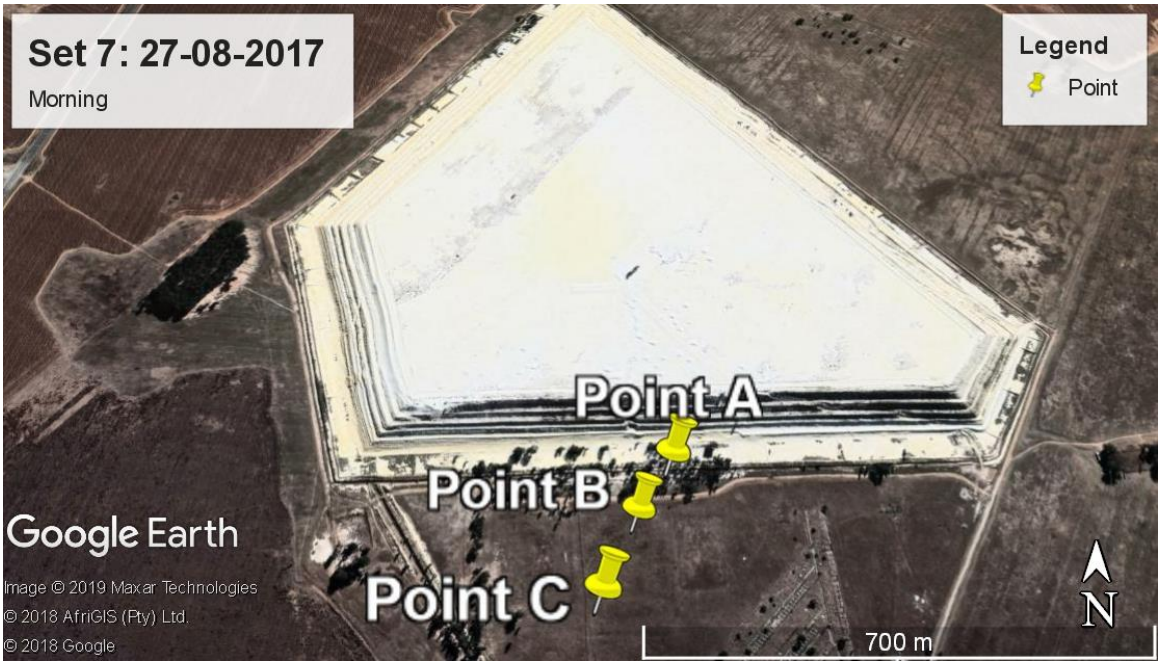


**Figure 5.21: Illustration of sampling points for set 7 (morning)**

*Table 5.15: Predicted concentrations for radon, RaA, RaB and the F factor for the morning downwind set 7 measurements*

| Distance (m) | time (s) | RaA (Bq/m³) | RaB (Bq/m³) | RaC (Bq/m³) | Rn (Bq/m³) | F factor |
|---|---|---|---|---|---|---|
| 0 (Point A) | 0 | 15.30 | 3.35 | 0 | 19.88 | 0.17 |
| 107.6 (Point B) | 58 | 16.20 | 3.65 | 0.12 | 19.88 | 0.18 |
| 242.7 (Point C) | 3180 | 19.76 | 15.57 | 10.59 | 19.75 | 0.72 |

*Table 5.16: Set 7 morning measurements of radon, radon daughters and F factor as functions of distance for the downwind trend*

| Distance (m) | RaA (Bq/m³) | RaB (Bq/m³) | Average Rn (Bq/m³) | F factor |
|---|---|---|---|---|
| 0 (Point A) | 15.3±2.3 | 3.35±0.42 | 19.88±0.32 | 0.168±0.023 |
| 107.6 (Point B) | 11.4±1.9 | 2.03±0.32 | 8.31±0.21 | 0.269±0.045 |
| 242.7 (Point C) | 6.7±1.5 | 1.05±0.26 | 8.13±0.20 | 0.152±0.038 |

Figure 5.22 depict three points for the morning set number 7. The average wind speeds ranged from 1.9 m/s at point A and reached the highest value of 4.0 m/s at point C. Point B 3.3 m/s. The wind direction fluctuated between $7.9^0$ (NNE) and $46.5^0$ (NE) at point A, between $7.5^0$ (NNE) and $23.9^0$ (NNE) at point B and between $322.3^0$ (NNW) and $355.1^0$ (NNW) at point C.

Figure 5.22 shows high concentrations of radon and that of RaA are almost equal at point A. The results at point A are similar to the one obtained in set 4 (section 5.5.1.4) at almost the same point. Again, a very similar morning pattern to the other morning sets was observed. As was the case in the set 4 (morning) results, high radon and RaA activity concentrations at A are associated with low wind speed, positive temperature gradient, weak mixing and stable atmosphere. The recorded wind speed at point A was the lowest at 1.9 m/s. The ratios of Rn:RaA and Rn:RaB are 1.3 and 5.9 respectively, whilst the F factor is 0.168 ± 0.023. The presence of high RaA and RaB activities is an indication that the gas is “old” and is predominantly of local origin.

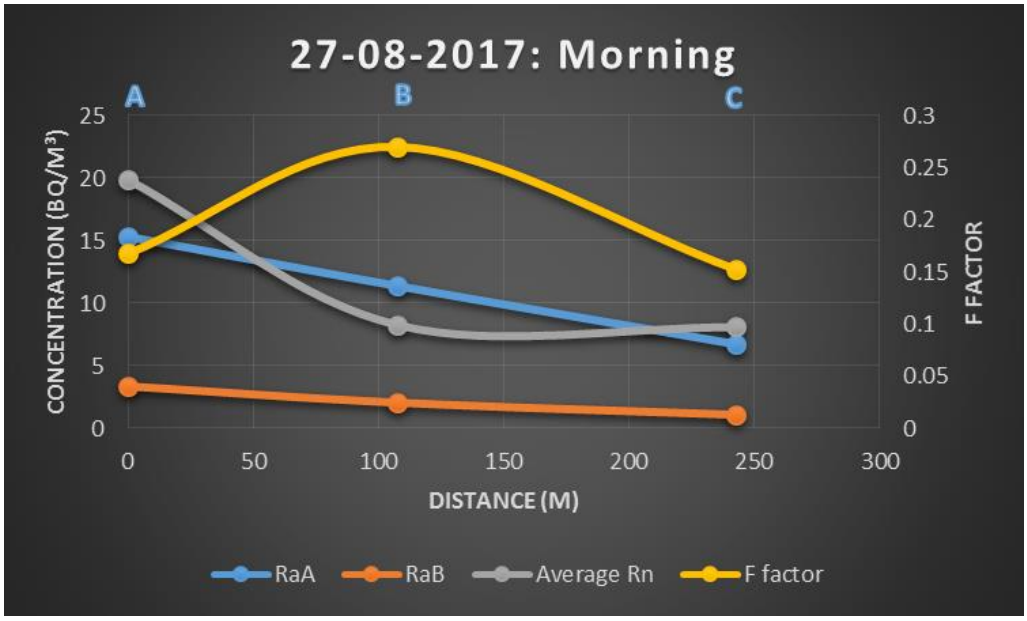


**Figure 5.22: Radon concentration (Rn), radon daughters' concentrations (RaA, RaB, RaC) and F factor as a function of distance from the tailing (Set 7, morning).**

From point A to point B, the concentration of radon decreased by 58.2%, RaA decreased by 25.8% and RaB decreased by 39.3%. The F factor increased by 60.8% from 0.168 ± 0.023 to 0.269 ± 0.045. The increasing F factor is due to increasing RaB and decreasing radon. This is due to the continued decay and dilution of radon with time and distance from the tailing, coupled with deposition of the already formed RaA.

From B to C, all the quantities are decreasing with time and distance, even though the radon decreased by just 2.2%. This shows that radon continues to decay and some of the radon and radon daughters get diluted in air as the wind speed increases and temperature rises.

From the results shown in table 5.15, relative uncertainties of radon from AlphaGUARD, RaA, RaB and F factor ranged from 1.6% at point A to 2.5% at point C, 14.7% at point A to 22.1% at point C, 13.1% at point A to 28.5% at point C and 13.9% at point A to 25.0% at point C respectively. These observations are consistent with previous results in terms of the

performance of the measuring instruments at different activities, and shows the better statistics obtained at higher concentrations.

### 5.5.2 “Follow the wind” results (Upwind)

Two sets of the results of radon concentration, radon daughters and the F factor are presented and compared, i.e. the predicted results based on Bateman calculations and the “follow the wind” measurements. The approach is similar to the downwind analysis discussed in section 5.5.1. The difference is that the measurements were taken against the direction of the wind.

#### 5.5.2.1 Set 1 (20- 08-2017: Upwind morning)

Figure 5.23 illustrate sampling positions measured against the direction of the wind (upwind). Like in downwind measurements discussed above, the starting point (point A) was the point closest to the tailings moving up. Measurements were taken upwind from point A (27$^0$49'28"S 26$^0$40'0" E) to point B (27$^0$49'30"S 26$^0$40'7" E), point C (27$^0$49'26"S 26$^0$40'10" E) and point D (27$^0$49'24"S 26$^0$40'9" E) in that order.

Table 5.16 and table 5.17 presents the predicted and measured results for set 1 morning activities and F factor in the upwind direction respectively. The predicted results are calculated based on the initial concentrations (measured at point A) and the time the radon gas has been in air.

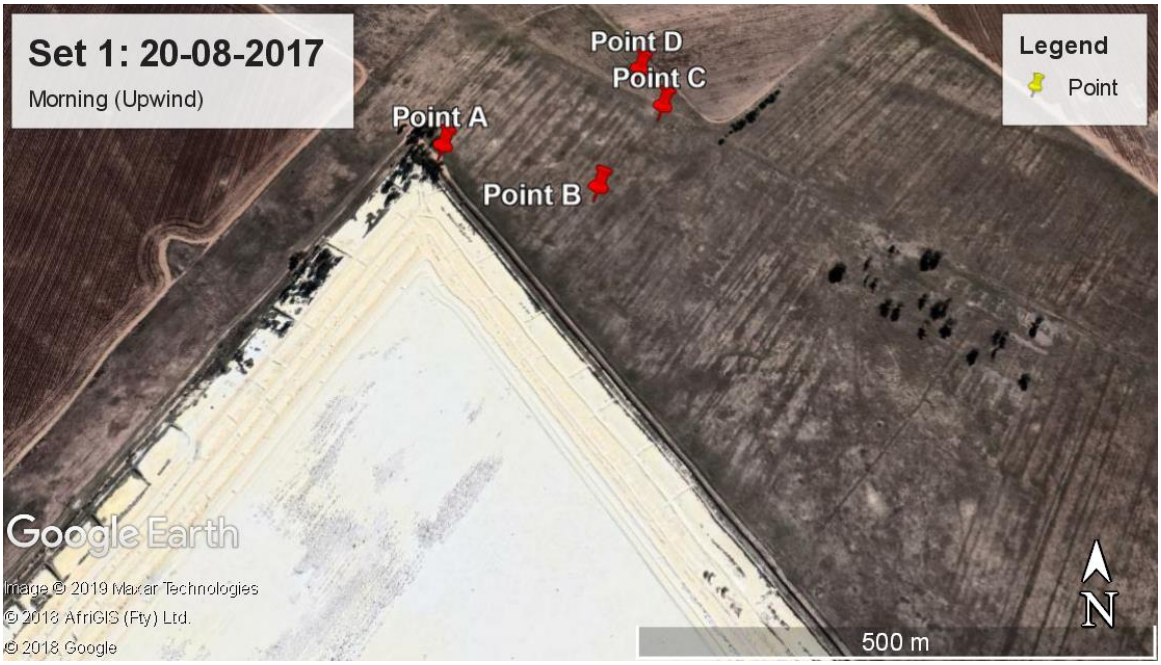


**Figure 5.23: Illustration of sampling positions measured against the direction of the wind (upwind) (Set 1, morning).**

*Table 5.17: Predicted concentrations for radon, RaA, RaB and the F factor for the morning upwind set 1 measurements*

| Distance (m) | time (s) | RaA (Bq/m³) | RaB (Bq/m³) | RaC (Bq/m³) | Rn (Bq/m³) | F factor |
|---|---|---|---|---|---|---|
| 0 (Point A) | 0 | 6.270 | 1.817 | 0 | 13.25 | 0.120 |
| 208.79 (Point B) | 34 | 7.109 | 1.887 | 0.036 | 13.25 | 0.131 |
| 356.76 (Point C) | 2340 | 13.191 | 8.789 | 4.843 | 13.18 | 0.588 |
| 432.57 (Point D) | 2460 | 13.123 | 11.637 | 9.392 | 13.12 | 0.834 |

*Table 5.18: Measured concentrations for radon, RaA, RaB and the F factor for the morning upwind set 1 measurements*

| Distance (m) | RaA (Bq/m³) | RaB (Bq/m³) | RaC (Bq/m³) | Rn (Bq/m³) | F factor |
|---|---|---|---|---|---|
| 0 (Point A) | 6.27±1.51 | 1.82±0.34 | 0 | 13.25±0.26 | 0.120±0.025 |
| 208.79 (Point B) | 5.30±1.27 | 1.71±0.28 | 0 | 8.44±0.21 | 0.170±0.033 |
| 356.76 (Point C) | 2.87±2.01 | 0 | 2.53±0.50 | 12.69±0.25 | 0.069±0.032 |
| 432.57 (Point D) | 12.42±1.61 | 7.39±0.46 | 0 | 15.81±0.28 | 0.323±0.026 |

Figure 5.24 illustrates the variation of measured radon concentration, radon daughter concentration and F factor with distance from the tailing (set 1 upwind) for the four points shown in figure 5.23. The average wind speeds ranged from 5.9 m/s at point D to the highest value of 6.3 m/s at point C.

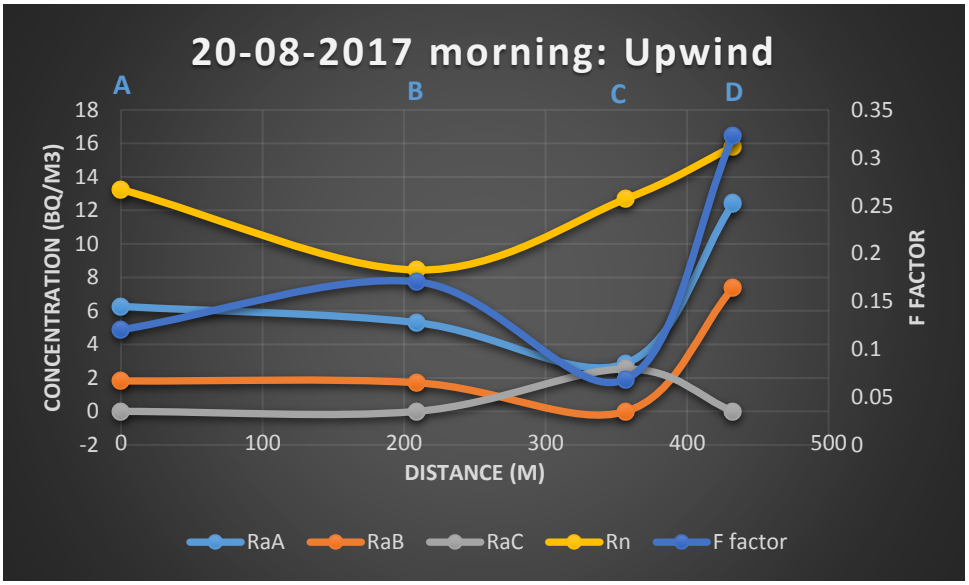


**Figure 5.24: Variation of measured radon concentration, radon daughter concentration and F factor with distance from the tailing (Set 1 upwind).**

The wind speeds corresponding to point A and B were 6.2 m/s and 6.1 m/s respectively. The wind direction fluctuated between 33.4$^0$ (NNE)

and 35.8$^0$ (NNE) at point A, 17.85$^0$ (NNE) and 25.7$^0$ (NNE) at point B, 1.8$^0$ (N) and 20.0$^0$ (NNE) at point C and 5.6$^0$ (N) and 10.1$^0$ (N) at D.

From figure 5.24, radon activity at point A is higher than that of RaA and RaB by factor of 2.1 and 7.3 respectively. The F factor value of 0.120 indicate that the air at point A is a mixture of "young" local radon and "old" gas from some distant background. Point D had the highest activity of radon, RaB as well as the F factor, indicating enough build-up time for the radon daughters to be accumulated.

The lowest radon activity was observed at point B. Point C shows a decrease in RaA and F factor, with increasing radon and RaC. The emergence of RaC is due to the continuous decay of RaA, whereas the increase in radon from C to D is due to mixed gas transported from the northern direction. This increase in RaA, RaB and F factor from C to D is partly due to the "old" decaying radon and the mixed gas from the northern direction.

From table 5.17, the largest estimated relative uncertainty of RaA (70%) and F factor (32%) were obtained at point C. High RaA uncertainty at low concentrations contributed to the elevated F factor uncertainty.

#### 5.5.2.2 Set 2 (26-08-2017: Upwind morning)

Figure 5.25 depicts sampling positions measured against the direction of the wind (upwind). The starting point (point A) was the point closest to the tailings moving up. Measurements were taken upwind from point A (27$^0$49'46"S 26$^0$40'15" E) to point B (27$^0$49'43"S 26$^0$40'18" E), point C (27$^0$49'40"S 26$^0$40'19" E) and point D (27$^0$49'36"S 26$^0$40'21" E) in that order.

Table 5.18 and table 5.19 show the predicted and measured results for set 2 morning activities and F factor in the upwind direction respectively. The predicted results are calculated based on the initial

concentrations (measured at point A) and the time the radon gas has been in air.

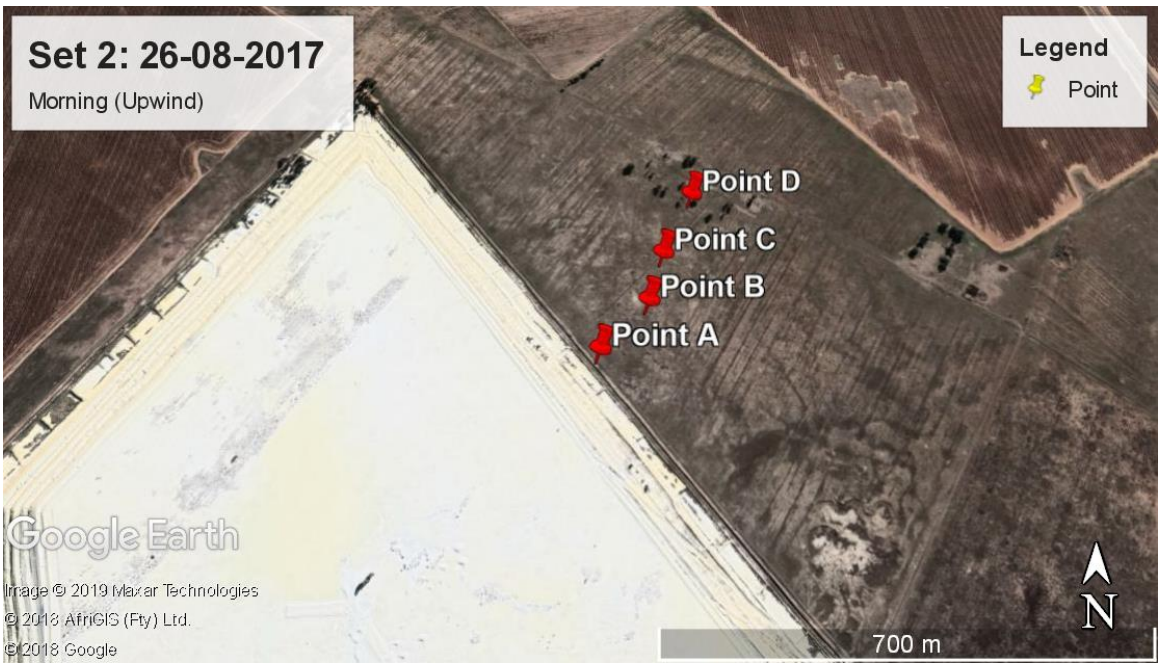


**Figure 5.25: Illustration of sampling positions measured against the direction of the wind (upwind) (Set 2, morning).**

*Table 5.19: Predicted concentrations for radon, RaA, RaB and the F factor for the morning upwind set 1 measurements at various distances from the tailings*

| Distance (m) | time (s) | RaA (Bq/m³) | RaB (Bq/m³) | RaC (Bq/m³) | Rn (Bq/m³) | F factor |
|---|---|---|---|---|---|---|
| 0 (Point A) | 0 | 5.281 | 0.982 | 0 | 3.800 | 0.279 |
| 123.8 (Point B) | 13 | 5.212 | 1.005 | 0.007 | 3.799 | 0.281 |
| 219.7 (Point C) | 3000 | 3.778 | 3.071 | 2.133 | 3.776 | 0.738 |
| 354.0 (Point D) | 3240 | 3.753 | 3.591 | 3.268 | 3.750 | 0.929 |

*Table 5.20: Measured concentrations for radon, RaA, RaB and the F factor for the morning upwind set 1 measurements at various distances from the tailings*

| Distance (m) | RaA (Bq/m³) | RaB (Bq/m³) | Rn (Bq/m³) | F factor |
|---|---|---|---|---|
| 0 (Point A) | 5.28±1.33 | 0.98±0.26 | 3.80±0.14 | 0.280±0.073 |
| 123.8 (Point B) | 5.01±1.31 | 0.93±0.26 | 8.44±0.21 | 0.119±0.032 |
| 219.7 (Point B) | 3.19±1.09 | 1.51±0.27 | 6.91±0.19 | 0.161±0.037 |
| 354.0 (Point B) | 4.99±1.27 | 0.24±0.25 | 1.48±0.09 | 0.438±0.180 |

Figure 5.26 show the variation of measured radon concentration, radon daughter concentration and F factor with distance from the tailing (set 2 upwind). The average wind speeds ranged from 6.2 m/s at point D to the highest value of 9.9 m/s at point A. Point B and C both recorded wind speed of 8.3 m/s.

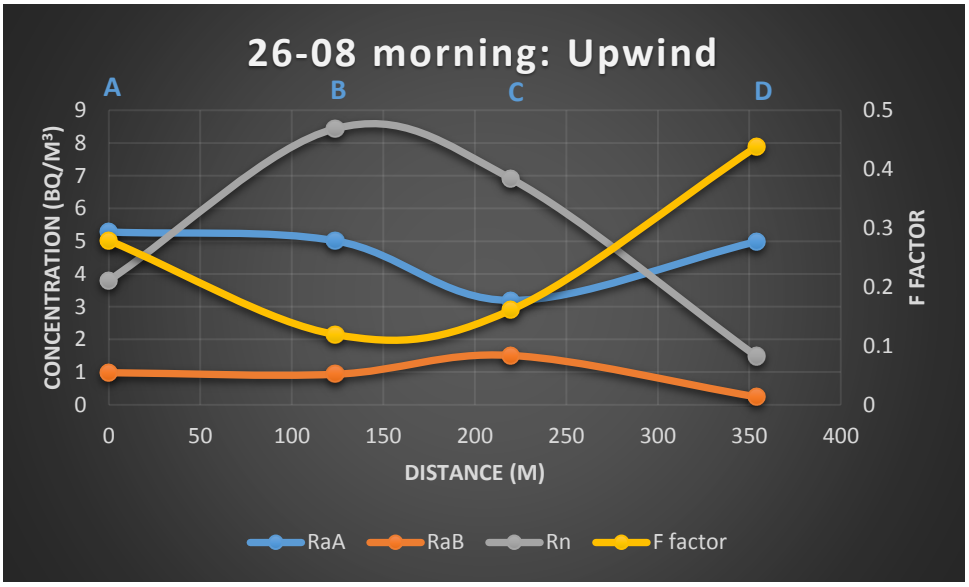


**Figure 5.26: Variation of measured radon concentration, radon daughter concentration and F factor with distance from the tailing (Set 2 upwind).**

As can be seen from figure 5.26, the concentration of RaA is higher than that of radon by a factor of 1.4 and RaB by a factor of 5.4. The gas is relatively “old” and mixed due to strong atmospheric mixing from high wind speed at A. From A to B, the radon increased by 122.1%, RaA and RaB showed slight decrease by 5.1% and 4.9% respectively. On the other hand the F factor decreased by 57.2%. The decrease in wind speed from 9.9 mms at point A to 8.3 m/s at point B reduced the dilution factor, thus increasing the radon concentration at B. RaA and RaB followed the normal decay with time as corroborated by the predicted measurements in table 5.18.

The radon gas decreased from B to C and continue to decreases to point D. The F factor increased from B to C and continued to increase and attain the highest value at point D. The presence of high RaA and high F factor at point D is an indication that the gas is “old”, with no mixing with the “young” air from the background.

Table 5.19 shows almost consistent relative uncertainty values throughout for RaA. On the other hand RaB show greater variation at point D with 102% relative uncertainty due to low activity of 0.24 Bq/m$^3$. In addition, the AlphaGUARD measured the lowest radon activity (1.48 ± 0.09 Bq/m$^3$) at point D with relative uncertainty of 33%. This contributed to larger relative uncertainty in the F factor of 59.5% compared to other measuring points.

#### 5.5.2.3 Set 3 (27-08-2017: Upwind morning)

Figure 5.27 depicts sampling positions measured against the direction of the wind (upwind). The starting point (point A) was the point closest to the tailings moving up. Measurements were taken upwind from point A (27$^0$49'30"S 26$^0$39’56" E) to point B (27$^0$49'27"S 26$^0$39'54" E), point C (27$^0$49'26"S 26$^0$39'51" E) and point D (27$^0$49'25"S 26$^0$39'47" E) in that order.


**Figure 5.27: Illustration of sampling positions measured against the direction of the wind (upwind) (Set 3, afternoon).**

The average wind speeds range from the lowest value of 2.5 m/s at point D to the highest value of 3.4 m/s at point A. Point B and C recorded wind speeds of 2.9 m/s and 3.2 m/s respectively. The wind direction fluctuated between 254.4 (WNW) and 272.8 (WNW) at point A, 2.2 (N) and 271.9 (WNW) at point B, 262.4 (WSW) and 296.3 (WNW) at point C and 268.5 (WSW) an 325.2 (NNW) at point D. Table 5.20 and table 5.21 show the predicted and measured results for set 3 morning activities and F factor in the upwind direction respectively.

Figure 5.28 illustrates that at point A, high activity concentrations of both radon and RaA were observed. This simultaneous elevation in both radon and RaA activity concentrations is associated with low wind speed, positive temperature gradient, weak mixing and stable atmosphere. The presence of high RaA and RaB activities is an indication that the gas is “old” and is predominantly of local origin.

*Table 5.21: Predicted concentrations of radon, RaA, RaB and the F factor for the morning upwind Set 3 measurements at various distances from the tailings*

| Distance (m) | time (s) | RaA (Bq/m³) | RaB (Bq/m³) | RaC (Bq/m³) | Rn (Bq/m³) | F factor |
|---|---|---|---|---|---|---|
| 0 (Point A) | 0 | 5.085 | 0.601 | 0 | 7.000 | 0.121 |
| 106.5 (Point B) | 463 | 6.666 | 1.597 | 0.266 | 6.993 | 0.232 |
| 196.6 (Point C) | 2940 | 6.954 | 5.441 | 3.676 | 6.950 | 0.709 |
| 299.2 (Point D) | 2940 | 6.911 | 6.508 | 5.776 | 6.907 | 0.908 |

*Table 5.22: Measured concentrations of radon, RaA, RaB and the F factor for the morning upwind Set 3 measurements at various distances from the tailings*

| Distance (m) | RaA (Bq/m³) | RaB (Bq/m³) | Rn (Bq/m³) | F factor |
|---|---|---|---|---|
| 0 (Point A) | 5.08±1.19 | 0.60±0.22 | 7.00±0.19 | 0.121±0.034 |
| 107 (Point B) | 2.84±0.92 | 0.68±0.21 | 7.91±0.20 | 0.082±0.026 |
| 197 (Point C) | 0.84±0.68 | 0 | 5.69±0.17 | 0.016±0.012 |
| 299 (Point D) | 1.94±0.83 | 0.75±0.21 | 7.25±0.19 | 0.081±0.027 |

From point A to point B, the activity concentration of radon increased by 13.0 %, RaA decreased by 44.2% and RaB increased by 12.9%. The F factor dropped by 66.9%, thereby representing a decrease in activity of radon daughters. The winds speeds are moderately low at around 2.5 m/s, therefore the decrease in radon daughters is predominantly due to radioactive decay with increasing radon gas.

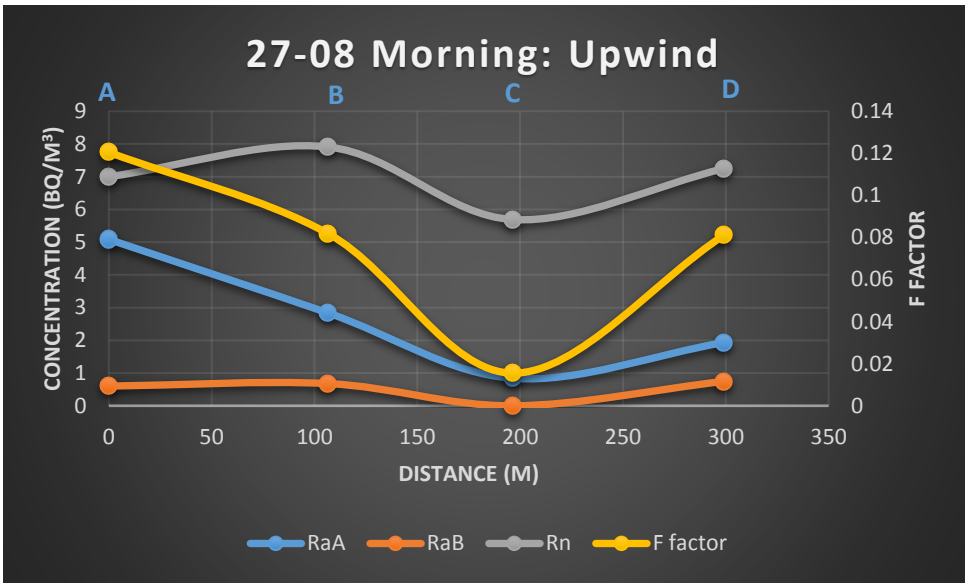


**Figure 5.28: Radon concentration (Rn), radon daughters' concentrations (RaA, RaB, RaC) and F factor as a function of distance from the tailing (Set 3, morning)**

From point B to point D, radon concentration first decreased by 28.1% at C, followed by a 27.4% increase at point D. Activity concentration of RaA decreased by 70.4% from B to C, then increased by 130.0% at D. The activity concentration of RaB at point C was 0 Bq/m$^3$. Therefore the air at C can be considered "young" with only RaA present. RaB increased from 0 Bq/m$^3$ at C to 0.75 ± 0.21 Bq/m$^3$ at D. The F factor decreased by 66.44% at point C due to the absence of RaB and RaC, with RaA as the only contributor. The ingrowth of RaB at point D increased the F factor by 422.4%.

There was no RaB and RaC at point C. Therefore the high RaA uncertainty at this point was the only contributor toward elevated uncertainty in the F factor value (80%) as depicted in table 5.21. The relative uncertainties in the measured radon concentrations by AlphaGUARD ranged from 14.9% at point B to 17.5% at point C.

## 5.6 Conclusion

The study demonstrated the effect of external meteorological effects on the distribution of radon and radon daughters some distance from the tailings and background. The results confirmed that activity concentrations of radon and its daughters do not remain constant even under same distances from a tailings or same wind speeds. Concentration changes by radioactive decay are overshadowed by other factors. Their magnitudes change with changing wind direction and local conditions of exhalation.

Looking at the downwind results, on average, the radon activity increased at distances ranging from 100 m to about 150 m from the base of the tailings at point A. This effect, depicted by a bump in figures 5.26 and 5.28, is consistent in all afternoon sets. If it can be replicated by the dispersion it will be proof that the radon measured is actually from the tailings, and can therefore be used as validation measurements.

The highest radon activity concentration around that area was 23.4 ± 0.34 Bq/m$^3$ recorded in the afternoon set. The highest radon increase was observed in set 6 from point A to point B by 162%. The predominant wind direction accompanying that increase was mainly from north-north-east (NNE). It can be thus be concluded that the main cause of radon deviation from the predicted values calculated using Bateman equations was due to other factors that appeared to be more prominent than radioactive decay. The F factor on average attained its highest value when the wind was blowing from NNE, while its lowest value and smallest change were obtained when the wind was blowing from WWN. The highest radon daughter concentrations which varied with location were recorded in the mornings.

On the upwind, the highest radon activity was 15.81 ± 0.28Bq/m$^3$ for the wind blowing from the northern direction at point D further away

from the dam, with the lowest value coming from the WNW. Overall, radon, radon progeny and the F factor decreased from point D (away from the tailings) to point A (closer to the tailings).

The observed fluctuations and conflicting effects which different meteorological conditions often have on the resultant atmospheric radon, radon daughters and F factor activities as functions of distance from the tailings downwind, made the interpretation of results difficult. Hence the need for dispersion calculation models to explain the results.

Uncertainty analysis for both F factor and concentrations of radon, RaA, RaB and in some instances RaC were carried out for each measurement described in the preceding sections in this chapter. The root sum of squares (RSS) method aims to be as inclusive as possible in terms of major sources of uncertainty that may have a large influence on the overall size of the uncertainty. Standard uncertainties, both Type A and Type B, were combined using the RSS method.

The results show that the magnitude of uncertainty of the AlphaGUARD for measuring radon activity was low and the instrument performed relatively well. Relative uncertainties of the AlphaGUARD ranged from 1.5% to 3.0%, with systematic uncertainties contributing between 9% and 18% of the total uncertainties per measurement and the remaining 82% to 91 % coming from random or statistical uncertainties. The major component of the systematic uncertainties was the instrument calibration error (type B) of 3%, whereas the statistical uncertainties emanated from the instrument's counting uncertainty.

The uncertainty of the individual radon decay products, the EEC and F factor measurements were calculated and reported on based on both Type A and Type B errors. The relative uncertainties for radon progeny measurements were relatively high at low activity concentrations, consistent with alpha particle counting at low environmental levels. Relative uncertainty for RaA ranged from 11% to up to 70%. RaB relative

uncertainties ranged from 6% to 151%. RaC concentrations were so low that they were mostly regarded as undetectable. For a RaC value of zero, the RaC error did not contribute to the relative uncertainty for both the EEC and F factor. It is inherent and unavoidable with environmental alpha counting to expect low alpha count rates in the low particle concentration environment.

Althought the F factor values presented with high error, the major conclusions about the validity of the dispersion model were drawn from the individual daughter concentrations, particularly RaA and RaB. From this perspective, the high errors in F values do not invalidate the positive agreement obtained.

# Chapter 6 Dispersion modelling

## 6.1 Introduction

Previous chapters presented a descriptive analysis of the data obtained from direct concentration measurements of radon and its decay products in outdoor air around the tailings dam. These measured concentrations are partly due to contributions from local processes like exhalation and diffusion. To quantitatively explain the measured radon and its daughters in chapter 5, a descriptive dispersion model that incorporates transport processes and weather data is essential. The dispersion model will serve as a link between different measurement points and provide a way to comprehend spatial variations and validate the model itself. The ISCST3 dispersion model, discussed in chapter 2, was used to study radon transport and local variation effects around the tailings dam.

This chapter provides a detailed account of data collection and formatting, data sources and data processing applied in ISCST3 dispersion modelling. Different raw data sets are transformed, manipulated and converted to compatible formats suitable for analysis. The model options parameters, followed by interpretation and analysis of the results are described in this chapter. Predicted results from ISCST3 modelling are compared with the measured observations. Finally, the model is validated by applying the "age" of the gas concept.

## 6.2 ISC-AERMOD input data information

There are five main categories of input data required by the ISC-AERMOD interface. These pathways are identified by a character pathway ID positioned at the beginning of each category. The model input categories and order are as follows:

- CO for identifying overall COntrol options pathway.
- SO for identifying SOurce/emission parameters information

- RE for identifying REceptor information.
- ME for identifying MEteorological conditions.
- OU for identifying OUtput options.

The application of these input data will vary depending on the type of source and model to be used. A summary of selected important modelling options used in this study for ISCST3 modelling runs are presented below for reference.

### 6.2.1 Control Options (CO) pathway

Control (CO) pathway is used to control the selection of modelling options as well as the operation of the ISC models. The following inputs were selected from the main control options:

- **ISC executable**: BREEZE, versions 02035 and 04269 (ISC-PRIME for wake effects)
- **Pollutant:** Radon
- **Half-life:** 328320 seconds
- **Elevated terrain:** Flat
- **Regulatory output options:** Concentration; Non-regulatory, rural
- **Receptor height:** 1.5 meters

### 6.2.2 Source/emission parameters (SO)

Source/emission parameters describe the release of emissions into the atmosphere. The types of air pollutant emission sources the model handles are commonly characterised as either point, area, open pit or volume sources. The input parameters vary depending on the source type. The main inputs from the source/emission options for this study were:

- **Number of Sources:** Multiple from all sides of the tailings dam and from external sources.

- **Output Contribution:** Combined pollutant concentrations from all sides and external contributor sources.
- **Type of Source:** Point (PRIME), Area and volume.
- **Height of Sources:** Varying from 0 (ground flat surface) to 30 meters (top of the dam).
- **Shape of Area:** Polygon.
- **Height of Tailings Dam:** 30 meters.
- **Emission Rates:** 0.102 $Bq.m^{-2}s^{-1}$, calculated in chapter 3 for area source. This value was corrected for discrepancies in side view area measurements from the modelling software and *Google Earth®*. The correction method and calculations are described in section 6.3.1.2 and the values of the corrected emission rates for area sources are given in appendix G.
- **Output:** $^{222}$Radon concentrations in $Bq/m^3$.

### 6.2.3 Meteorological data

Meteorological data required by the ISC short term model was used to simulate plume transport, rise, diffusion, deposition and dispersion. Five-minute weather data from 19–27 August 2017, for the Welkom – Odendaalsrus region was obtained from the South African Weather Service (SAWS) with anemometer height of 10 m. The ISCST3 has been programmed to accept hourly averaged meteorological data. As a result, the five-minute data was manipulated and averaged to hourly data suitable to be used in ISCST3 model.

The wind direction data required by the ISCST3 model uses the flow vector (direction is towards the direction of the wind) as input parameter while the wind direction data supplied by South African Weather Services (SAWS) is reported as the direction from where the wind is blowing. To correct this, the values of the wind direction were aligned and adjusted by $180^0$.

As per ISCST3 model format requirements, meteorological data files were processed and formatted as ASCII files in a form that can be read using FORTRAN format statements. Five input meteorological files for each day of measurement were prepared. A sample of the input meteorological ASCII file for day 1 (19-08-2017) is shown in table 6.1. The remaining daily meteorological input ASCII files are given in appendix D.

*Table 6.1: An input meteorological ASCII file*

```
 0364300    2017  0364300    2017
17 819 1 241.0000    5.5200 279.5 4  800.0  800.0
17 819 2 246.0000    5.6800 279.2 4  800.0  800.0
17 819 3 245.0000    5.5150 278.9 4  800.0  800.0
17 819 4 250.0000    4.9550 278.3 4  800.0  800.0
17 819 5 259.0000    4.3900 277.7 4  800.0  800.0
17 819 6 262.0000    4.2900 277.3 5  410.9  410.9
17 819 7 260.0000    4.1900 277.0 5  406.0  406.0
17 819 8 228.0000    2.6950 277.5 3 1000.0 1000.0
17 819 9 219.0000    2.9500 278.7 4  800.0  800.0
17 81910 223.0000    4.9500 280.8 4  800.0  800.0
17 81911 219.0000    5.2800 282.7 4  800.0  800.0
17 81912 207.0000    5.3350 284.9 4  800.0  800.0
17 81913 209.0000    5.0450 286.9 3 1000.0 1000.0
17 81914 211.0000    3.6300 288.9 1 1800.0 1800.0
17 81915 216.0000    2.7000 289.9 2 1400.0 1400.0
17 81916 228.0000    2.3600 290.4 2 1400.0 1400.0
17 81917 221.0000    2.5650 290.2 3 1000.0 1000.0
17 81918 221.0000    3.0050 289.3 5  343.9  343.9
17 81919 211.0000    3.0400 287.0 6  191.8  191.8
17 81920 221.0000    3.1300 284.8 6  194.7  194.7
17 81921 270.0000    2.9900 282.9 6  190.3  190.3
17 81922 264.0000    3.9450 282.6 5  394.0  394.0
17 81923 255.0000    5.9450 282.3 4  800.0  800.0
17 81924  55.0000    6.5250 282.0 5  506.7  506.7
```

From table 6.1, the station identification number and the year (0364300; 2017) are clearly marked as the first entries of the ASCII file and subsequent records are identically formatted to represent processed

hourly data for sampling and measurement durations. The required fields in each of these records are year, month, day, hour of day, wind direction (degrees), wind speed (meters per second), temperature (degrees Kelvin), atmospheric stability (A(1), B(2), C(3), D(4), E(5), F and G merged together (6)) and rural mixing height (meters). The vertical mixing heights were calculated from the Pasquil stability and wind speed values proposed by Clarke and Macdonald (1978). Conservative mixing heights corresponding to stability classes of 4, 3, 2 and 1 were used.

The meteorological wind roses covering the whole study domain are shown in figure 6.1 (a – e). Wind roses are graphical representations of the wind conditions of speed and conditions prevailing for Odendaalsrus area during the study period.

The area was characterised by the dominating average wind from the north, north-east and north-west during the winter months from June to August. The predominant directions were north-east for day 1 (100%) and day 4 (100%), north for day 2 (50%), and north-west for day 3(100%) and day 5 (90%).

Wind speeds for the area varied between 1.5 m/s (day 5) and 10.80 m/s (day 4) with calm periods (< 1.5 m/s) occurring for 10% of the time and wind speeds higher than 10.8 m/s occurring 11.1% of the time. The high wind speeds were mostly associated with winds from north-east whilst the low wind speed were associated with winds from north-west. Average daily minimum and maximum temperatures ranged from 9°C to 20°C during data collection period. There was no rainfall during this period.

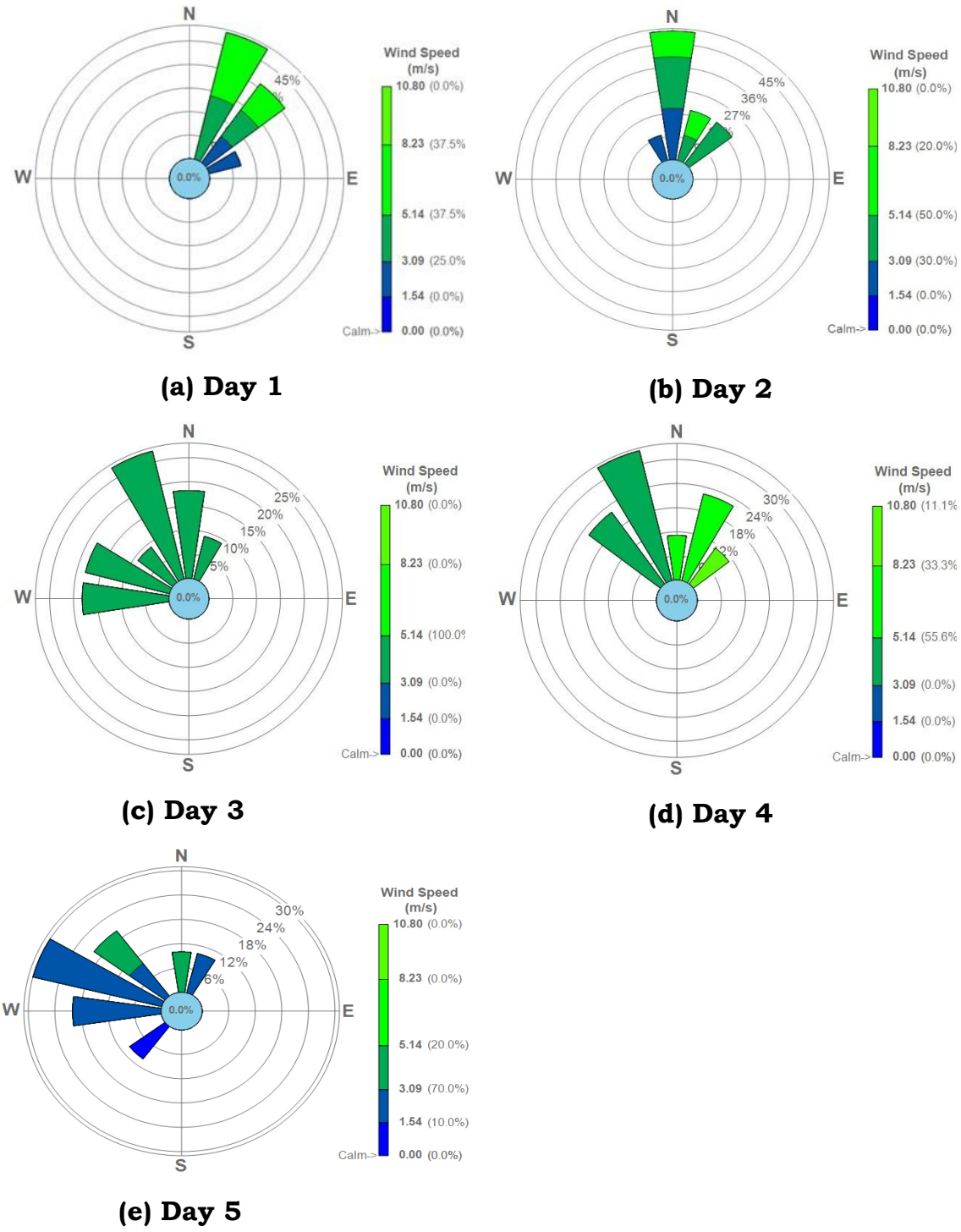


**Figure 6.1: Wind roses for the period 19 – 27 August 2017**

### 6.2.4 Receptor (RE) information

Discrete Cartesian Coordinates for 16 receptors at the height of 1.5 m above ground were used in the modelling. The receptor points for the

dispersion calculations were based on the coordinates of the points sampled during the “follow the wind” radon and daughter measurements described in chapter 5. Given that the multiple aerial and volume sources from the dam are not located at the same point, a Cartesian coordinate system in the ISCST3 model was chosen as the most convenient. The X and Y coordinates of the receptor were specified from the map view in the downwind direction.

### 6.2.5 Output (OU) options

The Output pathway in the ISCST3 defines the output format and options for the model runs. Hourly radon concentrations for each of the 16 receptors were generated through the 'POSTFILE' option in output specifications for ISCST3. The tabular output option, which presents the results in table format was selected. The model output predictions are due to specified source emissions from the tailings dam and does not include background concentrations.

## 6.3 Methodology

This study involved comprehensive validation of the ISCST3 model for predicting short-term radon concentrations in the ambient environment around an isolated tailings dam. All physical aspects of the source, including emission rates, dimensions, side areas, volume as well as geographical location were used as input data to the model. For the sake of accuracy, clarity and ease of modelling, the tailings dam was divided into five (5) sides and a top surface. These sides, which will be referred to in different modelling scenarios, are depicted in figure 6.2.


**Figure 6.2: Five (5) sides of the tailings dam**

### 6.3.1 Source/emission information

#### 6.3.1.1 Measurements of area and volume sources

Table 6.2 outlines different modelling approaches within the context of variables for volume and area sources (Schewe, Smith, 2009) applied in this study. The selection of these variables was based on the nature of the source (tailings) i.e. the size, geometry and the emission rate. Their choice was deemed the most representative of the source term.

*Table 6.2: Source characteristics used in ISCST3 volume or area source modelling (Schewe, Smith, 2009).*

| **Area Source** | **Volume Source** |
|---|---|
| Emissions in g/(s-m$^2$) | Emissions in g/s |
| Release height above ground | Release height – centre of volume |
| Length of x side | Initial lateral dimension ($\sigma_{yo}$) |
| Length of y side | Initial vertical dimension ($\sigma_{zo}$) |
| Orientation angle from north | |
| Initial vertical dimension ($\sigma_{zo}$) | |

The dimensions of the tailings (and hence the areas and volumes) were measured from the map view option of the ISCST3 source input. The image of the dam was downloaded from *Google Earth*® and saved as geo-referenced (JPG) image. The saved image was digitised, imported into ISCST3 and added to the Map view (GIS) of the ISCST3 as a base map.

Since the native raster image formats do not have internal geo-referencing information, it was necessary to specify image coordinates. This was done by choosing the south-west corner of the image and setting the image X and Y coordinates at that location as (0;0). The associated Easting X coordinate and Northing Y coordinate were both set at (0:0). To ensure that the image size corresponded to the scale of modelling domain within the BREEZE ISC, the distance scale was set by selecting any two points on the map and specifying the distance between those two points.

#### 6.3.1.2 Calculations of radon emission rates

All area and volume measurements used in the modelling were taken from *Google Earth*® and BREEZE software. These measurements assumed that the sides of the dam are smooth surfaces. But due to aging, coupled with years of erosion, the side surfaces of the dam have developed cracks and fissures, thus making them rough structures with grooves shown in figure 6.3. These gulleys and fissures represent a larger surface area than that projected area in which they occur. While the emission rates per unit surface area is probably the same, the larger surface implies a larger total emission from the side areas than from the flat top surface (Hasan, 2001).

To attain more accurate measurements of the side view surface areas, and to account for the effects of the cracks and grooves on the emission rates, two sets of representative measurements of length were taken on a two meter strip at each of the five sides of the dam. The first measurement was undertaken using a measuring tape over two meters. The second measurement was taken using a string, covering all the length of the surface, including the inside of the cracks up to the two meter point

measured with the tape. The average of the five string measurements from each of the five sides of the dam was calculated. The calculated average was used to correct all measured side view area values from *Google Earth*® and hence the emission rate. The measurements and the correction factors are given in table 6.3 below.

**Figure 6.3: The side view surface of the dam with cracks and fissures.**

*Table 6.3: Corrected side view surface measurements*

| Tailing Side | Tape length (m) | String length (m) | Correction factor (string/tape) |
|---|---|---|---|
| Side A | 2.00 | 2.45 | 1.23 |
| Side B | 2.00 | 2.48 | 1.24 |
| Side C | 2.00 | 2.54 | 1.27 |
| Side D | 2.00 | 2.63 | 1.32 |
| Side E | 2.00 | 2.47 | 1.24 |
| **Average** | **2.00** | **2.51** | **1.26** |

The source term for modelling is the emission rate (E), which in this case is the average radon flux of from the tailing measured in chapter 3 to

be 0.102 Bq/(m$^2$s). This value of the emission rate apply only to the top-view area sources. For side-view areas, the emission rates had to be corrected for the differences between the measured area (BREEZE) and the true areas (corrected terrain areas using *Google Earth®*) as explained and calculated table 6.3. The corrected emission rates were calculated using the relation:

$$E\ (corrected) = E\ (measured)\ \text{x}\ \frac{True\ area(terrain)}{Measured\ area\ (BREEZE)} \qquad (6.1)$$

The corrected emission rates for area sources are given in Appendix G.

### 6.3.2 Background Concentration

There are two contributors to the ambient radon concentration downwind of the tailings dam: radon contributed directly by the tailings dam and the background radon. These contributors should be separately accounted for in dispersion modelling. The ISCST3 modelling accounts solely for radon concentrations in the air that are due to emissions from the tailings dam. Therefore the predicted radon concentrations must be added to the background radon to obtain total radon concentration at a receptor site. The background concentrations account for contributions from natural sources, nearby sources and other unidentified sources excluded in the modelled inventory. Only then can the predicted and observed concentrations be appropriately compared.

The background concentrations were taken as the radon concentrations measured “upwind” to the tailings dam along the same line and wind direction as the “downward” modelling direction. A $\pm 10^0$ wind variation was allowed since there is no substantial concentration change within this degree range (Venkatram et al., 2004). These background concentrations were added to the modelled concentrations at each receptor location after accounting for the radioactive decay of the upwind radon (half-life of 3.82 days) (Andretta et al., 2006). The radioactive correction

was carried out by considering the duration required for radon to travel from the upwind edge of the source to the receptor location. This time was estimated by dividing the distance between the source and the receptor by the average wind speed.

By considering only radioactive decay, the corrected radon concentration at the receptor location, was approximated as:

$$C_{corrected} = C_{upwind} \text{ x } e^{-\lambda t} \quad (6.2)$$

where:

λ: radioactive decay constant of radon (2.1 x $10^{-6}$ s); and

t: the time taken for the radon to travel from the source to the receptor.

### 6.3.3 Modeling Scenarios and Analysis

Following the inconclusive results of the "follow the wind" approach in chapter 5, it was considered important to apply modelling techniques by taking into account the sensitivity of the source term to modelling. A series of modelling scenarios were undertaken using the ISCST3 for non-point sources (area and volume sources) and ISCST3-PRIME for virtual point sources (to account for building wake effect). The results from different scenarios were compared. Predicted concentrations were calculated for 1 hour averaging periods.

This study postulated that emissions from the total surface area of the dam, from all source areas in their true positions, should be the most realistic and the most accurate modelling option. However, a number of other geometries have been used in literature, and each may produce a different result. These different geometry scenarios were studied. The basic source term settings and modelling approaches that were applied to predict ambient radon concentrations are described below.

#### 6.3.3.1 Scenario 1: Total radon emitting surface area (True Geometry)

In this scenario, the tailings dam was modelled as an area source by taking into consideration the total surface area of the dam. This was to determine the effect of running an ISCST3 model for all the area sides of the dam as the total contributing source as opposed to the commonly used approach of ground-level flat area. The total geometry and dimensions of the dam were accounted for, including the slopes on the sides ($35^0$), the height (30 m), the top surface layer and cracks, gulleys and fissures on the side walls of the dam.

The ISCST3 model allows for modelling irregularly-shaped areas by subdividing the area into smaller areas of varying shapes, sizes, and orientations. The source inputs were inserted in the map view of the ICS after importing the image as describe in section 6.3.1 above. To model the dam as accurately as possible, the dam was further sub-divided into multiple areas, accounting for different dimensional variations at each side area. Each of the five sides of the dam was divided into 10 area segments, namely five top view and five side view in accordance with the design of the dam. This is illustrated in figure 6.4. The areas of each segment depicted in figures 6.4 and 6.5 were carefully measured as polygon areas in the model objects option of the ISCST3.

The emission heights varied from 0 m at ground level to 30 m at the top of the dam, depending on the area segment. A total of 51 area sources, comprising the sum of all the areas of each segment, including the top side of the dam, were used as source inputs in the model. A map view of the total area source, including all sides from the ISCST3 is shown in figure 6.6. The source terms, areas and corresponding heights are given in an extract ISCST3 model report file in appendix H.

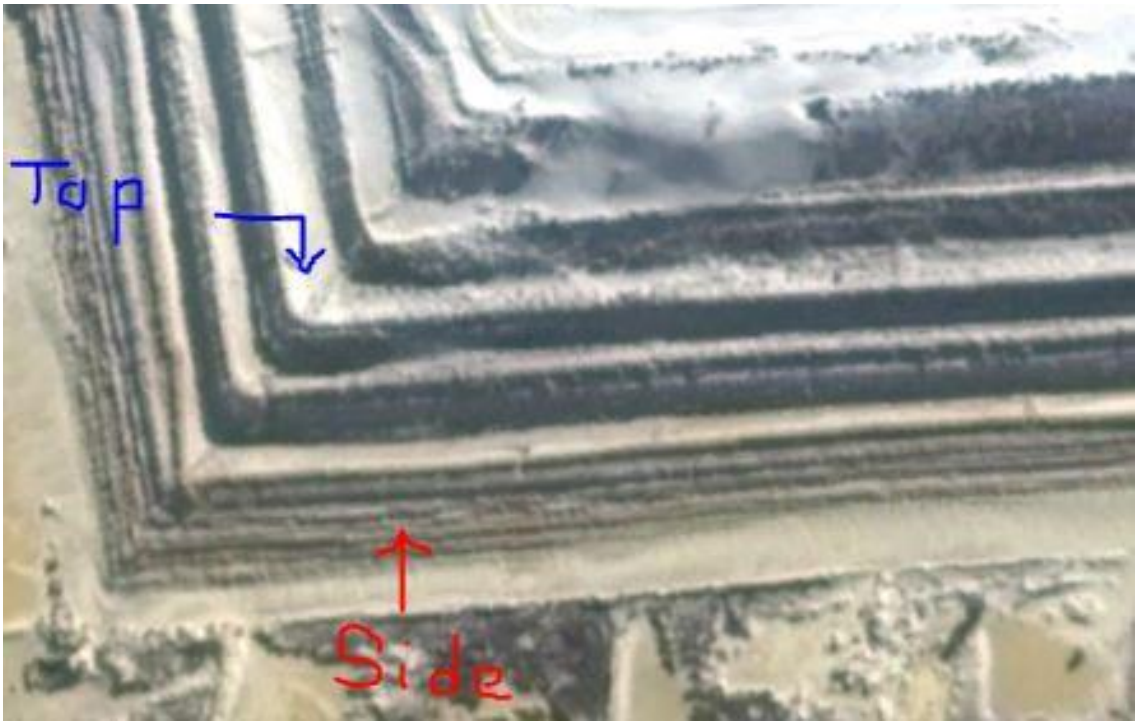


**Figure 6.4: A close up view of the segments of the side of the dam.**


**Figure 6.5: Measurements of each segment as polygon area for each of the 5 sides.**


**Figure 6.6: A map view of the total area source from ISCST3.**

### 6.3.3.2 Sensitivity analysis: total radon emitting surface area

A sensitivity analysis was performed to establish the impact of individual sides of the dam towards incremental radon concentration at different discrete receptor points. The analysis was carried out by separately modelling radon contribution from each of the five sides of the tailings dam. For this purpose, two representative days (day 3 morning and day 4 afternoon) were selected to establish the extent of radon contribution by each side on the receptor point downwind. Each side was modelled as multiple area sources the same way described in scenario 1 above and their contributions compared. An example of the modelling protocol for day 3 (side A) is illustrated in figure 6.7. The same protocol was applied on the other individual sides. The results of individual sides as well as total area contributions are discussed in section 6.4.

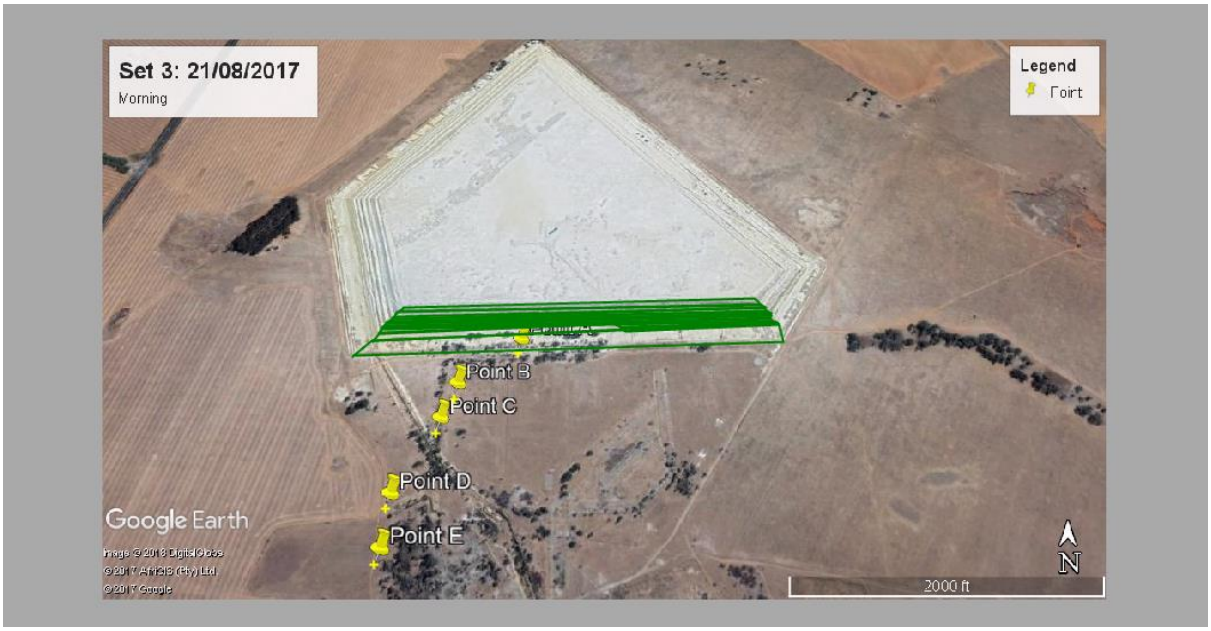


**Figure 6.7: Modelling protocol for day 3 (side A).**

### 6.3.3.3 Scenario 2: Ground level flat area source (flat terrain)

From literature review in chapter 2, most studies modelled radon by considering the tailings dam as a ground level flat area source. Figure 6.8 depicts the ground level flat surface area determined from the map view by tracing only the outline of the ground level surface.

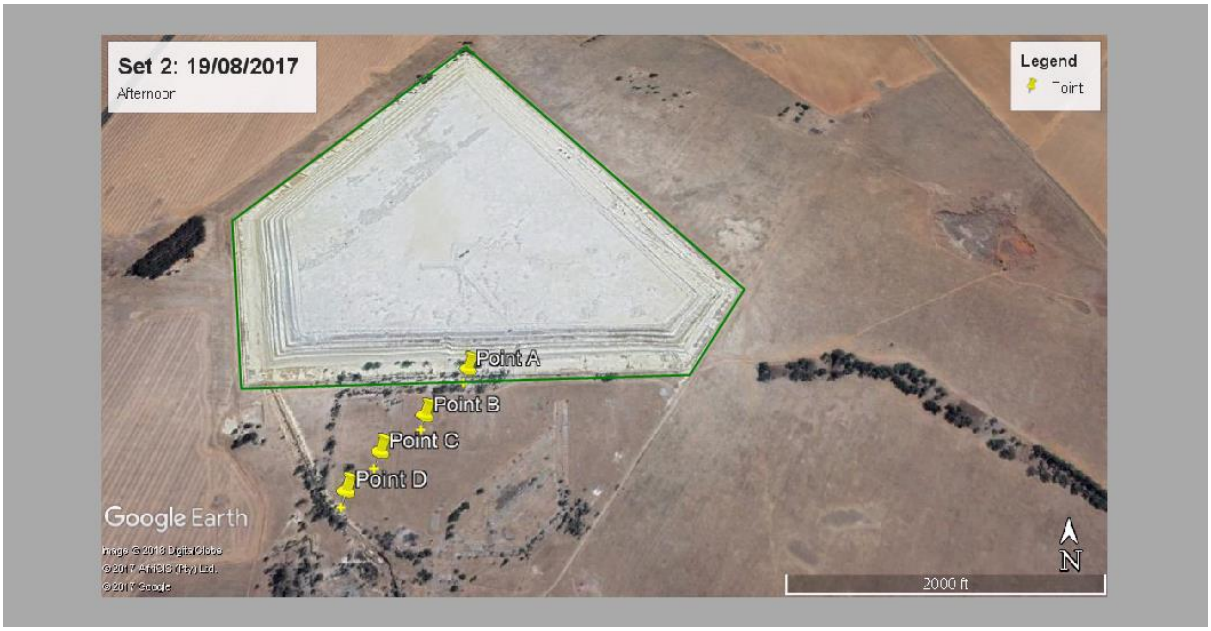


**Figure 6.8: Outline of the ground level surface.**

The area was automatically calculated by the ISC model and all other model input details were the same as in scenario 1.

#### 6.3.3.4 Scenario 3: Area source at the top of the dam

For the area source at the top of the dam, a similar approach to that described in scenario 2 above was applied. But in this case, the area source was considered to be the top area of the dam, which is 30 m above the ground as shown in figure 6.9. The area was modelled and calculated as a polygon area in the ISC source/emission parameters input mode.

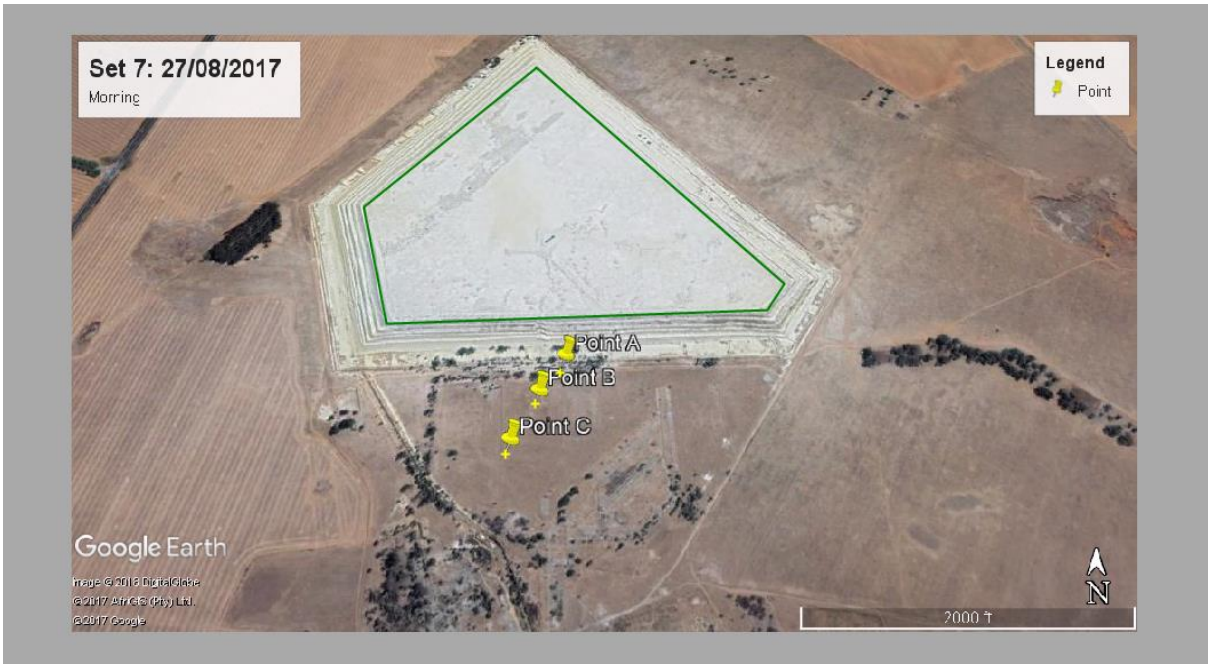


**Figure 6.9: Area source at the top of the dam.**

#### 6.3.3.5 Scenario 4: Volume source

Application of a volume source is common in modelling emissions escaping from buildings. To further evaluate the model, it was necessary to model the dam as a volume source as has been previously the case (van Vuuren et al., 1995, Strydom, 1999). The choice of the source input values

was to provide for the best source type representation as recommended in the ISCST3 User's Guide (U.S. EPA, 1995b, U.S. EPA, 1995a).

To comply with the ISCST3 modelling inputs stipulations, the ground-level flat area of the dam measured from *Google Earth*® was considered as the base area of the dam and was found to be 1.08E8 $m^2$. For ease of calculations, this ground base area was assumed to be a square. Because of the large size of the dam, the base area was subdivided into four (4) equal and smaller cubic volume sources. Each cube had a base area of 2.69E3 $m^2$.

As per ISCST3 model source input specifications, the emission rate for any volume source is given in grams per second (g/s). The conversion from Bq/($m^2$s) to g/($m^2$.s) in the flux input has been explained in section 2.8.3.2. For each of the four volume cubic sources, the emission rate was calculated from the exhalation flux and the base area relation:

$$Emission\ rate\ \left(\frac{g}{s}\right) = flux\left(\frac{g}{m^2 s}\right)\ x\ area\ of\ volume\ one\ cube\ (m^2) \qquad (6.3)$$

$$= 0.102\ \left(\frac{\mathrm{g}}{\mathrm{m^2 s}}\right)\ \mathrm{x}\ 269\ 490.77\ \mathrm{m^2}$$

$$= 2.86\ \mathrm{x}\ 10^4\ \mathrm{g/s}$$

The width of the tailings was taken as the minimum dimension of the tailings in order to avoid the bulk of the material being captured in the tailings wake. In this case, a virtual source is created by the model such that the emissions are released at half the height of the building (Bluett et al., 2004). Given that the height of the dam is 30 m, the initial release height was taken as the centre of the volume given by 30 m / 2 = 15 m.

#### 6.3.3.6 Scenario 5: Accounting for wake effects

Modelling point sources using the ISCST3 requires several input parameters that are not mandatory in modelling area or volume sources.

The virtual point source method proposed by (Turner, 1970) was used to model the wakes effect. This method estimated the impact of area sources by simulating the pollutant plume downwind from an area source as if it originated from a point source. The area source of the dam is replaced by a virtual point of equal total strength as the area source. To account for the initial dimensions of the source, the virtual point source is located at some calculated distance upwind (called virtual distance) of the actual area source position. The lateral spread of the plume from the virtual point was considered in such a way that it is comparable to the width of the area source. This is depicted in figure 2.14 in chapter 2 literature review.

The emission rates of the area sources are expressed in terms of activity or mass flux per unit area. Therefore the virtual point sources were adjusted accordingly as required by ISCST3 and set equal to those of area sources by applying equation (6.3). The recalculated point source emission rates for the five sides are given in table 6.4. The areas were measured from *Google Earth*® and the area flux was calculated in chapter 3.

*Table 6.4: Virtual point sources emission rates for each side of the tailings*

| **Side** | **Area Flux (Bq/(m².s))** | **Area (Google Earth) (m²)** | **Virtual point emission rate (Bq/s)** |
|---|---|---|---|
| A | 0.102 | 1.20E4 | 1.22E4 |
| B | 0.102 | 2.18E4 | 2.23E3 |
| C | 0.102 | 1.28E5 | 1.30E4 |
| D | 0.102 | 1.07E5 | 1.09E4 |
| E | 0.102 | 7.04E4 | 7.15E3 |

In addition to emission rate (Bq/s), the following input parameters were incorporated for virtual point modelling: temperature (0 K), exit velocity (varied) (m/s), stack height (1 m) and diameter (1 m). It should be pointed out that in the case where the emission temperature is same as the ambient temperature in the meteorological data file, as when the tailing stack is discharging air at the same temperature as the atmosphere, it is

required that the emission temperature be set to 0 K in the ISCST3, as this defaults the model to use the ambient temperature, hence the incorporated temperature input parameter of 0 K.

The equation used to calculate the lateral virtual distance in kilometres for the rural mode is given by (U.S. EPA, 1995b):

$$x_y = \left(\frac{\sigma_{y0}}{p}\right)^{\frac{1}{q}} \tag{6.4}$$

where p and q are the Pasquil stability dependent coefficients obtained from table 6.5 and $\sigma_{y0}$ is the standard deviation of the lateral concentration distribution at the source in meters.

*Table 6.5: Pasquil stability dependent coefficients*

| ***Pasquill Stability Category*** | ***p*** | ***q*** |
|---|---|---|
| A (1) | 209 | 0.89 |
| B (2) | 155 | 0.90 |
| C (3) | 103 | 0.92 |
| D (4) | 68 | 0.92 |
| E (5) | 51 | 0.92 |
| F (6) | 34 | 0.92 |

For surface based area sources, the initial standard deviation of the lateral concentration distribution $\sigma_{y0}$ was calculated by dividing the length of the side of the source S (m) by 4.3 (U.S. EPA, 1998):

$$\sigma_{y0} = \frac{S}{4.3} \tag{6.5}$$

Five sides of the tailings dam were individually modelled for wake effects. For each side, virtual points and distances were calculated from equation (6.4) and table 6.6.

The areas measured in table 6.4 were assumed to be square shaped as required by the ISCST3. The lengths of each side (S) and $\sigma_{y0}$ were found

by computing the square root of the area followed by the application of equation (6.5). The results are given in table 6.6 below for each side of the tailings dam.

*Table 6.6: Lengths of each side (S) and $\sigma_{y0}$*

| **Side** | **S (m)** | **$\sigma_{y0}$ (m)** |
|---|---|---|
| A | 346 | 81 |
| B | 148 | 34 |
| C | 357 | 83 |
| D | 328 | 76 |
| E | 265 | 62 |

The emission heights were calculated based on the height and the perimeter of the dam as proposed by (U.S. EPA, 1995b). For ground based virtual point sources, the emission height was calculated from the equation (U.S. EPA, 1995b):

$$\text{Emission height} = 2.5 \times \text{height of the dam} \quad (6.6)$$

$$= 2.5 \times 30 \text{ m}$$

$$= 75 \text{ m}$$

For virtual point sources that are within the perimeter of the dam, the emission height was calculated as follows (U.S. EPA, 1995b):

$$\text{Emission height} = \text{height of the dam} / 2.15 \quad (6.7)$$

$$= (30 \text{ m}) / 2.15$$

$$= 14 \text{ m}$$

The lateral virtual distances and corresponding emission heights calculated for each side, day and hour are depicted in figures 6.10 – 6.14 and tables 6.7 – 6.11 for day 2 afternoon downwind run.

*Table 6.7: Day 2 side A: Lateral distances and emission heights*

| Hour | Pasquill Stability Category | $\sigma_{y0}$ (m) | $\sigma_{y0}$/p (m) | 1/q | $x_y$ (km) | $x_y$ (m) | Emission height (m) |
|---|---|---|---|---|---|---|---|
| 13 | 2 | 80.52 | 0.52 | 1.11 | 0.49 | 485.68 | 14 |
| 14 | 1 | 80.52 | 0.39 | 1.12 | 0.34 | 342.16 | 14 |
| 15 | 2 | 80.52 | 0.52 | 1.11 | 0.49 | 485.68 | 14 |
| 16 | 2 | 80.52 | 0.52 | 1.11 | 0.49 | 485.68 | 14 |

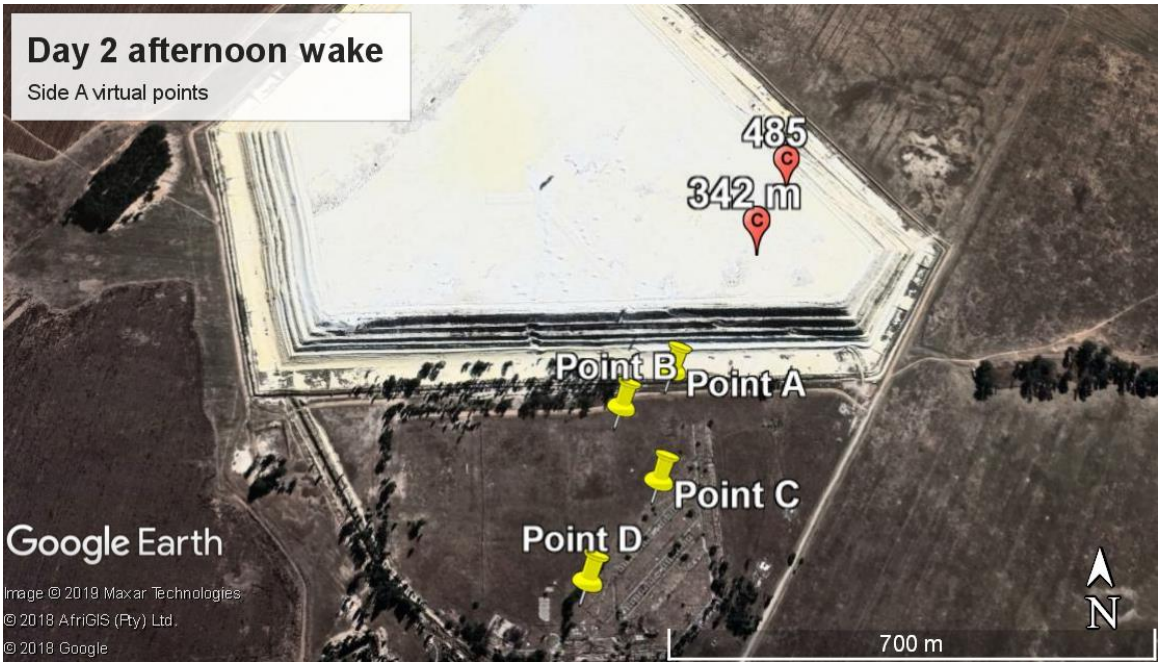


**Figure 6.10: Day 2 side A: Virtual point sources and receptors for wake modelling**

*Table 6.8: Day 2 side B: Lateral distances and emission heights*

| Hour | Pasquill Stability Category | $\sigma_{y0}$ (m) | $\sigma_{y0}/p$ (m) | 1/q | $x_y$ (km) | $x_y$ (m) | Emission height (m) |
|---|---|---|---|---|---|---|---|
| 13 | 2 | 34.36 | 0.22 | 1.11 | 0.19 | 188.94 | 75 |
| 14 | 1 | 34.36 | 0.16 | 1.12 | 0.13 | 131.42 | 75 |
| 15 | 2 | 34.36 | 0.22 | 1.11 | 0.19 | 188.94 | 75 |
| 16 | 2 | 34.36 | 0.22 | 1.11 | 0.19 | 188.94 | 75 |

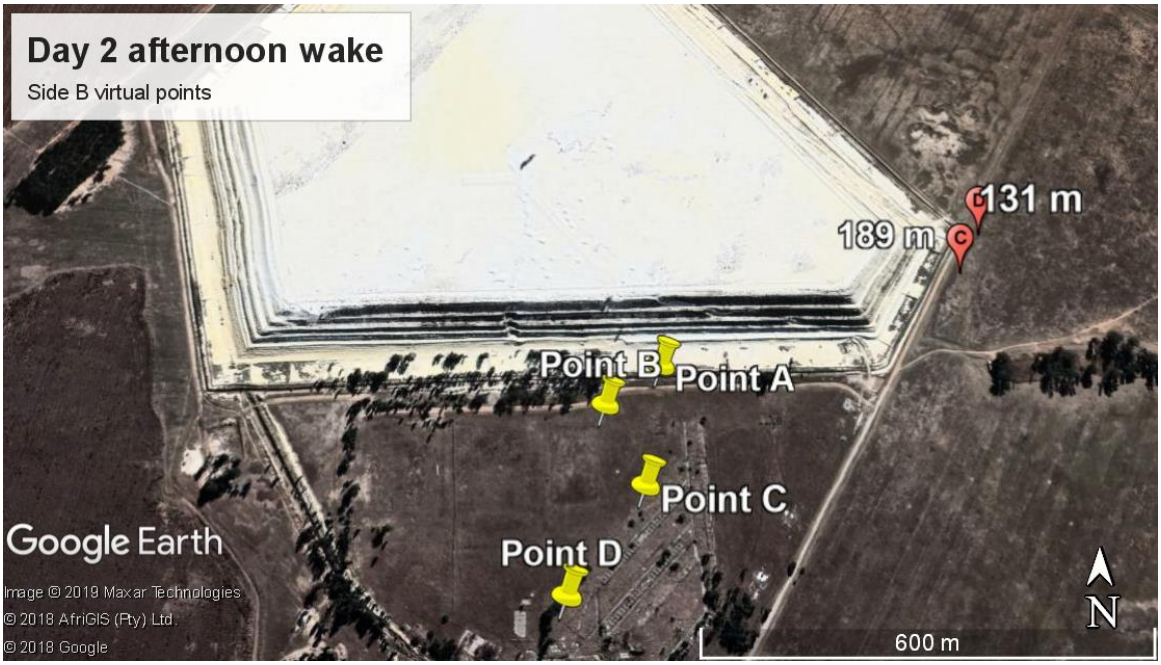


**Figure 6.11: Day 2 side B: Virtual point sources and receptors for wake modelling**

*Table 6.9: Day 2 side C: Lateral distances and emission heights*

| Hour | Pasquill Stability Category | $\sigma_{y0}$ | $\sigma_{y0}/p$ | 1/q | $x_y$ (km) | $x_y$ (m) | Emission height (m) |
|---|---|---|---|---|---|---|---|
| 13 | 2 | 83.04 | 0.54 | 1.11 | 0.50 | 502.56 | 75 |
| 14 | 1 | 83.04 | 0.40 | 1.12 | 0.35 | 354.22 | 75 |
| 15 | 2 | 83.04 | 0.54 | 1.11 | 0.50 | 502.56 | 75 |
| 16 | 2 | 83.04 | 0.54 | 1.11 | 0.50 | 502.56 | 75 |

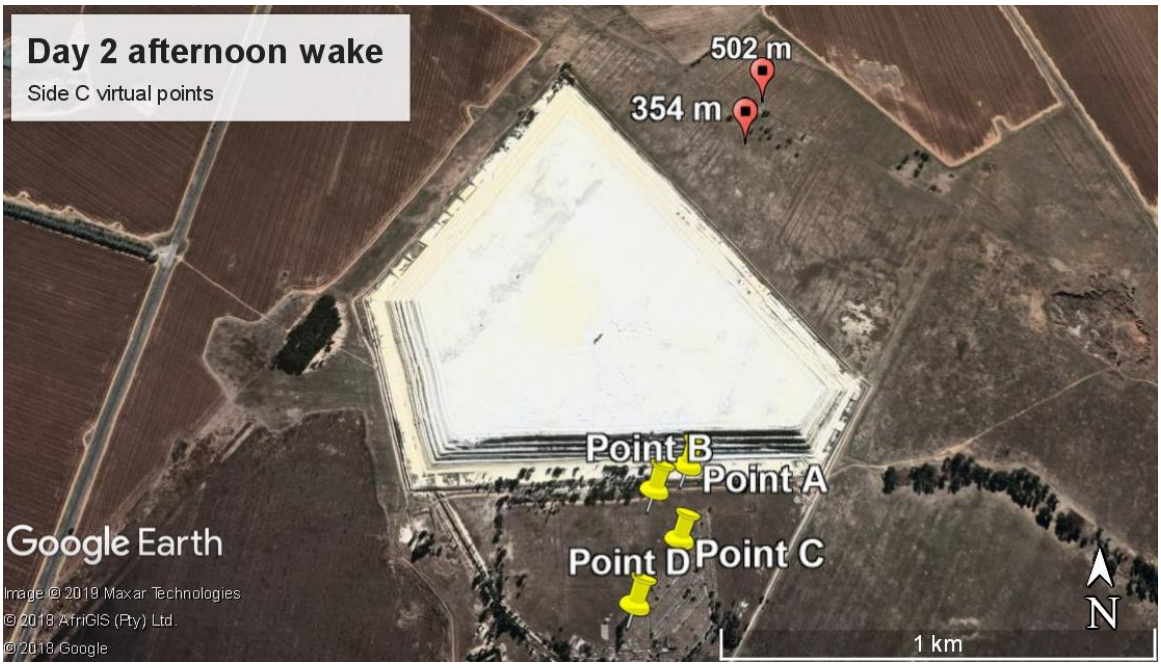


**Figure 6.12: Day 2 side C: Virtual point sources and receptors for wake modelling**

*Table 6.10: Day 2 side D: Lateral distances and emission heights*

| Hour | Pasquill Stability Category | $\sigma_{y0}$ | $\sigma_{y0}/p$ | 1/q | $x_y$ (km) | $x_y$ (m) | Emission height (m) |
|---|---|---|---|---|---|---|---|
| 13 | 2 | 76.22 | 0.49 | 1.11 | 0.46 | 457.01 | 75 |
| 14 | 1 | 76.22 | 0.36 | 1.12 | 0.32 | 321.70 | 75 |
| 15 | 2 | 76.22 | 0.49 | 1.11 | 0.46 | 457.01 | 75 |
| 16 | 2 | 76.22 | 0.49 | 1.11 | 0.46 | 457.01 | 75 |

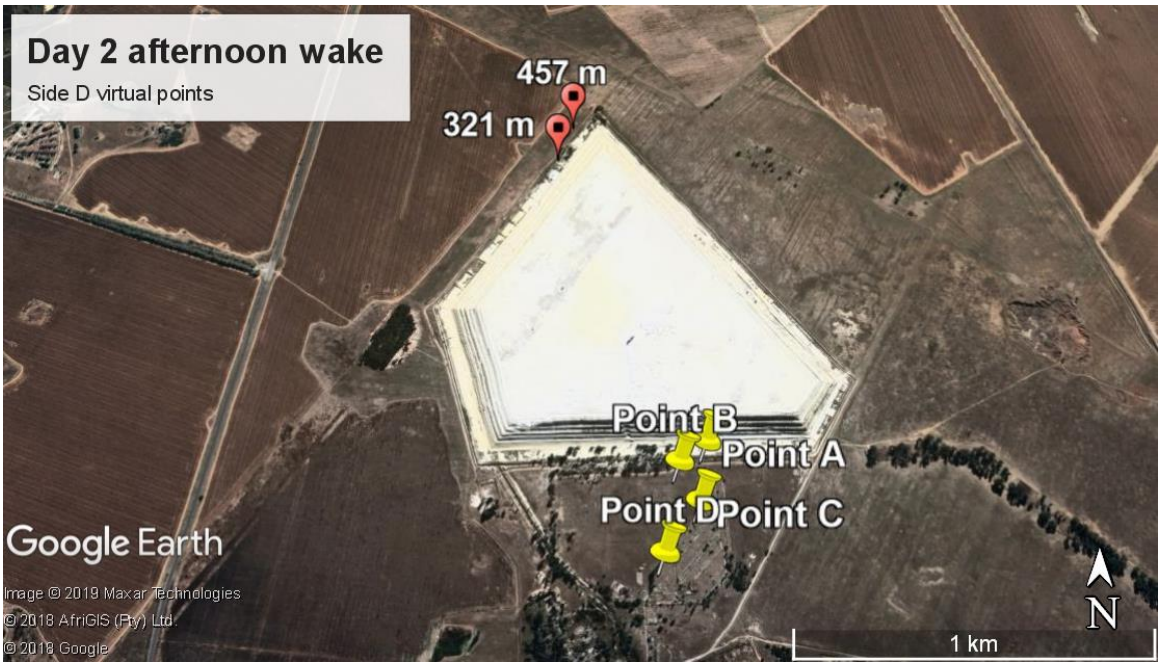


**Figure 6.13: Day 2 side D: Virtual point sources and receptors for wake modelling.**

*Table 6.11: Day 2 side E: Lateral distances and emission heights*

| Hour | Pasquill Stability Category | $\sigma_{y0}$ | $\sigma_{y0}/p$ | 1/q | $x_y$ (km) | $x_y$ (m) | Emission height (m) |
|---|---|---|---|---|---|---|---|
| 13 | 2 | 61.71 | 0.40 | 1.11 | 0.36 | 362 | 14 |
| 14 | 1 | 61.71 | 0.30 | 1.12 | 0.25 | 254 | 14 |
| 15 | 2 | 61.71 | 0.40 | 1.11 | 0.36 | 362 | 14 |
| 16 | 2 | 61.71 | 0.40 | 1.11 | 0.36 | 362 | 14 |

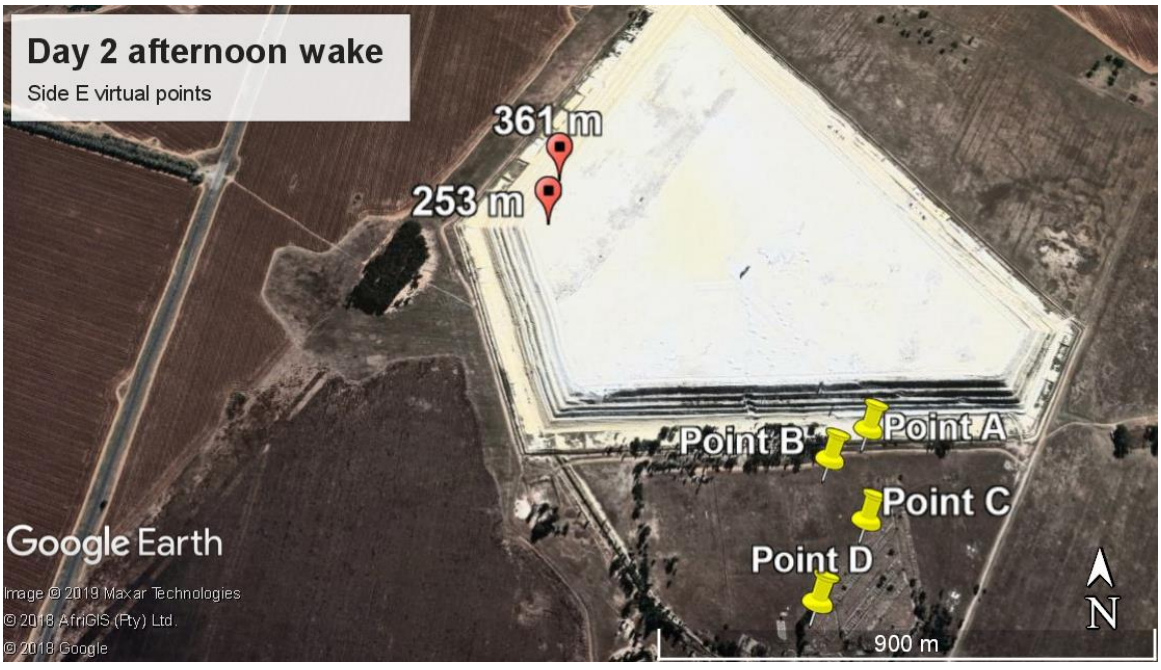


**Figure 6.14: Day 2 side E virtual point sources and receptors for wake modelling.**

### 6.3.4 Model validation - Statistical analysis

Model validation and correlation of model predictions with field measurements were computed using standard model validation statistics discussed in section 2.11. The validations were performed with respect to the four modelling scenarios described in section 6.4. The statistics used were index of agreement (*d*), Normalized Mean Square Error (NMSE), Geometric mean bias (MG), Fraction of predictions within a factor of two (FAC2) and Fractional Bias (FB) (see section 2.11.1).

### 6.3.5 Model validation - Source apportionment

The primary objective of this study is to apportion the source, i.e. identify the source as the main contributor to the measured radon to enable model validation. This will be achieved by isolating radon from other sources and calculating radon from the tailings dam measured at a particular receptor point using the dispersion model and "age" of the gas approach.

It has been established in chapter 2 that radon and radon daughters in the outdoor atmosphere are not in secular equilibrium. The F factor (or equilibrium factor) discussed in section 2.6.4 and 2.6.5 and their values calculated in chapter 5 were based on the ratio of the activity concentrations of the three short-lived radon daughters to the activity concentration of the parent radon gas. The F factor serves as an indication of the "age" of the gas after some time at some receptor.

To apportion the source by isolating radon from other sources, and to determine radon from the tailings dam using the model and "age" of the gas approach, a more direct and accurate method than F factor approach is suggested. This strategy involves calculating radon daughter activity concentration ratios as a means of determining the "age" of the gas. These ratios, together with modeled radon concentrations, will be used to prove

that the measured radon is from the tailings dam, thereby validating the model.

In chapter 5, it was discussed how hourly radon daughter concentrations and F factors were measured at different receptor points by following the wind direction ("follow the wind" approach). From the radon daughter measurements, RaA and RaB were dominant while the concentration of RaC was so low that it was mostly undetectable. It is therefore prudent that the comparative radon daughter to radon activity concentration ratios be limited to radon, RaA and RaB. Typical outdoor ratios for radon progeny concentrations are 0.8/1 for RaA/Rn; and 0.78/1 for RaB/Rn (Yamasaki et al., 1995) but this may not be applicable to the current scenario.

#### 6.3.5.1 "Age" of the gas approach – radon daughter to radon ratios

From the measured concentrations of radon, RaA and RaB in chapter 5, the RaA/Rn and RaB/Rn ratios were computed at all receptors. The radon travel time (time required for the measured daughter levels to grow in) from the tailings to the receptor was estimated from the calculated ratios and graph of the fractional activity of short lived radon daughters growing towards the radon level, plotted as a function of time. The graph was populated by normalising the pure radon concentration to an activity of 1 Bq/m$^3$ at time $t = 0$. The decay of radon and in-growth of radon daughters (RaA and RaB) after some time were calculated by applying Bateman equations. The normalised graph is shown in figure 6.15.

Using the activity ratios for both RaA and RaB from measured data, radon travel time from the source (tailings) to each receptor, or the "age" of the gas from the dam, was extrapolated from the graph in figure 6.10. The estimated times and the corresponding wind velocities from weather data, were subsequently used to calculate the backward distances from the receptor to the source.

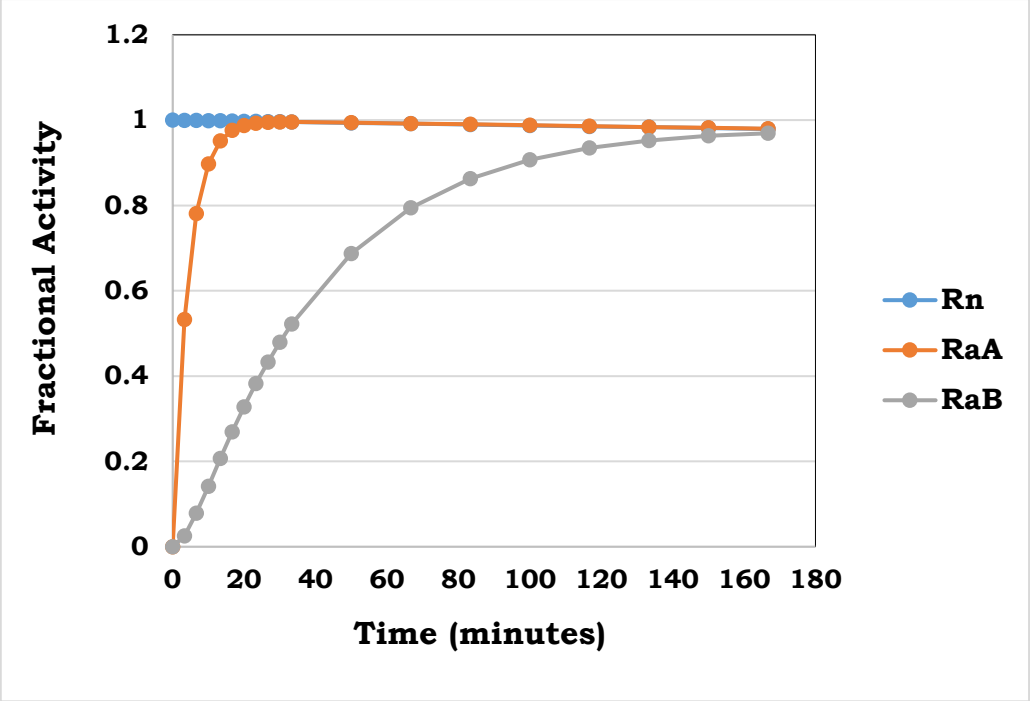


**Figure 6.15: Normalised in-growth of radon daughters' activities of an atmosphere initially containing pure $^{222}$Rn**

This method to establish source-receptor relationship and to trace back the origin of modeled and measured radon concentrations at the receptor, represents a kinematic back trajectory calculation of the air mass travelling from the tailings to the receptor, and was applied to estimate the distance from the source to the receptor. Similar work was reported by (Stohl, 1998).

Given the velocity ($v$, m/s) of radon from the tailings (wind velocity) and the transit step time ($\Delta t$) obtained from the graph in figure 6.10, the backward distance and hence the starting position, was calculated from the equation (Stohl, 1998):

$$X(t) = \Delta t \cdot v(t_0) \tag{6.8}$$

The application of equation (6.8) was based on the horizontal straight line distance traveled from the source to the receptor. Atmospheric turbulent mixing, meteorological parameters and vertical transport were not taken into consideration during the application of equation (6.8).

The use of a single back calculation for short range radon transport imposes the possibility of incurring uncertainties and errors. However, for short time scales, as is the case in this study, equation (6.8) can be considered to be sufficiently accurate (Stohl, 1998). Another consideration made during the application of this indirect radon detection approach using progeny is that during the sampling periods, weather conditions were calm with no air mass precipitation.

Each measuring point was treated independently, considering that the time difference between successive "follow the wind" measurements was about one hour. The calculated source points and distances from the receptor were populated on *Google Earth*® to locate their positions with respect to the tailings dam. The results were compared with the measured ones.

## 6.4 Results

### 6.4.1 Introduction

Dispersion modelling was carried out to simulate highest hourly average radon ground level concentrations from the tailings dam at different receptor locations. These averaging hourly periods were selected to facilitate the comparison of predicted radon concentrations with the measured concentrations by "follow the wind"' approach discussed in Chapter 5. Modeled concentrations from different modeling scenarios outlined in section 6.3 were quantified and compared. The sensitivity tests were performed with respect to the emission scenarios and model parameterisations. The only changes in model set up were the source parameters discussed in section 6.3. Other parameters taken from the original setup described in chapters 4 and 5 as well as section 6.3 were applied to all modeling calculations without change. Only point sources are affected by building downwash, as such, the wakes effect were evaluated with the enhanced ISCST3 version incorporating the PRIME algorithm.

The presented results highlight incremental radon contributions from contrasting source geometries. Modelled and measured concentrations for different source geometries at specified receptor points are tabulated and graphically presented. Discussions follow after the presentation of each subset of results.

Short term simulations are key to Gaussian models because of the model's assumption of steady state and homogeneous wind flow. It would therefore be befitting to conclude that the comparison of the predicted and observed 1-hour average radon concentrations presents a severe test for the performance of the model (Andretta et al., 2006).

### 6.4.2 Modeling scenarios – no wake effect

Table 6.12 presents comparative maximum 1-hour radon concentration results of three area source geometries and a volume source geometry predicted by the ISCST3 model from the tailings dam. The modeled results exclude contributions from other types of sources, wake effect and background concentration.

*Table 6.12: Modelled 1-hour ISCST3 Concentrations – No wakes and background*

| Date | Receptor point | Co-ordinates | Modelled Rn concentrations (Bq/m³) | | | |
|---|---|---|---|---|---|---|
| | | | True geometry | Flat ground-level area | Top level area | Volume Source |
| **19-08-2017 Morning** | | | | | | |
| **09:30** | A | 27⁰50'11"S 26⁰40'1" E | 0.51 | 1.10 | 0.07 | 0.39 |
| **11:12** | B | 27⁰50'16"S 26⁰39'57" E | 0.33 | 0.65 | 0.13 | 0.40 |
| **12:00** | C | 27⁰50'18"S 26⁰39'54" E | 0.33 | 0.57 | 0.15 | 0.43 |
| **Afternoon** | | | | | | |
| **13:32** | A | 27⁰50'11"S 26⁰40'4" E | 0.73 | 0.94 | 0.18 | 0.50 |
| **14:30** | B | 27⁰50'15"S 26⁰40'1" E | 0.42 | 0.36 | 0.084 | 0.23 |
| **15:26** | C | 27⁰50'18"S 26⁰39'58" E | 0.49 | 0.56 | 0.21 | 0.66 |
| **16:12** | D | 27⁰50'21"S 26⁰39'56" E | 0.47 | 0.54 | 0.12 | 0.40 |
| **20-08-2017 Afternoon** | | | | | | |
| **13:08** | A | 27⁰50'11"S 26⁰40'10" E | 0.53 | 0.68 | 0.12 | 0.51 |
| **13:54** | B | 27⁰50'13"S 26⁰40'7" E | 0.38 | 0.40 | 0.15 | 0.31 |
| **14:50** | C | 27⁰50'17"S 26⁰40'9" E | 0.44 | 0.47 | 0.22 | 0.54 |
| **15:49** | D | 27⁰50'22"S 26⁰40'5" E | 0.32 | 0.31 | 0.16 | 0.40 |
| **21-08-2017 Morning** | | | | | | |
| **07:39** | A | 27⁰50'11"S 26⁰40'0" E | 0.56 | 1.50 | 5.3E-2 | 0.79 |
| **08:35** | B | 27⁰50'15"S 26⁰39'56" E | 0.39 | 0.76 | 5.1E-2 | 0.94 |

| | | | | | | |
|---|---|---|---|---|---|---|
| **09:25** | C | 27°50'18"S 26°39'54" E | 0.35 | 0.60 | 6.5E-2 | 0.84 |
| **10:28** | D | 27°50'24"S 26°39'51" E | 1.1E-2 | 9.5E-3 | 5.4E-6 | 3.4E-2 |
| **11:14** | E | 27°50'28"S 26°39'51" E | 8.5E-5 | 6.8E-5 | 0 | 7.6E-3 |
| | | **Afternoon** | | | | |
| **13:00** | A | 27°50'10"S 26°40'22" E | 0.75 | 0.91 | 0.21 | 0.65 |
| **13:52** | B | 27°50'12"S 26°40'27" E | 0.62 | 0.57 | 0.14 | 0.51 |
| **15:24** | C | 27°50'15"S 26°40'35" E | 0.22 | 0.18 | 3.6E-2 | 0.22 |
| | | **26-08-2017 Afternoon** | | | | |
| **13:19** | A | 27°50'11"S 26°40'18" E | 0.41 | 0.55 | 0.10 | 0.48 |
| **14:12** | B | 27°50'15"S 26°40'20" E | 0.37 | 0.39 | 0.14 | 0.46 |
| **15:04** | C | 27°50'18"S 26°40'22" E | 0.41 | 0.46 | 0.20 | 0.71 |
| **16:04** | D | 27°50'22"S 26°40'26" E | 0.37 | 0.39 | 0.19 | 0.62 |
| | | **27-08-2017 morning** | | | | |
| **08:02** | A | 27°50'11"S 26°40'4" E | 0.79 | 1.90 | 4.9E-2 | 1.2 |
| **08:50** | B | 27°50'14"S 26°40'2" E | 0.55 | 0.81 | 0.20 | 0.85 |
| **09:43** | C | 27°50'18"S 26°40'0" E | 0.40 | 0.34 | 4.3 | 0.30 |

A closer look at table 6.12 reveal the sensitivity of the model to site specific data, particularly the source geometry and wind direction. In addition, the modelled concentrations close to the tailings dam (between 0 m – 150 m from the dam) are very sensitive to the height and definition (area or volume) of the source. Furthermore, very low radon modelled concentration values are obtained compared with measured values, which

indicates that the tailings dam is not the only contributing source of radon at the receptors.

As can be seen in the table, flat ground-level area source concentrations are the highest among the two other area sources and the volume source, whereas the top level area concentrations are the lowest of the four. These differences are expected and can be explained in terms of how the model treats each type of source.

The volume source utilises source dimensions to determine an initial lateral dimension of a virtual-point source plume at the emission point. This value (width of the source divided by 4.3) is a fraction of the actual measurements of the source. On the other hand, the ISCST3 integrates across the whole extent of the source to treat area sources, thereby giving the area source a much broader plume at the beginning of dispersion and transport. Besides, the ISCST3 models area sources as passive emissions, therefore concentrations at ground level are not subjected to the plume rise and exit velocity, the plume contacts the ground immediately after release. This explains the overall high radon concentrations for flat ground level sources compared to the other modelling source geometries, given that the receptor heights were set at near ground level height of 1.5 m.

Low concentrations from the elevated top level area source 30 m above the ground can be attributed to the certainty that the initial area source emissions at full height will be dispersed above the release height. In this instance, the impact of the plume is not realised on the ground near the tailings, but some distance downwind. At that point, the concentrations are significantly reduced relative to the exit concentrations because of meteorological influences and dilution factors as the plume moves further away from the tailings dam. The emission rates from the elevated top level source may be more or less equal to those of the flat ground level source, but their impact on the ground level receptor may be much lower (Theobald et al., 2012) as seen from the results in table 6.12.

Increasing the source height, decreases the concentration at or near the ground level (Stocker et al., 2016).

According to U.S. EPA (1995a) manual, volume sources are ideally suited for modelling different industrial sources like building roof monitors, whereas area sources are suited for ground or low level emissions with no plume rise. However, the EPA has left the choice of the specific method for different modelling scenarios to the discretion of the modeller.

The presented results in table 6.7 makes it difficult to compare and assess the effect of each modelling scenario on the receptors. To compare radon concentrations from different modelling scenarios and to establish their significance, modelled data were normalised and represented as a percentage of the baseline. The concentrations associated with modelling scenario 1 (true geometry) were taken as the baselines as per postulation. These baselines were chosen because this modelling scenario considers the total emitting surface area of the tailings dam as the source term and is regarded as the most accurate representation of the source term. Table 6.13 and figures 6.16 (a – g) provide tabulated and graphical comparisons of the ISCST3 results, emphasizing on the impact of different sources at the receptors.

As expected, results reported in table 6.13 reveals higher flat ground-level area source concentrations compared to other source terms. Relative to the baseline, 74% of the results from a total of 25 simulations for the flat ground source term, produced overestimated radon concentrations that are 1.04 – 2.74 times higher than the true geometry area source.

*Table 6.13: Normalised radon concentration comparisons of ISCST3 between baseline, flat ground area, top level area and volume sources*

| 19-08-2017 Morning | Distance (m) | Modelled Rn (% Baseline) | | | |
|---|---|---|---|---|---|
| | | True geometry area (Baseline) | Flat ground area | Top level area | Volume source |
| 09:30 | 0 (Point A) | 100.00 | 220.65 | 137.70 | 77.10 |
| 11:12 | 189.2 (Point B) | 100.00 | 198.73 | 39.24 | 121.32 |
| 12:00 | 291.8 (Point C) | 100.00 | 170.62 | 45.85 | 129.81 |
| **Afternoon** | | | | | |
| 13:32 | 0 (Point A) | 100.00 | 128.73 | 23.84 | 67.59 |
| 14:30 | 148.3 (Point B) | 100.00 | 85.16 | 19.92 | 54.83 |
| 15:26 | 272.0 (Point C) | 100.00 | 114.18 | 43.71 | 133.48 |
| 16:12 | 379.6 (Point D) | 100.00 | 114.67 | 24.66 | 85.71 |
| **20-08-2017 Afternoon** | | | | | |
| 13:08 | 0 (Point A) | 100.00 | 127.09 | 23.21 | 95.06 |
| 13:54 | 102.6 (Point B) | 100.00 | 105.64 | 39.50 | 80.08 |
| 14:50 | 237.7 (Point C) | 100.00 | 105.93 | 50.01 | 123.02 |
| 15:49 | 521.0 (Point D) | 100.00 | 96.34 | 50.61 | 124.57 |
| **21-08-2017 Morning** | | | | | |
| 07:39 | 0 (Point A) | 100.00 | 273.69 | 9.54 | 140.19 |
| 08:35 | 164.9 (Point B) | 100.00 | 197.43 | 13.15 | 243.94 |
| 09:25 | 272.5 (Point C) | 100.00 | 168.27 | 18.28 | 237.73 |

| | | | | | |
|---|---|---|---|---|---|
| 10:28 | 475.1 (Point D) | 100.00 | 83.31 | 0.05 | 301.37 |
| 11:14 | 598.6 (Point E) | 100.00 | 80.02 | 0.00 | 8.9E3 |
| **Afternoon** | | | | | |
| 13:00 | 0 (Point A) | 100.00 | 121.31 | 27.36 | 86.87 |
| 13:52 | 149.9 (Point B) | 100.00 | 91.34 | 22.23 | 81.28 |
| 15:24 | 392.5 (Point C) | 100.00 | 82.83 | 16.36 | 97.99 |
| **26-08-2017 Afternoon** | | | | | |
| 13:19 | 0 (Point A) | 100.00 | 132.17 | 25.11 | 115.39 |
| 14:12 | 135.1 (Point B) | 100.00 | 103.61 | 36.39 | 123.43 |
| 15:04 | 242.7 (Point C) | 100.00 | 113.34 | 48.90 | 173.56 |
| 16:04 | 407.6 (Point D) | 100.00 | 104.03 | 51.75 | 166.73 |
| **27-08-2017 Morning** | | | | | |
| 08:02 | 0 (Point A) | 100.00 | 240.36 | 6.18 | 158.92 |
| 08:50 | 107.6 (Point B) | 100.00 | 146.88 | 35.22 | 152.91 |
| 09:43 | 242.7 (Point C) | 100.00 | 85.26 | 10.70 | 76.03 |

The remaining 24% of the flat ground area source underestimated radon concentrations by factors of 0.83–0.96 compared to the true geometry area source.

The biggest overestimated difference of 2.73 higher than baseline, was obtained on day 3 (21-08-2017) morning at nearfield distance very close to the tailings. Coincidentally, the highest underestimated concentration of 0.83 times less than the baseline concentration was on the same day 3 afternoon at a distance of about 400 m from the tailings.

From table 6.13, it can be seen that flat ground-level area produced high estimations at distances close to the tailings, with the highest values observed in the mornings along the south-west wind direction. These phenomena associated with morning data can be primarily be attributed to radon gas stagnation and recirculation around the areas close to the tailings source. Stagnations reduce the air flow velocity or in some instances, stops the air movement altogether and in the process, increase ground concentration levels in the vicinity of the emitting source (Venegas, Mazzeo, 1999). This may also explain the high morning results measured near the source (see chapter 5 section 5.5.1.1 – 5.5.1.7), which showed not only high radon levels but also daughters. This condition is particularly prevalent during the calm morning conditions, when the temperatures and wind speeds are low. The observed highest overestimation is expected given that sampling occurred at the earliest time of the morning (7:39 am) compared to other sampling times, when the conditions for stagnation to occur were highly favourable. This led to higher radon concentrations on the ground, thus increasing the overestimation factor. Recirculation on the other hand, occurs when airborne radon is initially carried away from the tailings source, but return later to produce elevated radon concentrations near the source (Venegas, Mazzeo, 1999). Large recirculation values are observed during periods of strong turbulent mixing, higher wind speeds and increased temperatures (Venegas, Mazzeo, 1999). Therefore the recirculation process was mostly responsible for the high flat ground overestimation factor during the mid-morning and afternoon at receptors close to the tailings.

At the point of the highest underestimation for the flat ground source, the receptor is located along the south-east wind direction at 400m from the tailings. This region is characterised by low radon concentrations as has been observed in chapter 5. Furthermore, the point is beyond the recirculation zone and the afternoon conditions favoured strong mixing and vertical inversions. Hence the presence of low near ground concentrations around that area.

In general, elevated area sources produce lower concentrations at near-field ground level receptors (Turner, 1970, Zoumakis, 1998). This is corroborated by results from table 6.13 and figure 6.16 (a-g). The model underestimated the baseline (true geometry area) concentration by between 0.05% – 50.61%. Of note was that these underestimated results were consistent over all other modelling scenarios and source size domains described earlier in section 6.3.

Volume sources do not model plume rise and that may lead to over-estimation of ground-level concentrations at distances less than 0.5 km from the source. Hence volume sources generally will tend to predict higher concentrations than area and point sources. (Stocker et al., 2016).

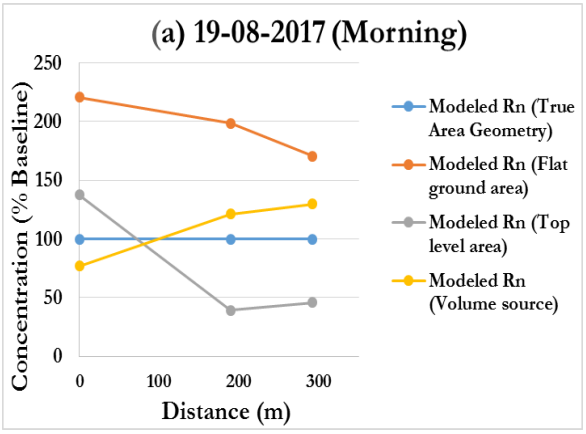


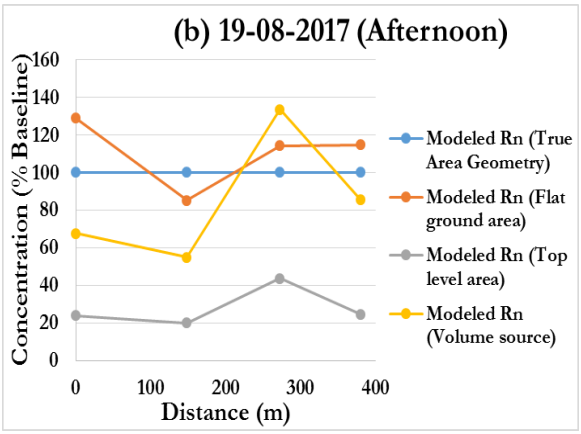


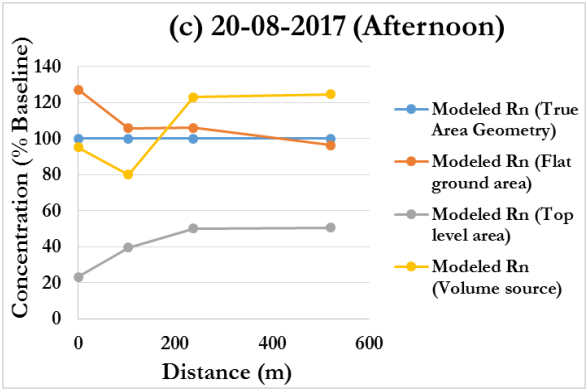


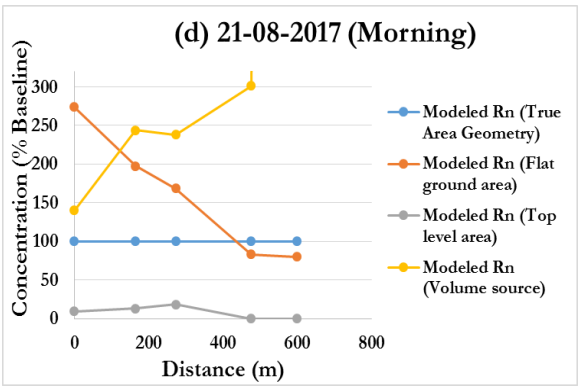

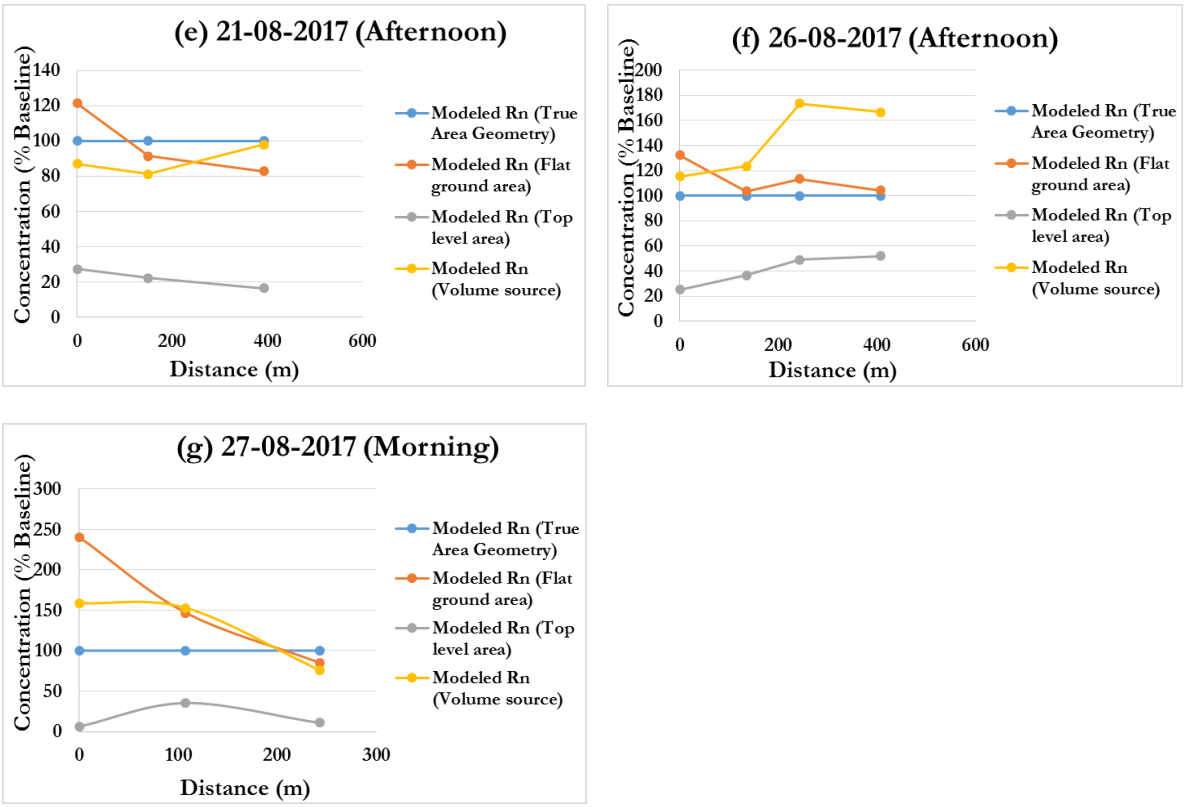


**Figure 6.16: Graphical comparisons of ISCST3 between baseline, flat ground area, top level area and volume sources**

As can be seen in table 6.13, the model over estimated volume concentrations for 60 % of the total runs. The biggest overestimated concentration difference was 3 times higher than the baseline concentration at a distance of 475.1 m from the source on day 3 morning. Conversely, the volume source results underestimated receptor concentrations for 40 % of the total runs, with the highest underestimated concentration of 0.55 times less than the baseline concentration at a distance of 148.3 m from the tailings dam on day 1 afternoon.

## 6.5 Sensitivity analysis: Individual side modelling

The contribution of each side of the dam towards the total radon concentration at the receptor point downwind is primarily a function of the downwind radon movement from the side to the receptor and the area emission rate. The concentration depends on the dilution, dispersion,

upwind meandering and advection. Modelled radon concentrations for day 3 and day 4 at each receptor point from each of the five sides are tabled in tables 6.14 and 6.16 respectively. Percentage contributions from each side toward the overall radon concentration at each receptor are given in tables 6.15 and 6.17 for day 3 and day 4 respectively.

- **Day 3 morning**

*Table 6.14: Individual side concentrations (day 3)*

| Receptor point | Co-ordinates | Side A (Bq/m³) | Side B (Bq/m³) | Side C (Bq/m³) | Side D (Bq/m³) | Side E (Bq/m³) | Total (Bq/m³) |
|---|---|---|---|---|---|---|---|
| A | 27⁰50'11"S 26⁰40'0" E | 0.41 | 0 | 8.6E-2 | 6.0E-4 | 0 | 0.46 |
| B | 27⁰50'15"S 26⁰39'56" E | 0.19 | 0 | 9.0E-5 | 0.11 | 0 | 0.30 |
| C | 27⁰50'18"S 26⁰39'54" E | 0.15 | 0 | 3.5E-4 | 0.10 | 0 | 0.25 |
| D | 27⁰50'24"S 26⁰39'51" E | 5.8E-4 | 0 | 0 | 2.9E-4 | 0.01 | 0.01 |
| E | 27⁰50'28"S 26⁰39'51" E | 1.4E-6 | 0 | 0 | 2.0E-6 | 8.1E-5 | 8.4E-5 |

Wind direction on day 3 morning varied with time between NNE and NNW. From receptor A to receptor E, the deviation angle between NNE (13.67⁰) and NNW (332.5⁰) was 41.17⁰ during sampling periods. Applying the "follow the wind" strategy under these conditions, it was revealed that the primary radon contributor was side A at all receptor points. As expected, radon concentration decreased with increasing distance from receptor A to receptor E.

*Table 6.15: Percentage contribution by each side (day 3)*

| Receptor point | Co-ordinates | Side A (%) | Side B (%) | Side C (%) | Side D (%) | Side E (%) | Total (%) |
|---|---|---|---|---|---|---|---|
| A | 27⁰50'11"S 26⁰40'0" E | 81 | 0 | 18.97 | 0.13 | 0 | 100 |
| B | 27⁰50'15"S 26⁰39'56" E | 64.7 | 0 | 0.03 | 35.27 | 0 | 100 |
| C | 27⁰50'18"S 26⁰39'54" E | 60.46 | 0 | 0.14 | 39.4 | 0 | 100 |
| D | 27⁰50'24"S 26⁰39'51" E | 5.24 | 0 | 0 | 2.62 | 92.14 | 100 |
| E | 27⁰50'28"S 26⁰39'51" E | 1.66 | 0 | 0 | 2.37 | 95.97 | 100 |

A closer look at each of the 5 receptor points in tables 6.14 and 6.15 show that only 3 sides contributed towards receptors A. B and C concentrations. There were no contributions from side B and side E at these three receptor points. At receptor A, the major contributor was side A (81%), followed by side C (18.97%) then side D (0.13%). At receptor B, the contribution of side A decreased from 81% recorded in receptor A to 64.7% whereas side D yielded the second highest contribution at 35.27 % with the least contributor being side C (0.03%). A similar pattern was observed for point C with major contributor side A (60.46%), followed by side D (39.4%) then side C (0.14%).

A different trend was observed at receptors D and E. The concentrations at these receptors were very low, with the main contributor being side E (92.14% and 95.97% for receptor D and E respectively). The second contributor for point D was side A with 5.24 % while for point E the second highest contributor was side D (2.37 %). The least contributors for points D and E were side D (2.62 %) and side A (1.66%) respectively. No contributions from side B and C were observed at receptor points D and E.

- **Day 4 afternoon**

*Table 6.16: Individual side concentrations (day 4)*

| Receptor point | Co-ordinates | Side A (Bq/m³) | Side B (Bq/m³) | Side C (Bq/m³) | Side D (Bq/m³) | Side E (Bq/m³) | Total (Bq/m³) |
|---|---|---|---|---|---|---|---|
| A | 27⁰50'11"S 26⁰40'18" E | 0.22 | 0 | 0.06 | 3.6E-3 | 0 | 0.29 |
| B | 27⁰50'15"S 26⁰40'20" E | 0.14 | 1.2E-4 | 0.07 | 6.3E-3 | 0 | 0.21 |
| C | 27⁰50'18"S 26⁰40'22" E | 0.14 | 0 | 8E-3 | 0.041 | 2.1E-5 | 0.19 |
| D | 27⁰50'22"S 26⁰40'26" E | 0.11 | 9.5E-5 | 0.01 | 0.039 | 1.8E-4 | 0.16 |

Day 4 afternoon wind direction varied between 337.84⁰ (NNW) and 315.75⁰ (NNW) during sampling. Similar to day 3, the main radon contributor was side A at all receptor points and the overall concentration decreased with increasing distance and deviation from the downwind direction from the source.

*Table 6.17: Percentage contribution by each side (day 4)*

| Receptor point | Co-ordinates | Side A (%) | Side B (%) | Side C (%) | Side D (%) | Side E (%) | Total (%) |
|---|---|---|---|---|---|---|---|
| A | 27⁰50'11"S 26⁰40'18" E | 77.25 | 0 | 21.5 | 1.25 | 0 | 100 |
| B | 27⁰50'15"S 26⁰40'20" E | 66.40 | 0.06 | 30.58 | 2.96 | 0 | 100 |
| C | 27⁰50'18"S 26⁰40'22" E | 73.67 | 0 | 4.42 | 21.90 | 0.01 | 100 |
| D | 27⁰50'22"S 26⁰40'26" E | 69.33 | 0.06 | 6.29 | 24.20 | 0.12 | 100 |

At receptor point A, only three (3) sides contributed towards radon concentration at this receptor. The major contributor is side A (77.25 %), followed by side C (21.5 %) then side D (1.25 %). No contributions were recorded from sides B and E. At receptor B, the contribution of side A

decreased from 77.25 % at receptor A to 66.40 % whereas side C yielded the second highest contribution at 30.58%. Side D with the third highest at 2.96 % and the smallest contributor being side B with 0.06 %. There was no contribution from side E. The only contribution from side E was observed at receptor C and D (0.01% and 0.12 % respectively). At these two receptors, side A still dominated, followed by side D.

Radon source orientations and wind direction have a direct effect on the downwind radon concentration. It is assumed that the highest average predicted and observed concentrations are expected when the mean wind direction deviation angle from the source to the receptor is close to zero (Isakov et al., 2004).

Furthermore, the source term is function of the area of release downwind to the receptors. The smaller the area source, the lower the total emission rates from the source and hence lower the radon concentration at the receptor point downwind. From these observations, it appears that the near source concentrations at receptors directly downwind will, in the short term (1-hour), be overestimated whereas the receptors located at large deviation angles from the mean wind direction will be underestimated.

The area of side B is the smallest compared to the other sides, hence its area source term will be the smallest, thus rendering day 4 concentrations low. It is therefore expected that the radon contributions due to this side will be minimal compared to other sides when they are all directly in line with receptors downwind. Overall, day 4 receptors experienced very low concentrations compared to day 3 due to their small area source term in line with mean wind direction.

## 6.6 Accounting for Wake effects

This study seeks to determine as accurately as possible, the quality of prediction of the ISCST3 models relative to the physics governing the

transport, dispersion and transformation of radon in the atmosphere. Therefore this section primarily addresses one of the main key gaps in modelling radon from the tailings dams by answering this question: "What is the contribution due to wakes effect, if any, on the ground level radon concentrations from the tailings dam?"

For each of the ISCST3 model runs described in table 6.12, a complementary 1-hour model run of ISC_PRIME was conducted to compute additional atmospheric dispersion due to the wake effects. The results of the wake modelling runs and the ISC-PRIME to ISC3ST concentration ratios are presented in tables 6.18 and 6.19 respectively.

From table 6.19, the 1-hour ISC-PRIME to ISCST3 radon concentration ratios range from 1.00 at distances far from the tailings dam to 2.39 at the distances very close to the source. These ratios indicate the increase in radon concentration due to wake effects. The highest ratio of 2.39 was found on the lee side of the tailings dam, very close to the dam for the top level area source. This is the near wake recirculation or cavity zone. This zone is characterized by significantly reduced wind speeds and intensive turbulence leading to rapid mixing (Olesen et al., 2005). Consequently, the plume is caught in the cavity, giving rise to increased concentrations very close to the leeward face of the dam. In this region, the effects of the wakes are very significant.

*Table 6.18: Wake modelling runs*

| Date | Receptor point | Co-ordinates | Modelled Rn concentrations (Bq/m³) | | | |
|---|---|---|---|---|---|---|
| | | | True geometry | Flat ground area | Top level area | Volume Source |
| **19-08-2017 Morning** | | | | | | |
| **09:30** | A | 27⁰50'11''S 26⁰40'1" E | 0.574 | 1.189 | 0.766 | 0.458 |
| **11:12** | B | 27⁰50'16"S 26⁰39'57" E | 0.326 | 0.648 | 0.128 | 0.396 |
| **12:00** | C | 27⁰50'18"S 26⁰39'54" E | 0.337 | 0.573 | 0.156 | 0.437 |
| **Afternoon** | | | | | | |

| | | | | | | |
|---|---|---|---|---|---|---|
| **13:32** | A | 27°50'11"S 26°40'4" E | 0.821 | 1.032 | 0.262 | 0.583 |
| **14:30** | B | 27°50'15"S 26°40'1" E | 0.436 | 0.373 | 0.097 | 0.245 |
| **15:26** | C | 27°50'18"S 26°39'58" E | 0.570 | 0.640 | 0.293 | 0.735 |
| **16:12** | D | 27°50'21"S 26°39'56" E | 0.472 | 0.541 | 0.119 | 0.405 |
| **20-08-2017 Afternoon** | | | | | | |
| **13:08** | A | 27°50'11"S 26°40'10" E | 0.575 | 0.719 | 0.164 | 0.548 |
| **13:54** | B | 27°50'13"S 26°40'7" E | 0.392 | 0.414 | 0.161 | 0.316 |
| **14:50** | C | 27°50'17"S 26°40'9" E | 0.472 | 0.498 | 0.252 | 0.573 |
| **15:49** | D | 27°50'22"S 26°40'5" E | 0.367 | 0.355 | 0.208 | 0.446 |
| **21-08-2017 Morning** | | | | | | |
| **07:39** | A | 27°50'11"S 26°40'0" E | 0.566 | 1.542 | 0.057 | 0.792 |
| **08:35** | B | 27°50'15"S 26°39'56" E | 0.433 | 0.809 | 0.097 | 0.989 |
| **09:25** | C | 27°50'18"S 26°39'54" E | 0.402 | 0.644 | 0.113 | 0.889 |
| **10:28** | D | 27°50'24"S 26°39'51" E | 0.012 | 0.010 | 5.43E-6 | 0.034 |
| **11:14** | E | 27°50'28"S 26°39'51" E | 0.000 | 0.000 | 0.000 | 0.008 |
| **Afternoon** | | | | | | |
| **13:00** | A | 27°50'10"S 26°40'22" E | 0.796 | 0.956 | 0.252 | 0.698 |
| **13:52** | B | 27°50'12"S 26°40'27" E | 0.678 | 0.623 | 0.192 | 0.561 |
| **15:24** | C | 27°50'15"S 26°40'35" E | 0.232 | 0.194 | 0.046 | 0.228 |
| **26-08-2017** | | | | | | |
| **13:19** | A | 27°50'11"S 26°40'18" E | 0.559 | 0.692 | 0.249 | 0.623 |
| **14:12** | B | 27°50'15"S 26°40'20" E | 0.449 | 0.462 | 0.212 | 0.536 |
| **15:04** | C | 27°50'18"S 26°40'22" E | 0.422 | 0.477 | 0.213 | 0.722 |
| **16:04** | D | 27°50'22"S 26°40'26" E | 0.382 | 0.397 | 0.203 | 0.630 |
| **27-08-2017** | | | | | | |
| **08:02** | A | 27°50'11"S 26°40'4" E | 0.843 | 1.949 | 0.103 | 1.307 |
| **08:50** | B | 27°50'14"S 26°40'2" E | 0.589 | 0.849 | 0.229 | 0.882 |
| **09:43** | C | 27°50'18"S 26°40'0" E | 0.398 | 0.340 | 0.043 | 0.303 |

*Table 6.19: ISC-PRIME to ISC3ST concentration ratios*

| Date | Receptor points | Distance (m) | ISC-PRIME to ISC3ST concentration ratios | | | |
|---|---|---|---|---|---|---|
| | | | True geometry area | Flat ground area | Top level area | Volume Source |
| **19-08-2017 Morning** | | | | | | |
| **09:30** | A | 0 | 1.129 | 1.058 | 1.093 | 1.167 |
| **11:12** | B | 189.2 | 1.001 | 1.001 | 1.003 | 1.001 |
| **12:00** | C | 291.8 | 1.008 | 1.004 | 1.016 | 1.006 |
| **Afternoon** | | | | | | |
| **13:32** | A | 0 | 1.118 | 1.092 | 1.497 | 1.175 |
| **14:30** | B | 148.3 | 1.029 | 1.034 | 1.146 | 1.053 |
| **15:26** | C | 272.0 | 1.159 | 1.139 | 1.364 | 1.119 |
| **16:12** | D | 379.6 | 1.007 | 1.006 | 1.029 | 1.008 |
| **20-08-2017 Afternoon** | | | | | | |
| **13:08** | A | 0 | 1.075 | 1.059 | 1.325 | 1.079 |
| **13:54** | B | 102.6 | 1.027 | 1.026 | 1.068 | 1.034 |
| **14:50** | C | 237.7 | 1.074 | 1.070 | 1.148 | 1.060 |
| **15:49** | D | 521.0 | 1.142 | 1.148 | 1.281 | 1.114 |
| **21-08-2017 Morning** | | | | | | |
| **07:39** | A | 0 | 1.006 | 1.002 | 1.067 | 1.005 |
| **08:35** | B | 164.9 | 1.120 | 1.061 | 1.909 | 1.049 |
| **09:25** | C | 272.5 | 1.135 | 1.080 | 1.740 | 1.057 |
| **10:28** | D | 475.1 | 1.019 | 1.022 | 1.000 | 1.006 |
| **11:14** | E | 598.6 | 1.000 | 1.000 | 1.000 | 1.000 |
| **Afternoon** | | | | | | |
| **13:00** | A | 0 | 1.062 | 1.051 | 1.228 | 1.072 |
| **13:52** | B | 149.9 | 1.085 | 1.093 | 1.383 | 1.105 |
| **15:24** | C | 392.5 | 1.044 | 1.053 | 1.267 | 1.045 |
| **26-08-2017 Afternoon** | | | | | | |
| **13:19** | A | 0 | 1.349 | 1.264 | 2.391 | 1.303 |
| **14:12** | B | 135.1 | 1.203 | 1.196 | 1.558 | 1.164 |
| **15:04** | C | 242.7 | 1.033 | 1.029 | 1.068 | 1.019 |
| **16:04** | D | 407.6 | 1.028 | 1.027 | 1.054 | 1.017 |

| | | | | | | |
|---|---|---|---|---|---|---|
| **27-08-2017 Morning 08:02** | A | 0 | 1.069 | 1.029 | 2.123 | 1.044 |
| **08:50** | B | 107.6 | 1.062 | 1.042 | 1.175 | 1.040 |
| **09:43** | C | 242.7 | 1.000 | 1.000 | 1.000 | 1.000 |

The distance beyond 250 m can be considered as the far-wake turbulence zone. In this region, the highest ratios observed were 1.74 (top level area), 1.159 (true geometry area), 1.148 (ground level area) and 1.114 (volume source) modeling at distances of 272.5 m, 272 m, 521 m and 521 m respectively. The far-wake zone is very unsteady and the airflow streamlines affect the wind speed and turbulence (Olesen et al., 2005). Accordingly, the highest values are obtained at different distances from the tailings dam. Further downwind of the tailings, the PRIME calculated fields of turbulence intensity, the slopes of the streamlines and wind speeds as a function of the shape of the projected tailings dam, gradually decay to atmospheric values and the ratio approaches 1. This is evident particularly during the late mornings when the temperatures and the wind speed are gradually increasing.

Another important observation is that the near-ground concentrations without wakes for the top level area modeling were generally the lowest compared to other modeling scenarios as discovered in section 6.6.2 above. However, accounting for the wakes effect increased the radon concentrations from tailings dam by up to 239% for the top level area source geometry. This is a very significant increase which was not previously accounted for in literature for radon modeling studies from the tailings dams.

In general, the inconsistent and intricate results in table 6.13 should not be surprising due to the complex nature of the ISCST-PRIME model itself. The radon concentrations predictions represented by the ratios in table 6.14 are highly influenced by a combination of the tailings geometry, meteorological conditions affecting the plume rise and hence, the wake specifications and cavity dimensions (Perry et al., 2004).

### 6.6.1 Measured vs modeled radon concentrations

To estimate the net incremental radon concentrations at each receptor point, upwind background concentrations measured in section 5.5.2 in line with each receptor point in terms of the wind direction, were added to the wakes incorporated modelled concentrations presented in table 6.18. This was performed to facilitate proper and adequate comparison of the modelled and measured concentrations. The computed radon concentrations at all receptors with respect to the four modelling scenarios are tabulated in table 6.20 and graphically presented in figures 6.17 (a – g).

*Table 6.20: Measured and modelled concentrations (background included)*

| Day and time | Receptor points | Distance (m) | Measured Rn Concentration (Bq/m³) | Modelled Rn Concentration (Bq/m³) | | | |
|---|---|---|---|---|---|---|---|
| | | | | True Area Geometry | Flat ground area | Top level area | Volume source |
| **Day 1 Morning 19-08-17** | | | | | | | |
| **09:30** | A | 0 | 10.3 | 8.946 | 9.560 | 9.138 | 8.830 |
| **11:12** | B | 189.2 | 8.5 | 8.763 | 9.084 | 8.565 | 8.832 |
| **12:00** | C | 291.8 | 8.4 | 7.241 | 7.477 | 7.060 | 7.341 |
| **Afternoon** | | | | | | | |
| **13:32** | A | 0 | 6.1 | 7.640 | 7.851 | 7.081 | 7.402 |
| **14:30** | B | 148.3 | 15.5 | 13.099 | 13.036 | 12.759 | 12.907 |
| **15:26** | C | 272.0 | 6.2 | 8.924 | 8.993 | 8.647 | 9.088 |
| **16:12** | D | 379.6 | 4.6 | 4.265 | 4.334 | 3.912 | 4.198 |
| **Day 2 Afternoon 20-08-17** | | | | | | | |
| **13:08** | A | 0 | 10.8 | 8.971 | 9.116 | 8.560 | 8.944 |
| **13:54** | B | 102.6 | 20.6 | 16.169 | 16.191 | 15.938 | 16.093 |
| **14:50** | C | 237.7 | 10.9 | 8.342 | 8.368 | 8.122 | 8.443 |
| **15:49** | D | 521,0 | 7.7 | 7.227 | 7.215 | 7.068 | 7.306 |
| **Day 3 Morning 21-08-17** | | | | | | | |

| | | | | | | | |
|---|---|---|---|---|---|---|---|
| **07:39** | A | 0 | 20.6 | 13.240 | 14.217 | 12.732 | 13.466 |
| **08:35** | B | 164.9 | 20.1 | 16.186 | 16.562 | 15.850 | 16.742 |
| **09:25** | C | 272.5 | 23.4 | 13.036 | 13.278 | 12.747 | 13.524 |
| **10:28** | D | 475.1 | 10.7 | 8.434 | 8.432 | 8.423 | 8.457 |
| **11:14** | E | 598.6 | 20.3 | 15.776 | 15.776 | 15.776 | 15.783 |
| **Afternoon** | | | | | | | |
| **13:00** | A | 0 | 13.1 | 6.588 | 5.884 | 6.330 | 6.588 |
| **13:52** | B | 149.9 | 20.5 | 7.561 | 7.129 | 7.498 | 7.561 |
| **15:24** | C | 392.5 | 8.4 | 8.076 | 7.928 | 8.109 | 8.076 |
| **Day 4 Afternoon 26-08-17** | | | | | | | |
| **13:19** | A | 0 | 6.2 | 7.410 | 7.543 | 7.100 | 7.474 |
| **14:12** | B | 135.1 | 13.4 | 8.277 | 8.290 | 8.039 | 8.364 |
| **15:04** | C | 242.7 | 10.9 | 8.303 | 8.357 | 8.094 | 8.603 |
| **16:04** | D | 407.6 | 8.38 | 7.364 | 7.379 | 7.185 | 7.612 |
| **Day 5 Morning 19-08-17** | | | | | | | |
| **08:02** | A | 0 | 19.9 | 9.218 | 10.324 | 8.479 | 9.683 |
| **08:50** | B | 107.6 | 8.3 | 8.987 | 9.247 | 8.628 | 9.280 |
| **09:43** | C | 242.7 | 8.1 | 8.831 | 8.772 | 8.475 | 8.736 |

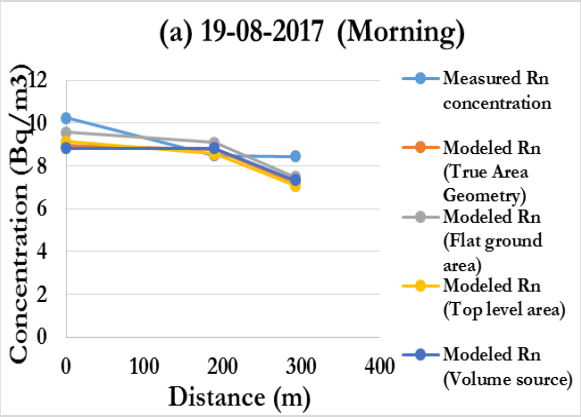


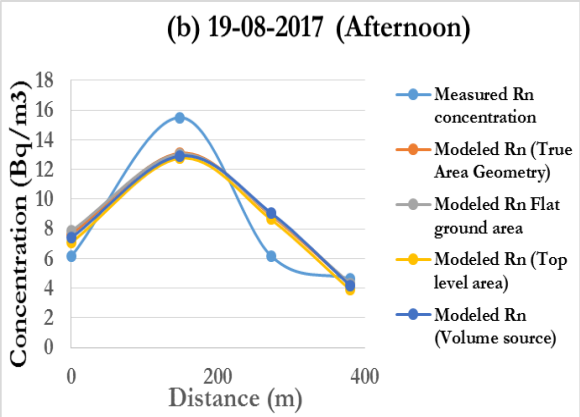

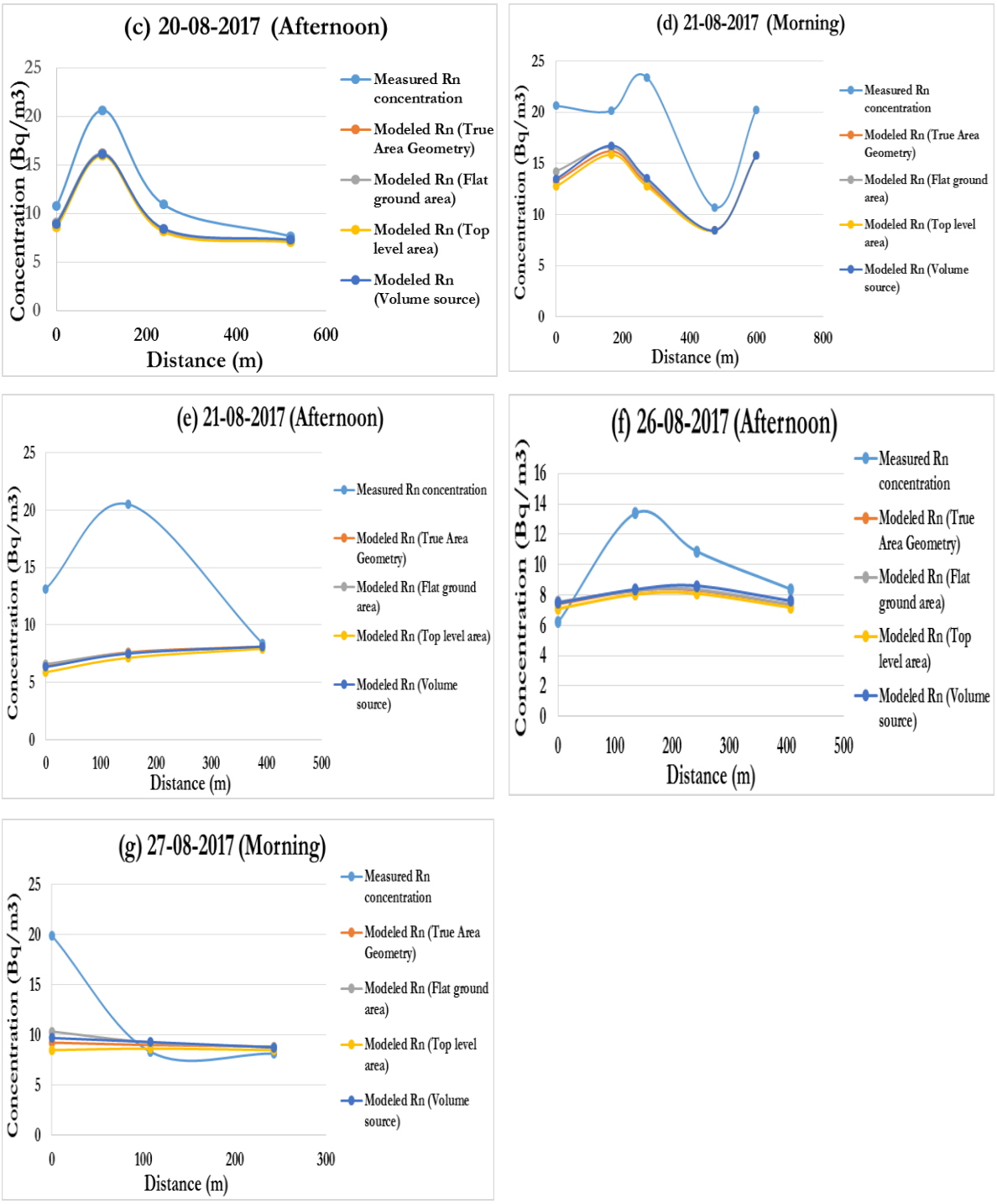


**Figure 6.17 (a - g): Graphical presentation of measured and modelled concentrations.**

The graphical patterns in figure 6.17 (a-g) reveal that measured and modelled curves follow a similar trend with regard to different peaks and dips. In all these cases except for (e), (f) and to an extent (g), there appears to be a good agreement between the measured and modelled radon in

terms of the trend of radon distribution at various distances from the source. In case of (e) and (f) the curves deviate significantly at two points, but at (g) this is true for only one point. Remarkably, all source geometries, when corrected for wake effects seem to produce almost the same results.

Common to all the results presented in figures 6.17 is that around the area close to the tailings, at distances in the region of 100 m – 150 m downwind, the tailings location, dimension and exit parameters play a very important role in radon distribution in that region (Stocker et al., 2016). Both modelled and measured concentrations exhibit deviations from the linear dependence of the total release inventory due to complex spatial distribution of the concentration field around this region. Within this distance, variations of both the wind speed and temperature follow the same sensitivity trend with distance from the tailings source. The peaks around this area for both morning and afternoon runs confirm this trend, which is consistent with the observations by Yegnan, Williamson and Graettinger (2002, 2003).

At distances greater than 200 m from the tailings, the predicted and modelled concentrations patterns are in agreement with the theoretical findings which describe an inverse relationship between the pollutant concentration and the downwind distance from the source (Chambers, Lowe and Stager, 1998). In this instance, the source dimension becomes less important and the predicted and measured concentrations exhibit linear dependence, thus levelling out (Bugai et al., 2015, Azlah, 2014).

### 6.6.2 Model validation: Statistical analysis

The statistical methods of index of agreement (IOA), fractional bias (FB), geometric mean bias (MG), normalized mean squared error (NMSE) and fraction of data satisfying the expression (FAC2) were used to quantitatively evaluate the performance of the ISCST3 model with respect to different modeling scenarios described in section 6.4. These values were

calculated using equations (2.39) – (2.43) in section 2.11.1. The results are shown in table 6.21.

*Table 6.21: Statistical analysis and model performance assessment*

| Day | Source term | Measured mean (Bq/m³) | Modelled mean (Bq/m³) | IOA (0.4 - 1.0) | FB (-0.5 - +0.5) | MG (0.75 - +1.25) | NMSE (< 0.5) | FAC2 (> 0.8) |
|---|---|---|---|---|---|---|---|---|
| **Day 1 Morning** | **True geometry (area)** | 9.063 | 8.339 | 0.632 | 0.083 | 1.087 | 0.013 | 1.087 |
| | **Flat ground level area** | | 8.730 | 0.800 | 0.037 | 1.038 | 0.007 | 1.038 |
| | **Top level area** | | 8.277 | 0.693 | 0.091 | 1.095 | 0.013 | 1.095 |
| | **Volume source** | | 8.357 | 0.632 | 0.081 | 1.085 | 0.014 | 1.085 |
| **Afternoon** | **True geometry (area)** | 8.113 | 8.527 | 0.926 | -0.05 | 0.951 | 0.059 | 0.951 |
| | **Flat ground area** | | 8.599 | 0.919 | -0.06 | 0.943 | 0.063 | 0.943 |
| | **Top level area** | | 8.145 | 0.829 | -0.004 | 0.996 | 0.058 | 0.996 |
| | **Volume source** | | 8.444 | 0.920 | -0.040 | 0.961 | 0.064 | 0.961 |
| **Day 2 Afternoon** | **True Geometry (area)** | 12.495 | 10.209 | 0.902 | 0.201 | 1.224 | 0.058 | 1.224 |
| | **Flat ground area** | | 10.254 | 0.904 | 0.197 | 1.218 | 0.056 | 1.218 |
| | **Top level area** | | 9.954 | 0.887 | 0.226 | 1.255 | 0.070 | 1.255 |
| | **Volume source** | | 10.229 | 0.899 | 0.199 | 1.222 | 0.058 | 1.222 |
| **Day 3 Morning** | **True Geometry (area)** | 19.016 | 13.353 | 0.637 | 0.350 | 1.424 | 0.158 | 1.424 |
| | **Flat ground area** | | 13.672 | 0.662 | 0.327 | 1.391 | 0.138 | 1.391 |
| | **Top level area** | | 13.124 | 0.619 | 0.367 | 1.449 | 0.174 | 1.449 |
| | **Volume source** | | 13.613 | 0.657 | 0.331 | 1.397 | 0.142 | 1.397 |
| **Afternoon** | **True Geometry (area)** | 14.003 | 7.422 | 0.431 | 0.614 | 1.887 | 0.670 | 1.887 |
| | **Flat ground area** | | 7.445 | 0.433 | 0.612 | 1.881 | 0.666 | 1.881 |

| | | | | | | | | |
|---|---|---|---|---|---|---|---|---|
| | **Top level area** | | 7.017 | 0.418 | 0.665 | 1.996 | 0.778 | 1.996 |
| | **Volume source** | | 7.349 | 0.427 | 0.623 | 1.905 | 0.691 | 1.905 |
| **Day 4 Afternoon** | **True Geometry (area)** | 9.708 | 7.900 | 0.551 | 0.205 | 1.229 | 0.113 | 1.229 |
| | **Flat ground area** | | 7.954 | 0.540 | 0.199 | 1.221 | 0.112 | 1.221 |
| | **Top level area** | | 7.666 | 0.559 | 0.235 | 1.266 | 0.127 | 1.266 |
| | **Volume source** | | 8.074 | 0.557 | 0.184 | 1.202 | 0.103 | 1.202 |
| **Day 5 Morning** | **True Geometry (area)** | 12.107 | 9.042 | 0.466 | 0.290 | 1.339 | 0.346 | 1.339 |
| | **Flat ground area** | | 9.478 | 0.512 | 0.244 | 1.277 | 0.266 | 1.277 |
| | **Top level area** | | 8.557 | 0.460 | 0.344 | 1.415 | 0.415 | 1.415 |
| | **Volume source** | | 9.263 | 0.479 | 0.266 | 1.307 | 0.310 | 1.307 |
| **All data set** | **True Geometry (area)** | 12.379 | 9.528 | 0.651 | 0.260 | 1.299 | 0.198 | 1.299 |
| | **Flat ground area** | | 9.713 | 0.667 | 0.241 | 1.274 | 0.180 | 1.274 |
| | **Top level area** | | 9.240 | 0.634 | 0.290 | 1.340 | 0.224 | 1.340 |
| | **Volume source** | | 9.614 | 0.657 | 0.251 | 1.340 | 0.189 | 1.288 |

The statistical analysis presented in Table 6.21 shows discrepancies amongst modelled outputs with respect to different modelling scenarios. The index of agreement, *d* shows that model's accuracy varies between 41.8% for top level area on day 3 afternoon and 92.6% for true geometry area on day 1 afternoon. From all data sets, the index of agreement across all four modelling scenarios indicates that the ground level area ($d$ = 0.667) performed satisfactorily when compared to volume source ($d$ = 0.675), true geometry area ($d$ = 0.651) and top level area ($d$ = 0.634) for the five days of measurements. The performance of the model across all modelling scenarios was poor on day 3 afternoon. Even though the ISCST3 model is not the perfect model, the model's performance on day 3 afternoon, which

yielded the lowest value of IOA, can be deemed acceptable because $d \geq 0.4$ (Kumar et al., 2006).

Fractional bias (FB) gives an indication (sign) of bias along the receptor and provides estimates of extremities in under predictions or over predictions. From table 16.21 the statistical evaluations of FB reveal different results for the various source terms that were studied. It can be observed that for all modelling scenarios, with the exception of day 1 afternoon, the FB values are positive, implying an over prediction of radon concentrations. The negative FB values is an indication of under prediction for all source terms. However, their values can be deemed acceptable seeing that these values are below -0.5 as recommended by Kumar et al. (2006). Notable deviation from acceptable limits suggested by Kumar et al. (2006) is observed on day 3 afternoon for all source terms. The FB values range from 0.612 (flat ground level area) to 0.665 (top level area). These values are beyond the 0.5 recommended limit of acceptable model fit. Moreover, day 3 afternoon anomalies correspond to the lowest values of index of agreement discussed above. In all other cases, the models can be deemed acceptable with high degree of reliability, particularly for flat ground area source.

The NMSE values for all the modelling scenarios and days, except day 3 afternoon, are found to be < 0.5, which also indicates satisfactory performance of the model for those modelling scenarios. Conversely, NMSE for day 3 afternoon exceeded the 0.5 limits across all modelling scenarios, ranging from 0.666 (flat ground area) to 0.778 (top level area). This trend is similar to that observed with FB values and IOA values.

An ideal and "perfect" model would mean that geometric mean bias, MG = 1, but that does not signify that the predicted values coincide with measured values. An MG greater than 1 indicate that the model over predicts and an MG less than 1 implies that the model under predicts. From table 16.21, the general overview is that MG is greater than 1 across all the modelling scenarios except for day 1 afternoon, where the MG

values are less than 1. The highest degree of over predictions was observed in day 3 afternoon, with the highest value of 1.996 for top level area. On the other hand, day 1 (morning) flat ground area recorded the lowest over predicted value of 1.038. Accordingly, there is high prevalence of over prediction, thus exceeding limits of acceptability. Only day 1 morning and day 2 afternoon yielded MG values that are less than 1.25 as recommend by Kumar et al. (2006) to regard the model as acceptable. Day 1 afternoon MG values are all under 1, indicating under prediction. These day 1 afternoon MG values were very close to 1, ranging from 0.943 (flat ground area) to 0.996 (top level area).

The FAC2 values for all model results were found to be > 0.8, signifying an acceptable performance by the model. However, the high FAC2 values for day 3 afternoon should be treated circumspectly. The FAC2 values ranges from 1.881 (flat ground area) to 1.996 (top level area), an increase of 88.1 % to 99.6 % from the ideal value of 1 (100 %).

In summary, ISCST3 showed a constant trend for all the scenarios, with minimum variability in the IOA, NMSE and FAC2 values. The only exception is day 3 afternoon for all results and to a lesser extent day 1 afternoon for FB values. The performance model assessment showed that day 3 afternoon modelled outputs did not correspond to the measured data, an indication that the model performed poorly.

### 6.6.3 Model validation: Source apportionment

Tabulated RaA and RaB to radon ratios measured in chapter 5 are listed in table 6.22.

For the purpose of analysis, ratio values greater than 1 were left out because it is not possible for daughter concentrations to be greater than the parent radon concentration. These values are receptor point A on day 1 morning, receptor point D on day 2 afternoon and receptor point B on day 5 morning. Receptor point B on day 2 afternoon was also excluded

because the concentrations of RaA and RaB were so low that they were not detectable. Only RaC was detected at that location as pointed out in chapter 5.

There is a common trait in the results shown in table 6.22. The RaA/Rn ratios are always greater than the RaB/Rn ratios. It is evident from figure 6.10 that RaA reached equilibrium with radon in about 20 minutes, while it took more than 2 hours for RaB to approach equilibrium.

*Table 6.22: Radon daughters to radon ratios (measured data inclusive of background)*

| Date and receptor point | RaA (Bq/m³) | RaB (Bq/m³) | Rn (Bq/m³) | RaA/Rn ratio | RaB/Rn ratio |
|---|---|---|---|---|---|
| **Day 1 (Morning)** | | | | | |
| **9:30 (A)** | 17.910 | 6.348 | 10.250 | 1.747 | 0.619 |
| **11:12 (B)** | 3.002 | 0.548 | 8.500 | 0.353 | 0.065 |
| **12:00 (C)** | 2.160 | 0.375 | 8.440 | 0.256 | 0.044 |
| **Day 1 (Afternoon)** | | | | | |
| **13:32 (A)** | 2.151 | 0.000 | 6.130 | 0.351 | 0.000 |
| **14:30 (B)** | 7.111 | 7.172 | 15.500 | 0.459 | 0.463 |
| **15:26 (C)** | 2.232 | 0.000 | 6.190 | 0.361 | 0.000 |
| **16:12 (D)** | 1.682 | 0.502 | 4.630 | 0.363 | 0.108 |
| **Day 2 (Afternoon)** | | | | | |
| **13:08 (A)** | 1.686 | 0.484 | 10.750 | 0.157 | 0.045 |
| **13:54 (B)** | 0.000 | 0.000 | 20.630 | 0.000 | 0.000 |
| **14:50 (C)** | 3.090 | 0.734 | 10.940 | 0.282 | 0.067 |
| **15:49 (D)** | 8.037 | 0.414 | 7.660 | 1.049 | 0.054 |
| **Day 3 (Morning)** | | | | | |

| | | | | | |
|---|---|---|---|---|---|
| **7:39 (A)** | 17.777 | 4.049 | 20.630 | 0.862 | 0.196 |
| **8:35 (B)** | 11.836 | 3.706 | 20.130 | 0.588 | 0.184 |
| **9:25 (C)** | 12.316 | 1.959 | 23.380 | 0.527 | 0.084 |
| **10:28 (D)** | 6.232 | 0.171 | 10.690 | 0.583 | 0.016 |
| **11:14 (E)** | 6.971 | 1.292 | 20.250 | 0.344 | 0.064 |
| **Day 3 (Afternoon)** | | | | | |
| **13:00 (A)** | 2.030 | 0.251 | 13.130 | 0.155 | 0.019 |
| **13:52 (B)** | 3.078 | 0.358 | 20.500 | 0.150 | 0.017 |
| **15:24 (C)** | 1.523 | 0.493 | 8.380 | 0.182 | 0.059 |
| **Day 4 (Afternoon)** | | | | | |
| **13:19 (A)** | 6.171 | 1.529 | 6.190 | 0.997 | 0.247 |
| **14:12 (B)** | 4.836 | 1.004 | 13.380 | 0.361 | 0.075 |
| **15:04 (C)** | 2.663 | 0.000 | 10.880 | 0.245 | 0.000 |
| **16:04 (D)** | 0.517 | 0.522 | 8.380 | 0.062 | 0.062 |
| **Day 5 (Morning)** | | | | | |
| **8:02 (A)** | 15.303 | 3.349 | 19.880 | 0.770 | 0.168 |
| **8:50 (B)** | 11.357 | 2.034 | 8.310 | 1.367 | 0.245 |
| **9:43 (C)** | 6.687 | 1.045 | 8.130 | 0.822 | 0.128 |

Considering only radon decay, more RaA will be formed in a short time compared to RaB, hence the ratio differences. In addition, atmospheric radon concentrations vary daily and its transport and dispersion depends on vertical temperature gradient, wind velocity and air turbulence.

The extreme daily ratios were 0.997:0.247 and 0.150:0.017 (RaA/Rn : RaB/Rn) on day 4 afternoon and day 3 afternoon respectively. From table

6.22, there are deviations from the radon decay and ingrowth of radon daughter illustrated in figure 6.15. This indicates that more complex processes are implicated. For example, radon gas with the "age" of about five minutes in figure 6.15 is expected to have an appropriate RaA/Rn ratio of about 0.7 and a corresponding RaB/Rn ratio of about 0.08. In contrast, the RaA/Rn ratio of 0.77 for day 5 morning in table 6.22 corresponds to a high RaB/Rn ratio of 0.168. In this instance, the air from the source may be subjected to some contamination.

From these ratios, a definite inference can be drawn concerning the "age" of radon daughters at each receptor point. The RaB/Rn ratio of 0.017 suggests a minimum growth period of about 3 minutes, given that RaB attains 1.7% of equilibrium in about 3 minutes. For the highest observed RaB/Rn value of about 0.247, the corresponding time of growth is about 16 minutes. Ingrowth period can increase or decrease depending on the level and type of contamination. That is, contamination by "clean" air will decrease the ratios whereas contamination by air containing radon daughters will increase the ratios.

The results of back-trajectory distance calculations are tabulated in table 6.23 and depicted in figures 6.18 – 2.28. These results excluded all the ratios that were greater than 1 and receptor point B on day 2 afternoon as highlighted earlier in this chapter. Two other results that were excluded are receptor B on day 1 (14:30 afternoon) and receptor A on day 4 (13:19 afternoon) due to extremely out of range distances stretching from four to nine kilometers.

*Table 6.23: Source apportionment results from back calculations*

| Date and receptor point | RaA/ Rn | RaB/ Rn | Bateman times (s) (RaA/Rn) | Bateman times (s) (RaB/Rn) | Velocity (m/s) | Distance (m) (RaA) | Distance (m) (RaB) |
|---|---|---|---|---|---|---|---|
| **Day 1 (Morning)** | | | | | | | |
| **11:12 (B)** | 0.353 | 0.065 | 125 | 350 | 5.3 | 660 | 1848 |
| **12:00 (C)** | 0.256 | 0.044 | 90 | 270 | 5.4 | 480 | 1441 |

| | | | | | | | |
|---|---|---|---|---|---|---|---|
| **Day 1 (Afternoon)** | | | | | | | |
| **13:32 (A)** | 0.351 | 0.000 | 125 | 0 | 5.1 | 631 | 0 |
| **15:26 (C)** | 0.361 | 0.000 | 176 | 0 | 2.7 | 475 | 0 |
| **16:12 (D)** | 0.363 | 0.108 | 177 | 490 | 2.4 | **418** | **1156** |
| **Day 2 (Afternoon)** | | | | | | | |
| **13:08 (A)** | 0.157 | 0.045 | 55 | 272 | 3.9 | 217 | 1072 |
| **14:50 (C)** | 0.282 | 0.067 | 98 | 350 | 3.2 | **311** | **1111** |
| **Day 3 (Morning)** | | | | | | | |
| **7:39 (A)** | 0.862 | 0.196 | 520 | 760 | 2.6 | 1352 | 1976 |
| **8:35 (B)** | 0.588 | 0.184 | 280 | 735 | 2.9 | 803 | 2108 |
| **9:25 (C)** | 0.527 | 0.084 | 200 | 420 | 4.2 | 843 | 177 |
| **10:28 (D)** | 0.583 | 0.016 | 280 | 80 | 5.2 | 1460 | 418 |
| **11:14 (E)** | 0.344 | 0.064 | 120 | 340 | 4.5 | **540** | **1530** |
| **Day 3 (Afternoon)** | | | | | | | |
| **13:00 (A)** | 0.155 | 0.019 | 55 | 165 | 2.7 | **149** | **446** |
| **13:52 (B)** | 0.150 | 0.017 | 53 | 160 | 3.3 | **176** | **530** |
| **15:24 (C)** | 0.182 | 0.059 | 70 | 330 | 3.8 | 264 | 1244 |
| **Day 4 (Afternoon)** | | | | | | | |
| **14:12 (B)** | 0.361 | 0.075 | 176 | 375 | 4.4 | 779 | 166 |
| **15:04 (C)** | 0.245 | 0.000 | 90 | 0 | 3.3 | 296 | 0 |
| **16:04 (D)** | 0.062 | 0.062 | 30 | 340 | 3.6 | 109 | 1229 |
| **Day 5 (Morning)** | | | | | | | |
| **8:02 (A)** | 0.770 | 0.168 | 180 | 700 | 1.8 | 322 | 1252 |
| **9:43 (C)** | 0.822 | 0.128 | 450 | 550 | 3.2 | 1449 | 1771 |

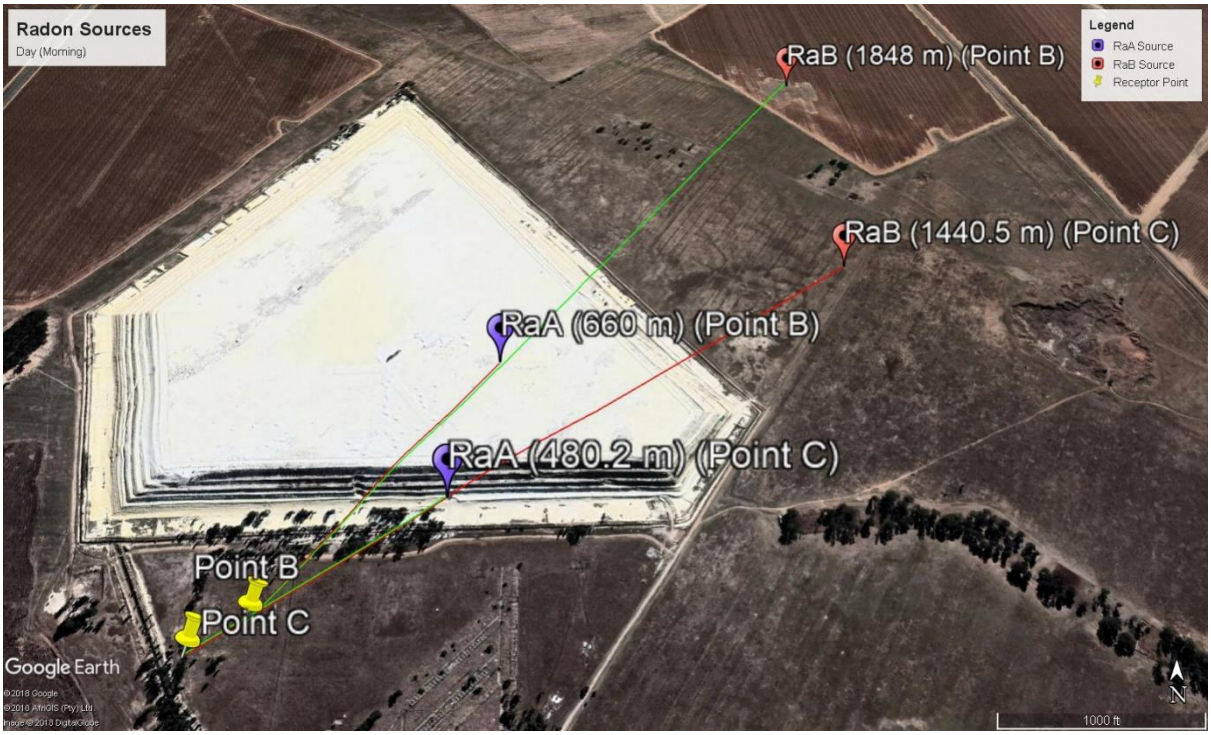


**Figure 6.18: Day 1 morning radon source origins from back calculations.**

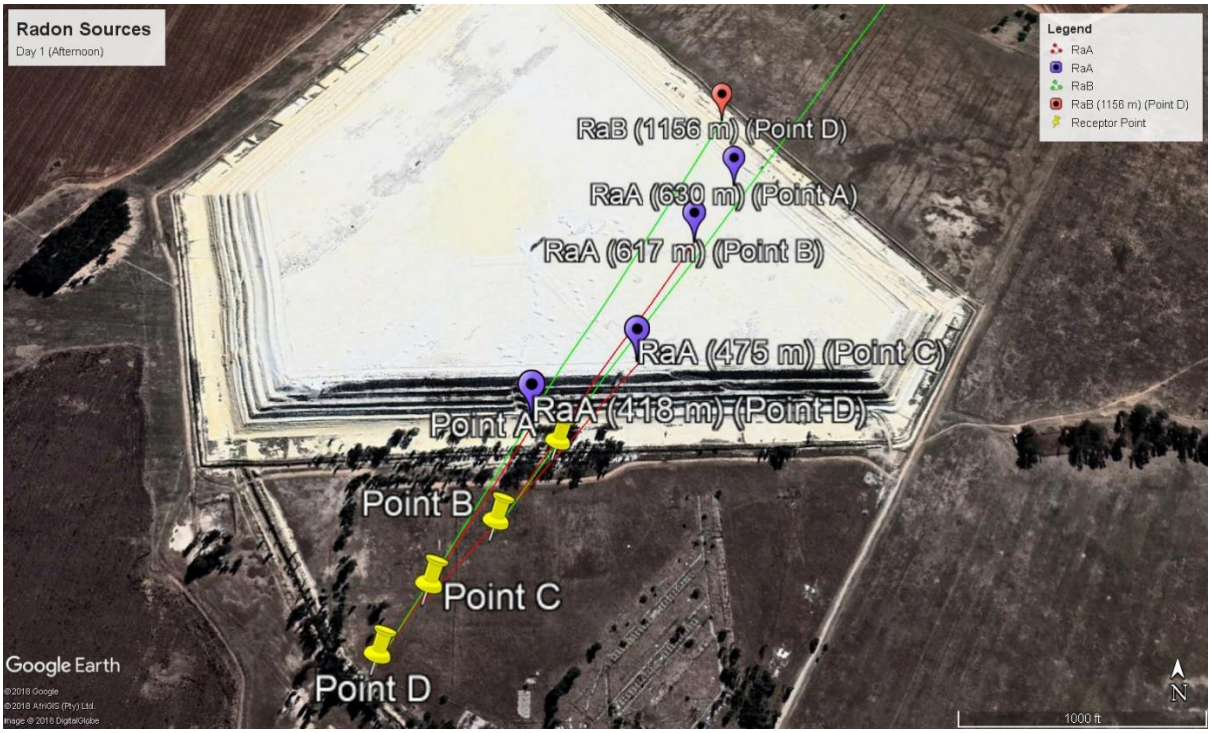


**Figure 6.19: Day 1 afternoon radon source origins from back calculations.**

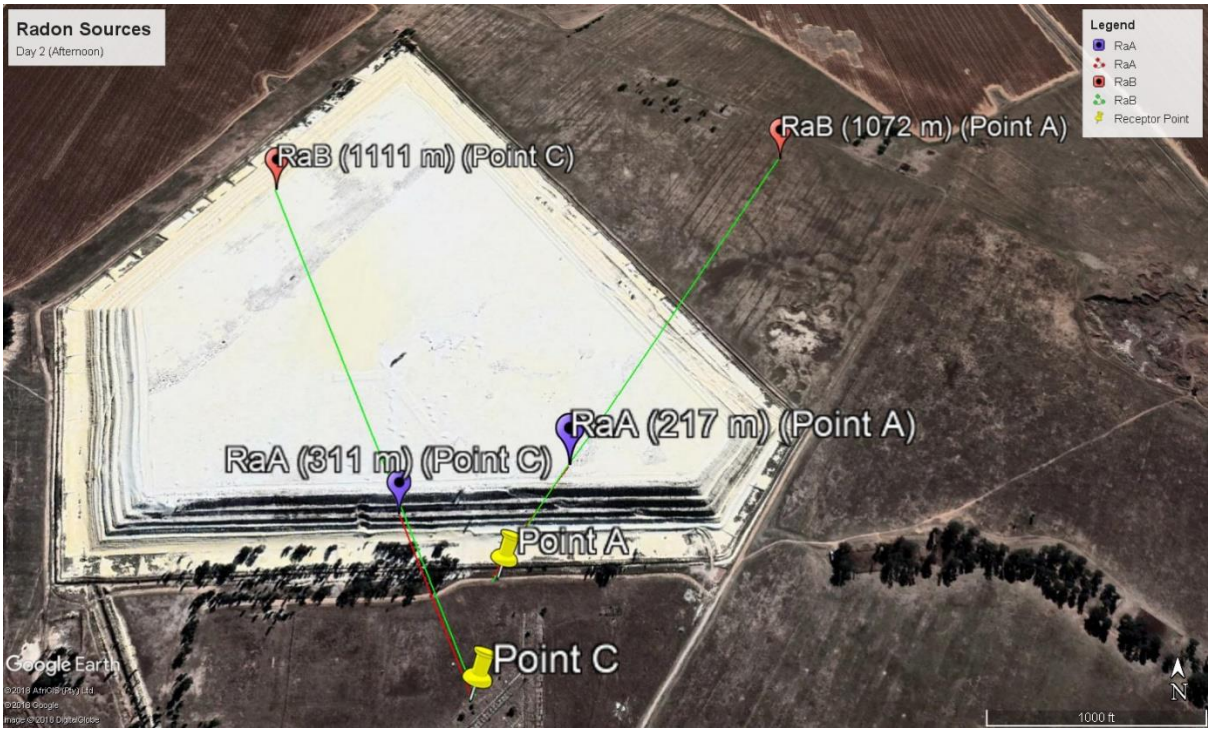


**Figure 6.20: Day 2 afternoon radon source origins from back calculations.**

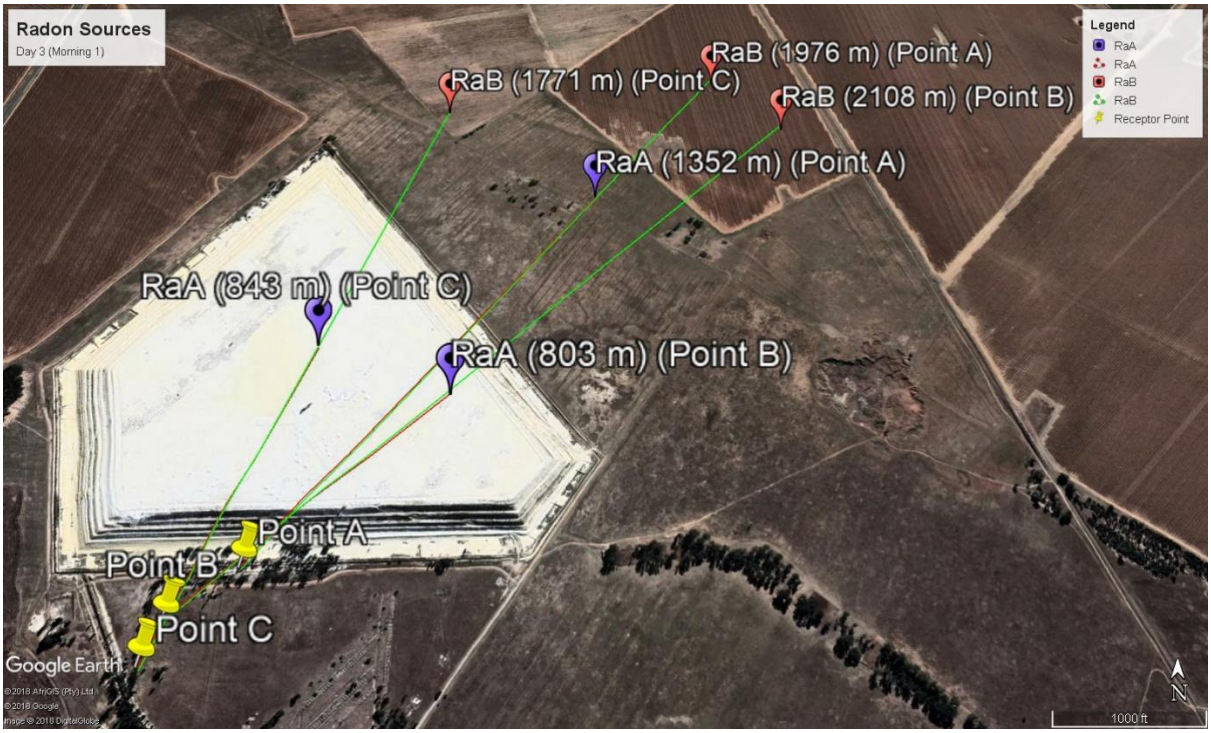


**Figure 6.21: Day 3 morning radon source origins from back calculations (Receptor A, B and C).**

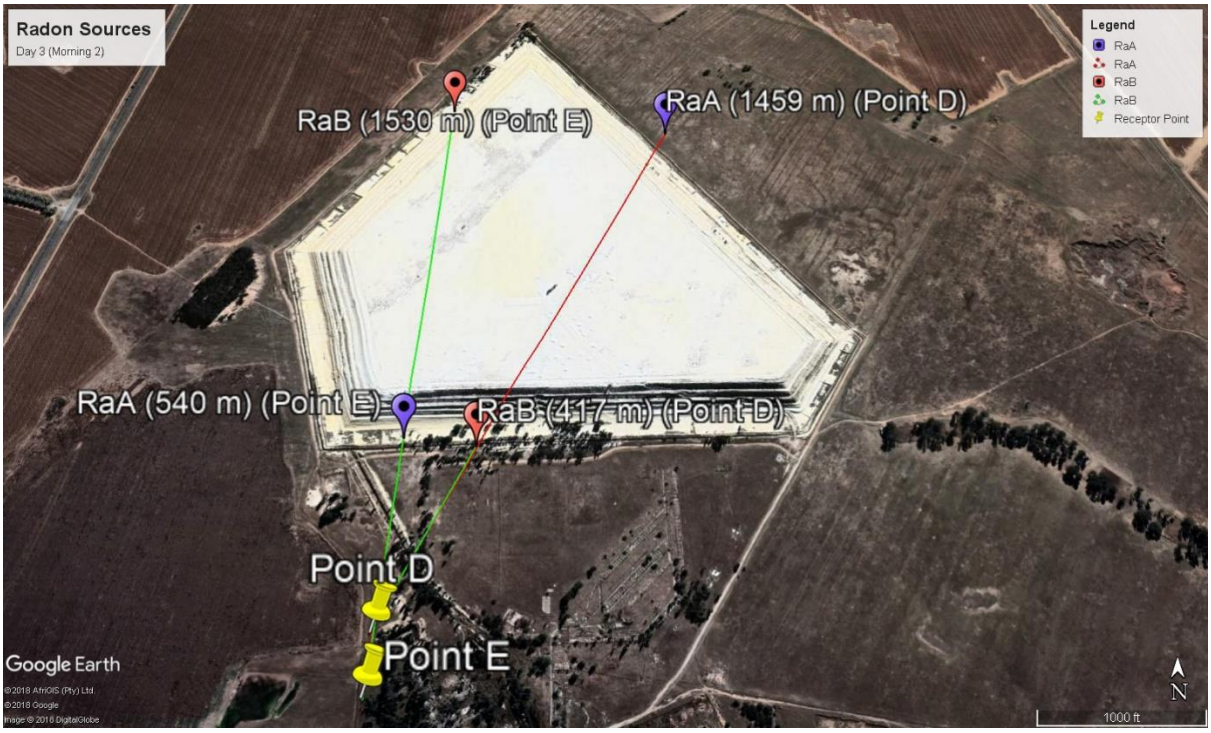


**Figure 6.22: Day 3 morning radon source origins from back calculations (Receptor D and E).**


**Figure 6.23: Day 3 afternoon radon source origins from back calculations (receptor point A).**


**Figure 6.24: Day 3 afternoon radon source origins from back calculations (receptor point B).**


**Figure 6.25: Day 3 afternoon radon source origins from back calculations (receptor point C).**

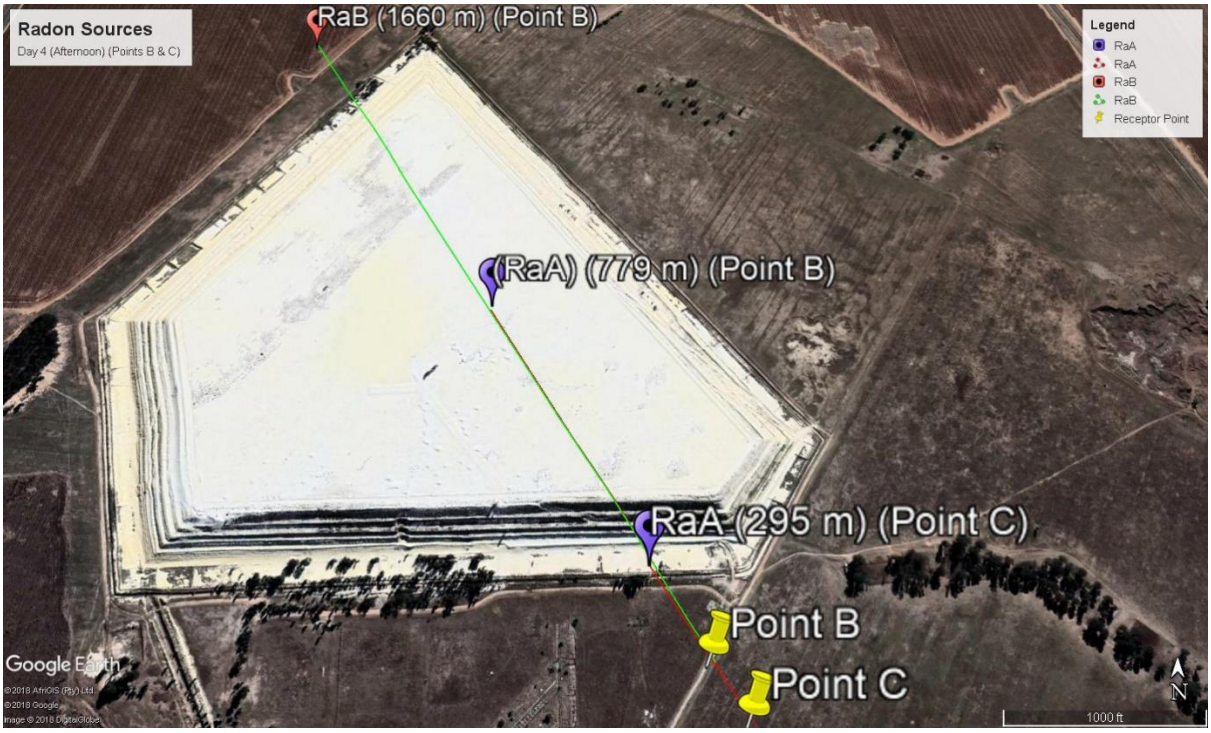


**Figure 6.26: Day 4 afternoon radon source origins from back calculations (receptor points B and C).**

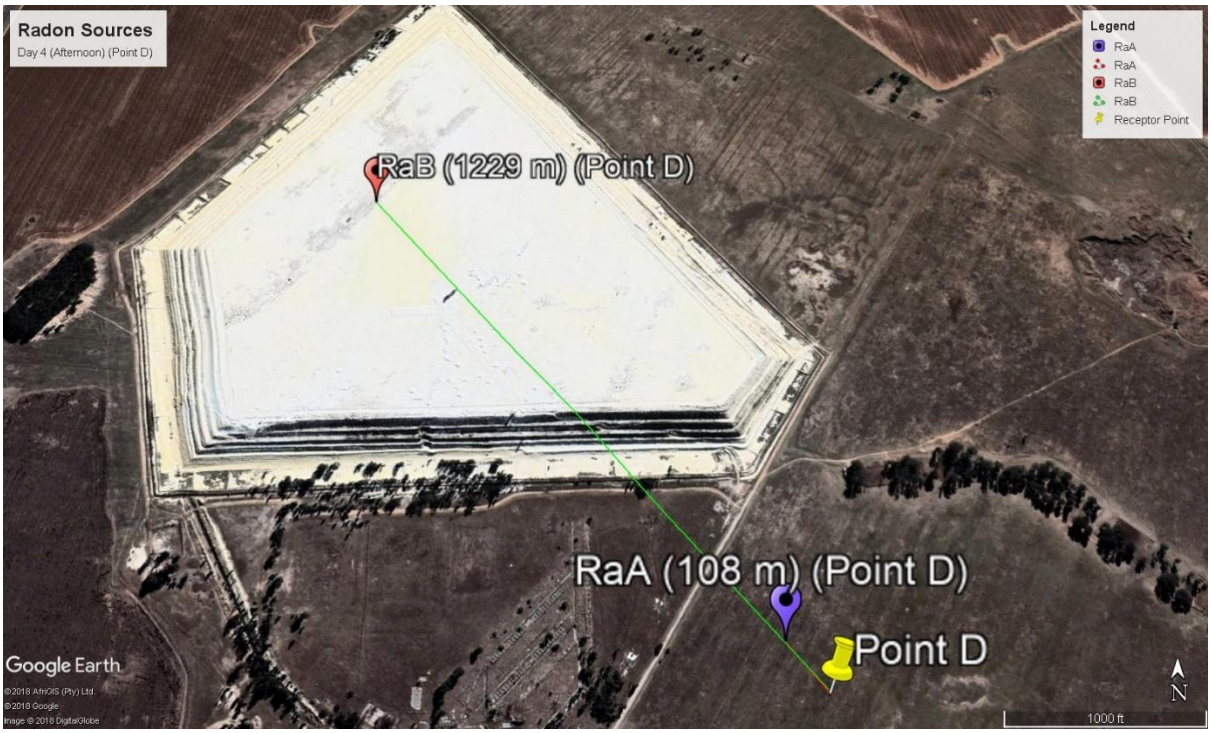


**Figure 6.27: Day 4 afternoon radon source origins from back calculations (receptor points D).**

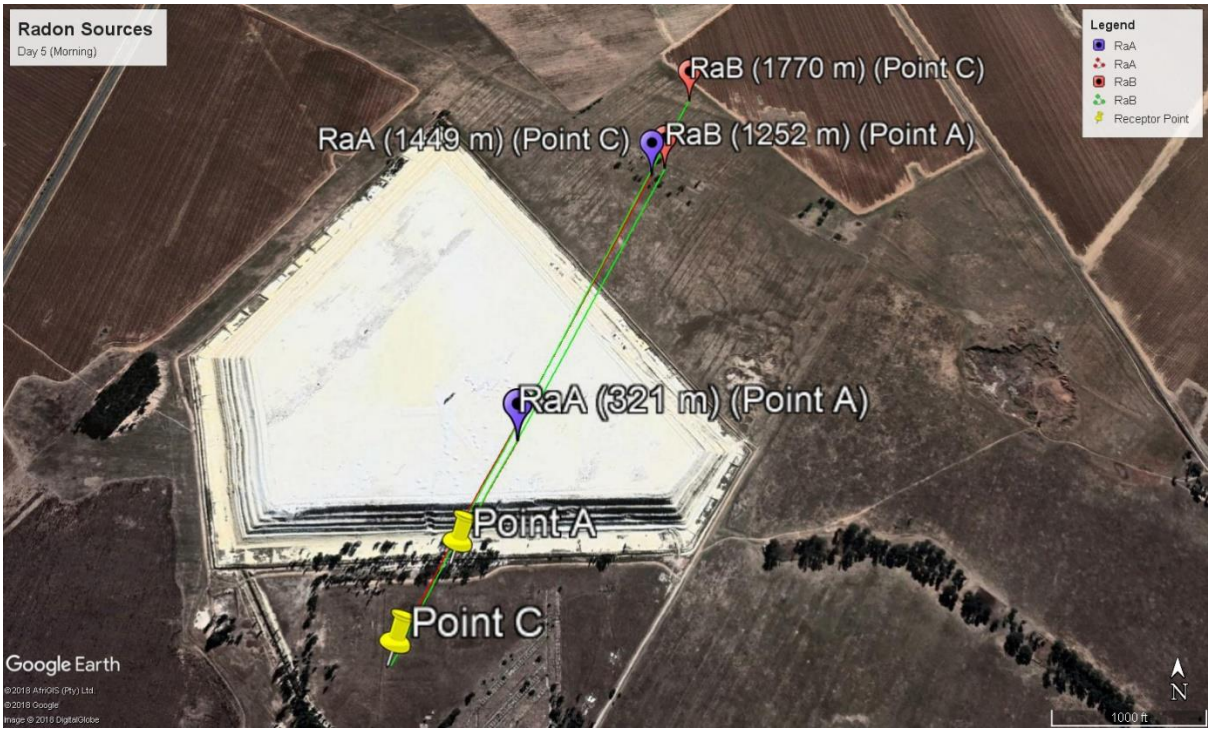


**Figure 6.28: Day 5 morning radon source origins from back calculations.**

A number of deductions can be made from figures 6.18 – 6.28. 76% of the RaA/Rn ratios shown by the purple place marks, indicate that the radon measured at the receptor points emanate somewhere on the tailings as predicted by the model, indicating that these measurements are indeed acceptable for validation purposes. These ratios lie close to the RaA-time line in figure 6.15. The other 24% of RaA/Rn ratios on day 3 morning (points A and D), day 3 afternoon (point C), day 4 afternoon (point D) and day 5 morning (point C) originate outside the perimeter up wind of the tailings dam, a deviation from the RaA-time relationship illustrated in figure 6.15.

The atmospheric radon concentration can be approximated by the RaA concentration in ambient air. Owing to its short half-life, RaA is the best indicator of how “young” or “fresh” radon is at the receptor. Furthermore, the short half-life of RaA implies that the distance travelled from the source to the receptor point will be shorter, hence most of the

back trajectories reflect the radon origin to be within the tailings dam perimeter.

Contrary to the RaA/Rn ratios, 47% of the RaB/Rn ratios, represented by red place marks, shows the radon source originating from within the perimeter of the tailings dam. The other 53% of the RaB/Rn ratios reflected radon emanating from outside the tailings dam. Similar to the RaA/Rn situation, the 47% that are found to originate from the tailings dam correspond to the RaB-time graph in figure 6.15. The remaining 53% that fell outside the perimeter of the dam deviated from the RaB-time graph.

The “back-calculation” or receptor model technique discussed above is very much idealised, assuming just straight line transport from the source to the receptor. As a result, this approach is not fully applicable in the real atmosphere. Given the limited information at hand, it is not possible to follow the path of radon air parcels from the source to the receptor with infinite accuracy. Radon movement from the source to the receptor may be distorted as it travels from the source such that it is divergently scattered along the direction of travel. The combined action of wind field inhomogeneities, decay properties, convective and turbulent motions may contribute to the deviation of the straight line path described above, resulting in a curved and whirling radon path (Stohl, 1996).

During the short-range radon transport, or microscale transport, the airflow trajectory or pathway is primarily influenced by emission source areas. Under these conditions, low RaA/Rn and RaB/Rn ratios indicate “fresh” radon at the receptor, which can be ascribed to the tailings dam given short distance and time of travel from the dam to the source. However, advective air mass motion can be responsible for variations in atmospheric radon concentrations (Arnold, Vargas and Ortega, 2009). Because of the long half-life of 3.8 days, accumulated radon originating from different sources far away from the tailings dam may be detected at near source receptors after travelling long distances in the atmosphere.

This has been particularly prominent in RaB/Rn ratio back calculations for the air mass traveling from north-east. Observations from the data presented in figures 6.13 – 6.23 suggest that most of the radon from RaA/Rn and RaB/Rn back calculations that originated from beyond the tailings dam upwind, emanated from the north-east wind direction. All the off-boundary origins are relatively close to the tailings dam, and there are no other radon sources in the zones where these occurred. Considering the uncertainties, it can be said that these cases also indicate radon originating from the large tailings dam source.

The most indicative results of model validation where both RaA and RaB sources originated from the dam according to the back calculations are obtained on day 1 afternoon (point D), day 2 afternoon (point D), day 3 morning (point E) and day 3 afternoon (points A and B). These periods are characterised by low daughter radon ratios ranging between 0.15 and 0.36 for RaA/Rn ratio and between 0.017 and 0.108 for RaB/Rn ratios. The wind speeds varied between 2.4 and 4.5 m/s. These findings are consistent with the modeled results indicating with high confidence that the radon sources measured at these points are primarily from the tailings dam. Hence, the validity of using the measured radon concentrations to validate the ISCST3 model has been demonstrated.

# Chapter 7 Summary and Conclusion

This chapter presents a summary of the aims, methodology and results of this study. Conclusions and the corresponding recommendations will be drawn from the findings of the study.

Regulation requires that doses to members of the public from a single activity be constrained to 250 µSv/y, and total allowable dose limit to the public of 1 mSv/y from all activities involving radiation. Conventionally, outdoor radon measurements are done with RGMs, which provide a close-up of emissions in space and time. But the RGMs cannot isolate the different radon contributors at the receptors. That is why dispersion modeling was used to isolate tailings radon from other contributors. To determine radon levels and their impact on the surrounding community settlements, direct radon measurements are acceptable as shown by Moshupya et al. (2019). If the aim is to determine tailings dam contributions e.g. for regulatory purposes, then dispersion modeling is the best option.

The ISCST3 Gaussian model as currently applied to radon from tailings dams has not being properly validated. To validate the model, radon and radon daughters were measured at different points around the tailings. In order to check whether the measured radon is from the tailings dam, a technique was developed that used the "age" of the gas and daughters as well as using the source apportionment method to prove that the radon measured is from the tailings.

The results of this study successfully demonstrated that with proper and accurate parameterisation and dispersion modeling, it is possible to simulate radon movement and validate the dispersion modelling that assess the environmental radon contribution from tailings dam. While previous methods have not been validated due to unreliable, assumed and insufficient input data as was the case with Dinis and Fiúza (2015), this study emphasised proper source quantification as well as full evaluation

and validation of the model with respect to radon measurements from the tailings dam.

Furthermore, the work has shown that dispersion modelling is not so difficult and that it can be used successfully. It should be noted that other radon sources like other tailings dams have to be extensive to affect radon levels. This was the case for the study of Moshupya et al. (2019) where a number of tailings could have contributed to high radon concentrations. In this study, an isolated dam was specifically chosen where there are no other sources. Still, the background upwind RGM values were high. If it is to know radon levels, then radon measurements are acceptable. If it is to know tailings dam contributions e.g. for regulatory purposes, dispersion modeling is the best option. T

## 7.1 Research findings

As pointed out in this thesis, radon flux (exhalation) is the source term for dispersion modeling, making it a very important parameter for quantifying radon release from the tailings dam. From different radon exhalation measurement methods applied to tailings that were reviewed, the passive diffusion tube method was identified as the most reliable and convenient method to determine radon exhalation from the Freddies 9 tailings dam. The radon exhalation rate (E) was found to vary from 0.045 Bq/($m^2$.s) to 0.443 Bq/($m^2$.s) with an average value of 0.102 Bq/($m^2$s) and a standard deviation of 0.087 Bq/($m^2$s). This value was found to be comparable to other results obtained by other expensive and time consuming methods.

The exhaled radon from the radium-bearing tailings dam will diffuse into the atmosphere. Long-term environmental radon passive assessment is a means to determine environmental impact of ambient radon concentration levels in the vicinity of the tailings dam. The ambient radon concentration values averaged over the surroundings within the radius of 2.5 km from the tailings range from 38 Bq/$m^3$ to 94 Bq/$m^3$, with a mean

concentration of 64 Bq/m$^3$. These values are below the 100 Bq/m$^3$ action level stipulated by the NNR with a slight average increase compared to background levels. About 20% of the concentrations measured were above the 80 Bq/m$^3$ action level in Germany. However, these results could not differentiate between various radon contributors at each measurement point, making it practically impossible to distinguish between NORM and TENORM contributions.

The concentration of airborne radon at any given place is influenced by locally exhaled radon and dispersed radon from other locations. To discriminate between different radon contributors a “follow-the-wind” approach was suggested. This method involved actively measuring radon gas, individual radon daughters, and the F factor at different upwind and downwind receptor points by following the wind direction at every hour. Measurements and calculations revealed strong influence by external meteorological factors on the distribution of radon and radon daughters at distances ranging from 0 m to 600 m from the tailings and background. The F factor, which indicates the “age” of the gas, and radon gas concentration increased to their highest values when the wind was blowing from north-northern-east (NNE). The highest radon daughter concentrations at various locations were recorded in the mornings. However, the interpretation of results was made difficult by fluctuating and conflicting effects which different meteorological conditions often have on the resultant atmospheric radon, radon daughters and F factor as functions of distance from the tailings downwind. To further explain these results, air dispersion modelling was done.

To quantitatively explain the results obtained in chapters 4 and 5 with regard to radon and radon daughter measurements, the ISCST3 code was used to evaluate radon transport and the effects of local variations of conditions around the tailings dam. One of the aims of the study was to improve on the accuracy and reliability of the dispersion modelling focussing primarily on the source term.

The source term measured in chapter 3 was corrected to account for cracks and fissures caused by erosion on the side of the tailings walls. In addition, the geometry of the tailings dam was modelled as accurately as possible by taking into account all emitting surfaces as sources. This increased the accuracy of the model predictions as compared to traditional approaches to modelling source terms from tailings dams. The corrected emission rates were therefore more realistic and representative of the true source term. Compared to the corrected emission rates, the model over predicted the flat ground area source by up to 274 %, under predicted the top level area source by up to 50% and over predicted the volume emission source by up to 300% in 60% of the modelling runs and under predicted by 55% in 40% of the volume model runs.

While the top-level area source term produce lower concentrations at near-field ground level receptors, taking into account the wakes effect increased the radon concentrations from tailings dam by up to 239% for the top level area source. This result is a strong indication of the necessity to include wake calculations in order to accurately estimate radon exposure from the tailings dam.

Model validation from statistical analysis showed a constant trend for all the scenarios, with minimum variability in the IOA, NMSE and FAC2 values. There is an under prediction in the bias on day 1 afternoon. In addition, the model performance did not meet the general specifications by Kumar et al. (2006) on day 3 afternoon, an indication that the model performed poorly. The model performance was particularly acceptable for true geometry area and flat ground area sources.

Further validation of the model was carried out by isolating radon from different contributors using the “age” of the gas approach and applying back trajectory calculations to identify source. The model was successfully validated by tracing the origin of radon back to the tailings as predicted by the model.

Given the performance of the model with regard to different modeling scenarios, the sensitivity test, wake effects and validation from statistical analysis, it can be concluded that the best representative modeling option is the true geometry area source.

From modeling results, the radon concentrations from the tailings at the receptors were found to be well below the action level of 100 Bq/m3 as per National Nuclear Regulator Act 47 of 1999. The highest concentration predicted by the model at the receptor point identified in the methodology section in chapter 5 and 6 from the true geometry source was found to be 0.84 Bq/m$^3$, which correspond to a dose of 0.012 mSv/y to the public due to radon from the tailings. This value is less than the 1 mSv/y dose constraint stipulated by NNR. It should however be noted that it was not the intention of this study to estimate highest dose values or the impact of the dam thereof. These values are mentioned as an aside.

Apart from modelling, the small contribution of the tailings is indicated by three independent experimental results:

- The difference between average upwind and downwind RGM measurements is very small and almost indiscernible.
- Alpha nuclear grab samples of radon concentration show very low levels upwind and downwind.
- The low radon level is corroborated by the daughter measurements, if radon concentration from the tailings is indeed higher, the daughter levels would also be.
- Radon “age”, deduced from daughter levels is very young, and indicates that radon measured downwind did indeed originate from the tailings. This was the gist of the project.

One crucial finding from the study was that the radon concentrations measured by the AlphaGUARD active detector in chapter 5 did not agree well with the concentrations from the passive RGM measurements in chapter 4 and those calculated by the ISCST3 model

around the tailings. The high RGM concentration results show that tailings are not the only source of radon contamination at the receptors. This follows from the observation that the model results could not explain the vast difference in concentrations recorded by both the RGM and the AlphaGUARD. It is therefore necessary to further investigate, identify, characterise and document sources of this excess radon exhaled at the site as well as any systematic errors that may contribute towards this anomaly.

The objectives outlined in chapter 1 have been achieved. The primary results based on the objectives were:

- to investigate the current methods of radon flux measurements from the tailings dams and to select the best method - achieved in chapter 3. The diffusion tube method was selected as the more reliable and convenient option.
- to select an existing representative tailings dam and measure its source term (flux) using the selected method - achieved in chapter 3. Radon flux was found to be 0.102 ± 0.087 Bq/($m^2$s).
- to measure radon gas concentrations at 116 locations around the tailings dam, as well as far from the source using Radon Gas Monitors - achieved in chapter 4. The average radon concentration and standard deviation measured are 64 Bq/$m^3$ and 11 Bq/$m^3$ respectively.
- to model the geometry of the selected tailings dam as accurately as possible – achieved in chapter 6.
- to apply the atmospheric dispersion software (including the wake effect) and local weather data to calculate radon concentrations in the surroundings of the tailings dam - achieved in chapter 6.
- to determine the contribution of a radon source at a location by measuring the F-factor, and deducing the “age” of the gas, compared to the “age” from background sources - achieved in chapter 5.
- to develop a new technique based on the “age” of the gas that will allow discrimination between the different radon contributors - achieved in chapters 5 and 6.

- to use the data and new technique to validate (or calibrate) the air dispersion model - achieved in chapter 6.
- to use the insight gained from this study to recommend the best modelling practise when using dispersion models to accurately estimate radon emissions from tailings dams - achieved in chapter 7.

## 7.2 Noteworthiness

This study contributes significantly to the current knowledge of radon assessment methods from mine tailings. Simulated impacts from tailings dam can be computed with increased accuracy and within an acceptable domain of certainty by taking into account previously omitted parameters like total emitting surface source area.

Previous work on validation of radon dispersion modeling applied only the statistical analysis equations formulated by the EPA – this is the first study that validated the ISCST3 model in field measurements for a gold-mine tailings facility. Consequently, potential adverse environmental influences due to radon from the tailings can be simulated with an increased degree of accuracy. In South Africa, the close proximity of the mine tailings to the residential areas may pose some health risks. The results of this study will serve as a useful tool for assessing the radiological impact for regulatory purposes.

## 7.3 Recommendations

ISCST3 model is not suitable for modeling plate out, deposition, dust and radon daughters. Therefore more evaluation should be carried out that would enable the modeling of radon daughters from the source to the receptor, taking into account all the factors affecting their transport

Radon exhalation is a continuous process that varies with meteorological factors of pressure, temperature, precipitation, etc. This

variation should be accounted for during modeling at various times of the day. Diurnal variations of radon exhalation from the tailings should be measured to account for variations in emission rates with location and meteorology during modeling and complex radon distribution trends observed in chapter 5. It may also be interesting to determine the effects of radon exhaled at the different receptor locations on the measured radon.

The project environment e.g. access, safety at night, remoteness etc. restricted any possibility of taking measurements at night. In addition, the idea of leaving measuring equipment unattended at night was also discouraged. This made the comparison and analysis of results difficult. On the other hand, the fact that Alpha guard and RGM measurements were not taken in the same period will not explain the large difference between RGM and grab samples. It is advisable that in future parallel similar measurements using another detector type be undertaken to properly compare the results.

Measurements on the tailings will not add much to the validation project, but a local weather station will. In this project, weather data was obtained from South African Weather Services (SAWS) as input modelling data. To reduce the uncertainty that may be arise due to other factors like proximity of the weather station to the measuring site, height etc., it is advisable that in future a portable weather station be used to measure weather data along with measurements of both radon and radon daughter levels.

# Appendices

## Appendix A: Principles of radon progeny measurements

Conceptually, sampling techniques for the radon progeny measurement can be divided into two broad categories depicted in figure 8.1 (A): (a) separated sampling and activity measurements, i.e., activity measurement is conducted after completion of sampling and collection cycle, or (b) combined sampling system and activity detection in one unit, i.e., activity measurement is performed during sampling (Hofmann et al., 2015, James, Strong, 1973, Porstendörfer, 1996).

Contrary to radon gas, which is almost homogenously distributed in space, radon progeny are solids attached to dust particles or deposited to the surfaces of the surrounding materials. As such, most of the methods used to measure radon progeny activity concentrations are based on drawing air at a known rate onto some filter (sampling), followed by alpha or beta counting using a suitable detector. The counting process can either give the gross count or the count rate of different particles at varying time intervals (Kadir et al., 2013).

Calculations of different radon progeny concentrations using time-interval counts or counting rates is based on the following assumptions: (i) for the duration of the sampling process, the concentrations remain constant; (ii) pump velocity, collection and counting efficiencies remain unchanged during measurement; and (iii) the influence of environmental parameters on measuring process is negligible (Kadir et al., 2013).

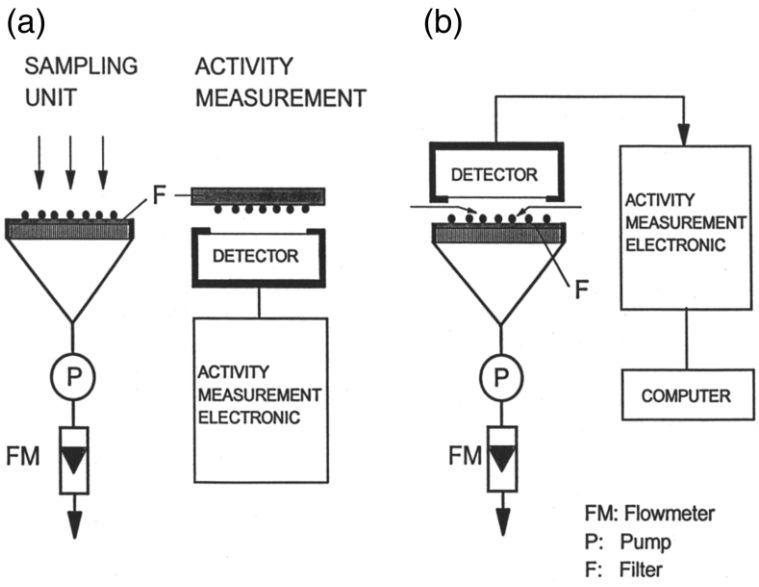


**Figure 0.1(A): Sampling techniques for radon progeny measurements: (a) separated sampling unit and activity measurement or (b) combined unit (Porstendörfer, 1996).**

Taking into account the above assumptions, the relationship between radon progeny concentrations and time-interval counts is governed by a set of differential equations (Bateman, 1910) that describe radon progeny activity build-up. This is achieved by considering that during the sampling and counting period, different radon progeny will accumulate and decay. Taking the ending point of sampling as the starting time of counting ($t'$= 0), the change in the progeny's number with time on the filter can be expressed as follows (Kadir et al., 2013, Jenkins, 2002):

$$\frac{dN_i(t)}{dt} = C_i v + \lambda_{i-1} N_{i-1}(t) - \lambda_i N_i(t), \quad (i = 1,2,3), \tag{0.1}$$

$$\frac{dN_i(t')}{dt'} = C_i v + \lambda_{i-1} N_{i-1}(t') - \lambda_i N_i(t'), \quad (i = 1,2,3). \tag{0.2}$$

where

equation 8.1 is for the sampling process;

equation 8.2 is for the decay process after sampling;

$v$ is flow rate (Lpm);

$\lambda_i$ is decay constant ($s^{-1}$);

$C_i$ is radon progeny's concentration (Bq·m$^{-3}$); and

$i$ = 1, 2, 3 represents $^{218}$Po, $^{214}$Pb, and $^{214}$Bi separately.

Consider that initially, number of particles is $N_i$ (t = 0) = 0 and $N_i$ ($t$' = 0) = $Ni$ ($T$) (where $T$ is the sampling time). Taking into account filter efficiency and detector counting efficiency, equations 8.1 and 8.2 can be solved to determine the number of radon progeny atoms on the filter during sampling and counting or decaying period. During the time interval of t $\epsilon$ [0 : $t_s$] where $t_s$ represents sampling time, the solution for equation 8.1 for the number of short-lived progeny $N_{s,i}$, (t) collected on a filter target is given by (Hofmann et al., 2015):

$$N_{s,Po}(t) = \frac{C_{Po}}{\lambda_{Po}}(1 - exp(-\lambda_{Po}t)) \tag{0.3}$$

$$N_{s,Pb}(t) = \left(\frac{C_{Po}}{\lambda_{Po}} + \frac{C_{Pb}}{\lambda_{Pb}}\right)(1 - exp(-\lambda_{Pb}t)) - \left(\frac{C_{Po}}{\lambda_{Po} - \lambda_{Pb}}\right)(exp(-\lambda_{Pb}t) - exp(-\lambda_{Po}t)) \tag{0.4}$$

$$\begin{aligned} N_{s,Bi}(t) = {} & \left(\frac{C_{Po}}{\lambda_{Po}} + \frac{C_{Pb}}{\lambda_{Pb}} + \frac{C_{Bi}}{\lambda_{Bi}}\right)(1 - exp(-\lambda_{Bi}t)) \\ & - \left(\frac{C_{Po}}{\lambda_{Bi} - \lambda_{Pb}} + \frac{C_{Pb}}{\lambda_{Bi} - \lambda_{Pb}}\right)(exp(-\lambda_{Pb}t) - exp(-\lambda_{Bi}t)) \\ & - \left(\frac{C_{Po}\lambda_{Pb}}{(\lambda_{Bi} - \lambda_{Pb})(\lambda_{Po} - \lambda_{Pb})}\right)(exp(-\lambda_{Pb}t) - exp(-\lambda_{Bi}t)) \\ & + \left(\frac{C_{Po}\lambda_{Pb}}{(\lambda_{Po} - \lambda_{Bi})(\lambda_{Po} - \lambda_{Pb})}\right)(exp(-\lambda_{Pb}t) - exp(-\lambda_{Po}t)) \end{aligned} \tag{0.5}$$

where Po, Pb and Bi stands $^{218}$Po, $^{214}$Pb and $^{214}$Bi respectively. The fourth progeny, $^{218}$Po has been deliberately omitted due to its short half-life of 164 µs.

During sampling, radon progeny is collected over the filter and the rate of collection (Bq/s) is defined as

$$C_i(s^{-1}) = \frac{C(i)V_{fl}S}{\lambda_i} \quad (0.6)$$

*C(i)* is the airborne radon progeny activity concentration (Bq $m^{-3}$);

$V_{fl}$ is the air flow through the sample ($m^3$); and

*S* the dimensionless collection efficiency of the target.

The build-up activity (A) of the respective isotopes during the sampling time $t_s$ and the measured decays (integral of the decay function in a given time interval $t_m$ after the sampling was stopped) is given in Figure 8.2 (A) (Hofmann et al., 2015). From the diagram, the featured times are designated such that $t_s$ = 1200 s, $t_d$ = 60 s and $t_m$ = 300 s. For the grab sampling method, a delay time interval $t_d$ is included to accommodate the delay between the end of sampling and the start of the measurement.

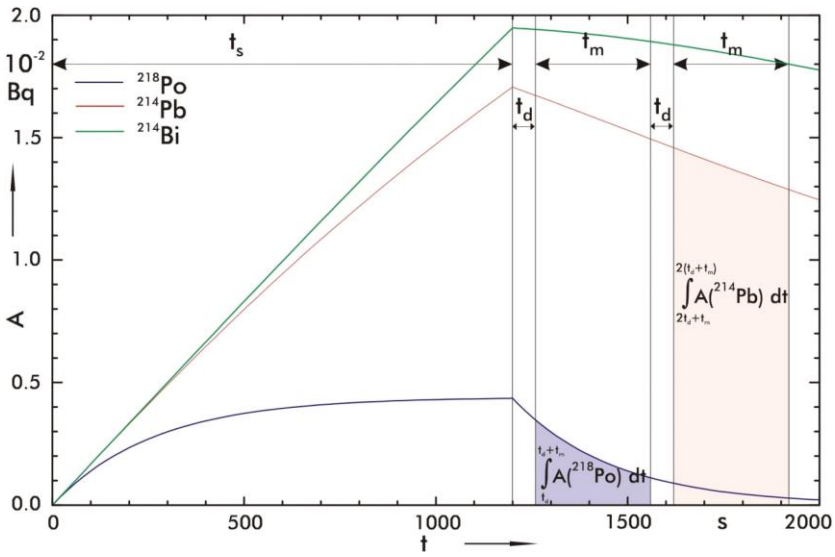


**Figure 0.2 (A): Collection and decay of short-lived radon progeny given an activity concentration C(RnP) of 1 Bq·$m^{-3}$ and a volume air flow $V_{fl}$ of $10^{-3}m^3$/min (Hofmann et al., 2015).**

After the collection is complete, the solution for equation 8.2 for the number of short-lived radon progeny on the target, $N_{di}$,($t > t_s$), is given by:

$$N_{d,Po}(t) = N_{c,Po}(t_s)exp(-\lambda_{Po}t) \quad (0.7)$$

$$N_{d,Pb}(t) = N_{c,Pb}(t_s)\, exp(-\lambda_{Pb}t) + \frac{N_{c,Po}(t_s)\lambda_{Po}}{\lambda_{Po} - \lambda_{Pb}}\, x\, (ex\, p(-\lambda_{Pb}t) - exp(-\lambda_{Po}t)) \quad (0.8)$$

$$N_{d,Bi}(t) = N_{c,Bi}(t_s)\, exp(-\lambda_{BI}t) + \frac{N_{c,Pb}(t_s)\lambda_{Pb}}{\lambda_{Bi} - \lambda_{Bi}}\, x\, (ex\, p(-\lambda_{Pb}t) - exp(-\lambda_{Bi}t)) + \left(\frac{N_{c,Po}(t_s)\lambda_{Po}\lambda_{Pb}}{(\lambda_{Bi} - \lambda_{Pb})(\lambda_{Po} - \lambda_{Pb})}\right)(ex\, p(-\lambda_{Pb}t) - ex\, p(-\lambda_{Bi}t)) + \left(\frac{N_{c,Po}(t_s)\lambda_{Po}\lambda_{Pb}}{(\lambda_{Po} - \lambda_{Bi})(\lambda_{Po} - \lambda_{Pb})}\right) x\, (ex\, p(-\lambda_{Bi}t) - exp(-\lambda_{Po}t)) \quad (0.9)$$

From figure 8.2 (A), it can be seen that there is a marked increase in the activity on the target during collection period $t \in [0: t_s]$ and a radioactive decay induced activity decrease after the end of the collection. During the time interval $t \in [t_d: t_d + t_m]$, the integral activity of the chosen isotope is the sum of the decays, $U$ on the target given by:

$$U_i(t_c, t_d, t_m) = \int_{t_d}^{t_d+t_m} N_{d,i}(t_c)\lambda_i\, dt \quad (0.10)$$

$$U_i(t_c, t_d, t_m) = \int_{t_d}^{t_d+t_m} A_i(t_c)\, dt \quad (0.11)$$

By applying spectra analysing technology, respective values of $U$ can be found by performing either gross α-count or α-β-counting rate of different particles in different delay time intervals.

## Appendix B: Moisture content, masses, areas, volumes, densities, porosity and fluxes

*Table A.1: Moisture content (mass fraction per dry weight)*

| Sample no | Mass of Beaker (g) | Mass of Beaker + "wet" soil (g) | Mass of "wet" soil (mW)(g) | Mass of beaker + "dry" soil (g) | Mass of dry soil (mD) (g) | mW - mD (g) | Dry weight mass fraction $M_w$ (g) |
|---|---|---|---|---|---|---|---|
| 1 | 184.2 | 434.2 | 250.0 | 412.2 | 228.0 | 22.0 | 0.10 |
| 2 | 188.3 | 438.6 | 250.3 | 420.9 | 232.6 | 17.7 | 0.08 |
| 3 | 188.4 | 438.2 | 249.8 | 423.3 | 234.9 | 14.9 | 0.06 |
| 4 | 193.0 | 443.0 | 250.0 | 419.3 | 226.3 | 23.7 | 0.10 |
| 5 | 190.0 | 440.0 | 250.0 | 424.3 | 234.3 | 15.7 | 0.07 |
| 6 | 191.6 | 442.2 | 250.6 | 423.3 | 231.7 | 18.9 | 0.08 |
| 7 | 189.4 | 440.1 | 250.7 | 419.3 | 229.9 | 20.8 | 0.09 |
| 8 | 184.4 | 439.2 | 254.8 | 422.8 | 238.4 | 16.4 | 0.07 |
| 9 | 190.0 | 441.1 | 251.1 | 423.6 | 233.6 | 17.5 | 0.07 |
| 10 | 186.6 | 437.2 | 250.6 | 404.5 | 217.9 | 32.7 | 0.15 |
| 11 | 186.7 | 437.4 | 250.7 | 419.7 | 233.0 | 17.7 | 0.08 |
| 12 | 190.1 | 440.5 | 250.4 | 425.8 | 235.7 | 14.7 | 0.06 |
| 13 | 189.4 | 439.9 | 250.5 | 426.0 | 236.6 | 13.9 | 0.06 |
| 14 | 188.5 | 438.7 | 250.2 | 423.0 | 234.5 | 15.7 | 0.07 |

| | | | | | | | |
|---|---|---|---|---|---|---|---|
| 15 | 191.6 | 442.0 | 250.4 | 415.4 | 223.8 | 26.6 | 0.12 |
| 16 | 193.1 | 443.7 | 250.6 | 433.2 | 240.1 | 10.5 | 0.04 |
| 17 | 184.2 | 434.7 | 250.5 | 414.2 | 230.0 | 20.5 | 0.09 |
| 18 | 188.4 | 439.1 | 250.7 | 423.7 | 235.3 | 15.4 | 0.07 |
| 19 | 190.0 | 440.5 | 250.5 | 425.2 | 235.2 | 15.3 | 0.07 |
| 20 | 191.6 | 442.2 | 250.6 | 428.1 | 236.5 | 14.1 | 0.06 |

*Table A.2: Mass, Areas, Volumes, Densities and Porosity (Short tubes)*

| **Tube #** | **Mass (kg)** | **Radius of tube (m)** | **Cross sectional area ($\pi r^2$) ($m^2$)** | **Sample thickness, L (m)** | **Sample volume ($m^3$)** | **Density of material ($kg/m^3$)** | **Specific Gravity ($kg/m^3$)** | **Porosity** |
|---|---|---|---|---|---|---|---|---|
| 1 | 0.268 | 0.0218 | 0.00149 | 0.112 | 0.000167 | 1602 | 2740 | 0.415 |
| 2 | 0.230 | 0.0218 | 0.00149 | 0.112 | 0.000167 | 1375 | 2740 | 0.498 |
| 3 | 0.235 | 0.0218 | 0.00149 | 0.112 | 0.000167 | 1405 | 2740 | 0.487 |
| 4 | 0.250 | 0.0218 | 0.00149 | 0.114 | 0.000170 | 1468 | 2740 | 0.464 |
| 5 | 0.250 | 0.0218 | 0.00149 | 0.112 | 0.000167 | 1494 | 2740 | 0.456 |
| 6 | 0.259 | 0.0218 | 0.00149 | 0.114 | 0.000170 | 1521 | 2740 | 0.445 |
| 7 | 0.280 | 0.0218 | 0.00149 | 0.112 | 0.000167 | 1674 | 2740 | 0.389 |
| 8 | 0.262 | 0.0218 | 0.00149 | 0.117 | 0.000175 | 1499 | 2740 | 0.453 |

| | | | | | | | | |
|---|---|---|---|---|---|---|---|---|
| 9 | 0.300 | 0.0218 | 0.00149 | 0.133 | 0.000199 | 1510 | 2740 | 0.449 |
| 10 | 0.265 | 0.0218 | 0.00149 | 0.115 | 0.000172 | 1543 | 2740 | 0.437 |
| 11 | 0.250 | 0.0218 | 0.00149 | 0.114 | 0.000170 | 1468 | 2740 | 0.464 |
| 12 | 0.270 | 0.0218 | 0.00149 | 0.117 | 0.000175 | 1545 | 2740 | 0.436 |
| 13 | 0.250 | 0.0218 | 0.00149 | 0.113 | 0.000169 | 1481 | 2740 | 0.459 |
| 14 | 0.320 | 0.0218 | 0.00149 | 0.145 | 0.000217 | 1478 | 2740 | 0.461 |
| 15 | 0.268 | 0.0218 | 0.00149 | 0.113 | 0.000169 | 1588 | 2740 | 0.42 |
| 16 | 0.251 | 0.0218 | 0.00149 | 0.109 | 0.000163 | 1542 | 2740 | 0.437 |
| 17 | 0.268 | 0.0218 | 0.00149 | 0.115 | 0.000172 | 1560 | 2740 | 0.431 |
| 18 | 0.250 | 0.0218 | 0.00149 | 0.110 | 0.000164 | 1522 | 2740 | 0.445 |
| 19 | 0.250 | 0.0218 | 0.00149 | 0.110 | 0.000164 | 1522 | 2740 | 0.445 |
| 20 | 0.263 | 0.0218 | 0.00149 | 0.112 | 0.000167 | 1572 | 2740 | 0.426 |

*Table A.3: Mass, Areas, Volumes, Densities and Porosity (Long tubes)*

| Tube # | Mass (kg) | Radius of tube (m) | Cross sectional area ($\pi r^2$) ($m^2$) | Sample thickness, L (m) | Sample volume ($m^3$) | Density of material ($kg/m^3$) | Specific Gravity ($kg/m^3$) | Porosity |
|---|---|---|---|---|---|---|---|---|
| 1 | 2.23 | 0.0218 | 0.00149 | 1.01 | 0.00151 | 1478 | 2740 | 0.461 |
| 2 | 2.30 | 0.0218 | 0.00149 | 1.01 | 0.00151 | 1525 | 2740 | 0.444 |
| 3 | 2.35 | 0.0218 | 0.00149 | 1.01 | 0.00151 | 1558 | 2740 | 0.432 |
| 4 | 2.39 | 0.0218 | 0.00149 | 1.01 | 0.00151 | 1584 | 2740 | 0.422 |
| 5 | 2.40 | 0.0218 | 0.00149 | 1.01 | 0.00151 | 1591 | 2740 | 0.419 |
| 6 | 2.20 | 0.0218 | 0.00149 | 1.01 | 0.00151 | 1458 | 2740 | 0.468 |
| 7 | 2.33 | 0.0218 | 0.00149 | 1.01 | 0.00151 | 1545 | 2740 | 0.436 |
| 8 | 2.38 | 0.0218 | 0.00149 | 1.01 | 0.00151 | 1578 | 2740 | 0.424 |
| 9 | 2.35 | 0.0218 | 0.00149 | 1.01 | 0.00151 | 1558 | 2740 | 0.432 |
| 10 | 2.40 | 0.0218 | 0.00149 | 1.01 | 0.00151 | 1591 | 2740 | 0.419 |
| 11 | 2.32 | 0.0218 | 0.00149 | 1.01 | 0.00151 | 1538 | 2740 | 0.439 |
| 12 | 2.30 | 0.0218 | 0.00149 | 1.01 | 0.00151 | 1525 | 2740 | 0.446 |
| 13 | 2.23 | 0.0218 | 0.00149 | 1.01 | 0.00151 | 1478 | 2740 | 0.461 |
| 14 | 2.30 | 0.0218 | 0.00149 | 1.01 | 0.00151 | 1525 | 2740 | 0.444 |
| 15 | 2.40 | 0.0218 | 0.00149 | 1.01 | 0.00151 | 1591 | 2740 | 0.419 |

| | | | | | | | | |
|---|---|---|---|---|---|---|---|---|
| 16 | 2.40 | 0.0218 | 0.00149 | 1.01 | 0.00151 | 1591 | 2740 | 0.419 |
| 17 | 2.40 | 0.0218 | 0.00149 | 1.01 | 0.00151 | 1591 | 2740 | 0.419 |
| 18 | 2.30 | 0.0218 | 0.00149 | 1.01 | 0.00151 | 1525 | 2740 | 0.444 |
| 19 | 2.30 | 0.0218 | 0.00149 | 1.01 | 0.00151 | 1525 | 2740 | 0.444 |
| 20 | 2.30 | 0.0218 | 0.00149 | 1.01 | 0.00151 | 1525 | 2740 | 0.444 |

*Table A.4: Flux calculations (Short tubes)*

| Sample No | Porosity (p) | Sample thickness, L (m) | Air height, h (m) | pL | pL/h | CΛpL | 1+ pL/h | Exposure time (T) (h) | Exposure time (T) (s) | (1+pL/h)T | Flux (Bq/(m.s)) |
|---|---|---|---|---|---|---|---|---|---|---|---|
| 1 | 0.46 | 0.112 | 1.05 | 0.052 | 0.049 | 339.08 | 1.05 | 144 | 518400 | 151.07 | 6.5E-4±7.2E-5 |
| 2 | 0.44 | 0.112 | 1.05 | 0.050 | 0.047 | 158.36 | 1.05 | 144 | 518400 | 150.81 | 3.1E-4±3.7E-5 |
| 3 | 0.43 | 0.112 | 1.05 | 0.048 | 0.046 | 349.35 | 1.05 | 144 | 518400 | 150.63 | 6.7E-4±7.4E-5 |
| 4 | 0.42 | 0.114 | 1.05 | 0.048 | 0.046 | 186.76 | 1.05 | 144 | 518400 | 150.59 | 3.6E-4±4.3E-5 |
| 5 | 0.42 | 0.112 | 1.05 | 0.047 | 0.045 | 155.88 | 1.04 | 144 | 518400 | 150.44 | 3.0E-4±3.7E-5 |
| 6 | 0.47 | 0.114 | 1.05 | 0.053 | 0.051 | 401.79 | 1.05 | 144 | 518400 | 151.31 | 7.8E-4±8.5E-5 |
| 7 | 0.44 | 0.112 | 1.05 | 0.049 | 0.047 | 420.03 | 1.05 | 144 | 518400 | 150.70 | 8.1E-4±8.8E-5 |

| | | | | | | | | | | | |
|---|---|---|---|---|---|---|---|---|---|---|---|
| 8 | 0.42 | 0.117 | 1.05 | 0.050 | 0.047 | 208.43 | 1.05 | 144 | 518400 | 150.81 | 4.0E-4±4.7E-5 |
| 9 | 0.43 | 0.133 | 1.05 | 0.057 | 0.055 | 525.76 | 1.05 | 144 | 518400 | 151.87 | 1.0E-3±1.1E-4 |
| 10 | 0.42 | 0.115 | 1.05 | 0.048 | 0.046 | 276.55 | 1.05 | 144 | 518400 | 150.61 | 5.3E-4±6.0E-5 |
| 11 | 0.44 | 0.114 | 1.05 | 0.050 | 0.048 | 273.49 | 1.05 | 144 | 518400 | 150.86 | 5.3E-4±5.9E-5 |
| 12 | 0.44 | 0.117 | 1.05 | 0.052 | 0.049 | 467.71 | 1.05 | 144 | 518400 | 151.12 | 9.0E-4±9.7E-5 |
| 13 | 0.46 | 0.113 | 1.05 | 0.052 | 0.050 | 262.51 | 1.05 | 144 | 518400 | 151.14 | 5.1E-4±5.8E-5 |
| 14 | 0.44 | 0.145 | 1.05 | 0.064 | 0.061 | 682.62 | 1.06 | 144 | 518400 | 152.82 | 1.3E-3±1.4E-4 |
| 15 | 0.42 | 0.113 | 1.05 | 0.047 | 0.045 | 88.12 | 1.05 | 144 | 518400 | 150.50 | 1.7E-4±2.4E-5 |
| 16 | 0.42 | 0.109 | 1.05 | 0.046 | 0.044 | 104.79 | 1.04 | 144 | 518400 | 150.27 | 2.0E-4±2.7E-5 |
| 17 | 0.42 | 0.115 | 1.05 | 0.048 | 0.046 | 151.20 | 1.05 | 144 | 518400 | 150.61 | 2.9E-4±3.6E-5 |
| 18 | 0.44 | 0.11 | 1.05 | 0.049 | 0.046 | 181.80 | 1.05 | 144 | 518400 | 150.69 | 3.5E-4±4.2E-5 |
| 19 | 0.44 | 0.11 | 1.05 | 0.049 | 0.046 | 648.64 | 1.05 | 144 | 518400 | 150.69 | 1.3E-3±1.3E-4 |
| 20 | 0.44 | 0.112 | 1.05 | 0.050 | 0.047 | 342.40 | 1.05 | 144 | 518400 | 150.81 | 6.6E-4±7.3E-5 |
| | | | | | | | | | **Average** | | **6.0E-5±6.7E-5** |

*Table A.5: Flux calculations (Long tubes)*

| Sample No | Porosity (p) | Sample thickness, L (m) | Air height, h (m) | pL | pL/h | CΛpL | 1+ pL/h | Exposure time (T) (h) | Exposure time (T) (s) | (1+pL/h)T | Flux (Bq/(m.s)) |
|---|---|---|---|---|---|---|---|---|---|---|---|
| 1 | 0.46 | 1.01 | 1.05 | 0.47 | 0.44 | 14804.82 | 1.44 | 144 | 518400 | 207.79 | 2.9E-2±2.9E-3 |
| 2 | 0.44 | 1.01 | 1.05 | 0.45 | 0.43 | 15020.62 | 1.43 | 144 | 518400 | 205.44 | 2.9E-2±2.9E-3 |
| 3 | 0.43 | 1.01 | 1.05 | 0.44 | 0.42 | 21639.04 | 1.42 | 144 | 518400 | 203.76 | 4.2E-2±4.2E-3 |
| 4 | 0.42 | 1.01 | 1.05 | 0.43 | 0.41 | 29201.53 | 1.41 | 144 | 518400 | 202.42 | 5.6E-2±5.7E-3 |
| 5 | 0.42 | 1.01 | 1.05 | 0.42 | 0.40 | 9528.81 | 1.40 | 144 | 518400 | 202.09 | 1.8E-2±1.9E-3 |
| 6 | 0.47 | 1.01 | 1.05 | 0.47 | 0.45 | 17367.65 | 1.45 | 144 | 518400 | 208.79 | 3.4E-2±3.4E-3 |
| 7 | 0.44 | 1.01 | 1.05 | 0.44 | 0.42 | 19089.66 | 1.42 | 144 | 518400 | 204.43 | 3.7E-2±3.8E-3 |
| 8 | 0.42 | 1.01 | 1.05 | 0.43 | 0.41 | 25732.10 | 1.41 | 144 | 518400 | 202.76 | 5.0E-2±5.0E-3 |
| 9 | 0.43 | 1.01 | 1.05 | 0.44 | 0.42 | 19640.14 | 1.42 | 144 | 518400 | 203.76 | 3.8E-2±3.9E-3 |
| 10 | 0.42 | 1.01 | 1.05 | 0.42 | 0.40 | 100377.15 | 1.40 | 144 | 518400 | 202.09 | *1.9E-1*±1.9E-2 |
| 11 | 0.44 | 1.01 | 1.05 | 0.44 | 0.42 | 13983.42 | 1.42 | 144 | 518400 | 204.77 | 2.7E-2±2.8E-3 |

| | | | | | | | | | | | |
|---|---|---|---|---|---|---|---|---|---|---|---|
| 12 | 0.44 | 1.01 | 1.05 | 0.45 | 0.43 | 31003.15 | 1.43 | 144 | 518400 | 205.44 | 6.0E-2±6.1E-3 |
| 13 | 0.46 | 1.01 | 1.05 | 0.47 | 0.44 | 11417.88 | 1.44 | 144 | 518400 | 207.79 | 2.2E-2±2.3E-3 |
| 14 | 0.44 | 1.01 | 1.05 | 0.45 | 0.43 | 10656.32 | 1.43 | 144 | 518400 | 205.44 | 2.1E-2±2.1E-3 |
| 15 | 0.42 | 1.01 | 1.05 | 0.42 | 0.40 | 14552.72 | 1.40 | 144 | 518400 | 202.09 | 2.8E-2±2.9E-3 |
| 16 | 0.42 | 1.01 | 1.05 | 0.42 | 0.40 | 10309.73 | 1.40 | 144 | 518400 | 202.09 | 2.0E-2±2.1E-3 |
| 17 | 0.42 | 1.01 | 1.05 | 0.42 | 0.40 | 25240.33 | 1.40 | 144 | 518400 | 202.09 | 4.9E-2±4.9E-3 |
| 18 | 0.44 | 1.01 | 1.05 | 0.45 | 0.43 | 33616.40 | 1.43 | 144 | 518400 | 205.44 | 6.5E-2±6.6E-3 |
| 19 | 0.44 | 1.01 | 1.05 | 0.45 | 0.43 | 31220.38 | 1.43 | 144 | 518400 | 205.44 | 6.0E-2±6.1E-3 |
| 20 | 0.44 | 1.01 | 1.05 | 0.45 | 0.43 | 15062.03 | 1.43 | 144 | 518400 | 205.44 | 2.9E-2±3.0E-3 |
| | | | | | | | | | **Average** | | **4.5E-2±4.6E-3** |

**Appendix C: Bateman recurrence equation**

$$f_{00} = \exp(-\lambda_0 t)$$

$$f_{11} = \exp(-\lambda_1 t)$$

$$f_{22} = \exp(-\lambda_2 t)$$

$$f_{33} = \exp(-\lambda_3 t)$$

where $\lambda_0$, $\lambda_1$ , $\lambda_2$ , and $\lambda_3$ are the decay constants for $^{222}Rn$ , $^{218}Po$ , $^{214}Pb$ , $^{214}Bi$ , respectively ($s^{-1}$), and t is the time (s).

The $f_{ij}$ factors are defined as follows:

$f_{01} = \frac{(f_{00} - f_{11})}{(\lambda_1 - \lambda_0)}$ (for decay of initially present $^{222}Rn$ to $^{218}Po$ )

$f_{12} = \frac{(f_{11} - f_{22})}{(\lambda_2 - \lambda_1)}$ (for decay of initially present $^{218}Po$ to $^{214}Pb$)

$f_{23} = \frac{(f_{22} - f_{33})}{(\lambda_3 - \lambda_2)}$ (for decay of initially present $^{214}Pb$ to $^{214}Bi$)

$f_{02} = \frac{(f_{01} - f_{12})}{(\lambda_2 - \lambda_0)}$ (for decay of initially present $^{222}Rn$ to $^{214}Pb$)

$f_{13} = \frac{(f_{12} - f_{23})}{(\lambda_3 - \lambda_1)}$ (for decay of initially present $^{218}Po$ to $^{214}Bi$)

$f_{03} = \frac{(f_{02} - f_{13})}{(\lambda_3 - \lambda_0)}$ (for decay of initially present $^{222}Rn$ to $^{214}Bi$)

The recurrence nature of this process can easily be seen from this sequence of equations. Once all the "$f$ factors" have been defined, then solving for the concentrations of radon and radon progeny is simple.

$$C_0 = C_{0.0} f_{00}$$

$$C_1 = C_{0.0} \lambda_1 f_{00} + C_{1.0} f_{11}$$

$$C_2 = C_{0.0}\lambda_1\lambda_2 f_{02} + C_{1.0}\lambda_2 f_{12} + C_{2.0} f_{22}$$

$$C_3 = C_{0.0}\lambda_1\lambda_2\lambda_3 f_{03} + C_{1.0}\lambda_2\lambda_3 f_{13} + C_{2.0}\lambda_3 f_{23} + C_{3.0} f_{33}$$

where $C_{0.0}$, $C_{1.0}$, $C_{2.0}$, and $C_{3.0}$ are the initial concentrations (or activities) of $^{222}Rn$ , $^{218}Po$ , $^{214}Pb$ , and $^{214}Bi$, respectively ( Bq $m^{-3}$ or Bq) and $C_0$, $C_1$, $C_2$, and $C_3$ are the concentrations (or activities) of $^{222}Rn$ , $^{218}Po$ , $^{214}Pb$ , and $^{214}Bi$, respectively (Bq $m^{-3}$ or Bq), as a function of time.

## Appendix D: Weather data for Odendalsrus

*Table A.6: Summarised weather data for sampling periods. The weather station measured wind at a height of 10 m. This was accounted for by the dispersion model and the values were converted to ground level.*

| Date | Time | Position | Wind speed (m/s) | Temperature (ºC) | Wind direction (degrees) | Standard Deviation on wind direction (degrees) |
|---|---|---|---|---|---|---|
| **19-08-2017** | 09:30 | 27º50'11''S 26º40'1" E | 5.59 | 10.38 | 38.52 | 9.48 |
| | 11:12 | 27º50'16"S 26º39'57" E | 5.68 | 14.56 | 26.90 | 10.39 |
| | 12:00 | 27º50'18"S 26º39'54" E | 4.64 | 15.86 | 28.98 | 15.26 |
| | | | | | | |
| | 13:32 | 27º50'11"S 26º40'4" E | 3.18 | 17.45 | 27.36 | 21.39 |
| | 14:30 | 27º50'15"S 26º40'1" E | 2.22 | 17.46 | 62.75 | 21.78 |
| | 15:26 | 27º50'18"S 26º39'58" E | 2.85 | 17.10 | 33.98 | 16.74 |
| | 16:12 | 27º50'21"S 26º39'56" E | 3.28 | 16.48 | 52.01 | 11.44 |
| | | | | | | |

| | | | | | | |
|---|---|---|---|---|---|---|
| **20-08-2017** | 07:50 | 27⁰49'28"S 26⁰40'0" E | 4.71 | 8.62 | 35.43 | 8.78 |
| | 09:18 | 27⁰49'30"S 26⁰40'7" E | 5.66 | 12.75 | 18.64 | 11.06 |
| | 09:57 | 27⁰49'26"S 26⁰40'10" E | 5.60 | 14.74 | 6.19 | 13.49 |
| | 10:38 | 27⁰49'24"S 26⁰40'9" E | 5.00 | 15.35 | 5.73 | 14.42 |
| | | | | | | |
| | 13:08 | 27⁰50'11"S 26⁰40'10" E | 3.41 | 18.66 | 23.07 | 17.95 |
| | 13:54 | 27⁰50'13"S 26⁰40'7" E | 2.99 | 19.34 | 359.93 | 22.61 |
| | 14:50 | 27⁰50'17"S 26⁰40'9" E | 2.69 | 19.17 | 355.06 | 20.77 |
| | 15:49 | 27⁰50'22"S 26⁰40'5" E | 2.67 | 18.86 | 347.22 | 19.18 |
| | | | | | | |
| **21-08-2017** | 07:39 | 27⁰50'11"S 26⁰40'0" E | 3.72 | 10.27 | 13.66 | 9.33 |
| | 08:35 | 27⁰50'15"S 26⁰39'56" E | 4.97 | 13.68 | 4.32 | 11.77 |
| | 09:25 | 27⁰50'18"S 26⁰39'54" E | 5.13 | 16.00 | 6.22 | 11.83 |

| | | | | | | |
|---|---|---|---|---|---|---|
| | 10:28 | 27⁰50'24"S 26⁰39'51" E | 4.37 | 18.53 | 339.74 | 14.23 |
| | 11:14 | 27⁰50'28"S 26⁰39'51" E | 3.45 | 20.24 | 332.50 | 15.73 |
| | | | | | | |
| | 13:00 | 27⁰50'10"S 26⁰40'22" E | 3.50 | 22.44 | 313.74 | 20.23 |
| | 13:52 | 27⁰50'12"S 26⁰40'27" E | 3.72 | 23.35 | 284.30 | 15.80 |
| | 15:24 | 27⁰50'15"S 26⁰40'35" E | 3.81 | 23.47 | 277.88 | 15.17 |
| | | | | | | |
| **26-08-2017** | 08:51 | 27⁰49'46"S 26⁰40'15" E | 8.26 | 12.78 | 41.49 | 8.10 |
| | 09:43 | 27⁰49'43"S 26⁰40'18" E | 7.65 | 14.63 | 31.58 | 9.25 |
| | 10:33 | 27⁰49'40"S 26⁰40'19" E | 6.74 | 16.23 | 26.61 | 11.40 |
| | 11:27 | 27⁰49'36"S 26⁰40'21" E | 5.95 | 18.37 | 10.66 | 12.53 |
| | | | | | | |
| | 13:19 | 27⁰50'11"S 26⁰40'18" E | 4.42 | 21.48 | 337.84 | 17.65 |

| | | | | | | |
|---|---|---|---|---|---|---|
| | 14:12 | 27⁰50'15"S 26⁰40'20" E | 3.45 | 22.02 | 334.52 | 21.53 |
| | 15:04 | 27⁰50'18"S 26⁰40'22" E | 3.75 | 21.85 | 318.49 | 15.43 |
| | 16:04 | 27⁰50'22"S 26⁰40'26" E | 3.46 | 21.74 | 315.75 | 14.07 |
| | | | | | | |
| **27-08-2017** | 08:02 | 27⁰50'11"S 26⁰40'4" E | 2.89 | 12.56 | 19.00 | 11.68 |
| | 08:50 | 27⁰50'14"S 26⁰40'2" E | 3.21 | 15.06 | 0.55 | 14.40 |
| | 09:43 | 27⁰50'18"S 26⁰40'0" E | 3.80 | 16.70 | 322.63 | 12.68 |
| | | | | | | |
| | 11:51 | 27⁰49'30"S 26⁰39'56" E | 2.41 | 21.05 | 282.24 | 22.69 |
| | 13:01 | 27⁰49'27"S 26⁰40'54" E | 1.80 | 22.45 | 324.32 | 34.14 |
| | 13:50 | 27⁰49'26"S 26⁰39'51" E | 1.67 | 22.73 | 303.27 | 30.50 |

## Appendix E: Flowrates, sampling times, background counts and gross counts

*Table A.7: Flowrates, sampling times, background and gross counts*

| Date | Time | Position | Flow rate (L/min) | Sampling time (minutes) | Background counts (cpm) | Gross count 1 | Gross count 2 | Gross count 3 |
|---|---|---|---|---|---|---|---|---|
| **19-08-2017** | 09:30 | 27⁰50'11''S 26⁰40'1" E | 14 | 10 | 0.99 | 17.30 | 14.50 | 24.60 |
| **DOWNWIND** | 11:12 | 27⁰50'16"S 26⁰39'57" E | 14 | 10 | 0 | 8.33 | 11.70 | 5.60 |
| | 12:00 | 27⁰50'18"S 26⁰39'54" E | 14 | 10 | 0 | 4.66 | 5.62 | 3.00 |
| | | | | | | | | |
| | 13:32 | 27⁰50'11"S 26⁰40'4" E | 14 | 10 | 0.99 | 3.66 | 2.75 | 2.60 |
| | 14:30 | 27⁰50'15"S 26⁰40'1" E | 14 | 10 | 0.99 | 6.99 | 22.2 | 32.60 |
| | 15:26 | 27⁰50'18"S 26⁰39'58" E | 14 | 10 | 0.99 | 4.33 | 3.25 | 2.20 |
| | 16:12 | 27⁰50'21"S 26⁰39'56" E | 14 | 10 | 0 | 3.33 | 4.00 | 3.00 |
| **UPWIND** | | | | | | | | |
| **20-08-2017** | 07:50 | 27⁰49'28"S 26⁰40'0" E | 14 | 10 | 0.99 | 10.20 | 12.00 | 12.20 |

| | | | | | | | | |
|---|---|---|---|---|---|---|---|---|
| | 09:18 | 27⁰49'30"S 26⁰40'7" E | 14 | 10 | 0 | 7.66 | 7.24 | 7.99 |
| | 09:57 | 27⁰49'26"S 26⁰40'10" E | 14 | 10 | 0 | 20.70 | 31.9 | 8.79 |
| | 10:38 | 27⁰49'24"S 26⁰40'9" E | 14 | 10 | 0 | 8.99 | 10.60 | 27.10 |
| **DOWNWIND** | | | | | | | | |
| | 13:08 | 27⁰50'11"S 26⁰40'10" E | 14 | 10 | 0 | 2.33 | 1.87 | 2.20 |
| | 13:54 | 27⁰50'13"S 26⁰40'7" E | 14 | 10 | 0 | 3.33 | 7.12 | 2.00 |
| | 14:50 | 27⁰50'17"S 26⁰40'9" E | 14 | 10 | 0 | 4.33 | 3.00 | 3.40 |
| | 15:49 | 27⁰50'22"S 26⁰40'5" E | 14 | 10 | 0 | 11.7 | 3.37 | 2.60 |
| **DOWNWIND** | | | | | | | | |
| **21-08-2017** | 07:39 | 27⁰50'11"S 26⁰40'0" E | 14 | 10 | 0.99 | 29.30 | 27.50 | 24.80 |
| | 08:35 | 27⁰50'15"S 26⁰39'56" E | 14 | 10 | 0 | 20.00 | 21.70 | 19.40 |
| | 09:25 | 27⁰50'18"S 26⁰39'54" E | 14 | 10 | 0 | 21.00 | 16.20 | 12.00 |
| | 10:28 | 27⁰50'24"S 26⁰39'51" E | 14 | 10 | 0.99 | 11.30 | 8.49 | 5.80 |

| | | | | | | | | |
|---|---|---|---|---|---|---|---|---|
| | 11:14 | 27⁰50'28"S 26⁰39'51" E | 14 | 10 | 0 | 9.66 | 5.25 | 6.00 |
| **DOWNWIND** | | | | | | | | |
| | 13:00 | 27⁰50'10"S 26⁰40'22" E | 14 | 10 | 0 | 5.33 | 6.25 | 3.00 |
| | 13:52 | 27⁰50'12"S 26⁰40'27" E | 14 | 10 | 0 | 4.66 | 2.37 | 2.00 |
| | 15:24 | 27⁰50'15"S 26⁰40'35" E | 14 | 10 | 0 | 2.34 | 2.37 | 2.40 |
| **UPWIND** | | | | | | | | |
| **26-08-2017** | 08:51 | 27⁰49'46"S 26⁰40'15" E | 14 | 10 | 0 | 9.33 | 8.12 | 6.00 |
| | 09:43 | 27⁰49'43"S 26⁰40'18" E | 14 | 10 | 0 | 8.99 | 7.99 | 5.80 |
| | 10:33 | 27⁰49'40"S 26⁰40'19" E | 14 | 10 | 0 | 5.00 | 6.87 | 7.19 |
| | 11:27 | 27⁰49'36"S 26⁰40'21" E | 14 | 10 | 0.99 | 8.66 | 6.75 | 5.40 |
| **DOWNWIND** | | | | | | | | |
| | 13:19 | 27⁰50'11"S 26⁰40'18" E | 14 | 10 | 0 | 7.99 | 4.87 | 6.60 |
| | 14:12 | 27⁰50'15"S 26⁰40'20" E | 14 | 10 | 0 | 8.33 | 7.37 | 5.80 |
| | 15:04 | 27⁰50'18"S 26⁰40'22" E | 14 | 10 | 0.99 | 4.33 | 3.37 | 3.40 |

| | | | | | | | | |
|---|---|---|---|---|---|---|---|---|
| | 16:04 | 27⁰50'22"S 26⁰40'26" E | 14 | 10 | 0 | 1.67 | 3.87 | 3.00 |
| **DOWNWIND** | | | | | | | | |
| **27-08-2017** | 08:02 | 27⁰50'11"S 26⁰40'4" E | 14 | 10 | 0.99 | 25.3 | 23.6 | 21.2 |
| | 08:50 | 27⁰50'14"S 26⁰40'2" E | 14 | 10 | 0 | 19.00 | 15.00 | 11.80 |
| | 09:43 | 27⁰50'18"S 26⁰40'0" E | 14 | 10 | 0.99 | 11.00 | 9.74 | 8.99 |
| **UPWIND** | | | | | | | | |
| | 11:51 | 27⁰49'30"S 26⁰39'56" E | 14 | 10 | 0 | 8.33 | 5.25 | 3.80 |
| | 13:01 | 27⁰49'27"S 26⁰40'54" E | 14 | 10 | 0 | 4.33 | 3.50 | 3.40 |
| | 13:50 | 27⁰49'26"S 26⁰39'51" E | 14 | 10 | 0.99 | 1.67 | 2.87 | 3.15 |
| | 14:39 | 27⁰49'25"S 26⁰39'47" E | 14 | 10 | 0 | 3.00 | 3.50 | 3.60 |

## Appendix F: Radon, daughter concentrations, EEC and F factor

*Table A.8: Radon, daughter concentrations, EEC and F factor*

| Date | Time | Position | C (RaA) (Bq/m³) | C (RaB) (Bq/m³) | C (RaC) (Bq/m³) | EEC (Bq/m³) | Average Rn (AlphaGuard) (Bq/m³) | F factor |
|---|---|---|---|---|---|---|---|---|
| **19-08-2017** | 09:30 | 27°50'11"S 26°40'1" E | 17.91±1.90 | 6.35±0.45 | 0 | 5.15±0.44 | 10.25±0.23 | 0.502±0.044 |
| **DOWNWIND** | 11:12 | 27°50'16"S 26°39'57" E | 3.00±1.30 | 0.55±0.26 | 0.41±0.34 | 0.76±0.40 | 8.50±0.21 | 0.089±0.047 |
| | 12:00 | 27°50'18"S 26°39'54" E | 2.16±0.97 | 0.38±0.20 | 0.05±0.26 | 0.44±0.30 | 8.44±0.21 | 0.052±0.036 |
| | | | | | | | | |
| | 13:32 | 27°50'11"S 26°40'4" E | 2.15±0.84 | 0 | 0 | 0.23±0.09 | 6.13±0.18 | 0.037±0.014 |
| | 14:30 | 27°50'15"S 26°40'1" E | 7.11±1.66 | 7.17±0.51 | 0 | 4.44±0.44 | 15.50±0.28 | 0.287±0.029 |
| | 15:26 | 27°50'18"S 26°39'58" E | 2.23±0.88 | 0 | 0 | 0.23±0.09 | 6.19±0.19 | 0.039±0.015 |
| | 16:12 | 27°50'21"S 26°39'56" E | 1.68±0.85 | 0.50±0.20 | 0 | 0.44±0.19 | 4.63±0.16 | 0.094±0.041 |
| **UPWIND** | | | | | | | | |
| **20-08-2017** | 07:50 | 27°49'28"S 26°40'0" E | 6.27±1.51 | 1.82±0.34 | 0 | 1.59±0.33 | 13.25±0.26 | 0.120±0.025 |
| | 09:18 | 27°49'30"S 26°40'7" E | 5.30±1.27 | 1.71±0.28 | 0 | 1.44±0.28 | 8.44±0.21 | 0.170±0.033 |

| | | | | | | | | |
|---|---|---|---|---|---|---|---|---|
| | 09:57 | 27⁰49'26"S 26⁰40'10" E | 2.87±2.01 | 0 | 2.53±0.50 | 0.87±0.40 | 12.69±0.25 | 0.069±0.032 |
| | 10:38 | 27⁰49'24"S 26⁰40'9" E | 12.42±1.61 | 7.39±0.46 | 0 | 5.11±0.40 | 15.81±0.28 | 0.323±0.026 |
| **DOWNWIND** | | | | | | | | |
| | 13:08 | 27⁰50'11"S 26⁰40'10" E | 1.69±0.69 | 0.48±0.18 | 0 | 0.43±0.16 | 10.75±0.23 | 0.039±0.015 |
| | 13:54 | 27⁰50'13"S 26⁰40'7" E | 0 | 0 | 0.68±0.24 | 0.26±0.09 | 20.63±0.32 | 0.013±0.005 |
| | 14:50 | 27⁰50'17"S 26⁰40'9" E | 3.09±0.91 | 0.73±0.20 | 0 | 0.70±0.20 | 10.94±0.24 | 0.064±0.018 |
| | 15:49 | 27⁰50'22"S 26⁰40'5" E | 8.04±1.30 | 0.41±0.19 | 0 | 1.06±0.23 | 7.66±0.19 | 0.138±0.031 |
| **DOWNWIND** | | | | | | | | |
| **21-08-2017** | 07:39 | 27⁰50'11"S 26⁰40'0" E | 17.8±2.4 | 4.05±0.47 | 0 | 3.95±0.50 | 20.63±0.32 | 0.192±0.024 |
| | 08:35 | 27⁰50'15"S 26⁰39'56" E | 11.8±2.1 | 3.71±0.42 | 0 | 3.15±0.43 | 20.13±0.32 | 0.157±0.022 |
| | 09:25 | 27⁰50'18"S 26⁰39'54" E | 12.3±1.9 | 1.96±0.35 | 0 | 2.30±0.38 | 23.38±0.34 | 0.099±0.016 |
| | 10:28 | 27⁰50'24"S 26⁰39'51" E | 6.2±1.4 | 0.17±0.26 | 0 | 0.74±0.28 | 10.69±0.23 | 0.069±0.026 |
| | 11:14 | 27⁰50'28"S 26⁰39'51" E | 6.9±1.3 | 1.29±0.25 | 0 | 1.40±0.27 | 20.25±0.32 | 0.069±0.013 |
| **DOWNWIND** | | | | | | | | |
| | 13:00 | 27⁰50'10"S 26⁰40'22" E | 2.03±1.02 | 0.25±0.21 | 0 | 0.38±0.32 | 13.13±0.26 | 0.029±0.024 |

| | | | | | | | | |
|---|---|---|---|---|---|---|---|---|
| | 13:52 | 27⁰50'12"S 26⁰40'27" E | 3.08±0.88 | 0.36±0.18 | 0 | 0.51±0.18 | 20.50±0.32 | 0.025±0.009 |
| | 15:24 | 27⁰50'15"S 26⁰40'35" E | 1.52±0.71 | 0.49±0.19 | 0 | 0.41±0.17 | 8.38±0.21 | 0.049±0.020 |
| **UPWIND** | | | | | | | | |
| **26-08-2017** | 08:51 | 27⁰49'46"S 26⁰40'15" E | 5.28±1.33 | 0.98±0.26 | 0 | 1.06±0.27 | 3.80±0.14 | 0.280±0.073 |
| | 09:43 | 27⁰49'43"S 26⁰40'18" E | 5.01±1.31 | 0.93±0.26 | 0 | 1.00±0.27 | 8.44±0.21 | 0.119±0.032 |
| | 10:33 | 27⁰49'40"S 26⁰40'19" E | 3.19±1.09 | 1.51±0.27 | 0 | 1.11±0.25 | 6.91±0.19 | 0.161±0.037 |
| | 11:27 | 27⁰49'36"S 26⁰40'21" E | 4.99±1.27 | 0.24±0.25 | 0 | 0.65±0.26 | 1.48±0.09 | 0.438±0.177 |
| **DOWNWIND** | | | | | | | | |
| | 13:19 | 27⁰50'11"S 26⁰40'18" E | 6.17 ±1.23 | 1.53±0.26 | 0 | 1.44±0.26 | 6.19±0.18 | 0.232±0.042 |
| | 14:12 | 27⁰50'15"S 26⁰40'20" E | 4.84±1.27 | 1.00±0.26 | 0 | 1.02±0.26 | 13.38±0.26 | 0.077±0.019 |
| | 15:04 | 27⁰50'18"S 26⁰40'22" E | 2.66±0.92 | 0 | 0 | 0.28±0.10 | 10.88±0.24 | 0.026±0.009 |
| | 16:04 | 27⁰50'22"S 26⁰40'26" E | 0.52±0.69 | 0.52±0.20 | 0 | 0.32±0.17 | 8.38±0.21 | 0.039±0.021 |
| **DOWNWIND** | | | | | | | | |
| **27-08-2017** | 08:02 | 27⁰50'11"S 26⁰40'4" E | 15.3±2.3 | 3.35±0.42 | 0 | 3.33±0.46 | 19.88±0.32 | 0.168±0.023 |
| | 08:50 | 27⁰50'14"S 26⁰40'2" E | 11.4±1.9 | 2.03±0.32 | 0 | 2.24±0.37 | 8.31±0.21 | 0.269±0.045 |

| | | | | | | | | |
|---|---|---|---|---|---|---|---|---|
| | 09:43 | 27⁰50'18"S 26⁰40'0" E | 6.7±1.5 | 1.05±0.26 | 0 | 1.24±0.31 | 8.13±0.20 | 0.152±0.038 |
| **UPWIND** | | | | | | | | |
| | 11:51 | 27⁰49'30"S 26⁰39'56" E | 5.08±1.19 | 0.60±0.22 | 0 | 0.84±0.24 | 7.00±0.19 | 0.121±0.034 |
| | 13:01 | 27⁰49'27"S 26⁰40'54" E | 2.84±0.92 | 0.68±0.21 | 0 | 0.65±0.20 | 7.91±0.20 | 0.082±0.026 |
| | 13:50 | 27⁰49'26"S 26⁰39'51" E | 0.84±0.68 | 0 | 0 | 0.09±0.07 | 5.69±0.17 | 0.016±0.012 |
| | 14:39 | 27⁰49'25"S 26⁰39'47" E | 1.94±0.83 | 0.75±0.21 | 0 | 0.59±0.19 | 7.25±0.19 | 0.081±0.027 |

## Appendix G: Corrected side-view emissions

*Table A.9: Corrected side-view emissions*

| Source | top length(m) | Corrected top length (m) | bottom length(m) | Corrected bottom length(m) | Height (m) | Corrected height (m) | base area(m²) | Corrected areas (m²) | Breeze area (A) (m²) | Correction Factor Area (A) | Corrected Emission rate (A) (m²) |
|---|---|---|---|---|---|---|---|---|---|---|---|
| ***Side A: corrected side view areas*** | | | | | | | | | | | |
| ***level 1 (bottom)*** | 964.33 | 1212.16 | 982.22 | 1234.65 | 10.46 | 13.15 | 10181.12 | 16086.67 | 8426.89 | 1.91 | 0.19 |
| ***level 2*** | 957.03 | 1202.99 | 951.67 | 1196.25 | 10.46 | 13.15 | 9983.15 | 15773.87 | 5284.57 | 2.98 | 0.30 |
| ***level 3*** | 946.46 | 1189.70 | 933.75 | 1173.72 | 10.46 | 13.15 | 9834.14 | 15538.42 | 5558.24 | 2.80 | 0.28 |
| ***level 4*** | 921.22 | 1157.97 | 903.15 | 1135.26 | 10.46 | 13.15 | 9542.08 | 15076.95 | 11936.22 | 1.26 | 0.13 |
| ***level 5 (top most)*** | 903.15 | 1135.26 | 882.74 | 1109.60 | 10.46 | 13.15 | 9340.81 | 14758.94 | 31183.46 | 0.47 | 0.05 |
| ***Side B: corrected side view areas*** | | | | | | | | | | | |
| ***level 1 (bottom)*** | 221.00 | 277.80 | 225.60 | 283.58 | 10.46 | 13.15 | 2335.87 | 3690.79 | 1220.81 | 3.02 | 0.31 |
| ***level 2*** | 208.38 | 261.93 | 215.43 | 270.80 | 10.46 | 13.15 | 2216.67 | 3502.45 | 899.28 | 3.89 | 0.40 |
| ***level 3*** | 195.95 | 246.31 | 204.69 | 257.30 | 10.46 | 13.15 | 2095.48 | 3310.97 | 917.86 | 3.61 | 0.37 |
| ***level 4*** | 177.96 | 223.70 | 186.12 | 233.95 | 10.46 | 13.15 | 1904.26 | 3008.83 | 1132.72 | 2.66 | 0.27 |
| ***level 5 (top most)*** | 153.72 | 193.23 | 170.36 | 214.14 | 10.46 | 13.15 | 1695.05 | 2678.26 | 1542.44 | 1.74 | 0.18 |

| | | | | | | | | | | | |
|---|---|---|---|---|---|---|---|---|---|---|---|
| ***Side C: corrected side view areas*** | | | | | | | | | | | |
| ***level 1 (bottom)*** | 324.32 | 407.67 | 331.43 | 416.61 | 10.46 | 13.15 | 3429.80 | 5419.25 | 5967.39 | 0.91 | 0.09 |
| ***level 2*** | 1209.35 | 1520.15 | 1245.47 | 1565.56 | 10.46 | 13.15 | 12839.54 | 20287.11 | 3895.51 | 5.21 | 0.53 |
| ***level 3*** | 1170.18 | 1470.92 | 1186.79 | 1491.80 | 10.46 | 13.15 | 12327.76 | 19478.46 | 6589.75 | 2.96 | 0.30 |
| ***level 4 (top most)*** | 1119.18 | 1406.81 | 1142.09 | 1435.61 | 10.46 | 13.15 | 11827.21 | 18687.57 | 9553.04 | 1.96 | 0.20 |
| ***Side D: corrected side view areas*** | | | | | | | | | | | |
| ***level 1 (bottom)*** | 489.92 | 615.83 | 505.20 | 635.04 | 10.46 | 13.15 | 5204.82 | 8223.86 | 5448.37 | 1.51 | 0.15 |
| ***level 2*** | 882.01 | 1108.69 | 888.46 | 1116.79 | 10.46 | 13.15 | 9260.16 | 14631.51 | 2044.92 | 7.16 | 0.73 |
| ***level 3*** | 833.41 | 1047.60 | 836.56 | 1051.56 | 10.46 | 13.15 | 8734.51 | 13800.96 | 2866.58 | 4.81 | 0.49 |
| ***level 4*** | 811.85 | 1020.50 | 821.72 | 1032.90 | 10.46 | 13.15 | 8544.13 | 13500.14 | 2823.09 | 4.78 | 0.49 |
| ***level 5 (top most)*** | 776.47 | 976.02 | 799.52 | 1005.00 | 10.46 | 13.15 | 8242.96 | 13024.29 | 2454.03 | 5.31 | 0.54 |
| ***Side D: corrected side view areas*** | | | | | | | | | | | |
| ***level 1 (bottom)*** | 483.05 | 607.19 | 507.28 | 637.65 | 10.46 | 13.15 | 5179.76 | 8184.28 | 4896.18 | 1.67 | 0.17 |
| ***level 2*** | 467.55 | 587.71 | 475.69 | 597.94 | 10.46 | 13.15 | 4933.47 | 7795.12 | 1444.57 | 5.40 | 0.55 |
| ***level 3*** | 453.79 | 570.41 | 462.06 | 580.81 | 10.46 | 13.15 | 4790.21 | 7568.76 | 1656.64 | 4.57 | 0.46 |
| ***level 4*** | 440.31 | 553.47 | 447.30 | 562.26 | 10.46 | 13.15 | 4642.50 | 7335.38 | 1452.06 | 5.05 | 0.51 |

| | | | | | | | | | | | |
|---|---|---|---|---|---|---|---|---|---|---|---|
| ***level 5 (top most)*** | 418.03 | 525.46 | 432.21 | 543.29 | 10.46 | 13.15 | 4447.04 | 7026.55 | 3903.97 | 1.80 | 0.18 |
| ***Side E: corrected side view areas*** | | | | | | | | | | | |
| ***level 1 (bottom)*** | 483.05 | 607.19 | 507.28 | 637.65 | 10.46 | 13.15 | 5179.76 | 8184.28 | 4896.18 | 1.67 | 0.17 |
| ***level 2*** | 467.55 | 587.71 | 475.69 | 597.94 | 10.46 | 13.15 | 4933.47 | 7795.12 | 1444.57 | 5.40 | 0.55 |
| ***level 3*** | 453.79 | 570.41 | 462.06 | 580.81 | 10.46 | 13.15 | 4790.21 | 7568.76 | 1656.64 | 4.57 | 0.46 |
| ***level 4*** | 440.31 | 553.47 | 447.30 | 562.26 | 10.46 | 13.15 | 4642.50 | 7335.38 | 1452.06 | 5.05 | 0.51 |
| ***level 5 (top most)*** | 418.03 | 525.46 | 432.21 | 543.29 | 10.46 | 13.15 | 4447.04 | 7026.55 | 3903.97 | 1.80 | 0.18 |

## Appendix H: Modelling report extract (day 3 morning)

```
1                    ISCST3 - (DATED 02035)
              ISC3MSPx     PC (32 BIT) VERSION  4.1.3
             (C) COPYRIGHT 1991-2010, Trinity Consultants
 Run Began on  5/18/2018 at  1:03:05

 ** BREEZE ISC
 ** Trinity Consultants
 ** VERSION  8.0

 CO STARTING
 CO TITLEONE  Day 3 Downwind (Morning)
 CO MODELOPT  CONC  RURAL
 CO RUNORNOT  RUN
 CO AVERTIME  1  2  3  4  PERIOD
 CO POLLUTID  RADON
 CO HALFLIFE  328320
 CO TERRHGTS  FLAT
 CO FLAGPOLE  1.5
 CO FINISHED
```

```
1 *** ISCST3 - VERSION 02035 ***    ***  Day 3 Downwind (Morning)
***        05/18/18

                                        ***     MODEL SETUP OPTIONS SUMMARY       ***

 - - - - - - - - - - - - - - - - - - - - - - - - - - - - - - - - - - - - - - - - - - - - - - - - - - - - - - - - - -
- - - - - - - - - -

 **Intermediate Terrain Processing is Selected

 **Model Is Setup For Calculation of Average CONCentration Values.

 **Model Uses User-Specified Options:
            1. Final Plume Rise.
            2. Stack-tip Downwash.
            3. Buoyancy-induced Dispersion.
            4. Calms Processing Routine.
            5. Not Use Missing Data Processing Routine.
            6. Default Wind Profile Exponents.
            7. Default Vertical Potential Temperature Gradients.

 **Model Assumes Receptors on FLAT Terrain.

 **Model Accepts FLAGPOLE Receptor Heights.
```

```
 **Model Calculates  4 Short Term Average(s) of:    1-HR    2-HR    3-HR    4-HR
     and Calculates PERIOD Averages

 **This Run Includes:     51 Source(s);       1 Source Group(s); and        5 Receptor(s)

 **The Model Assumes A Pollutant Type of:  RADON

 **Model Set To Continue RUNning After the Setup Testing.
 **NOTE:  The Following Flags May Appear Following CONC Values:  c for Calm Hours
                                                                 m for Missing Hours
                                                                 b for Both Calm and Missing Hours

 **Misc. Inputs:  Anem. Hgt. (m) =    10.00 ;    Decay Coef. =   0.2111E-05 ;    Rot. Angle =     0.0
Emission Units = GRAMS/SEC                                    ;
Emission Rate Unit Factor =   0.10000E+07
Output Units    = MICROGRAMS/M**3

                                          *** AREAPOLY SOURCE DATA ***

             NUMBER EMISSION RATE    LOCATION OF AREA   BASE     RELEASE  NUMBER      INIT.    EMISSION RATE
   SOURCE     PART.  (GRAMS/SEC        X         Y      ELEV.    HEIGHT  OF VERTS.     SZ      SCALAR VARY
```

```
      ID        CATS.   /METER**2)    (METERS) (METERS) (METERS) (METERS)            (METERS)       BY
 - - - - - - - - - - - - - - - - - - - - - - - - - - - - - - - - - - - - - - - - - - - - - - - - - - - - - -
- - - - - - - - - -

   S4CY3043      0   0.10160E+00     537.3     524.1     0.0     0.00       6          0.00
   S4CY3044      0   0.20117E+00     579.2     554.7     3.0     3.00       6          0.00
   S4CY3045      0   0.23914E+00    1110.4     586.4     3.0     3.00       6          0.00

                                    ***
***        01:03:05
                     *** THE FIRST  11 HOURS OF METEOROLOGICAL DATA ***

      FILE:   C:\Users\Komati\Desktop\DISPER~1\AREAS-~1\METFIL~1\DWD3.ASC
      FORMAT: (4I2,2F9.4,F6.1,I2,2F7.1,f9.4,f10.1,f8.4,i4,f7.2)
      SURFACE STATION NO.: 364300                    UPPER AIR STATION NO.: 364300
                    NAME: UNKNOWN                                  NAME: UNKNOWN
                    YEAR:   2017                                   YEAR:   2017

              FLOW    SPEED  TEMP  STAB  MIXING HEIGHT (M)  USTAR  M-O LENGTH   Z-0 IPCODE PRATE
 YR MN DY HR VECTOR   (M/S)    (K)  CLASS   RURAL   URBAN    (M/S)      (M)        (M)        (mm/HR)
 - - - - - - - - - - - - - - - - - - - - - - - - - - - - - - - - - - - - - - - - - - - - - - - - - - - - - -
- - - - - - - - - - - - - -
```

| | | | | | | | | | | | | |
|---|---|---|---|---|---|---|---|---|---|---|---|---|
| 17 | 08 | 21 | 07 | 194.0 | 3.72 | 283.2 | 4 | 800.0 | 800.0 | 0.0000 | 0.0 | 0.0000 | 0 | 0.00 |
| 17 | 08 | 21 | 08 | 184.0 | 4.97 | 286.7 | 4 | 800.0 | 800.0 | 0.0000 | 0.0 | 0.0000 | 0 | 0.00 |
| 17 | 08 | 21 | 09 | 186.0 | 5.13 | 289.0 | 4 | 800.0 | 800.0 | 0.0000 | 0.0 | 0.0000 | 0 | 0.00 |
| 17 | 08 | 21 | 10 | 158.0 | 4.37 | 291.5 | 3 | 1000.0 | 1000.0 | 0.0000 | 0.0 | 0.0000 | 0 | 0.00 |
| 17 | 08 | 21 | 11 | 153.0 | 3.45 | 293.2 | 3 | 1000.0 | 1000.0 | 0.0000 | 0.0 | 0.0000 | 0 | 0.00 |
| 17 | 08 | 21 | 12 | 153.0 | 3.45 | 293.2 | 3 | 1000.0 | 1000.0 | 0.0000 | 0.0 | 0.0000 | 0 | 0.00 |
| 17 | 08 | 21 | 13 | 134.0 | 3.50 | 295.4 | 2 | 1400.0 | 1400.0 | 0.0000 | 0.0 | 0.0000 | 0 | 0.00 |
| 17 | 08 | 21 | 14 | 104.0 | 3.72 | 296.4 | 3 | 1000.0 | 1000.0 | 0.0000 | 0.0 | 0.0000 | 0 | 0.00 |
| 17 | 08 | 21 | 15 | 98.0 | 3.61 | 296.7 | 3 | 1000.0 | 1000.0 | 0.0000 | 0.0 | 0.0000 | 0 | 0.00 |
| 17 | 08 | 21 | 16 | 98.0 | 3.81 | 296.5 | 3 | 1000.0 | 1000.0 | 0.0000 | 0.0 | 0.0000 | 0 | 0.00 |
| 17 | 08 | 21 | 17 | 103.0 | 3.61 | 295.8 | 3 | 1000.0 | 1000.0 | 0.0000 | 0.0 | 0.0000 | 0 | 0.00 |

*** DISCRETE CARTESIAN RECEPTOR POINTS ***

** CONC OF RADON IN MICROGRAMS/M**3 **

| X-COORD (M) | Y-COORD (M) | CONC | X-COORD (M) | Y-COORD (M) | CONC |
|---|---|---|---|---|---|
| 893.80 | 527.50 | 497625.78125 | 755.50 | 430.20 | 451275.56250 |
| 717.10 | 355.60 | 428887.09375 | 607.70 | 194.60 | 442830.96875 |
| 583.70 | 74.40 | 431744.28125 | | | |

1 *** ISCST3 - VERSION 02035 *** *** Day 3 Downwind (Morning)
*** 05/18/18
***
*** 01:03:05

*** DISCRETE CARTESIAN RECEPTOR POINTS ***

** CONC OF RADON IN MICROGRAMS/M**3 **

| X-COORD (M) | Y-COORD (M) | CONC | X-COORD (M) | Y-COORD (M) | CONC |
|---|---|---|---|---|---|
| 893.80 | 527.50 | 413075.43750 | 755.50 | 430.20 | 383129.96875 |
| 717.10 | 355.60 | 358988.28125 | 607.70 | 194.60 | 361327.03125 |
| 583.70 | 74.40 | 364185.93750 | | | |

1 *** ISCST3 - VERSION 02035 *** *** Day 3 Downwind (Morning)
*** 05/18/18

*** DISCRETE CARTESIAN RECEPTOR POINTS ***

** CONC OF RADON IN MICROGRAMS/M**3 **

X-COORD (M) Y-COORD (M) CONC X-COORD (M) Y-COORD (M) CONC

| | | | | | |
|---|---|---|---|---|---|
| 893.80 | 527.50 | 469442.34375 | 755.50 | 430.20 | 428560.40625 |
| 717.10 | 355.60 | 405587.50000 | 607.70 | 194.60 | 415663.09375 |
| 583.70 | 74.40 | 409224.84375 | | | |

*** DISCRETE CARTESIAN RECEPTOR POINTS ***

** CONC OF RADON IN MICROGRAMS/M**3 **

| X-COORD (M) | Y-COORD (M) | CONC | X-COORD (M) | Y-COORD (M) | CONC |
|---|---|---|---|---|---|
| 893.80 | 527.50 | 536891.50000 | 755.50 | 430.20 | 426886.34375 |
| 717.10 | 355.60 | 441007.53125 | 607.70 | 194.60 | 11376.85938 |
| 583.70 | 74.40 | 1265.12195 | | | |

1 *** ISCST3 - VERSION 02035 *** *** Day 3 Downwind (Morning)
*** 05/18/18

*** DISCRETE CARTESIAN RECEPTOR POINTS ***

** CONC OF RADON IN MICROGRAMS/M**3 **

| X-COORD (M) | Y-COORD (M) | CONC | X-COORD (M) | Y-COORD (M) | CONC |
|---|---|---|---|---|---|

| | | | | | |
|---|---|---|---|---|---|
| 893.80 | 527.50 | 474983.46875 | 755.50 | 430.20 | 405008.28125 |
| 717.10 | 355.60 | 399997.87500 | 607.70 | 194.60 | 186351.93750 |
| 583.70 | 74.40 | 182725.53125 | | | |

*** DISCRETE CARTESIAN RECEPTOR POINTS ***

** CONC OF RADON IN MICROGRAMS/M**3 **

| X-COORD (M) | Y-COORD (M) | CONC | X-COORD (M) | Y-COORD (M) | CONC |
|---|---|---|---|---|---|
| 893.80 | 527.50 | 693084.18750 | 755.50 | 430.20 | 597125.87500 |
| 717.10 | 355.60 | 465963.00000 | 607.70 | 194.60 | 1883.99255 |
| 583.70 | 74.40 | 85.13104 | | | |

*** DISCRETE CARTESIAN RECEPTOR POINTS ***

** CONC OF RADON IN MICROGRAMS/M**3 **

| X-COORD (M) | Y-COORD (M) | CONC | X-COORD (M) | Y-COORD (M) | CONC |
|---|---|---|---|---|---|

| | | | | | |
|---|---|---|---|---|---|
| 893.80 | 527.50 | 693084.18750 | 755.50 | 430.20 | 597125.87500 |
| 717.10 | 355.60 | 465963.00000 | 607.70 | 194.60 | 1883.99255 |
| 583.70 | 74.40 | 85.13104 | | | |

1 *** ISCST3 - VERSION 02035 *** *** Day 3 Downwind (Morning) ***
*** 05/18/18

** CONC OF RADON IN MICROGRAMS/M**3 **

| X-COORD (M) | Y-COORD (M) | CONC | X-COORD (M) | Y-COORD (M) | CONC |
|---|---|---|---|---|---|
| 893.80 | 527.50 | 693084.25000 | 755.50 | 430.20 | 597125.87500 |
| 717.10 | 355.60 | 465963.03125 | 607.70 | 194.60 | 1883.99268 |
| 583.70 | 74.40 | 85.13104 | | | |

*** DISCRETE CARTESIAN RECEPTOR POINTS ***

** CONC OF RADON IN MICROGRAMS/M**3 **

| X-COORD (M) | Y-COORD (M) | CONC | X-COORD (M) | Y-COORD (M) | CONC |
|---|---|---|---|---|---|
| 893.80 | 527.50 | 641020.00000 | 755.50 | 430.20 | 540379.31250 |

| | | | | | |
|---|---|---|---|---|---|
| 717.10 | 355.60 | 457644.50000 | 607.70 | 194.60 | 5048.28125 |
| 583.70 | 74.40 | 478.46140 | | | |

** CONC OF RADON IN MICROGRAMS/M**3 **

| X-COORD (M) | Y-COORD (M) | CONC | X-COORD (M) | Y-COORD (M) | CONC |
|---|---|---|---|---|---|
| 893.80 | 527.50 | 584033.62500 | 755.50 | 430.20 | 501067.09375 |
| 717.10 | 355.60 | 432980.43750 | 607.70 | 194.60 | 94117.95312 |
| 583.70 | 74.40 | 91405.31250 | | | |

** CONC OF RADON IN MICROGRAMS/M**3 **

| X-COORD (M) | Y-COORD (M) | CONC | X-COORD (M) | Y-COORD (M) | CONC |
|---|---|---|---|---|---|
| 893.80 | 527.50 | 726952.06250 | 755.50 | 430.20 | 297140.06250 |
| 717.10 | 355.60 | 54917.87500 | 607.70 | 194.60 | 3.31294 |
| 583.70 | 74.40 | 0.00000 | | | |

*** DISCRETE CARTESIAN RECEPTOR POINTS ***

** CONC OF RADON IN MICROGRAMS/M**3 **

| X-COORD (M) | Y-COORD (M) | CONC | X-COORD (M) | Y-COORD (M) | CONC |
|---|---|---|---|---|---|
| 893.80 | 527.50 | 888811.93750 | 755.50 | 430.20 | 4171.97412 |
| 717.10 | 355.60 | 0.00000 | 607.70 | 194.60 | 0.00000 |
| 583.70 | 74.40 | 0.00000 | | | |

*** DISCRETE CARTESIAN RECEPTOR POINTS ***

** CONC OF RADON IN MICROGRAMS/M**3 **

| X-COORD (M) | Y-COORD (M) | CONC | X-COORD (M) | Y-COORD (M) | CONC |
|---|---|---|---|---|---|
| 893.80 | 527.50 | 807881.93750 | 755.50 | 430.20 | 150656.01562 |
| 717.10 | 355.60 | 27458.93750 | 607.70 | 194.60 | 1.65647 |
| 583.70 | 74.40 | 0.00000 | | | |

*** DISCRETE CARTESIAN RECEPTOR POINTS ***

** CONC OF RADON IN MICROGRAMS/M**3 **

| X-COORD (M) | Y-COORD (M) | CONC | X-COORD (M) | Y-COORD (M) | CONC |
|---|---|---|---|---|---|
| 893.80 | 527.50 | 673396.31250 | 755.50 | 430.20 | 412.49677 |
| 717.10 | 355.60 | 0.00000 | 607.70 | 194.60 | 0.00000 |
| 583.70 | 74.40 | 0.00000 | | | |

*** DISCRETE CARTESIAN RECEPTOR POINTS ***

** CONC OF RADON IN MICROGRAMS/M**3 **

| X-COORD (M) | Y-COORD (M) | CONC | X-COORD (M) | Y-COORD (M) | CONC |
|---|---|---|---|---|---|
| 893.80 | 527.50 | 763053.25000 | 755.50 | 430.20 | 100574.84375 |
| 717.10 | 355.60 | 18305.95898 | 607.70 | 194.60 | 1.10431 |
| 583.70 | 74.40 | 0.00000 | | | |

*** DISCRETE CARTESIAN RECEPTOR POINTS ***

** CONC OF RADON IN MICROGRAMS/M**3 **

| X-COORD (M) | Y-COORD (M) | CONC | X-COORD (M) | Y-COORD (M) | CONC |
|---|---|---|---|---|---|
| 893.80 | 527.50 | 638050.81250 | 755.50 | 430.20 | 390.84604 |

| | | | | | |
|---|---|---|---|---|---|
| 717.10 | 355.60 | 0.00000 | 607.70 | 194.60 | 0.00000 |
| 583.70 | 74.40 | 0.00000 | | | |

*** DISCRETE CARTESIAN RECEPTOR POINTS ***

** CONC OF RADON IN MICROGRAMS/M**3 **

| X-COORD (M) | Y-COORD (M) | CONC | X-COORD (M) | Y-COORD (M) | CONC |
|---|---|---|---|---|---|
| 893.80 | 527.50 | 655723.68750 | 755.50 | 430.20 | 401.67139 |
| 717.10 | 355.60 | 0.00000 | 607.70 | 194.60 | 0.00000 |
| 583.70 | 74.40 | 0.00000 | | | |

*** DISCRETE CARTESIAN RECEPTOR POINTS ***

** CONC OF RADON IN MICROGRAMS/M**3 **

| X-COORD (M) | Y-COORD (M) | CONC | X-COORD (M) | Y-COORD (M) | CONC |
|---|---|---|---|---|---|
| 893.80 | 527.50 | 731802.62500 | 755.50 | 430.20 | 75528.84375 |
| 717.10 | 355.60 | 13729.46875 | 607.70 | 194.60 | 0.82824 |
| 583.70 | 74.40 | 0.00000 | | | |

*** DISCRETE CARTESIAN RECEPTOR POINTS ***

** CONC OF RADON IN MICROGRAMS/M**3 **

| X-COORD (M) | Y-COORD (M) | CONC | X-COORD (M) | Y-COORD (M) | CONC |
|---|---|---|---|---|---|
| 893.80 | 527.50 | 884363.50000 | 755.50 | 430.20 | 3074.88135 |
| 717.10 | 355.60 | 0.00000 | 607.70 | 194.60 | 0.00000 |
| 583.70 | 74.40 | 0.00000 | | | |

*** DISCRETE CARTESIAN RECEPTOR POINTS ***

** CONC OF RADON IN MICROGRAMS/M**3 **

| X-COORD (M) | Y-COORD (M) | CONC | X-COORD (M) | Y-COORD (M) | CONC |
|---|---|---|---|---|---|
| 893.80 | 527.50 | 649360.00000 | 755.50 | 430.20 | 292000.78125 |
| 717.10 | 355.60 | 240419.43750 | 607.70 | 194.60 | 114739.77344 |
| 583.70 | 74.40 | 111737.25000 | | | |

*** DISCRETE CARTESIAN RECEPTOR POINTS ***

** CONC OF RADON IN MICROGRAMS/M**3 **

| X-COORD (M) | Y-COORD (M) | CONC | (YYMMDDHH) | X-COORD (M) | Y-COORD (M) | CONC | (YYMMDDHH) |
|---|---|---|---|---|---|---|---|
| 893.80 | 527.50 | 888811.93750 | (17082114) | 755.50 | 430.20 | 597125.87500 | (17082111) |
| 717.10 | 355.60 | 492494.00000 | (17082107) | 607.70 | 194.60 | 487993.93750 | (17082107) |
| 583.70 | 74.40 | 462674.43750 | (17082107) | | | | |

1 *** ISCST3 - VERSION 02035 *** *** Day 3 Downwind (Morning) *** 05/18/18

*** DISCRETE CARTESIAN RECEPTOR POINTS ***

** CONC OF RADON IN MICROGRAMS/M**3 **

| X-COORD (M) | Y-COORD (M) | CONC | (YYMMDDHH) | X-COORD (M) | Y-COORD (M) | CONC | (YYMMDDHH) |
|---|---|---|---|---|---|---|---|
| 893.80 | 527.50 | 884363.50000 | (17082117) | 755.50 | 430.20 | 597125.87500 | (17082112) |

```
           717.10       355.60   465963.00000  (17082111)                  607.70       194.60
397667.90625  (17082108)

           583.70        74.40   400814.09375  (17082108)

1 *** ISCST3 - VERSION 02035 ***    ***  Day 3 Downwind (Morning)
***        05/18/18

                                        *** THE SUMMARY OF MAXIMUM PERIOD (    11 HRS) RESULTS ***

                                     ** CONC OF RADON    IN MICROGRAMS/M**3                          **

GROUP ID                        AVERAGE CONC               RECEPTOR  (XR, YR, ZELEV, ZFLAG)   OF TYPE  GRID-
ID


 ALL      1ST HIGHEST VALUE IS  649360.00000 AT (     893.80,      527.50,      0.00,      1.50)  DC
NA
          2ND HIGHEST VALUE IS  292000.78125 AT (     755.50,      430.20,      0.00,      1.50)  DC
NA
          3RD HIGHEST VALUE IS  240419.43750 AT (     717.10,      355.60,      0.00,      1.50)  DC
NA
          4TH HIGHEST VALUE IS  114739.77344 AT (     607.70,      194.60,      0.00,      1.50)  DC
NA
          5TH HIGHEST VALUE IS  111737.25000 AT (     583.70,       74.40,      0.00,      1.50)  DC
NA


                                        *** THE SUMMARY OF HIGHEST  1-HR RESULTS ***

                                     ** CONC OF RADON    IN MICROGRAMS/M**3                          **

GROUP ID                         AVERAGE CONC     (YYMMDDHH)            RECEPTOR  (XR, YR, ZELEV, ZFLAG)
OF TYPE  GRID-ID
```

```
 ALL       HIGH  1ST HIGH VALUE IS  888811.93750  ON 17082114: AT (     893.80,      527.50,      0.00,
1.50)  DC       NA

           HIGH  2ND HIGH VALUE IS  884363.50000  ON 17082117: AT (     893.80,      527.50,      0.00,
1.50)  DC       NA

           HIGH  3RD HIGH VALUE IS  726952.06250  ON 17082113: AT (     893.80,      527.50,      0.00,
1.50)  DC       NA

           HIGH  4TH HIGH VALUE IS  693084.18750  ON 17082111: AT (     893.80,      527.50,      0.00,
1.50)  DC       NA


  --------- Summary of Total Messages --------

 A Total of            0 Fatal Error Message(s)

 A Total of            0 Warning Message(s)

 A Total of            0 Informational Message(s)

    ******** FATAL ERROR MESSAGES ********

                ***  NONE  ***

    ********   WARNING MESSAGES   ********

                ***  NONE  ***

      **********************************

    *** ISCST3 Finishes Successfully ***

    **********************************
```

## Appendix I: Calibration data for Eberline SPA-1A field instruments

### A. Calibration levels for Eberline SPA-1A.

*Table A.10: Eberline SPA-1A Calibration factors*

| HIGH VOLTAGE | INPUT SENSITIVITY | UNITS | NOMINAL VALUES | | CALIBRATION FIELDS | |
|---|---|---|---|---|---|---|
| | | | "CC=" | "DT(SEC)" | SET "CC" AT | SET "DT" AT |
| 650V | 10 mV | cpm | 5.00-01 | 1.00-05 | 10K cpm | Fixed |

### B. Chi-Square Calculations

Chi-Square test was used as an operational check to determine if the Eberline alpha counter was performing consistently or not. This test is used a measure of the reproducibility of the results obtained from the counter. For a sample size of 10 measurements, and therefore 9 degrees of freedom, the 95% confidence limits for $\chi^2$are 16.92 and 3.33 respectively (IAEA-TECDOC-602, 1991). When test results fall between 16.92 and 3.33 it indicates stable HV, SCA settings, amplifiers (base line shift or gain stability), counters (time base variations). In addition, there no instabilities with regards to any electronic influence coming from ground loops or control signals for electrical devices. The chi-square test depends solely on the statistic pattern coming from a radioactive source.

Using the americium-241 ($^{241}$Am) source, 10 different counts each one-minute long were undertaken using the Ebeline alpha counter and the total number of counts for each of the 10 measurements noted a recorded. The calculation of the chi-square was based on the equation 8.12 (IAEA-TECDOC-1599, 2007) below and the results are presented in table A.11.

$$\chi^2 = \sum_{i=1}^{n} \frac{(N_i - \bar{N})^2}{\bar{N}} \tag{8.12}$$

where

$n$ number of measurements;

$\chi^2$ Chi-Square

$N_i$ Individual measurement

$\bar{N}$ Mean

*Table A.11. Chi-Square calculations*

| **COUNT NUMBER** | **COUNTS (mins) ($N_i$)** | **COUNT MINUS MEAN ($N_i - \bar{N}$)** | **COUNT MINUS MEAN SQUARED $(N_i - \bar{N})^2$** |
|---|---|---|---|
| 1 | 234 | -0.3 | 0.09 |
| 2 | 242 | 7.7 | 59.29 |
| 3 | 214 | -20.3 | 412.09 |
| 4 | 256 | 21.7 | 470.89 |
| 5 | 253 | 18.7 | 349.69 |
| 6 | 235 | 0.7 | 0.49 |
| 7 | 244 | 9.7 | 94.09 |
| 8 | 218 | -16.3 | 265.69 |
| 9 | 221 | -13.3 | 176.89 |
| 10 | 226 | -8.3 | 68.89 |
| **MEAN ($\bar{N}$)** | **234** | | |
| **SUM** | | | **1898.10** |

$$\chi^2 = \sum_{i=1}^{n} \frac{(N_i - \bar{N})^2}{\bar{N}}$$

$$\chi^2 = \frac{1898.1}{234{,}3} = 8.10$$

## Appendix J: AlphaGUARD error propagation

*Table A.12: Radon error calculations (AlphaGUARD)*

| Date | Time | Position | Average Rn (AlphaGuard) (Bq/m³) | Counts (cpm) (Statistical) | Poissson Distribution | Systematic uncertainties (Bq/m³) | Total uncertainties (Bq/m³) | Rel. % uncertainty |
|---|---|---|---|---|---|---|---|---|
| **19-08-2017** | 09:30 | 27⁰50'11''S 26⁰40'1" E | 10.25 | 5.13 | 0.23 | 0.03 | 0.23 | 2.2 |
| **DOWNWIND** | 11:12 | 27⁰50'16"S 26⁰39'57" E | 8.50 | 4.25 | 0.21 | 0.03 | 0.21 | 2.5 |
| | 12:00 | 27⁰50'18"S 26⁰39'54" E | 8.44 | 4.22 | 0.21 | 0.03 | 0.21 | 2.5 |
| | | | | | | | | |
| | 13:32 | 27⁰50'11"S 26⁰40'4" E | 6.13 | 3.07 | 0.18 | 0.03 | 0.18 | 2.9 |
| | 14:30 | 27⁰50'15"S 26⁰40'1" E | 15.50 | 7.75 | 0.28 | 0.03 | 0.28 | 1.8 |
| | 15:26 | 27⁰50'18"S 26⁰39'58" E | 6.19 | 3.10 | 0.18 | 0.03 | 0.19 | 2.9 |
| | 16:12 | 27⁰50'21"S 26⁰39'56" E | 4.63 | 2.32 | 0.15 | 0.03 | 0.16 | 3.3 |
| **UPWIND** | | | | | | | | |

| | | | | | | | | |
|---|---|---|---|---|---|---|---|---|
| **20-08-2017** | 07:50 | 27⁰49'28"S 26⁰40'0" E | 13.25 | 6.63 | 0.26 | 0.03 | 0.26 | 2.0 |
| | 09:18 | 27⁰49'30"S 26⁰40'7" E | 8.44 | 4.22 | 0.21 | 0.03 | 0.21 | 2.5 |
| | 09:57 | 27⁰49'26"S 26⁰40'10" E | 12.69 | 6.35 | 0.25 | 0.03 | 0.25 | 2.0 |
| | 10:38 | 27⁰49'24"S 26⁰40'9" E | 15.81 | 7.91 | 0.28 | 0.03 | 0.28 | 1.8 |
| **DOWNWIND** | | | | | | | | |
| | 13:08 | 27⁰50'11"S 26⁰40'10" E | 10.75 | 5.38 | 0.23 | 0.03 | 0.23 | 2.2 |
| | 13:54 | 27⁰50'13"S 26⁰40'7" E | 20.63 | 10.32 | 0.32 | 0.03 | 0.32 | 1.6 |
| | 14:50 | 27⁰50'17"S 26⁰40'9" E | 10.94 | 5.47 | 0.23 | 0.03 | 0.24 | 2.2 |
| | 15:49 | 27⁰50'22"S 26⁰40'5" E | 7.66 | 3.83 | 0.20 | 0.03 | 0.19 | 2.6 |
| **DOWNWIND** | | | | | | | | |
| **21-08-2017** | 07:39 | 27⁰50'11"S 26⁰40'0" E | 20.63 | 10.32 | 0.32 | 0.03 | 0.32 | 1.6 |
| | 08:35 | 27⁰50'15"S 26⁰39'56" E | 20.13 | 10.07 | 0.32 | 0.03 | 0.32 | 1.6 |
| | 09:25 | 27⁰50'18"S 26⁰39'54" E | 23.38 | 11.69 | 0.34 | 0.03 | 0.34 | 1.5 |

| | | | | | | | | |
|---|---|---|---|---|---|---|---|---|
| | 10:28 | 27°50'24"S 26°39'51" E | 10.69 | 5.35 | 0.23 | 0.03 | 0.23 | 2.2 |
| | 11:14 | 27°50'28"S 26°39'51" E | 20.25 | 10.13 | 0.32 | 0.03 | 0.32 | 1.6 |
| **DOWNWIND** | | | | | | | | |
| | 13:00 | 27°50'10"S 26°40'22" E | 13.13 | 6.57 | 0.26 | 0.03 | 0.26 | 2.0 |
| | 13:52 | 27°50'12"S 26°40'27" E | 20.50 | 10.25 | 0.32 | 0.03 | 0.32 | 1.6 |
| | 15:24 | 27°50'15"S 26°40'35" E | 8.38 | 4.19 | 0.20 | 0.03 | 0.21 | 2.5 |
| **UPWIND** | | | | | | | | |
| **26-08-2017** | 08:51 | 27°49'46"S 26°40'15" E | 3.80 | 1.90 | 0.14 | 0.03 | 0.14 | 3.7 |
| | 09:43 | 27°49'43"S 26°40'18" E | 8.44 | 4.22 | 0.21 | 0.03 | 0.21 | 2.5 |
| | 10:33 | 27°49'40"S 26°40'19" E | 6.91 | 3.46 | 0.19 | 0.03 | 0.19 | 2.7 |
| | 11:27 | 27°49'36"S 26°40'21" E | 1.48 | 0.74 | 0.09 | 0.03 | 0.09 | 6.2 |
| **DOWNWIND** | | | | | | | | |
| | 13:19 | 27°50'11"S 26°40'18" E | 6.19 | 3.10 | 0.18 | 0.03 | 0.18 | 2.9 |

| | | | | | | | | |
|---|---|---|---|---|---|---|---|---|
| | 14:12 | 27°50'15"S 26°40'20" E | 13.38 | 6.69 | 0.26 | 0.03 | 0.26 | 1.9 |
| | 15:04 | 27°50'18"S 26°40'22" E | 10.88 | 5.44 | 0.23 | 0.03 | 0.24 | 2.2 |
| | 16:04 | 27°50'22"S 26°40'26" E | 8.38 | 4.19 | 0.20 | 0.03 | 0.21 | 2.5 |
| **DOWNWIND** | | | | | | | | |
| **27-08-2017** | 08:02 | 27°50'11"S 26°40'4" E | 19.88 | 9.94 | 0.32 | 0.03 | 0.32 | 1.6 |
| | 08:50 | 27°50'14"S 26°40'2" E | 8.31 | 4.16 | 0.20 | 0.03 | 0.21 | 2.5 |
| | 09:43 | 27°50'18"S 26°40'0" E | 8.13 | 4.07 | 0.20 | 0.03 | 0.20 | 2.5 |
| **UPWIND** | | | | | | | | |
| | 11:51 | 27°49'30"S 26°39'56" E | 7.00 | 3.50 | 0.19 | 0.03 | 0.19 | 2.7 |
| | 13:01 | 27°49'27"S 26°40'54" E | 7.91 | 3.96 | 0.20 | 0.03 | 0.20 | 2.5 |
| | 13:50 | 27°49'26"S 26°39'51" E | 5.69 | 2.85 | 0.17 | 0.03 | 0.17 | 3.0 |
| | 14:39 | 27°49'25"S 26°39'47" E | 7.25 | 3.63 | 0.19 | 0.03 | 0.19 | 2.7 |

## Appendix K: Radon daughter, EEC and F factor error calculations

*Table A.13: Radon daughter, EEC and F factor errors*

| Date | Time | Position | Counting errors (Poisson Distribution) | | | Systematic Uncertainty (Bq/m³) | Total Radon Daughter uncertainties (Bq/m³) | | | EEC (Total Uncertainties) | F factor Uncertainty |
|---|---|---|---|---|---|---|---|---|---|---|---|
| | | | RaA | RaB | RaC | | RaA | RaB | RaC | | |
| **19-08-2017** | 09:30 | 27°50'11"S 26°40'1" E | 1.95 | 0.43 | 0.00 | 0.12 | 1.96 | 0.45 | 0.00 | 0.44 | 0.044 |
| **DOWNWIND** | 11:12 | 27°50'16"S 26°39'57" E | 1.31 | 0.23 | 0.32 | 0.12 | 1.31 | 0.26 | 0.35 | 0.40 | 0.048 |
| | 12:00 | 27°50'18"S 26°39'54" E | 0.96 | 0.17 | 0.24 | 0.12 | 0.97 | 0.21 | 0.26 | 0.31 | 0.037 |
| | | | | | | | | | | | |
| | 13:32 | 27°50'11"S 26°40'4" E | 0.83 | 0.00 | 0.00 | 0.12 | 0.84 | 0.00 | 0.00 | 0.09 | 0.014 |
| | 14:30 | 27°50'15"S 26°40'1" E | 1.65 | 0.50 | 0.00 | 0.12 | 1.66 | 0.51 | 0.00 | 0.44 | 0.029 |
| | 15:26 | 27°50'18"S 26°39'58" E | 0.87 | 0.00 | 0.00 | 0.12 | 0.88 | 0.00 | 0.00 | 0.09 | 0.015 |
| | 16:12 | 27°50'21"S 26°39'56" E | 0.84 | 0.16 | 0.00 | 0.12 | 0.85 | 0.20 | 0.00 | 0.19 | 0.042 |
| **UPWIND** | | | | | | | | | | | |
| **20-08-2017** | 07:50 | 27°49'28"S 26°40'0" E | 1.51 | 0.32 | 0.00 | 0.12 | 1.51 | 0.34 | 0.00 | 0.33 | 0.025 |

| | | | | | | | | | | | |
|---|---|---|---|---|---|---|---|---|---|---|---|
| | 09:18 | 27⁰49'30"S 26⁰40'7" E | 1.27 | 0.00 | 0.32 | 0.12 | 1.27 | 0.00 | 0.34 | 0.26 | 0.032 |
| | 09:57 | 27⁰49'26"S 26⁰40'10" E | 2.01 | 0.31 | 0.00 | 0.12 | 2.01 | 0.34 | 0.00 | 0.38 | 0.030 |
| | 10:38 | 27⁰49'24"S 26⁰40'9" E | 1.60 | 0.44 | 0.00 | 0.12 | 1.61 | 0.46 | 0.00 | 0.40 | 0.026 |
| **DOWNWIND** | | | | | | | | | | | |
| | 13:08 | 27⁰50'11"S 26⁰40'10" E | 0.68 | 0.13 | 0.00 | 0.12 | 0.69 | 0.18 | 0.00 | 0.17 | 0.015 |
| | 13:54 | 27⁰50'13"S 26⁰40'7" E | 0.86 | 0.00 | 0.22 | 0.12 | 0.87 | 0.00 | 0.25 | 0.18 | 0.009 |
| | 14:50 | 27⁰50'17"S 26⁰40'9" E | 0.90 | 0.17 | 0.00 | 0.12 | 0.91 | 0.21 | 0.00 | 0.20 | 0.018 |
| | 15:49 | 27⁰50'22"S 26⁰40'5" E | 1.27 | 0.15 | 0.00 | 0.12 | 1.28 | 0.19 | 0.00 | 0.23 | 0.031 |
| **DOWNWIND** | | | | | | | | | | | |
| **21-08-2017** | 07:39 | 27⁰50'11"S 26⁰40'0" E | 2.42 | 0.46 | 0.00 | 0.12 | 2.42 | 0.47 | 0.00 | 0.50 | 0.024 |
| | 08:35 | 27⁰50'15"S 26⁰39'56" E | 2.05 | 0.41 | 0.00 | 0.12 | 2.06 | 0.42 | 0.00 | 0.43 | 0.022 |
| | 09:25 | 27⁰50'18"S 26⁰39'54" E | 1.95 | 0.33 | 0.00 | 0.12 | 1.95 | 0.35 | 0.00 | 0.38 | 0.016 |
| | 10:28 | 27⁰50'24"S 26⁰39'51" E | 1.41 | 0.23 | 0.00 | 0.12 | 1.42 | 0.26 | 0.00 | 0.28 | 0.026 |
| | 11:14 | 27⁰50'28"S 26⁰39'51" E | 1.30 | 0.22 | 0.00 | 0.12 | 1.30 | 0.25 | 0.00 | 0.27 | 0.013 |
| **DOWNWIND** | | | | | | | | | | | |

| | | | | | | | | | | | |
|---|---|---|---|---|---|---|---|---|---|---|---|
| | 13:00 | 27°50'10"S 26°40'22" E | 1.01 | 0.17 | 0.24 | 0.12 | 1.02 | 0.21 | 0.27 | 0.32 | 0.024 |
| | 13:52 | 27°50'12"S 26°40'27" E | 0.87 | 0.13 | 0.00 | 0.12 | 0.88 | 0.18 | 0.00 | 0.18 | 0.009 |
| | 15:24 | 27°50'15"S 26°40'35" E | 0.70 | 0.14 | 0.00 | 0.12 | 0.71 | 0.19 | 0.00 | 0.17 | 0.020 |
| **UPWIND** | | | | | | | | | | | |
| **26-08-2017** | 08:51 | 27°49'46"S 26°40'15" E | 1.32 | 0.23 | 0.00 | 0.12 | 1.33 | 0.26 | 0.00 | 0.27 | 0.073 |
| | 09:43 | 27°49'43"S 26°40'18" E | 1.30 | 0.23 | 0.00 | 0.12 | 1.31 | 0.26 | 0.00 | 0.27 | 0.032 |
| | 10:33 | 27°49'40"S 26°40'19" E | 1.09 | 0.24 | 0.00 | 0.12 | 1.10 | 0.27 | 0.00 | 0.25 | 0.037 |
| | 11:27 | 27°49'36"S 26°40'21" E | 1.26 | 0.22 | 0.00 | 0.12 | 1.27 | 0.25 | 0.00 | 0.26 | 0.178 |
| **DOWNWIND** | | | | | | | | | | | |
| | 13:19 | 27°50'11"S 26°40'18" E | 1.22 | 0.23 | 0.00 | 0.12 | 1.23 | 0.26 | 0.00 | 0.26 | 0.043 |
| | 14:12 | 27°50'15"S 26°40'20" E | 1.26 | 0.22 | 0.00 | 0.12 | 1.27 | 0.26 | 0.00 | 0.26 | 0.020 |
| | 15:04 | 27°50'18"S 26°40'22" E | 0.91 | 0.17 | 0.00 | 0.12 | 0.92 | 0.21 | 0.00 | 0.20 | 0.019 |
| | 16:04 | 27°50'22"S 26°40'26" E | 0.68 | 0.16 | 0.00 | 0.12 | 0.69 | 0.20 | 0.00 | 0.18 | 0.021 |
| **DOWNWIND** | | | | | | | | | | | |
| **27-08-2017** | 08:02 | 27°50'11"S 26°40'4" E | 2.25 | 0.42 | 0.00 | 0.12 | 2.25 | 0.44 | 0.00 | 0.46 | 0.023 |

| | | | | | | | | | | | |
|---|---|---|---|---|---|---|---|---|---|---|---|
| | 08:50 | 27°50'14"S 26°40'2" E | 1.87 | 0.32 | 0.00 | 0.12 | 1.87 | 0.34 | 0.00 | 0.37 | 0.045 |
| | 09:43 | 27°50'18"S 26°40'0" E | 1.47 | 0.28 | 0.00 | 0.12 | 1.48 | 0.30 | 0.00 | 0.31 | 0.038 |
| **UPWIND** | | | | | | | | | | | |
| | 11:51 | 27°49'30"S 26°39'56" E | 1.19 | 0.18 | 0.00 | 0.12 | 1.19 | 0.22 | 0.00 | 0.24 | 0.034 |
| | 13:01 | 27°49'27"S 26°40'54" E | 0.91 | 0.17 | 0.00 | 0.12 | 0.92 | 0.21 | 0.00 | 0.20 | 0.026 |
| | 13:50 | 27°49'26"S 26°39'51" E | 0.67 | 0.16 | 0.19 | 0.12 | 0.68 | 0.20 | 0.00 | 0.17 | 0.031 |
| | 14:39 | 27°49'25"S 26°39'47" E | 0.82 | 0.17 | 0.00 | 0.12 | 0.83 | 0.21 | 0.00 | 0.20 | 0.027 |

*Table A.14: Relative percentage errors – radon daughter, EEC and F factor*

| Date | Time | Position | Relative % Uncertainties | | | EEC % Uncertainties | F-factor % Uncertainties |
|---|---|---|---|---|---|---|---|
| | | | RaA | RaB | RaC | | |
| **19-08-2017** | 09:30 | 27⁰50'11"S 26⁰40'1" E | 11 | 7 | 0 | 8 | 9 |
| **DOWNWIND** | 11:12 | 27⁰50'16"S 26⁰39'57" E | 44 | 48 | 84 | 54 | 54 |
| | 12:00 | 27⁰50'18"S 26⁰39'54" E | 45 | 55 | 544 | 70 | 71 |
| | | | | | | | |
| | 13:32 | 27⁰50'11"S 26⁰40'4" E | 39 | 0 | 0 | 39 | 39 |
| | 14:30 | 27⁰50'15"S 26⁰40'1" E | 23 | 7 | 0 | 10 | 10 |
| | 15:26 | 27⁰50'18"S 26⁰39'58" E | 40 | 0 | 0 | 40 | 40 |
| | 16:12 | 27⁰50'21"S 26⁰39'56" E | 50 | 40 | 0 | 44 | 44 |
| **UPWIND** | | | | | | | |
| **20-08-2017** | 07:50 | 27⁰49'28"S 26⁰40'0" E | 24 | 19 | 0 | 21 | 21 |
| | 09:18 | 27⁰49'30"S 26⁰40'7" E | 24 | 0 | 0 | 18 | 19 |
| | 09:57 | 27⁰49'26"S 26⁰40'10" E | 70 | 0 | 0 | 30 | 31 |
| | 10:38 | 27⁰49'24"S 26⁰40'9" E | 13 | 6 | 0 | 8 | 8 |
| **DOWNWIND** | | | | | | | |
| | 13:08 | 27⁰50'11"S 26⁰40'10" E | 41 | 37 | 0 | 39 | 39 |

| | | | | | | | |
|---|---|---|---|---|---|---|---|
| | 13:54 | 27⁰50'13"S 26⁰40'7" E | 0 | 0 | 36 | 71 | 71 |
| | 14:50 | 27⁰50'17"S 26⁰40'9" E | 29 | 28 | 0 | 29 | 29 |
| | 15:49 | 27⁰50'22"S 26⁰40'5" E | 16 | 47 | 0 | 22 | 22 |
| **DOWNWIND** | | | | | | | |
| **21-08-2017** | 07:39 | 27⁰50'11"S 26⁰40'0" E | 14 | 12 | 0 | 13 | 13 |
| | 08:35 | 27⁰50'15"S 26⁰39'56" E | 17 | 11 | 0 | 14 | 14 |
| | 09:25 | 27⁰50'18"S 26⁰39'54" E | 16 | 18 | 0 | 17 | 17 |
| | 10:28 | 27⁰50'24"S 26⁰39'51" E | 23 | 151 | 0 | 38 | 38 |
| | 11:14 | 27⁰50'28"S 26⁰39'51" E | 19 | 20 | 0 | 19 | 19 |
| **DOWNWIND** | | | | | | | |
| | 13:00 | 27⁰50'10"S 26⁰40'22" E | 50 | 83 | 264 | 84 | 84 |
| | 13:52 | 27⁰50'12"S 26⁰40'27" E | 29 | 50 | 0 | 36 | 36 |
| | 15:24 | 27⁰50'15"S 26⁰40'35" E | 47 | 38 | 0 | 41 | 41 |
| **UPWIND** | | | | | | | |
| **26-08-2017** | 08:51 | 27⁰49'46"S 26⁰40'15" E | 25 | 26 | 0 | 26 | 26 |
| | 09:43 | 27⁰49'43"S 26⁰40'18" E | 26 | 27 | 0 | 27 | 27 |
| | 10:33 | 27⁰49'40"S 26⁰40'19" E | 34 | 18 | 0 | 23 | 23 |
| | 11:27 | 27⁰49'36"S 26⁰40'21" E | 25 | 102 | 0 | 40 | 41 |
| **DOWNWIND** | | | | | | | |

| | | | | | | | |
|---|---|---|---|---|---|---|---|
| | 13:19 | 27⁰50'11"S 26⁰40'18" E | 20 | 17 | 0 | 18 | 18 |
| | 14:12 | 27⁰50'15"S 26⁰40'20" E | 26 | 25 | 0 | 26 | 26 |
| | 15:04 | 27⁰50'18"S 26⁰40'22" E | 34 | 0 | 0 | 73 | 73 |
| | 16:04 | 27⁰50'22"S 26⁰40'26" E | 134 | 38 | 0 | 55 | 55 |
| **DOWNWIND** | | | | | | | |
| **27-08-2017** | 08:02 | 27⁰50'11"S 26⁰40'4" E | 15 | 13 | 0 | 14 | 14 |
| | 08:50 | 27⁰50'14"S 26⁰40'2" E | 16 | 17 | 0 | 17 | 17 |
| | 09:43 | 27⁰50'18"S 26⁰40'0" E | 22 | 29 | 0 | 25 | 25 |
| **UPWIND** | | | | | | | |
| | 11:51 | 27⁰49'30"S 26⁰39'56" E | 23 | 37 | 0 | 28 | 28 |
| | 13:01 | 27⁰49'27"S 26⁰40'54" E | 32 | 31 | 0 | 31 | 32 |
| | 13:50 | 27⁰49'26"S 26⁰39'51" E | 80 | 0 | 0 | 197 | 197 |
| | 14:39 | 27⁰49'25"S 26⁰39'47" E | 43 | 28 | 0 | 33 | 33 |

## Appendix L: Upwind and downwind average radon concentrations

*Table A.15: Upwind average radon concentrations*

| Monitor no | Downwind Rn concentration (Bq.m$^{-3}$) | St Dev (Bq.m$^{-3}$) |
|---|---|---|
| 10 | 54 | 8 |
| 11 | 61 | 14 |
| 12 | 53 | 8 |
| 13 | 61 | 8 |
| 14 | 65 | 15 |
| 16 | 83 | 16 |
| 17 | 62 | 9 |
| 20 | 72 | 15 |
| 21 | 77 | 16 |
| 22 | 38 | 8 |
| 23 | 54 | 9 |
| 25 | 58 | 9 |
| 26 | 53 | 8 |
| 27 | 57 | 8 |
| 28 | 61 | 14 |
| 29 | 50 | 8 |
| 85 | 69 | 15 |
| 86 | 52 | 14 |
| 88 | 67 | 9 |
| 90 | 53 | 8 |
| 92 | 69 | 9 |
| 94 | 62 | 8 |
| 95 | 50 | 8 |
| 96 | 56 | 8 |
| 98 | 75 | 16 |
| 100 | 64 | 15 |
| 101 | 80 | 9 |
| 102 | 77 | 16 |
| 103 | 70 | 9 |
| 104 | 40 | 13 |
| 105 | 47 | 9 |
| 106 | 63 | 15 |
| 107 | 69 | 16 |
| 108 | 68 | 16 |
| 110 | 74 | 9 |
| **Min** | **38** | **8** |
| **Max** | **83** | **16** |
| **Average** | **62** | **11** |
| **SD (Mean)** | **11** | |

*Table A.16: Downwind average radon concentrations*

| Monitor no | Downwind Rn concentration (Bq.m$^{-3}$) | St Dev (Bq.m$^{-3}$) |
|---|---|---|
| 1 | 65 | 13 |
| 2 | 85 | 17 |
| 3 | 75 | 16 |
| 4 | 82 | 16 |
| 5 | 74 | 15 |
| 6 | 82 | 9 |
| 7 | 67 | 9 |
| 8 | 59 | 15 |
| 9 | 67 | 9 |
| 15 | 62 | 14 |
| 18 | 72 | 15 |
| 19 | 77 | 16 |
| 24 | 70 | 15 |
| 30 | 55 | 9 |
| 31 | 61 | 8 |
| 32 | 67 | 15 |
| 33 | 55 | 9 |
| 34 | 58 | 9 |
| 35 | 61 | 8 |
| 36 | 54 | 8 |
| 37 | 58 | 14 |
| 38 | 89 | 18 |
| 39 | 58 | 9 |
| 40 | 59 | 14 |
| 41 | 63 | 9 |
| 42 | 62 | 15 |
| 43 | 75 | 16 |
| 44 | 58 | 14 |
| 45 | 63 | 15 |
| 46 | 53 | 14 |
| 47 | 46 | 8 |
| 48 | 55 | 8 |
| 49 | 73 | 16 |
| 50 | 52 | 12 |
| 51 | 43 | 9 |
| 52 | 72 | 15 |
| 53 | 76 | 16 |
| 54 | 68 | 15 |
| 55 | 70 | 15 |
| 56 | 66 | 15 |
| 57 | 66 | 15 |
| 57 | 66 | 15 |

| | | |
|---|---|---|
| 59 | 62 | 9 |
| 60 | 73 | 16 |
| 61 | 48 | 13 |
| 62 | 59 | 8 |
| 63 | 56 | 8 |
| 64 | 57 | 8 |
| 65 | 56 | 14 |
| 66 | 49 | 8 |
| 67 | 68 | 15 |
| 68 | 56 | 8 |
| 69 | 80 | 16 |
| 70 | 58 | 9 |
| 71 | 78 | 16 |
| 72 | 65 | 9 |
| 73 | 65 | 15 |
| 74 | 72 | 16 |
| 75 | 94 | 18 |
| 76 | 68 | 10 |
| 78 | 94 | 18 |
| 80 | 45 | 8 |
| 81 | 71 | 16 |
| 82 | 71 | 16 |
| 83 | 60 | 9 |
| 84 | 55 | 9 |
| 121 | 63 | 9 |
| 122 | 54 | 15 |
| 125 | 55 | 9 |
| 126 | 74 | 16 |
| 127 | 53 | 14 |
| 128 | 71 | 16 |
| 129 | 56 | 10 |
| 130 | 60 | 15 |
| 131 | 53 | 9 |
| 132 | 62 | 15 |
| 133 | 59 | 9 |
| 135 | 61 | 9 |
| **Min** | **43** | **8** |
| **Max** | **94** | **18** |
| **Average** | **65** | **11** |
| **SD (Mean)** | | **10** |

# References

Abdel-Rahman, A.A. 2008, "On the Atmospheric Dispersion and Gaussian Plume Model", *2nd International Conference on WASTE MANAGEMENT, WATER POLLUTION, AIR POLLUTION, INDOOR CLIMATE (WWAI'08)*, pp. 31.

Abu-Jarad, F., Fremlin, J.H. and Bull, R. 1980, "A study of radon emitted from building materials using plastic alpha-track detectors", *Physics in Medicine and Biology,* vol. 25, pp. 683-694.

Aggarwal, A., Haritash, A.M. and Kansal, G. 2014, "Air Pollution Modelling – A Review ", *International Journal of Advanced Technology in Engineering and Science,* vol. 02, no. 06, pp. 355-364.

Akber, R. and Pfitzner, J. 1994, "Atmospheric concentrations of radon and radon daughters in Jabiru East", *Technical Memorandum 45*. [online] Darwin Northern Territory: Supervising Scientist For The Alligators Region. Available at: https://www.environment.gov.au/system/files/resources/c2898fde-634f-4652-9f1c-48041d5a4cee/files/tm45.pdf [Accessed 22 Jan. 2019].

Al Jubori, M. 2016, *Atmospheric Modelling*, Master of Environmental Sanitation edn, Universiteit Gent.

Al-Azmi, D., Mustapha, A. and Karunakara, N. 2012, "Radon adsorbed in activated charcoal—a simple and safe radiation source for teaching practical radioactivity in schools and colleges", *Physics Education,* vol. 47, no. 4, pp. 471-475.

Aldenkamp, F.J., De Meijer, R.J., Put, L.W. and Stoop, P. 1992, "An assessment of in situ radon exhalation measurement, and the relation between free and bound exhalation rates", *Radiation Protection Dosimetry,* vol. 45, pp. 449-453.

Altic, N. 2014, *Pilot Study Report for Radon Exhalation Measurements at Oak Ridge*. [online] Oak Ridge, Tennessee: Oak Ridge Institute for Science and Education. Available at: https://www.nrc.gov/docs/ML1414/ML14141A242.pdf [Accessed 19 Sep. 2014].

Altic, N. (2011). *Technical Bases and Guidance for Radon Flux Monitoring at Uranium Mill Tailing Sites*. [online] Rockville, MD.: Oak Ridge Institute for Science and Education. Available at: https://adamswebsearch2.nrc.gov/webSearch2/main.jsp?AccessionNumber=ML11186A899 [Accessed 18 Sep. 2014].

Amasi, A.I., Mtei, K.M., Dinh, C.N. and Jodlowski, P. 2015, "Radon Mass Exhalation Rates of Selected Building Materials in Tanzania", *Journal of Environment and Earth Science,* vol. 5, no. 21.

Amin, R.M. 2015, "A study of radon emitted from building materials using solid state nuclear track detectors", *Journal of Radiation Research and Applied Sciences,* vol. 8, no. 4, pp. 516-522.

Andretta, M., Leonzio, B., Lucialli, P. and Righi, S. 2006, "Application of the ISCST3 model to an industrial area: comparison between predicted and observed concentrations", *Risk Analysis V: Simulation and Hazard Mitigation*, pp. 187.

Andriamanatena, R., Bacmeister, G.U., Freyer, K., Ghose, R., Jönsson, G., Kleis, T., Treutler, H.-. and Enge, W. 1997, "Modelling of solid state nuclear track detector devices for radon measurements", *Radiation Measurements,* vol. 28, no. 1–6, pp. 657-662.

AquiSim Consulting 2014, "Richards Bay Mining, Zulti South Project: Prospective Radiological Public Safety and Impact Assessment", Report *no ASC-1031K-1*. [online] AquiSim Consulting (Pty) Ltd. Available at: https://www.aquisim.co.za/index.php/services/radiation-protection-and-radioactive-waste-management. [Accessed 14 Aug. 2018].

Argyropoulos, C.D., Sideris, G.M., Christolis, M.N., Nivolianitou, Z. and Markatos, N.C. 2010, 'Modelling pollutants dispersion and plume rise from large hydrocarbon tank fires in neutrally stratified atmosphere', *Atmospheric Environment,* 44(6), pp. 803-813.

Arnold, D., Vargas, A., Vermeulen, A.T., Verheggen, B. and Seibert, P. 2010, "Primary Analysis of radon origin by backward atmospheric transport modelling ", *Atmospheric Environment,* vol. 44, no. 4, pp. 494-502.

Arnold, D., Vargas, A., and Ortega, X. 2009, 'Analysis of outdoor radon progeny concentration measured at the Spanish radioactive aerosol automatic monitoring network', *Applied Radiation and Isotopes,,* 67(5), pp. 833-838.

Arnold, D., Vargas, A., Vermeulen, A.T., Verheggen, B. and Seibert, P. 2010a, "Analysis of radon origin by backward atmospheric transport modelling", *Atmospheric Environment,* vol. 44, no. 4, pp. 494-502.

Arya, S.P. (ed) 1999, *Air Pollution Meteorology and Dispersion*, Oxford University Press, Oxford.

Ashok, G.V., Nagaiah, N. and Shiva Prasad, N.G. 2008, "Radon daughters' concentration in air and exposure of joggers at the

university campus of Bangalore, India", *Isotopes in Environmental and Health Studies,* vol. 44, no. 4, pp. 325-333.

ATSDR 2012, *Draft Toxicological Profile for Radon*, Agency for Toxic Substances and Disease Registry, Atlanta, GA.

Ayotte, J., Flanagan, S. and Morrow, W. 2007, "Occurrence of Uranium and 222 Radon in Glacial and Bedrock Aquifers in the Northern United States", *1993-2003 Scientific Investigations Report 2007-5037*. New England: U.S. Geological Survey.

Azlah, N. 2014, *Modeling and Evaluation of Pollutant Emissions from Industrial Biofilters by Dispersion Models*, Master of Applied Science in Chemical Engineering edn, University of Waterloo, Waterloo, Ontario, Canada.

Bandyopadhyay, A. 2009, "Prediction of ground level concentration of sulfur dioxide using ISCST3 model in Mangalore industrial region of India", *Clean Technologies and Environmental Policy,* vol. 11, pp. 173-188.

Barooah, D. 2005, *STUDY OF ENVIRONMENTAL RADON LEVELS USING LR-115 NUCLEAR TRACK DETECTORS IN SOME COAL AND OIL RICH AREAS OF ASSAM SHELF*, PhD edn, Gauhati University, Assam, India.

Barratt, R. 2001, "Atmospheric dispersion modelling: an introduction to practical applications" in *Business and the Environment: Practitioner Series*, 1st edn, Earthscan, London, UK.

Baruah, D.M.B., Deka, P.C. and Rahman, M. 2013, "Measurement of radium concentration and radon exhalation rate in soil samples using SSNTDs", *African Review of Physics,* vol. 8, pp. 215-218.

Basit, A., Espinosa, F., Avila, R., Raza, S. and Irfan, N. 2008, "Simulation of atmospheric dispersion of radionuclides using an Eulerian–Lagrangian modelling system", *Journal of Radiological Protection,* vol. 28, no. 4.

Bateman, H. 1910, "The solution of a system of differential equations occurring in the theory of radioactive transformations", *In Proc. Cambridge Philos. Soc,* vol. 15, no. no. pt V, pp. 423-427.

Bavarnegin, E., Vahabi-moghaddam, M., Babakhani, A. and Fathabadi, N. 2012, "Analytical study of radionuclide concentration and radon exhalation rate in market available building materials of Ramsar", *Journal of Theoretical and Applied Physics,* vol. 6, no. 5.

Behera, S.N., Sharma, M., Dikshit, O. and Shukla, S.P. 2011, "GIS-Based Emission Inventory, Dispersion Modeling, and Assessment for Source Contributions of Particulate Matter in an Urban Environment", *Water, Air, and Soil Pollution,* vol. 218, pp. 423-426.

BEIR VI 1999, *Health effects of exposure to radon,* National Academy Press, Washington, D.C.

Belot, Y. *Estimating air quality close to radium-bearing waste piles*. Unpublished.

BIPM, IEC, IFCC, ISO, IUPAC, IUPAP and OIML 2008 Evaluation of measurement data *Guide to the Expression of Uncertainty in Measurement* 1st edn www.bipm.org/utils/common/documents/jcgm/JCGM 100 2008 E.pdf

Blaauboer, R.O. and Smetsers, R.C.G.M. 1997, "Outdoor Concentrations of the Equilibrium-Equivalent Decay Products of 222Rn in the Netherlands and the Effect of Meteorological Variables", *Radiation Protection Dosimetry,* vol. 69, no. 1, pp. 7-18.

Bluett, J., Gimson, N., Fisher, G., Heydenrych, C., Freeman, T. and Godfrey, J. 2004, *Good Practice Guide for Atmospheric Dispersion Modelling*, Ministry for the Environment, Manatū Mō Te Taiao, Wellington, New Zealand.

Bollhöfer, A. 2007, *The geographical variability of airborne radon concentration at the rehabilitated Nabarlek mine site during the dry season 2005*. Internal Report 527. [online] Darwin, NT: Supervising Scientist Division. Available at: https://www.environment.gov.au/system/files/resources/a87c12ac-4359-4a81-805b-adcc61e830f6/files/ir527.pdf [Accessed 14 May 2015].

Bollhöfer, A., Storm, J., Martin, P. and Tims, S. 2003, *Geographic variability in radon exhalation at the rehabilitated Nabarlek uranium mine, Northern Territory*, Australian Government.

Borak, T.B. 1986, "Randomization of grab-sampling strategies for estimating the annual exposure of U miners to Rn daughters", *Health Physics,* vol. 50, pp. 465.

Botha, J.C. 1998, "Validation of the Electret Radon Monitor as an Underground Radon Dosimeter", *Proceedings of the 38th SAAPMB and the 1st SARPA Congress* SAAPMB, 12 - 13 May 1998.

Botha, M.A., Ellis, J.F. and Forbes, P.B.C. 2009, "Modelled environmental risk-values for low cost housing developments on

rehabilitated gold-tailings dams: scientific paper", *Clean Air Journal = Tydskrif vir Skoon Lug,* vol. 17, no. 2, pp. 14-17.

Bowers, J., Anderson, A. and Hargraves, W. 1982, *Tests of the Industrial Source Complex (ISC) Dispersion Model at the Armco Middle-town, Ohio Steel Mill*. EPA-450/4-82-006. [online] Research Triangle Park, NC: U.S. EPA. Available at: https://nepis.epa.gov › Exe › ZyPURL [Accessed 27 Oct. 2017].

Brenner, D.J. 1989, *Radon: Risk and Remedy,* 1st edn., New York: W.H. Freeman.

Breslin, A.J., George, A.C. and Weinsteinm, M.S. 1969, *Investigation of the Radiological Chamcteristics of Uranium Mine Atmospheres*, US AEC, Health and Safety Laboratory, New York.

Brunke, E.G., Labuschagne, C., Parker, B., van der Spuy, D. and Whittlestone, S. 2002, "Cape Point GAW Station 222Rn detector: factors affecting sensitivity and accuracy", *Atmospheric Environment,* vol. 36, pp. 2257-2262.

Bugai, D., Kozak, M., van Blerk, J., Avila, R. and Kovalets, I. 2015, *Remediation of the Zapadnoe Uranium Tailings Facility: Radiological Safety Assessment*, Sweden SSM – Ukrainian Ministry of Energy and Coal Industry, Kiev, Stockholm.

Busigin, A. and Phillips, C.R. 1980, "Uncertainties in the measurement of airborne radon daughters", *Health Physics,* vol. 39, pp. 943.

Busigin, A., van der Vooren, A.W. and Phillips, C.R. 1978, *Attached and Unattached Radon Daughters: Measurements and Measurement Techniques in Uranium Mines and in the Laboratory*, [online] Atomic Energy Control Board, Ottawa, Canada. Available at: http://www.iaea.org/inis/collection/NCLCollectionStore/_Public/15/025/15025849.pdf [Accessed 08 May 2017].

Cember, H., 1989. *Introduction to Health Physics*. 2nd ed. New York: Pergamon.

Chałupnik, S. and Wysocka, M. 2003, "Measurements of radon exhalation from soil – development of the method and preliminary results", *Journal of Mining Science,* vol. 39, no. 2, pp. 199-206.

Chambers, D.B., Lowe, L.M. and Stager, R.H. 1998, *Long Term Population Dose Due to Radon (Rn-222) Released from Uranium Mill Tailings*, [online] SENES Consultants Limited, Ontario, Canada. Available at: Available at: https://www.osti.gov/etdeweb/servlets/purl/20200868 [Accessed 08 May 2017].

Chambers, S.D., Wang, F., Williams, A.G., Xiaodong, D., Zhang, H., Lonati, G., Crawford, J., Griffiths, A.D., Ianniello, A. and Allegrini, I. 2015, "Quantifying the influences of atmospheric stability on air pollution in Lanzhou, China, using a radon-based stability monitor", *Atmospheric Environment,* vol. 107, pp. 233-243.

Chang, J.C. and Hanna, S.R. 2004, "Air quality model performance evaluation", *Meteorology and Atmospheric Physics,* vol. 87, no. 1-3, pp. 167-196.

Chen, C.J., Weng, P.S. and Chu, T.C. 1993, "Radon exhalation rate from various building materials", *Health Physics,* vol. 64, pp. 613-619.

Chen, J. and Marro, L. 2011, "Assessment of radon equilibrium factor from distribution parameters of simultaneous radon and radon progeny measurements", *Radiation and Environmental Biophysics,* vol. 50, pp. 597-601.

Choudhary, A.K. 2014, "Measurement of radon activity and exhalation rate in soil samples from Banda district, India", *Radiation Protection and Environment,* vol. 37, no. 3-4, pp. 161-164.

Clarke, R.H. and Macdonald, H.F. 1978, "Radioactive releases from nuclear installations: Evaluation of accidental atmospheric discharges", *Progress in Nuclear Energy,* vol. 2, no. 2, pp. 77-152.

Cliff, K.D. 1978, "The measurement of low concentrations of radon-222 daughters in the air, with emphasis on RaA assessment", *Physics in Medicine and Biology,* vol. 23, pp. 55.

Cooper, J.R. 2012, "Radiation protection principles", *JOURNAL OF RADIOLOGICAL PROTECTION,* vol. 32, no. 1, pp. N81-N88.

Countess, R.J. 1976, "Radon flux measurement with a charcoal canister", *Health Physics,* vol. 31, pp. 455-456.

Daraktchieva, Z., Miles, J.C.H. and McColl, N. 2014, "Radon, the lognormal distribution and deviation from it ", *Journal of Radiological Protection,* vol. 34, no. 1, pp. 183-190.

S. Darby, D. Hill, A. Auvinen, J. M. Barros-Dios, H. Baysson, F. Bochicchio, H. Deo, R. Falk, F. Forastiere, M. Hakama, I. Heid, L. Kreienbrock, M. Kreuzer, F. Lagarde, I. Mäkeläinen, C. Muirhead, W. Oberaigner, G. Pershagen, A. Ruano-Ravina, E. Ruosteenoja, A. Schaffrath Rosario, M. Tirmarche, L. Tomášek, E. Whitley, H. E. Wichmann and R. Doll 2005, 'Radon In Homes And Risk Of Lung Cancer: Collaborative Analysis Of Individual Data From 13 European Case-Control Studies', *British Medical Journal,* 33(7485), pp. 223-226.

De Luca, N., Coppari, E., Di Carlo, P. and Pitari, G. 2014, "Atmospheric radon in the surface layer: a box model constrained with meteorological data", In: *7th International Conference on Environmental and Geologicals Science and Engineering: Energy, Environmental and Structural Engineering*. [online] Salerno: WSEAS Press, pp.109-115. Available at: http://www.wseas.org/main/books/2014/Salerno/ENED.pdf [Accessed 27 Nov. 2017].

de Villiers, D. 2018, "Radiological Impact due to the Tailings Dams in the Vicinity of the Proposed Spitzland Development", *SciRAD Consulting (Pty) Ltd*, Hartebeespoort. Available at: https://sahris.sahra.org.za/sites/default/files/additionaldocs/Appendix%20K%20Radiation_0.pdf [Accessed 28 April 2018]

Demirarslan, K.O., Çetin Doğruparmak, Ş. and Karademir, A. 2017, "Evaluation of three pollutant dispersion models for the environmental assessment of a district in Kocaeli, Turkey", *Global NEST Journal,* vol. 19, no. 1, pp. 37-48.

Deyuan, T. 1991, "Analysis of Radon-222 Daughters In Air", *J.Radioanal.Nucl.Chem.,Letters,* vol 154, no 1, pp. 5-21.

Dinh Chau, N., Chruściel, E. and Prokólski, Ł. 2005, "Factors controlling measurements of radon mass exhalation rate", *Journal of Environmental Radioactivity,* vol. 82, no. 3, pp. 363-369.

Dinis, M.L. and Fiúza, A. 2015, *Simulation of Liberation and Dispersion of Radon from a Waste Disposal,* CIGAR, Oporto. Available at: https://paginas.fe.up.pt/~cigar/html/documents/SimulationofLiberationandDispersionofRadonfromaWasteDisposal.pdf [Accessed 14 May 2015]

Dinis, M.L. and Fiúza, A. 2014, "Modeling Radionuclide Distribution and Transport at a Legacy Site", *Procedia Earth and Planetary Science,* vol. 8, no. 0, pp. 64-69.

Doğruparmak, Ş.Ç., Karademir, A. and Ayberk, S. 2009, "Dispersion Model Predictions of NOx Emissions: Case Study from Kocaeli, Turkey", *Fresenius Environmental Bulletin,* vol. 18, no. 8, pp. 1497-1502.

Doi, M. and Kobayashi, S. 1996, "Surveys of radon isotopes in indoor and outdoor air in Japan", *Environment International,* vol. 22, no. Suppl, pp. S649-S655.

Dore, A.J., Carslaw, D.C., Braban, C., Cain, M., Chemel, C., Conolly, C., Derwent, R.G., Griffiths, S.J., Hall, J., Hayman, G., Lawrence, S., Metcalfe, S.E., Redington, A., Simpson, D., Sutton, M.A., Sutton, P.,

Tang, Y.S., Vieno, M., Werner, M. and Whyatt, J.D. 2015, "Evaluation of the performance of different atmospheric chemical transport models and inter-comparison of nitrogen and sulphur deposition estimates for the UK" , *Atmospheric Environment,* vol. 119, pp. 131-143.

Douglas, P. 2013, *Bioaerosol emissions from open window composting facilities: Emission characterisation and dispersion modelling improvements*, PhD edn, University of Cranfield.

Drew, G.H., Tamer Vestlund, A., Jordinson, G., Taha, M.P.M., Smith, R., Tyrrel, S., Longhurst, P.J. and Pollard, J.T. 2007, "Progress towards a best practise method for modelling dispersion of bioaerosols from composting facilities.", *11th International Waste Management and Landfill Symposium.*

Droullard, R.F. 1982, "Instrumentation for measuring uranium miner exposure to radon daughters", *Radiation Hazards in Mining*, pp. 332.

Dullard, R. and Holub, R. 1977, "Continuous working level measurements using alpha or beta detectors", *IH; Report of Investigations: RI-8237.* Denver, CO: Department of the Interior, Bureau of Mines.

Duenas, C., Fernandez, M.C., Carretero, J., Liger, E. and Perez, M. 1997, "Release of 222Rn from some soils", *Annales Geophysicae,* vol. 15, pp. 124-133.

Durand, J.F. 2012, "The impact of gold mining on the Witwatersrand on the rivers and karst system of Gauteng and North West Province, South Africa", *African Earth Sciences,* vol. AES 1751, no. 10.1016/j.jafrearsci.

Eappen, K.P., Nair, R.N. and Mayya, Y.S. 2008, "Simultaneous measurement of radon and thoron using Lucas scintillation cell", *Radiation Measurements*, vol. 43, no.1, pp. 91-97.

Eappen, K.P., Mayya, Y.S., Patnaik, R.L. and Kushwaha, H.S. 2006, "Estimation of radon progeny equilibrium factors and their uncertainty bounds using solid state nuclear track detectors", *Radiation Measurements*, vol. 41, no.3, pp. 342-348.

Edwards, G. 1992, "Uranium: The Deadliest Metal", *Perception Magazine,* vol. 10, no. 2.

El-Harbawi, M. 2013, "Air quality modelling, simulation, and computational methods: a review", *Environmental Reviews,* vol. 21, pp. 149-179.

EPA 1994, *Development and Testing of a Dry Deposition Algorithm (Revised)*, U.S. EPA, Research Triangle Park, NC. Available at: https://nepis.epa.gov/Exe/ZyNET.exe/2000EA8F.TXT?ZyActionD=ZyDocument&Client=EPA&Index=1991+Thru+1994&Docs=&Query=&Time=&EndTime=&SearchMethod=1&TocRestrict=n&Toc=&TocEntry=&QField=&QFieldYear=&QFieldMonth=&QFieldDay=&IntQFieldOp=0&ExtQFieldOp=0&XmlQuery=&File=D%3A%5Czyfiles%5CIndex%20Data%5C91thru94%5CTxt%5C00000012%5C2000EA8F.txt&User=ANONYMOUS&Password=anonymous&SortMethod=h%7C-&MaximumDocuments=1&FuzzyDegree=0&ImageQuality=r75g8/r75g8/x150y150g16/i425&Display=hpfr&DefSeekPage=x&SearchBack=ZyActionL&Back=ZyActionS&BackDesc=Results%20page&MaximumPages=1&ZyEntry=1&SeekPage=x&ZyPURL [Accessed 21 June 2017]

EPA 1992, *Development and Evaluation of a Revised Area Source Algorithm for the Industrial Source Complex Short Term Model*, U.S. EPA, Research Triangle Park, NC.

Evans, R.D. 1969, "Engineers Guide to the Elementary Behavior Of Radon Daughters", *Health Physics,* vol. 17, no. 2, pp. 229-252.

Faulkner, W.B., Shaw, B.W. and Grosch, T. 2008, "Sensitivity of two dispersion models (AERMOD and ISCST3) to input parameters for a rural ground-level area source.", *Journal of the Air and Waste Management Association,* vol. 58, no. 10, pp. 1288-1296.

Ferry, C., Richon, P., Beneito, A. and Robé, M. 2001, "Radon exhalation from uranium mill tailings: experimental validation of a 1-D model", *Journal of Environmental Radioactivity,* vol. 54, no. 1, pp. 99-108.

Fleming, Z.L., Monks, P.S. and Manning, A.J. 2012, "Review: Untangling the influence of air-mass history in interpreting observed atmospheric composition", *Atmospheric Research*, vol. 104-105, pp. 1-39.

Folkerts, K.H., Keller, G. and Muth, H. 1984, "Experimental investigations on diffusion and exhalation of 222Ra and 220Rn from building materials", *Radiation Protection Dosimetry,* vol. 7, pp. 41-44.

Forster, C., Stohl, A. and Seibert, P. 2007, "Parameterization of Convective Transport in a Lagrangian Particle Dispersion Model and Its Evaluation", *Journal of Applied Meteorology and Climatology,* vol. 46, no. 4, pp. 403-422.

Furuta, S., Ito, K. and Ishimori, Y. 2002, "Measurements of radon around closed uranium mines", *Journal of Environmental Radioactivity*, vol. 62, no. 1, pp. 97-114.

Georakis, K.S., Smith, J.W., Goodfellow, H.D. and Pye, J. 1995, "Review and evaluation of models estimating the minimum atmospheric dilution of gases exhausted near buildings", *Journal of the Air and Waste Management Association,* vol. 45, pp. 722-729.

George, A.C. 2007, "World History of Radon Research and Measurement from the Early 1900's to Today", *17th National Radon Conference*, ed. Curt Hopkins, Conference of Radiation Control Program Directors, Inc. (CRCPD), Frankfort, Kentucky, 9-12 September 2007. Available at: https://cdn.ymaws.com/www.crcpd.org/resource/collection/38E6A758-FF50-4C78-A8DD-03672B1FD0C6/November07RB.pdf [Accessed 24 Oct. 2014].

Gifford Jr., F.A. 1976, "Consequences of effluent releases", *Nuclear Safety,* vol. 17, no. 1, pp. 68-86.

Godish, T. 2000, *Indoor Environmental Quality,* CRC Press, eBook ISBN: 978-1-4200-5674-7.

Goosen, C.A., Strydom, R. and Leuschner, A.H. 1993, *The assessment of the dose to the public due to the radioactivity content of the South African mine tailings dams*, Atomic Energy Corporation of South Africa Ltd, Pretoria. Unpublished.

Grossi, C., Vargas, A., Camacho, A., López-Coto, I., Bolívar, J.P., Xia, Y. and Conen, F. 2011, "Inter-comparison of different direct and indirect methods to determine radon flux from soil", *Radiation Measurements,* vol. 46, no. 1, pp. 112-118.

Guan, C., Jianping, C. and Guo, Q. 2006, "Discussion of influencing factors on the radon exhalation rate and theoretical model", *Chinese Journal of Radiological Medicine and Protection,* vol. 26, no. 5, pp. 520-524.

Guedalia, D., Ntsila, A., Druilhet, A. and Fontan, J. 1980, "Monitoring of the atmospheric stability above an urban and suburban site using solar and radon measurements", *Journal of Applied Meteorology and Climatology,* vol. 19, pp. 839-848.

Gulia, S., Shiva Nagendra, S.M. and Khare, M. 2014, "Performance Evaluation of Iscst3, Adms-Urban and Aermod for Urban Air Quality Management in a Mega City of India", *International Journal of Sustainable Development and Planning,* vol. 9, no. 6, pp. 778-793.

Guo, Q., Sun, K. and Cheng, J. 2004, "Methodology Study on Evaluation of Radon Flux from Soil in China", *Radiat. Prot. Dosimetry,* vol. 112, no. 2, pp. 291-296.

Haider, B. and Jacobi, W. 1974, "A new monitor for long term measurement of radon daughter activity in mines", *3rd International Congress, IRPA, CONF-730907-P@.*

Hall, D.J., Spanton, A.M., Bennett, M., Dunkerley, F., Griffiths, R.F., Fisher, B.E.A. and Timmis , R.J. 2002, "Evaluation of new generation atmospheric dispersion models", *Journal of Environment and Pollution,* vol. 18, no. 1, pp. 22-32.

Hanna, S.R., Egan, B.A., Purdum, J. and Wagler, J. 2001, "Evaluation of the ADMS, AERMOD, and ISC3 Dispersion Models with the OPTEX, Duke Forest, Kincaid, Indianapolis and Lovett Field Datasets", *International Journal of Environment and Pollution,* vol. 16, pp. 301-314.

Hasan, K. 2001, "Study of Spatial/Temporal Patterns of Radon Releases from the K-65 Silos, using Dispersion Modeling and Gis: A Case Study At The Department Of Energy's Fernald Environmental Management Project, Cincinnati, Ohio". *Masters*. University of Cincinnati. Available at: https://etd.ohiolink.edu/pg_10?::NO:10:P10_ETD_SUBID:78643 [Accessed 13 Oct. 2016].

Hassan, N.M., Hosoda, M., Ishikawa, T., Sorimachi, A., Sahoo, S.K., Tokonami, S. and Fukushi, M. 2009, "Radon Migration Process and Its Influence Factors; Review", *Jpn. J. Health Phys,* vol. 44, no. 2, pp. 219-231.

Hendriks, P.H.G.M., Maučec, M. and de Meijer, R.J. 2002, "*M*CNP modelling of scintillation-detector γ-ray spectra from natural radionuclides" *Applied Radiation and Isotopes*, vol. 57, no. 3, PII S0969-8043(02)00118-5, pp. 449-457.

Hill, A. 1975, "Rapid measurement of radon decay products, unattached fractions and working level values of mine atmospheres", *Health Physics,* vol. 28, pp. 472.

Hill, J.M. 1986, *Radon and its daughters in the Hong Kong environment*, PhD edn, University of Hong Kong, Pokfulam, Hong Kong SAR.

Hirao, S., Yamazawa, H., Moriizumi, J., Yoshioka, K. and Iida, T. 2008, "Development and Verification of Long-Range Atmospheric Radon-222 Transport Model", *Journal of Nuclear Science and Technology,* vol. 45, no. Supp 6, pp. 166-172.

Hofman, R. 2011, *Application of Advanced Data Assimilation Methods in Off-Site Consequence Assessment*, Ph.D. edn, Czech Technical University, Prague.

Hofmann, W., Arvela, H.S., Harley, N.H., Marsh, J.W., McLaughlin, J., Röttger, A. and Tokonami, S. 2015, "Report 88", *Journal of the International Commission on Radiation Units and Measurements,* vol. 12, no. 2, pp. NP-NP.

Hoinaski, L., Franco, D. and de, M.L. 2017, "An analysis of error propagation in AERMOD lateral dispersion using Round Hill II and Uttenweiller experiments in reduced averaging times", *Environmental technology,* vol. 38, no. 5, pp. 639-651.

Holmes, N.S. and Morawska, L. 2006, "A review of dispersion modelling and its application to the dispersion of particles: An overview of different dispersion models available", *Atmospheric Environment,* vol. 40, no. 30, pp. 5902-5928.

Holmgren, R.M. 1974, "Working Levels of Radon Daughters in Air Determined from Measurements of RaB+RaC", *Health Physics,* vol. 27, pp. 141.

Holmgren, R.M., Wagner, W.W., Lloyd, R.D. and Pendleton, R.C. 1977, "Relative filter efficiencies for sampling radon daughters in air", *Health Physics,* vol. 32, pp. 297.

Hosch, W.L. 2019, *Navier-Stokes equation,* Available at: *https://www.britannica.com/science/Navier-Stokes-equation* (Accessed: 28 August 2017).

Hosoda, M., Sorimachi, A., Yasuoka, Y., Ishikawa, T., Sahoo, S.K., Furukawa, M., Hassan, N.M., Tokonami, S. and Uchida, S. 2009, "Simultaneous Measurements of Radon and Thoron Exhalation Rates and Comparison with Values Calculated by UNSCEAR Equation", *Journal of Radiation Research,* vol. 50, pp. 333-343.

Howard, A.J., Johnson, B.K. and Strange, W.P. 1990, "A high-sensitivity detection system for radon in air", *Nuclear Instruments and Methods in Physics Research Section A: Accelerators, Spectrometers, Detectors and Associated Equipment*, vol. 293, no. 3, pp. 589-595.

Hu, S.J. and Tan, S.K. 2000, "Radon and its progeny in outdoor air", *ASEAN Journal on Science and Technology for Development,* vol. 17, no. 2, pp. 65-70.

Human, C.F. and Botha, J.C. 1998, *The assessment of potential radiation hazards to members of the public from gold mines in the Klerksdorp, Orkney, Stilfontein and Hartebeesfontein areas*, Anglogold. Unpublished.

Hunt, J. 2014, "Occupational radiation protection in the workplace involving exposure to radon". In: *International Conference on*

*Occupational Radiation Protection*. [online] Vienna: ICRP. Available at: http://www-ns.iaea.org/tech-areas/communication-networks/orpnet/documents/cn223/8-hunt-presentation.pdf [Accessed 12 Sep. 2017].

IAEA 2013, "Measurement and Calculation of Radon Releases from NORM Residues", *Technical Reports Series No 474*. [online] Vienna: International Atomic Energy Agency. Available at: https://www-pub.iaea.org/MTCD/Publications/PDF/trs474_webfile.pdf [Accessed 19 Sep. 2014].

IAEA 2007, "Quality Control Procedures Applied to Nuclear Instruments", *Proceedings of a Technical Meeting",* International Atomic Energy Agency, Vienna, 23–24 August 2007, pp. 43.

IAEA 2008, "Naturally Occurring Radioactive Material (Norm V)", *Proceedings Of The Fifth International Symposium On Naturally Occurring Radioactive Material",* International Atomic Energy Agency, Vienna, 19–22 March 2007, pp. 1.

IAEA 1992, "Measurement and Calculation of Radon Releases from Uranium Mill Tailings", Technical *Reports Series No 333*. Vienna: International Atomic Energy Agency.

IAEA 1988, "Quality Control of Nuclear Medicine Instruments", *IAEA-TECDOC-602*, Vienna: International Atomic Energy Agency.

ICRP 2010, 'Lung Cancer Risk from Radon and Progeny and Statement on Radon', *Ann. ICRP,* 40(1), pp. 1-64.

ICRP 2009, "International Commission on Radiological Protection Statement on Radon", *ICRP Ref 00/902/09*. [online] Ottawa: ICRP Publication. Available at: http://www.icrp.org/docs/ICRP_Statement_on_Radon(November_2009).pdf [Accessed 17 Jun. 2015].

Ielsch, G., Ferry, C., Tymen, G. and Robé, M.C. 2002, "Study of a predictive methodology for quantification and mapping of the radon-222 exhalation rate", *Journal of Environmental Radioactivity,* vol. 63, no. 1, pp. 15-33.

Iida, T., Ikebe, Y. and and Tojo, K. 1991, "An electrostatic radon monitor for measurements of environmental radon", *Res. Lett. Atmos. Electr.,* vol. 11, pp. 55-59.

Iida, T., Ikebe, Y., Suzuki, K., Ueno, K., Wang, Z. and Jin, Y. 1996, *Continuous measurements of outdoor radon concentrations at various locations in East Asia.*

Iimoto, T., Shirakata, Y., Tokonami, S., Furukawa, M. and Kurosawa, R. 1998, "Continuous 220Rn concentration monitor using an electrostatic collection method,", *Radiation Protection Dosimetry,* vol. 77, pp. 185-189.

Isakov, V., Sax, T., Venkatram, A., Pankratz, D., Heumann, J. and Fitz, D. 2004, "Near-field dispersion modeling for regulatory applications.", *Journal of the Air and Waste Management Association,* vol. 54, no. 4, pp. 473-482.

Ishimori, Y., Lange, K., Martin, P., Mayya, Y.S. and Phaneuf, M. 2013, *Measurement and Calculation of Radon Releases from NORM Residues. Technical Reports Series No 474. [online] Vienna: International Atomic Energy Agency.* Available at: https://www-pub.iaea.org/MTCD/Publications/PDF/trs474_webfile.pdf [Accessed 19 Sep. 2014].

Ishimori, Y. and Maruo, Y. 2005, "Radon exhalation rate monitoring in/around the closed uranium mine sites in Japan", *Proceedings of the International Congress Series,* vol. 1276, no. 0, pp. 291-292.

James, A.C. and Strong, J.C. 1973, *"A radon daughter monitor for use in mines" Proceedings of the 3rd International Congress of the Radiation Protection Association, U.S.* , AEC, Springfield, Virginia.

Jenkins, P.H. 2002, "Equations for modeling of grab samples of radon decay products", *Health Physics,* vol. 83, no. 2, pp. S48-S51.

Jiránek, M. and Fronka, A. 2008, "New technique for the determination of radon diffusion coefficient in radon proof membranes", *Radiat. Prot. Dosim,* vol. 130, pp. 22-25.

Jonassen, N. and Hayes, E.I. 1974, "Measurements of Low Concentrations of the Short-Lived Radon-222 Daughters in the Air by Alpha Spectroscopy", *Health Physics,* vol. 26, pp. 104.

Jönsson, G. 1997, "The nuclear track detector—A tool in radon measurements", *Radiation Measurements,* vol. 28, no. 1–6, pp. 695-698.

Jönsson, G. 1995, "Radon gas — where from and what to do?", *Radiation Measurements,* vol. 25, no. 1–4, pp. 537-546.

Jönsson, G. 1991, "Solid state nuclear track detectors in radon measurements indoors and in the soil", *International Journal of Radiation Applications and Instrumentation.Part D.Nuclear Tracks and Radiation Measurements,* vol. 19, no. 1–4, pp. 335-338.

Jönsson, G. 1987, "Indoor radon gas and its detection with Kodak plastic film", *International Journal of Radiation Applications and Instrumentation.Part D.Nuclear Tracks and Radiation Measurements,* vol. 13, no. 1, pp. 85-91.

Jönsson, G., Baixeras, C., Enge, W., Freyer, K., Treutler, H.-., Monnin, M.M. and Sciocchetti, G. 1995, "Criteria for indoor radon concentration — an experimental study considering especially the Leipzig-Halle brown coal area", *Radiation Measurements,* vol. 25, no. 1–4, pp. 627-630.

Kadir, A., Zhang, L., Guo, Q. and Liang, L. 2013, "Efficiency Analysis and Comparison of Different Radon Progeny Measurement Methods", *The Scientific World Journal,* vol. 2013, no. Article ID 269168, pp. 6.

Kakati, R.K., Kakati, L. and Ramachandran, T.V. 2013, "Measurement of Uranium, Radium and Radon Exhalation Rate of Soil Samples from Karbi Anglong District of Assam, India using EDXRF and Can Technique Method", *APCBEE Procedia,* vol. 5, no. 0, pp. 186-191.

Kamal, H., Doulatdarb, R. and Mehdizadeha, S. 2007, "Indoor radon monitoring in Northern Iran using passive and active measurements", *Journal of Environmental Radioactivity,* vol. 95, no. 1, pp. 39.

Karam, A. and Venter, N. 2007, "Affordable housing on contaminated land in Johannesburg : research article", *Acta Structilia : Journal for the Physical and Development Sciences,* vol. 14, no. 2, pp. 35-37.

Kawaji, M., Pai, H.L. and Phillips, C.R. 1981, "Use of gross filter activities in a continous working level monitor", *Health Physics,* vol. 40, no. 4, pp. 543-548.

Keith, S., Doyle, J.R. and Harper, C. 2012, *Toxicological Profile for Radon,* Agency for Toxic Substances and Disease Registry (US), Atlanta (GA).

Kerr, G.D. 1975, *Measurement of radon progeny concentrations in air by alpha-particle spectrometey*, ak Ridge National Lab., Tennessee, (USA).

Khan, A., Busigin, A. and Phillips, C.R. 1982, "An optimized scheme for measurement of the concentrations of the decay products of radon and thoron", *Health Physics,* vol. 42, pp. 809.

Kojima, H. 1996, "The equilibrium factor between radon and its daughters in the lower atmosphere", *Environment International, vol.* 22, no. 1, pp. 187-192.

Kotrappa, P. and Jester, W.A. 1993, "Electret ion chamber radon monitors measure dissolved 222Rn in water", *Health Physics,* vol. 64, pp. 397-405.

Kotrappa, P. and Stieff, F. 2008, "Electret Ion Chambers (EIC) To Measure Radon Exhalation Rates from Building Materials", *Proceedings of the American Association of Radon Scientists and Technologists 2008 International Symposium* AARST, Las Vegas NV, September 14-17,.

Kotrappa, P. and Stieff, L.R. 1994, "Application of NIST Rn-222 emanation standards for calibrating Rn-222 monitors", *Radiation Protection Dosimetry,* vol. 55, pp. 211-218.

Kovalets, I.V., Asker, C., Khalchenkov, A.V., Persson, C. and Lavrova, T.V. 2017, "Atmospheric dispersion of radon around uranium mill tailings of the former Pridneprovsky Chemical Plant in Ukraine", *Journal of Environmental Radioactivity,* vol.172, Supplement C, pp. 173-190.

Kozłowska, B., Mazur, J., Kozak, K., Walencik-Łata, A. and Baic, B. 2016, "Investigation of the influence of chamber construction parameters on radon exhalation rate", *NUKLEONIKA,* vol. 61, no. 3, pp. 269-273.

Kraner, H.W., Schroeder, G.L. and Evans, R.D. (eds) 1964, *Measurements of the effect of atmospheric variables on radon-222 flux and soil-gas concentrations*, Univerdsity of Chicago Press.

Krewski, D., Lubin, J., Zielinski, J., Alavanja, M., Catalan, V., Field, R., Klotz, J., Létourneau, E., Lynch, C., Lyon, J., Sandler, D., Schoenberg, J., Steck, D., Stolwijk, J., Weinberg, C. and Wilcox, H. 2006, "A combined analysis of North American case-control studies of residential radon and lung cancer.", *J. Toxicol. Environ. Health A.,* vol. 69, no. 7, pp. 533.

Kritidis, P., Uzunov, I. and Miniv, L. 1977, "Precision Alpha-Counting Methods for Determination of Radon Daughters in Air", *Nuclear Instrumentation Methods,* vol. 143, pp. 299.

Križman, M.J., Rojc, J. and Peter, J.E. 2010, "Radon events in the U-mine environment and related radiation exposure", *NUKLEONIKA,* vol. 55, no. 4, pp. 529-533.

Krizman, M. and Stegnar, P. 1992, "Environmental impact of the 'Zirovski Vrh' uranium mine on the enhancement of outdoor radon concentrations', *Radiation Protection Dosimetry, vol.* 24, no. 22, pp. 723-728.

Kumar, A., Dixit, S., Varadarajan, C., Vijayan, A. and Masuraha, A. 2006, "Evaluation of the AERMOD dispersion model as a function of atmospheric stability for an urban area", *Environmental Progress,* vol. 25, no. 2, pp. 141-151.

Kumar, A., Bellam, N.K. and Sud, A. 1999, "Performance of an industrial source complex model: Predicting long-term concentrations in an urban area", *Environmental Progress,* vol. 18, no. 2, pp. 93-100.

Kümmel, M., Dushe, C., Müller, S. and Gehrcke, K. 2014, "Outdoor 222Rn-concentrations in Germany – part 1 – natural background", *Journal of Environmental Radioactivity,* vol. 132, no. 0, pp. 123-130.

Kusnetz, H.L. 1956, "Radon daughters in mine atmospheres: A field method for determining concentrations", *Industrial Hygiene Quarterly,* vol. 17, no. 1, pp. 85-88.

Lawrence, C.E., Akber, R.A., Bollhöfer, A. and Martin, P. 2009, "Radon-222 exhalation from open ground on and around a uranium mine in the wet-dry tropics", *Journal of Environmental Radioactivity,* vol. 100, no. 1, pp. 1-8.

Lazaridis, M. 2011, *First Principles of Meteorology and Air Pollution,* 1st edn, Springer.

Leach, V.A. and Chandler, W.P. 1992, "Atmospheric dispersion of radon gas and its decay products under stable conditions in arid regions of Australia", *Environmental Monitoring and Assessment,* vol. 20, no. 1, pp. 1-17.

Leung, H. 1987, *Properties and Measurement of the Progeny of Radon and Thoron.* Ph.D. University of Toronto.

Liefferink, M. 2011, *Comments on GDARD Project: Reclamation of mine residue areas for development purposes*, Federation for a Sustainable Environment, Johannesburg, South Africa. Available at: http://www.fse.org.za/Downloads/COMMENTS%20ON%20GDARD%20PROJECT%20FINAL.pdf [Accessed 19 Jun. 2014].

Liland, A. 2015, *Modelling of radionuclide distribution in contaminated nuclear and NORM sites*, Woodhead Publishing.

Lindsay, R., de Meijer, R.J., Maleka, P.P., Newman, R.T., Motlhabane, T.G.K. and de Villiers, D. 2004a, "Monitoring the radon flux from gold-mine dumps by γ-ray mapping", *Nucl. Instrum. Methods. Phys. Res. B,* vol. 213, no. 0, pp. 775-778 .

Lindsay, R., Newman, R.T. and Speelman, W.J. 2008, "A study of airborne radon levels in Paarl houses (South Africa) and associated

source terms, using electret ion chambers and gamma-ray spectrometry", *Applied Radiation and Isotopes,* vol. 66, no. 11, pp. 1611-1614.

Lopez, A., Guedalia, D., Servant, J. and Fontan, J. 1974, "Advantages of the Use of Radioactive Tracers $^{222}Rn$ and $^{212}Pb$ for the Study of Aitken Nuclei within the Lower Troposphere", *Journal of Geophysical Research,* vol. 79, pp. 1243-1252.

López-Coto, I., Mas, J.L., Bolivar, J.P. and García-Tenorio, R. 2009, "A short-time method to measure the radon potential of porous materials", *Applied Radiation and Isotopes,* vol. 67, no. 1, pp. 133-138.

Lorber, M., Eschenroeder, A. and Robinson, R. 2000, "Testing the USA EPA's ISCST-Version 3 model on dioxins: a comparison of predicted and observed air and soil concentrations", *Atmospheric Environment,* vol. 34, no. 23, pp. 3995-4010.

Lubin, J., Wang, Z., Boice, J.J., Xu, Z., Blot, W., De Wang, L. and Kleinerman, R. 2004, "Risk of lung cancer and residential radon in China: pooled results of two studies.", *Int J Cancer.,* vol. 109, no. 1, pp. 132.

Maeda, L.Y. and Hobbs, W.E. 1996, "Outdoor Radon Concentrations in The Vicinity of an Active Home Radon Mitigation System", *Proceedings of the 1996 International Radon Symposium,* pp. 4.1.

Maged, A.F. and Ashral, F.A. 2005, "Radon exhalation rate of some building materials used in Egypt.", *Environmental Geochemistry and Health,* vol. 27, pp. 485-489.

Mahapatra, A.D. and Ramjeawon, T. 2011, "Prediction of Ground-Level Concentration of Sulfur Dioxide Downwind of an Industrial Estate in Mauritius Using the ISCST3 Model and Selection of Air Pollution Control Systems", *Journal of Water, Air and Soil Pollution,* vol. 219, pp. 203-213.

Maiello, M.L. and Hoover, M.D. (eds) 2010, *Radioactive Air Sampling Methods*, CRC Press, pp 389-406.

Marcazzan, G.M. and Persico, F. 1996, "Evaluation of mixing layer depth in Milan town from temporal variation of atmospheric radioactive aerosols", *Journal of Aerosol Science,* vol. 27, no. 24, pp. S21.

Martz, D.E., Holleman, D.F., McCurdy, D.E. and Schiager, K.J. 1969, "Analysis of Atmospheric Concentrations of RaA, RaB, and RaC by Alpha Spectroscopy", *Health Physics,* vol. 17, pp. 131.

Matiullah, Rehman, S., Rehman, S., Mati, N. and Ahmad, S. 2005, "Some more new etchants for a CR-39 detector", *Radiation Measurements,* vol. 39, no. 5, pp. 551-555.

Mayya, Y.S. 2004, "Theory of radon exhalation into accumulators placed at the soil–atmosphere interface", *Radiation Protection Dosimetry,* vol. 111, no. 3, pp. 305-318.

MBendi 2012, June 2012-last update, *Gold Mining in South Africa - Overview* [Homepage of MBendi], [Online]. Available: http://www.mbendi.com/indy/ming/gold/af/sa/p0005.htm [2012, June 2012].

Megumi, K. and Mamuro, T. 1973, "Radon and Thoron Exhalation from the Ground", *Journal of Geophysical Research,* vol. 78, pp. 1804.

Miles, J. 2004, "Methods of radon measurement and devices", Czech Republic, pp. 377.

Moed, B.A., Nazaroff, W.W. and Sextro, R.G. 1988, "Soil as a source of indoor radon: Generation, migration and entry" in *Radon and its Decay Products in Indoor Air*, eds. W.W. Nazaroff and A.V. Nero Jr., John Wiley and Sons, New York, , pp. 57-112.

Momeni, M.H., Yuan, Y. and Zielen, A.J. 1979, *Uranium Dispersion and Dosimetry (UDAD) Code*, Argonne National Laboratory, for the U.S. Nuclear Regulatory Commission.

Momeni, M.H. 1979, *Radon and radon-daughter concentrations in air in the vicinity of the Anaconda Uranium Mill,* Washington, DC : The Commission ; Springfield, Va.: Available from National Technical Information Service, 1979.

Moshupya, P., Abiye, T., Mouri, H., Levin, M., Strauss, M. and Strydom, R. 2019," Assessment of radon concentration and impact on human health in a region dominated by abandoned gold mine tailings: A case from the West Rand area, Krugersdorp, South Africa". *Journal of Geosciences*, vol. 9, pp. 466.

Mudd, G.M. 2008, "Radon releases from Australian uranium mining and milling projects: assessing the UNSCEAR approach", *Journal of environmental radioactivity,* vol. 99, no. 2, pp. 288-315.

Nappo, C.J., Caneill, J.Y., Furman, R.W., Gifford, F.A., Kaimal, J.C., Kramer, M.L., Lockhart, T.J., Pendergast, M.M., Pielke, R.A., Randerson, D., Shreffler, J.H. and Wyngaard, J.C. 1982, "The Workshop on the Representativeness of Meteorological Observations, June 1981, Boulder, Colo", *Bulletin of the American Meteorological Society,* vol. 63, no. 7, pp. 761-764.

Nazaroff, W.W. 1983, "Radon Daughter Carousel: An Automated Instrument for Measuring Indoor Concentrations of 218Po, 214Pb, 214Bi", *Review of Scientific Instrumentation,* vol. 54, pp. 1227.

Nazaroff, W.W., Nero, A.V. and Revzan, K. (eds) 1981, *Alpha Spectroscopic Techniques for Field Measurements of Radon Daughters*, Wiley Eastern Limited, New Dehli.

Nazaroff, W.W. 2010, *A residential radon daughter monitor based on alpha spectroscopy*, MSc edn, University of California, California.

Nazaroff, W.W. 1984, "Optimizing the total-alpha three-count technique for measuring concentrations of radon progeny in residences", *Health Physics,* vol. 46, pp. 395.

Nazaroff, W.W. and Nero, A.V. 1988, *Radon and Its Decay Products in Indoor Air,* John Wiley and Sons, New York.

NCRP 1988, "Measurement of Radon and Radon Daughters in Air", *Report No. 97.* Bethesda, MD: National Council on Radiation Protection and Measurements.

Neshuku, M.N. 2012, *Comparison of the performance of two atmospheric dispersion models (AERMOD and ADMS) for open pit mining sources of air pollution*, Masters of Science in Applied Science: Environmental Technology edn, University of Pretoria, Pretoria, South Africa.

Ng, F.M.F., Nikezic, D. and Yu, K.N. 2007, "Long-term measurements of equilibrium factor with electrochemically etched CR-39 SSNTD", *Nuclear Instruments and Methods in Physics Research Section B: Beam Interactions with Materials and Atoms,* vol. 263, no. 1, pp. 279-283.

Nikolaev, V.A. and Ilić, R. 1999, "Etched track radiometers in radon measurements: a review", *Radiation Measurements,* vol. 30, no. 1, pp. 1-13.

Nuclear Energy Agency 1982, "Long-term Radiological Aspects of Mangement of Wastes from Uranium Mining and Milling",. In: *International Symposium on Management of Wastes from Uranium Mining and Milling.* [online] Paris: Organisation for Economic Co-orperation and Development. Available at: http://www.iaea.org/inis/collection/NCLCollectionStore/_Public/14/784/14784138.pdf [Accessed 15 Mar. 2016].

Ojha, C.S.P., Mena, M., Guttikunda, S., Gurjar, B.R. and Lei, W. 2010, "Air Pollution Modeling: Theory and Application" in *Air Pollution: Health and Environmetal Impacts*, eds. B.R. Gurjar, L.T. Molina and C.S.P. Ojha, 1st edn, CRC Press, Boca Raton, Florida, pp. 45.

Odendaalsrus climate: Average Temperature, weather by month, Odendaalsrus weather averages - Climate-Data.org. 2019. Odendaalsrus climate: Average Temperature, weather by month, Odendaalsrus weather averages - Climate-Data.org. [ONLINE] Available at: https://en.climate-data.org/africa/south-africa/free-state/odendaalsrus-26385/. [Accessed 01 October 2019].

Olesen, H.R., Løfstrøm, P., Berkowicz, R. and Ketzel, M. 2005, *Regulatory odour model development: Survey of modelling tools and datasets with focus on building effects* , National Environmental Research Institute, Denmark.

Olesen, H.R., Løfstrøm, P., Berkowicz, R. & Ketzel, M. 2005, "*Regulatory odour model development: Survey of modelling tools and datasets with focus on building effects",* National Environmental Research Institute, Denmark. 62 pp. - NERI Technical Report No. 541. Available at: http://technical-reports.dmu.dk

Ongori, J.N., Lindsay, R., Newman, R.T. and Maleka, P.P. 2015, "Determining the radon exhalation rate from a gold mine tailings dump by measuring the gamma radiation", *Journal of Environmental Radioactivity,* vol. 140, no. 0, pp. 16-24.

Ott, W. 1990, "A physical explanation of the lognormality of pollutant concentrations", *Journal of the Air and Waste Management Association,* vol. 40, no. 10, pp. 1378-1383.

Ott, W.R. 1995, *Environmental Statistics and Data Analysis,* Lewis Publishers, Boca Raton, FL.

Oudwater, S.A. 2017, *Modeling of dust emission in dimension stone quarry*, Master's Thesis edn, Aalto University.

Paine, R.J. and Lew, F. 1997, "Results of the Independent Evaluation of ISCST3 and ISC-PRIME", *TR-2460026*, Palo Alto, California: Electric Power Research Institute Available at: https://www3.epa.gov/scram001/7thconf/iscprime/evalrpt.pdf. [Accessed 20 July 2017].

PARC RGM 2018, *Radon Analysis*. Available: http://www.parcrgm.co.za/.

PARC RGM 2019, *Personal communication, 20 September.*

Parc Scientific 1995, *A method for determination of Rn exhalation parameters of porous materials*, Parc Scientific (Pty) Ltd, Cresta.

Pasini, A., Salzano, R. and Attanasio, A. 2014, "Modeling Radon Behavior for Characterizing and Forecasting Geophysical Variables at the

Atmosphere–Soil Interface" in *Recent Trends in Modelling of Environmental Contaminants*, ed. D. Sengupta, 1st edn, Springer, India, pp. 213-237.

Pasquill, F. 1961, "The estimation of the dispersion of windborne material", *The Meteorological Magazine,* vol. 90, no. 1063, pp. 33-49.

Perry, S.G., Cimorelli, A.J., Paine, R.J., Brode, R.W., Weil, J.C., Venkatram, A., Wilson, R.B., Lee, R.F. and Peters, W.D. 2004, "AERMOD: A Dispersion Model for Industrial Source Applications. Part II: Model Performance against 17 Field Study Databases", *Journal of Applied Meteorology,* vol. 44, no. 694, pp. 708.

Petzer, G. 2018, *Air Quality Impact Assessment for the Proposed Spitzland Development near Roodepoort, Gauteng*, Environmental Impact Management Services (EIMS), Halfway House.

Pogorski, S.R. and Phillips, C.R. 1985, "Monte Carlo simulation of uncertainties in three-count total alpha radon progeny measurement techniques", *Nuclear Instruments and Methods in Physics Research Section A: Accelerators, Spectrometers, Detectors and Associated Equipment,* vol. 241, no. 2–3, pp. 539-553.

Porstendörfer, J. 1994, "Properties and Behaviour of Radon and Thoron and their Decay Products in the Air", *Journal of Aerosol Science,* vol. 25, no. 2, pp. 219-263.

Porstendörfer, J. and Gründel, M. 2005, "Radon decay products in outdoor air", *Radioactivity in the Environment*, vol. 7, Supplement C, pp. 56-65.

Porstendörfer, J. 1996, "Radon: Measurements related to dose", *Environment International*, vol. 22, Supplement 1, pp. 563-583.

Prabha, J. and Singh, G. 2006, "Comparison and Performance Evaluation of Dispersion Models and ISCST3 for a Gold Mine at Goa", *Journal of Industrial Pollution Control,* vol. 22, no. 2, pp. 297-303.

Prasad, Y., Prasad, G., Gusain, G.S., Choubey, V.M. and Ramola, R.C. 2008, "Radon exhalation rate from soil samples of South Kumaun Lesser Himalayas, India", *Radiation Measurements,* vol. 43, pp. S369-S374.

Pressyanov, D.S., Guelev, M.G. and Sharkov, B.G. 1995, "Radon and radon progeny outdoors in a valley of enhanced natural radioactivity", *Atmospheric Environment*, vol 29, no. 23, pp. 3433-3439.

Quindos Poncela, L.S., Fernandez, P.L., Arozamena, J.G. and Fernandez, C.S. 2005, "A method for measuring active radon diffusion coefficients in radon barriers by using modified Lucas cells", *Radiat. Meas,* vol. 39, pp. 87-89.

Quindos, L.S., Newton, G.J., Cheng, Y. and Yeh, H. 1988, "Measuring Rn Progeny By the Three-Interval Counting Methods: The Influence of 222Rn Progeny", *Health Physics,* vol. 55, no. 3, pp. 565-569.

Raabe, O.G. and Wrenn, M.E. 1969, "Analysis of the activity of radon daughter samples by weighted least squares", *Health Physics,* vol. 17, pp. 593.

Rad Elec Inc. 2018, , *Radon in Air*. Available: https://www.radelec.com/radon_monitoring.html.

Rama Krishna, T.V.B.P.S., Reddy, M.K., Reddy, R.C. and Singh, R.N. 2005, "Impact of an industrial complex on the ambient air quality: Case study using a dispersion model", *Atmospheric Environment,* vol. 39, no. 29, pp. 5395-5407.

Ramola, R.C. and Choubey, V.M. 2004, "Measurement of radon exhalation rate from soil samples of Garhwali Himalaya", *J. Radioanal. Nucl. Chem,* vol. 256, pp. 219-233.

Raviart, S., Richon, P., Haristoy, D., Robé, M.C., Belot, Y., Kümmel, M., Düshe, C. and Ullman, W. 1996, "Field determination of the time-varying equilibrium factor between 222Rn and its short-lived decay products in the atmosphere above a waste-rock pile", *Environment International,* vol. 22, Supplement 1, pp. 279-286.

Reeves, D. 2001, *Understanding and Adapting to New Dispersion Models,*, Oregon: Trinity Consultants. Available at: https://www.environmental-expert.com/articles/understanding-and-adapting-to-new-dispersion-models-published-in-the-oregon-insider-december-2001-271870 [Accessed 28 April 2018].

Riswadkar, R.M. and Kumar, A. 1994, "Evaluation of the Industrial Source Complex short-term model in a large-scale multiple source region for different stability classes", *Environmental Monitoring and Assessment,* vol. 33, no. 1, pp. 19-32.

Rogers, V.C. and Nielson, K.K. 1981, "A complete description of radon diffusion in earthen materials", *Proceedings ofthe 4th symposium on uranium mill tailings management.* Geotechnical Engineering Program, Colorado State University, Fort Collins, Colorado, USA, 26–27 October 1981, pp. 247.

Rogers, V.C., Nielson, K.K. and Kalkwarf, D.R 1984, "Radon Attenuation Handbook for Uranium Mill Tailings Cover Design", *NUREG/CR-3533*, Richland: Pacific Northwest Laboratory. Available at: https://www.osti.gov/servlets/purl/6883619 [Accessed 03 Feb. 2016].

Rolle, R. 1972, "Rapid Working Level Monitoring", *Health Physics,* vol. 22, pp. 222.

Rozas, S., Idoeta, R., Alegría, N. and Herranz, M. 2016, "Radiological characterisation and radon equilibrium factor in the outdoor air of a post-industrial urban area", *Journal of Environmental Radioactivity*, vol. 151, Part 1, pp. 126-135.

Saegusa, J., Yamasaki, K., Tsujimoto, T., Yamauchi, T. and Shimo, M. 1996, "Development of an apparatus for measuring ground exhalation rates of 222Rn and 220Rn", *Environment International,* vol. 22, Supplement 1, no. 0, pp. 483-490.

Sahoo, B.K., Mayya, Y.S., Sapra, B.K., Gaware, J.J., Banerjee, K.S. and Kushwaha, H.S. 2010, "Radon exhalation studies in an Indian uranium tailings pile", *Radiation Measurements,* vol. 45, no. 2, pp. 237-241.

Sahu, P., Mishra, D.P., Panigrahi, D.C., Jha, V., Patnaik, R.L. and Sethy, N.K. 2014, "Radon emanation from backfilled mill tailings in underground uranium mine", *Journal of Environmental Radioactivity,* vol. 130, no. 0, pp. 15-21.

Sakashita, T., Doi, M., Nakamura, Y. and Iida, T. 2004, "A case study of radon-222 transport from continental North-East Asia to the Japanese islands in winter by numerical analysis", *Journal of Environmental Radioactivity,* vol. 72, no. 3, pp. 245-257.

Samuelsson, C. 1990, "The Closed-Can Exhalation Method for Measuring Radon", *Journal of Research of the National Institute of Standards and Technology,* vol. 95, no. 2, pp. 167.

Samuelsson, C. and Pettersson, H. 1984, "Exhalation of $^{222}$Rn from porous materials", *Radiation Protection Dosimetry,* vol. 7, pp. 95-100.

Sarkar, U., Longhurst, P.J. and Hobbs, S.E. 2003, "Community modelling: a tool for correlating estimates of exposure with perception of odour from municipal solid waste (MSW) landfills", *Journal of Environmental Management,* vol. 68, no. 2, pp. 133-140.

Sasaki, T., Gunji, Y. and Okuda, T. 2006, "Transient diffusion measurement of radon in Japanese soils from a mathematical viewpoint", *J. Nucl. Sci. Technol,* vol. 43, pp. 806-810.

Schery, S.D., Gaeddert, D.H. and Wilkening, M.H. 1984, "Factors affecting exhalation of radon from a gravelly sandy loam", *Journal of Geophysical Research,* vol. 89, no. D5, pp. 7299-7309.

Schewe, G.J. and Smith, P.J. 2009, "Sensitivity of AERMOD in Modeling Fugitive Dust Emission Sources"*, Paper No. 31*, Covington, KY: Trinity Consultants. Available at: https://www.trinityconsultants.com › Media › Technical-Papers › PDF. [Accessed 20 May 2018].

Schroeder, A.J. 2006, *Comparison of Two Dispersion Models: A Bulk Petroleum Storage Terminal Case Study*, Trinity Consultants, Dallas, TX. Available at: https://www.trinityconsultants.com › media › technical-papers › pdf. [Accessed 20 May 2018].

Schulman, L.L. and Hanna, S.R. 1986, "Evaluation of Downwash Modifications to the Industrial Source Complex Model", *Journal of the Air Pollution Control Association,* vol. 36, no. 3, pp. 258-264.

Schulte, D.D., Modi, M.R., Henry, C.G., Stowell, R.R., Billesbach, D.P., Hoff, S.J. & Jacobson, L.D. 2007, 'Modeling odor dispersion from a swine facility using AERMOD' *Paper presented at International Symposium on Air Quality and Waste Management for Agriculture,* Broomfield, CO, United States, 9/16/07 - 9/19/07, . Available at: https://www.researchgate.net/publication/267916986_Modeling_odor_dispersion_from_a_swine_facility_using_AERMOD [Accessed 23 May 2018].

Scott, R.D. and Mackenzie, A.B. 1985, "Measurement of low 222Rn activities by means of surface barrier detectors", *Nuclear Instruments and Methods in Physics Research Section A: Accelerators, Spectrometers, Detectors and Associated Equipment*, vol. 238, no. 1, pp. 160-164.

Scott, R.D. and Mackenzie, A.B. 1984, "Detection of 222Rn by use of silicon surface-barrier detectors", *The International Journal of Applied Radiation and Isotopes,* vol. 35, no. 4, pp. 301-303.

Severino, C.T. 2014, *Real-time measurement of radon activity and mixed radiation fields characterization with silicon pixel detector*, der Philosophisch edn, der Universität Bern, Enna, Italia.

Sharma, N., Singh, J., Esakki, S.C. and Tripathi, R.M. 2016, "A study of the natural radioactivity and radon exhalation rate in some cements used in India and its radiological significance", *Journal of Radiation Research and Applied Sciences,* vol. 9, no. 1, pp. 47-56.

Sharma, S. and Chandra, A. 2008, "Simulation of Air Quality using an ISCST3 Dispersion Model", *Clean Soil, Air, Water,* vol. 36, no. 1, pp. 118-124.

Sheridan, B.A., Hayes, E.T., Curran, T.P. and Dodd, V.A. 2004, "A dispersion modelling approach to determining the odour impact of intensive pig production units in Ireland", *Bioresource Technology,* vol. 91, pp. 145-152.

Siaway, G., Mose, D. and Metcalf, J. 2009, "Evaluation Of Indoor Radon Potential In Northern Virginia Using Spacial Autocorrelation, Gis-Application And 3-D Visualization", *Proceedings of the Annual International Conference on Soils,* vol. 14, no. 1, Article 12. Available at: https://scholarworks.umass.edu/soilsproceedings/vol14/iss1/12 [Accessed 09 Sep. 2018]

Silverman, K.C., Tell, J.G., Sargent, E.V. and Qiu, Z. 2007, "Comparison of the Industrial Source Complex and AERMOD Dispersion Models: Case Study for Human Health Risk Assessment ", *Journal of the Air and Waste Management Association,* vol. 57, no. 12, pp. 1439-1446.

Simons, R., Karam, A., Viruly, F., Baloyi, H., Mokoena, D. and Venter, N. 2006, "Affordable and Middle Class Housing on Johannesburg's Mining Sites: A Benefit-Cost Analysis", *Development Southern Africa*, vol. 25, no. 1, pp. 3-20, DOI: 10.1080/03768350701836145.

Singh, K., Singh, M., Singh, S., Sahota, H.S. and Papp, Z. 2005, "Variation of radon (222Rn) progeny concentrations in outdoor air as a function of time, temperature and relative humidity", *Radiation Measurements*, vol. 39, no. 2, pp. 213-217.

Smetana, R. and Novak, J. 1996, "The Dispersion of Radon in the Straz-Hamr Area of the Czech Republic as an Effect af Uranium Mining and Related Activities", *Uranium exploration data and techniques applied to the preparation of radioelement maps*, Proceedings of a Technical Committee meeting, Vienna, 13–17 May 1996, pp. 353-364.

Solecki, A.T. and Tchorz-Trzeciakiewicz, D.E. 2011, "Radon exhalation from the Upper Silesian coal ashes", *Geochemical Journal,* vol. 45, pp. 491-496.

Somogyi, G., Hafez, A.H., Hunyadi, I. and Szilagly, M.T. 1986, "Measurement of exhalation and diffusion parameters of radon in solids by plastic tracks detector", *Nuclear Track Radiation Measurement,* vol. 12, no. 1-6, pp. 701-704.

South Africa.info 2012, 03 June 2012-last update, *Free State province, South Africa* [Homepage of Big Media Publishers], [Online]. Available:

http://www.southafrica.info/about/geography/free-state.htm#ixzz1tuFrBxcn [2012, June 03].

Sportisse, B. 2007, "A review of current issues in air pollution modeling and simulation", *Computational Geosciences,* vol. 11, no. 2, pp. 159-181.

Srivastava, A. 2004, "An overview of an indoor radon study carried out in dwellings in India and Bangladesh during the last decade using solid state nuclear track detectors", *Journal of Environmental Radioactivity,* vol. 78, no. 1, pp. 113-121.

Steffens, J.T., Heist, D., Perry, S. and Zhang, K.M. 2017, "Modeling the effects of a solid barrier on pollutant dispersion under various atmospheric 2 stability conditions", *International Journal of Disaster Risk Science,* vol. 5, no. 3, pp. 214-226.

Stieff, L.R., Kotrappa, P., Rechcigl, J.E. and Nobel, C. 1994, "Measurement of the radon surfacce flux from undisturbed soil using electret ion chambers", *Proceedings of the International Radon Symposium III*, pp. 2.1-2.7.

Stocker, J., Ellis, A., Smith, S., Carruthers, D., Venkatram, A., Dale, W. and Attree, M. 2016, "A review of the limitations and uncertainties of modelling pollutant dispersion from non-point sources", *Report no ADMLC/2015/06*, Cambridge: UK Atmospheric Dispersion Modelling Liaison Committee, [Online]. Available at: https://admlc.files.wordpress.com/2014/05/fm1019_cerc_admlc_final_mar16.pdf [Accessed 10 Sep. 2018].

Stohl, A., Forster, C., Frank, A., Seibert, P. and Wotawa, G. 2005, "Technical note: The Lagrangian particle dispersion model FLEXPART version 6.2", *Atmospheric Chemistry and Physics,* vol. 5, pp. 2461-2474.

Stohl, A. 1998, "Computation, accuracy and applications of trajectories—A review and bibliography", *Atmospheric Environment,* vol. 32, no. 6, pp. 947-966.

Stohl, A. 1996, "Trajectory statistics-A new method to establish source-receptor relationships of air pollutants and its application to the transport of particulate sulfate in Europe", *Atmospheric Environment*, vol. 30, no. 4, pp. 579-587.

Strydom et al 1998, "Assessment of Radiological Dose Due to Incremental Radioactivity Increases in Cleared Former Mine Land", *Proceedings of the 38th SAAPMB and the 1st SARPA Congress,* SAAPMB, South Africa, 12th to the 15th of May 1998.

Strydom, R. 2002, *Personal communication.*

Strydom, R. 2000, *Personal communication.*

Strydom, R. 1999, *Assessment of public radiological exposure via the air pathway from surface operations of Durban Roodepoort Deep Gold Mining Co Ltd*, Parc Scientific, IFAFI, South Africa.

Strydom, R. 1996, "Radon Source Terms of Identified Sources at Western Areas GM Site", Parc Scientific, Ifafi, South Africa.

Sullivan, D.A., Holdsworth, M. and Hlinka, D.J. 2004, "Monte Carlo-based dispersion modeling of off-gassing releases from the fumigant metam-sodium for determining distance", *Atmospheric Environment,* vol. 38, no. 16, pp. 2471-2481.

Taha, M.P.M., Drew, G.H., Tamer, A., Hewings, G., Jordinson, G.M., Longhurst, P.J. and Pollard, S.J.T. 2007, "Improving bioaerosol exposure assessments of composting facilities – comparative modelling of emissions from different compost ages and processing activities", *Atmospheric Environment,* vol. 41, pp. 4504-4519.

Talha, S.A., de Meijer, R.J., Lindsay, R., Newman, R.T., Maleka, P.P. and Hlatshwayo, I.N. 2010, "In-field radon measurement in water: a novel approach", *Journal of Environmental Radioactivity,* vol. 101, no. 12, pp. 1024-1031.

Tan, K., Liu, Z., Xia, L., Lv, J. and Hu, H. 2012, "The influence of fractal size distribution of covers on radon exhalation from uranium mill tailings", *Radiation Measurements,* vol. 47, no. 2, pp. 163-167.

Tan, Y., Xiao, D., Yuan, H., Tang, Q. and Liub, X. 2013, "Revision for measuring radon exhalation rate in open loop", *Journal of Instrumentation*, vol. 8, pp. T01004.

Theobald, M.R., Løfstrøm, P., Walker, J., Andersen, H.V., Pedersen, P., Vallejo, A. and Sutton, M.A. 2012, "An intercomparison of models used to simulate the short-range atmospheric dispersion of agricultural ammonia emissions", *Environmental Modelling & Software,* vol. 37, pp. 90-102.

Thomas, J.W. 1972, "Measurement of radon daughters in air", *Health Physics,* vol. 23, no. 6, pp. 783-789.

Thomas, J.W. 1970, "Modification of the Tsivoglou method for radon daughters in air", *Health Physics,* vol. 19, pp. 691.

Thomson, D.J. and Manning, A.J. 2001, "Along-Wind Dispersion In Light Wind Conditions", *Boundary-Layer Meteorology,* vol. 98, no. 2, pp. 341-358.

Tokonami, S., Iimoto, T., Ichiji, T., Fujitaka, K. and Kurosawa, R. 1996, "Continuous radon monitor using a two-filter method", *Radiation Protection Dosimetry,* vol. 63, pp. 123-126.

Tomasek, L., Rogel, A., Tirmarche, M., Mitton, N. and Laurier, D. 2008, "Lung cancer in French and Czech uranium miners: radon-associated risk at low exposure rates and modifying effects of time since exposure and age at exposure.", *Radiat Res,* vol. 169, no. 2, pp. 125-137.

Tremblay, R.J., Leclerc, A., Mathieu, C., Pepin, R. and Townsend, M.G. 1979, "Measurement of Radon Progeny Concentration in Air by Alpha Particle Counting During and After Air Sampling", *Health Physics,* vol. 36, pp. 401.

Tsivoglou, E.C., Ayer, H.E. and Holaday, D.A. 1953, "Occurrence of non-equilibrium atmospheric mixtures of radon and its daughters", *Nucleonics,* vol. 11, pp. 40.

Tufail, M., Mirza, S.M., Mahmood, A., Qureshi, A.A., Yasir Arfat, and Khan, H.A. 2000, "Application of a “closed-can” technique for measuring radon exhalation from mine samples of Punjab, Pakistan", *Journal of Environmental Radioactivity,* vol. 50, no. 3, pp. 267-275.

Turner, D 2015, "Disposal of By-products at the Douglas Mine Site, Application for Works Approval", *Technical Report NO. 141*, Kanagulk: ARPANSA. [Online]. Available at: https://www.epa.vic.gov.au/our-work/licences-and-approvals/public-participation/featured-applications/iluka-douglas-mine-site/~/media/Files/Our%20work/Iluka%20WA/Works%20approval%20application/ILUKA-_Works-Approval-Application-and-Attachments.pdf [Accessed 23 Nov. 2017].

Turner, D.B. 1970, "Workbook of atmospheric dispersion estimates", *Environmental Health Series Pollution AP-26*, U.S. EPA, Triangle Park, North Carolina. [Online]. Available at: https://nepis.epa.gov/Exe/ZyNET.exe/9101GKEZ.txt?ZyActionD=ZyDocument&Client=EPA&Index=Prior%20to%201976&Docs=&Query=&Time=&EndTime=&SearchMethod=1&TocRestrict=n&Toc=&TocEntry=&QField=&QFieldYear=&QFieldMonth=&QFieldDay=&UseQField=&IntQFieldOp=0&ExtQFieldOp=0&XmlQuery=&File=D%3A%5CZYFILES%5CINDEX%20DATA%5C70THRU75%5CTXT%5C00000022%5C9101GKEZ.txt&User=ANONYMOUS&Password=anonymous&SortMethod=h%7C-&MaximumDocuments=1&FuzzyDegree=0&ImageQuality=r75g8/r75

g8/x150y150g16/i425&Display=hpfr&DefSeekPage=x&SearchBack=ZyActionL&Back=ZyActionS&BackDesc=Results%20page&MaximumPages=1&ZyEntry=1 [Accessed 07 Aug. 2018].

U.S. EPA 2005, *Guidelines for Carcinogen Risk Assessment,* Report no EPA/630/P-03/001F, Washington, DC: Risk Assessment Forum. [Online]. Available at: https://www.epa.gov/risk/guidelines-carcinogen-risk-assessment [Accessed 10 June 2018].

U.S. EPA 1998, *A Comparison of CALPUFF with ISC3, Report no EPA-454/R-98-020*, Research Triangle Park,: Office of Air Quality Planning and Standards. [Online]. Available at: https://www3.epa.gov/scram001/7thconf/calpuff/calisc3.pdf [Accessed 04 July 2018].

U.S. EPA 1995a, *User's Guide for the Industrial Source Complex (ISC3) Dispersion Models Volume I - User Instructions, Report no EPA-454/B-95-003a*, North Carolina: Office of Air Quality Planning and Standards, Emissions, Monitoring, and Analysis Division. [Online]. Available at: https://www3.epa.gov/scram001/userg/regmod/isc3v1.pdf [Accessed 28 May 2018].

U.S. EPA 1995b, *User's Guide for the Industrial Source Complex (ISC3) Dispersion Models Volume I - User Instructions, Report no EPA-454/B-95-003b*, North Carolina: Office of Air Quality Planning and Standards, Emissions, Monitoring, and Analysis Division. [Online]. Available at: https://www3.epa.gov/scram001/userg/regmod/isc3v2.pdf [Accessed 06 May 2018].

U.S. EPA 1993, *Selection Criteria for Mathematical Models Used in Exposure Assessments: Atmospheric Dispersion Models, Report no EPA/600/8-91/038*, Washington, DC: Office of Air Research and Development. [Online]. Available at: https://nepis.epa.gov/Exe/ZyNET.exe/30001LIV.TXT?ZyActionD=ZyDocument&Client=EPA&Index=1991+Thru+1994&Docs=&Query=&Time=&EndTime=&SearchMethod=1&TocRestrict=n&Toc=&TocEntry=&QField=&QFieldYear=&QFieldMonth=&QFieldDay=&IntQFieldOp=0&ExtQFieldOp=0&XmlQuery=&File=D%3A%5Czyfiles%5CIndex%20Data%5C91thru94%5CTxt%5C00000001%5C30001LIV.txt&User=ANONYMOUS&Password=anonymous&SortMethod=h%7C-&MaximumDocuments=1&FuzzyDegree=0&ImageQuality=r75g8/r75g8/x150y150g16/i425&Display=hpfr&DefSeekPage=x&SearchBack=ZyActionL&Back=ZyActionS&BackDesc=Results%20page&MaximumPages=1&ZyEntry=1&SeekPage=x&ZyPURL [Accessed 28 May 2018].

U.S. EPA 1992, *Indoor Radon and Radon Decay Product Measurement Device Protocols, Report no EPA-402-R-92-004*, Washington, DC: Office

of Radiation Programs. [Online]. Available at: https://nepis.epa.gov/Exe/ZyNET.exe/94001H1B.txt?ZyActionD=ZyDocument&Client=EPA&Index=1991%20Thru%201994&Docs=&Query=&Time=&EndTime=&SearchMethod=1&TocRestrict=n&Toc=&TocEntry=&QField=&QFieldYear=&QFieldMonth=&QFieldDay=&UseQField=&IntQFieldOp=0&ExtQFieldOp=0&XmlQuery=&File=D%3A%5CZYFILES%5CINDEX%20DATA%5C91THRU94%5CTXT%5C00000034%5C94001H1B.txt&User=ANONYMOUS&Password=anonymous&SortMethod=h%7C-&MaximumDocuments=1&FuzzyDegree=0&ImageQuality=r75g8/r75g8/x150y150g16/i425&Display=hpfr&DefSeekPage=x&SearchBack=ZyActionL&Back=ZyActionS&BackDesc=Results%20page&MaximumPages=1&ZyEntry=1 [Accessed 18 Apr. 2017].

UNSCEAR 2008, *Sources and Effects of Ionizing Radiation, Report to the General Assembly with Scientific Annexes*, United Nations Scientific Committee on the Effects of Atomic Radiation, United Nations, New York.

UNSCEAR 2000, *Report to the General Assembly, with Scientific Annexes: Sources and effects of ionizing radiation*, United Nations Scientific Committee on the Effects of Atomic Radiation, United Nations, New York.

van As, D., Leuschner, A., Bain, C. and Grundling, A. 1992, Public Exposure to Radioactivity from Mine Dumps through Atmospheric and Aquatic Pathways. In: *Workshop on the Disposal of Mining Waste*. Midrand, 12 - 13 Nov. 1992.

van Vuuren, D.B.J., Strydom, R., Roberts, D.A. and van der Linde, A. 1995, *GU9301: Final Report. Assessment of the radiological impact to the public from surface works on mines: Radon and dust exposure pathways*, CSIR, Auckland Park, South Africa.

Venegas, L.E. and Mazzeo, N.A. 1999, "Atmospheric stagnation, recirculation and ventilation potential of several sites in Argentina", *Atmospheric Research,* vol. 52, no, 1, pp. 43-57.

Venkatram, A., Isakov, V., Yuan, J. and Pankratz, D. 2004, "Modeling dispersion at distances of meters from urban sources"*, Atmospheric Environment,* vol. 38, no. 28, pp. 4633-4641.

Vinuesa, J.F. and Galmarini, S. 2007, "Characterization of the 222Rn family turbulent transport in the convective atmospheric boundary layer", *Atmospheric Chemistry and Physics,* vol. 7, pp. 697-712.

von Oertzen, G., Gaoseb, F., Schneeweiss, R., Cloete, R. and Mutota, A. 2016, *Radiation Management Plan, Report no JK20/MMP/001*, Namibia: Rössing Uranium Limited. [Online]. Available at:

https://www.rossing.com/files/reports-research/Rossing%20Uranium%20Radiation%20Management%20Plan%202016.pdf [Accessed 24 September 2018].

Watson, S.J., Jones, A.L., Oatway, W.B. and Hughes, J.S. (2005) *Ionising Radiation Exposure of the UK Population: 2005 Review, Report no HPA-RPD-001*, Oxfordshire: Public Health England. [Online]. Available at: https://www.gov.uk/government/publications/ionising-radiation-exposure-of-the-uk-population-2005-review [Accessed 14 June 2012].

Wendel, G. 1998, "Radioactivity in mines and mine water—sources and mechanisms", *The Journal of The South African Institute of Mining and Metallurgy,* vol. 98, no. 2, pp. 87-92.

Whittlestone, S. and Zahorowski, W. 1998, "Baseline radon detectors for shipboard use: development and deployment in the First Aerosol Characterization Experiment (ACE 1)", *Journal of Geophysical Research,* vol. 103, pp. 16743-16751.

WHO 2009, "Radon measurements" in *WORLD HEALTH ORGANISATION HANDBOOK ON INDOOR RADON: A PUBLIC HEALTH PERSPECTIVE*, ed. Hajo Zeeb, and Ferid Shannoun, WHO Press, Geneva, Switzerland, pp. 2`.

Wilkening, M.H., Clements, W.E., & Stanley, D. 1972, "Radon 222 flux measurements in widely separated regions (CONF-720805--P2)". Gesell, T.F. (Ed.). United States

Willmott, C.J. 1982, "Some Comments on the Evaluation of Model Performance", *American Meteorological Society,* vol. 63, no. 11, pp. 1309-1313.

Willmott, C.J. and Wicks, D.E. 1980, "An Empirical Method for the Spatial Interpolation of Monthly Precipitation Within California", *Physical Geography,* vol. 1, pp. 59-73.

Winde, F. and Sandham, L.A. 2004, "Uranium pollution of South African streams - An overview of the situation in gold mining areas of the Witwatersrand", *GeoJournal,* vol. 61, no. 2, pp. 131-149.

Windfinder. 2019. Wind & weather statistics Welkom Airport - Windfinder . [ONLINE] Available at: https://www.windfinder.com/windstatistics/welkom. [Accessed 01 October 2019].

Winkler, R., Ruckerbauer, F., Trautmannsheimer, M., Tschiersch, J. and Karg, E. 2001, "Diurnal and seasonal variation of the equilibrium state between short-lived radon decay products and radon gas in

ground-level air ", *Radiation and Environmental Biophysics,* vol. 40, pp. 115-123.

Woebkenberg, M.L. and Woodfin, W.J. 1983, "NIOSH-developed systems for monitoring equipment evaluations", *Proceedings of Third Annual National Symposium on Recent Advances in the Measurement of Pollutants in Ambient Air and Stationary Sources.* Raleigh, NC: EPA-600/9-84-00

Wortmann, H. 2007, *Sedimentation and desication of gold mine tailings*, Master of Engineering (Geotech) edn, University of Pretoria, Pretoria.

Wu, Q., Pan, Z., Liu, S. and Wang, C. 2016, "Outdoor radon concentration in China", *Nukleonika,* vol. 61, no. 3, pp. 373-378.

Wymer, D. 1997, "Exclusion, exemption and clearance in the mining and minerals industry: Practical application to South African operations", *Proceedings of a specialists' meeting on application of the concepts of exclusion, exemption and clearance: Implications for the management of radioactive materials Working material,* International Atomic Energy Agency (IAEA), Vienna, 6 - 9 May 1997, pp. 302.

Xie, D., Wang, H. and Kearfott, K.J. 2012, "Modeling and experimental validation of the dispersion of 222Rn released from a uranium mine ventilation shaft", *Atmospheric Environment,* vol. 60, no. 0, pp. 453-459.

Xie, D., Wang, H., Kearfott, K.J., Liu, Z. and Mo, S. 2014, "Radon dispersion modeling and dose assessment for uranium mine ventilation shaft exhausts under neutral atmospheric stability", *Journal of Environmental Radioactivity,* vol. 129, no. 0, pp. 57-62.

Yamasaki, T., Iida, T., Shimo, M. and Ikebe, Y. 1995, "Continuous Measurements of Outdoor Radon and Its Progeny Concentrations", *Japanese Journal of Health Physics,* vol. 30, no. 2, pp. 149-154.

Yegnan, A., Williamson, D.G. and Graettinger, A.J. 2003, "Corrigendum to “Uncertainty analysis in air dispersion modeling” [Environmental Modelling and Software 17 (7) 639–649 (2002)]", *Environmental Modelling and Software,* vol. 18, no. 4, pp. 393.

Yegnan, A., Williamson, D.G. and Graettinger, A.J. 2002, "Uncertainty analysis in air dispersion modeling", *Environmental Modelling & Software,* vol. 17, no. 7, pp. 639-649.

Yousef, H.A., El-Farrash, A.H., Ela, A.A. and Merza, Q. 2015, "Measurement of Radon Exhalation Rate in Some Building Materials Using Nuclear Track Detectors", *World Journal of Nuclear Science and Technology,* vol. 5, pp. 141-148.

Youssef, H.A., Embaby, A.A., El-Farrash, A.H. and Laken, H.A. 2015, "Radon Exhalation Rate in Surface Soil of Graduate's Villages in West Nile Delta, Egypt, Using Can Technique", *International Journal of Recent Scientific Research,* vol. 6, no. 4, pp. 3440-3446.

Yu, L., Mallants, D. and Olyslaegers, G. 2011, "Assessment of radon release from concrete components in the Dessel low-level waste near surface disposal facility", *Report no CO-90-10-2446-00,* SCK•CEN, Brussel, Belgium.

Yu, K.N., Young, E.C.M., Stokes, M.J. and Lo, C.H. 1997, "A survey of radon properties in underground shopping centers in Hong Kong", *Applied Radiation and Isotopes,* vol. 48, no. 6, pp. 863-866.

Zannetti P. (ed) 1990, *Gaussian Models. In: Air Pollution Modeling*, Springer, Boston, MA.

Zannetti, P. (ed) 1990, *Air Pollution Modeling: Theories, Computational Methods and Available Software*, 1st edn, Springer US, New York.

Zefon International 2018, *, Filter Membranes and Media.* Available: http://www.zefon.com/store/air-monitoring-filter-media/.

Zhuo, W., Furukawa, M. and TokonamiI, S. 2007, "A Naturally Ventilated Accumulator for Integrating Measurements of Radon Flux from Soil", *Journal of Nuclear Science and Technology,* vol. 44, no. 8, pp. 1100-1105.

Zoumakis, N.M. 1998, "Characteristics of Maximum Concentrations from Multiple Point Sources", *Journal of Applied Meteorology,* vol. 37, pp. 730-739.